

# UC Santa Barbara

## UC Santa Barbara Electronic Theses and Dissertations

### Title

Thermodynamic measurements of ultra-clean van der Waals heterostructures

### Permalink

<https://escholarship.org/uc/item/9p65j39g>

### Author

Zibrov, Alexander A

### Publication Date

2019

Peer reviewed|Thesis/dissertation

University of California  
Santa Barbara

# Thermodynamic measurements of ultra-clean van der Waals heterostructures

A dissertation submitted in partial satisfaction  
of the requirements for the degree

Doctor of Philosophy  
in  
Physics

by

Alexander A. Zibrov

Committee in charge:

Professor Andrea Young, Chair  
Professor David Weld  
Professor Cenke Xu

September 2019

The Dissertation of Alexander A. Zibrov is approved.

---

Professor David Weld

---

Professor Cenke Xu

---

Professor Andrea Young, Committee Chair

August 2019

Thermodynamic measurements of ultra-clean van der Waals heterostructures

Copyright © 2019

by

Alexander A. Zibrov

For my wife Alla, Tuba the dog and Maks the cat.

## Acknowledgements

This goes without saying, but the work presented in this thesis is a result of dedicated work by many people. I would like to start with François Parmentier for being a friend and helping me get oriented in the field at the early stages of setting up the lab, and Leo Li for always having good advice and for teaching me how to make van der Waals heterostructures.

I could not be more grateful to the people that I did experiments with once the lab got off the ground and with whom I've been improving our fabrication techniques. This is a shout out of course to Haoxin Zhou and Carlos Kometter. Haoxin, your artistic approach to cleanroom procedures were essential to the lab's success. Carlos, I have learned to rely on the electronics you've built and I can't imagine doing measurements without them; thank you for being my friend and supporting my former-Linux-nerd obsessions with automating things and "neat" programming.

Eric Spanton, I know that I can always ask you a question, no matter how stupid, and that I can always count on a thoughtful and sincere answer. Your knowledge and understanding of physics are something I strive to reach.

I would like to thank Mike Zaletel, our go-to theorist — there was never a question you could not answer. Maksym Serbyn and Rao Peng, thank you for your help with the trilayer graphene paper.

A big thank you to the Young lab (Fig. 0.1). I really benefited from the expertise brought by the postdocs Joshua Island, Gregory Polshyn, Fangyuan Yang and Yu Saito; and the hard work, blood and sweat of the undergrads that set an admirable standard for all of us in the lab. Marec Serlin and Charlie Tschirhart, we shared many laughs together and now that you've begun to reap the rewards from your experiments I am rooting for you and excited to see what comes next! Liam Cohen and Alex Potts, I am

sad to be leaving so soon after you have joined the lab, as I had a great time working with you!

And finally, I would like to thank Andrea Young. You've put us all together and made the magic of physics happen. Whenever things went wrong in the experiments, it was your infectious passion and drive that helped me plow through. *Thank you!*

And finally-finally, I would like to thank my parents and my wife Alla for their support. I am forever grateful to Alla for letting me pursue my passion for physics 6000 miles away.



Figure 0.1: Young Lab (left to right): Alex Cui, François Parmentier, Rex Bai, Joey Incandela, Raymond Zhu, James Ehrets, Avi Shragai, Carlos Kometter, Eric Spanton, Andrea Young, Haoxin Zhou, Marec Serlin, Charles Tschirhart, Yuxuan Zhang, Fangyuan Yang, Alex Potts, Joshua Island, Yu Saito, Liam Cohen and Grisha Polshyn, *thank you guys!*

# Curriculum Vitæ

Alexander A. Zibrov

## Education

- 2019 Ph.D. in Physics (Expected), University of California, Santa Barbara.
- 2017 M.A. in Physics, University of California, Santa Barbara.
- 2011 M.A. (equivalent) in opto-electronic device engineering, Bauman Moscow State Technical University, Moscow, Russia.

## Publications

1. **A. A. Zibrov**, P. Rao, C. Kometter, E. M. Spanton, J. I. A. Li, C. R. Dean, T. Taniguchi, K. Watanabe, M. Serbyn, A. F. Young. “Emergent Dirac gullies and gully-symmetry breaking quantum Hall states in ABA trilayer graphene.” *Physical Review Letters*, **121**, 167601 (2019)
2. **A. A. Zibrov**<sup>†</sup>, E. M. Spanton<sup>†</sup>, H. Zhou, C. Kometter, T. Taniguchi, K. Watanabe, A. F. Young. “Even-denominator fractional quantum Hall states at an isospin transition in monolayer graphene.” *Nature Physics*, **14**, pp. 930-935 (2018).
3. E. M. Spanton<sup>†</sup>, **A. A. Zibrov**<sup>†</sup>, H. Zhou, T. Taniguchi, K. Watanabe, M. P. Zaletel, A. F. Young. “Observation of fractional Chern insulators in a van der Waals heterostructure.” *Science*, **360**(6384), pp. 62-66 (2018)
4. B.M. Hunt, J.I.A. Li, **A. A. Zibrov**, L. Wang, T. Taniguchi, K. Watanabe, J. Hone, C. R. Dean, M. Zaletel, R.C. Ashoori, A. F. Young. “Direct measurement of discrete valley and orbital quantum numbers in bilayer graphene.” *Nature Communications* **8**, Article number: 948 (2017).
5. **A. A. Zibrov**, C. R. Kometter, T. Taniguchi, K. Watanabe, M. P. Zaletel, A. F. Young. “Tunable interacting composite fermion phases in a half-filled bilayer graphene Landau level.” *Nature*, **549**, pp. 360-364 (2017).

<sup>†</sup> Equal contributions



## Abstract

Thermodynamic measurements of ultra-clean van der Waals heterostructures

by

Alexander A. Zibrov

When interactions between electrons dominate over their kinetic energies, this can lead to emergent collective states with new quantum degrees of freedom described in terms of quasiparticles. These collective states can fall into two distinct categories: either the interactions lead to a breaking of an underlying symmetry, or electrons can form topologically ordered states characterized by a degenerate ground state in the zero temperature limit. The condition for strong interactions is met in two-dimensional electron systems (2DES) immersed in high magnetic fields, where electron kinetic energies quench into a ladder of dispersionless Landau levels broadened by disorder. Landau levels are an example of a topological band, characterized by a Chern number  $\mathcal{C} \in \mathbb{Z}$ . Correlated electron states then appear at partial filling of a Landau level — these are called fractional quantum Hall states.

In this thesis, I present a series of magneto-capacitance measurements of the thermodynamic density of states of low-disorder dual-gated graphene/boron nitride heterostructures – two-dimensional materials that can be isolated and later reassembled into stacks of designer properties. In such devices, we observe the elusive even-denominator fractional quantum Hall states at half filling of mono- and bilayer graphene. For monolayer graphene, we propose a scenario where the observed states are multicomponent states that incorporate correlations between electrons on different carbon sublattices. In the bilayer graphene case, the observed even-denominator states are single-component and potentially host non-Abelian excitations, i.e. quasiparticles with fractional statistics,

that are neither fermions or bosons.

Moreover, if we introduce a twist between the graphene and boron nitride layers, a periodic moiré potential will appear. As a result of the interplay between a magnetic field and the moiré potential, new Hofstadter bands with Chern numbers  $\mathcal{C} \neq 1$  can arise, in which we observe fractional Chern insulators — a generalization of fractional quantum Hall states to bands with a higher Chern index.

# Contents

<b>Curriculum Vitae</b>	<b>vii</b>
<b>Abstract</b>	<b>viii</b>
<b>1 Introduction</b>	<b>1</b>
<b>2 van der Waals materials in high magnetic fields</b>	<b>7</b>
2.1 Integer (IQHE) and fractional (FQHE) quantum Hall effects . . . . .	7
2.2 van der Waals heterostructures . . . . .	17
2.3 Graphene . . . . .	21
<b>3 Capacitive probe of the density of states of 2DEGs</b>	<b>28</b>
3.1 Overview . . . . .	28
3.2 Example: Capacitance probe of trilayer graphene band structure . . . . .	31
<b>4 Even-Denominator FQH effect in monolayer graphene</b>	<b>45</b>
<b>5 Even-Denominator FQH effect in bilayer graphene</b>	<b>59</b>
<b>6 Fractional Chern Insulators in bilayer graphene</b>	<b>75</b>
<b>7 Outlook</b>	<b>88</b>
<b>A Capacitance Bridge</b>	<b>93</b>
A.1 Penetration field capacitance . . . . .	93
A.2 Symmetric and anti-symmetric capacitances in BLG . . . . .	94
A.3 Lumped model . . . . .	98
A.4 How to make a transistor mount? . . . . .	101
<b>B Supplementary materials for Chapter 3</b>	<b>104</b>
B.1 Model and Methods . . . . .	104
B.2 Refinement of tight-binding parameters . . . . .	109

B.3	Effect of interactions: Hartree Fock approximation . . . . .	118
<b>C</b>	<b>Supplementary materials for Chapter 4</b>	<b>126</b>
C.1	Materials and Methods . . . . .	126
C.2	Supplementary Figures . . . . .	127
C.3	Calculation of $\nu = 0$ phase diagram . . . . .	139
<b>D</b>	<b>Supplementary materials for Chapter 5</b>	<b>143</b>
D.1	Device fabrication . . . . .	143
D.2	Capacitance circuit . . . . .	144
D.3	Measurement of electronic compressibility and thermodynamic energy gaps	147
D.4	Measurement of layer polarizability, $\partial p/\partial p_0$ . . . . .	150
D.5	Single particle model . . . . .	154
D.6	Numerical simulations . . . . .	155
D.7	Additional data . . . . .	165
<b>E</b>	<b>Supplementary materials for Chapter 6</b>	<b>174</b>
E.1	Materials and methods . . . . .	174
E.2	Supplementary text . . . . .	176
	<b>Bibliography</b>	<b>207</b>

# Chapter 1

## Introduction

An isolated electron is relatively simple to describe, but a collection of many electrons can be more than just the sum of its parts. In a metal, electrons can superconduct if cooled below a critical temperature, but the behavior of a sole electron cannot immediately explain this phenomenon. The essence of this problem is captured by *emergence* (Fig. 1.1a), the existence of some organizational law that causes the many-body system to behave differently from its interacting constituents. Collective states of many electrons can be conveniently described in terms of *quasi-particles*, emergent long-lived quantum degrees of freedom whose quantum numbers can differ dramatically from those of the constituent electrons. These quasi-particles can be created, destroyed, detected and ultimately manipulated in a physics experiment, giving us a glimpse into the underlying electron correlations.

If the interactions between electrons are much stronger than any other energy scale, the resulting collective states can fall into two distinct categories: either the interactions lead to a breaking of underlying symmetries, or electrons can form topologically ordered states characterized by a degenerate ground state in the limit of zero temperature. In this thesis, I show examples of both. The textbook example of a state with topological

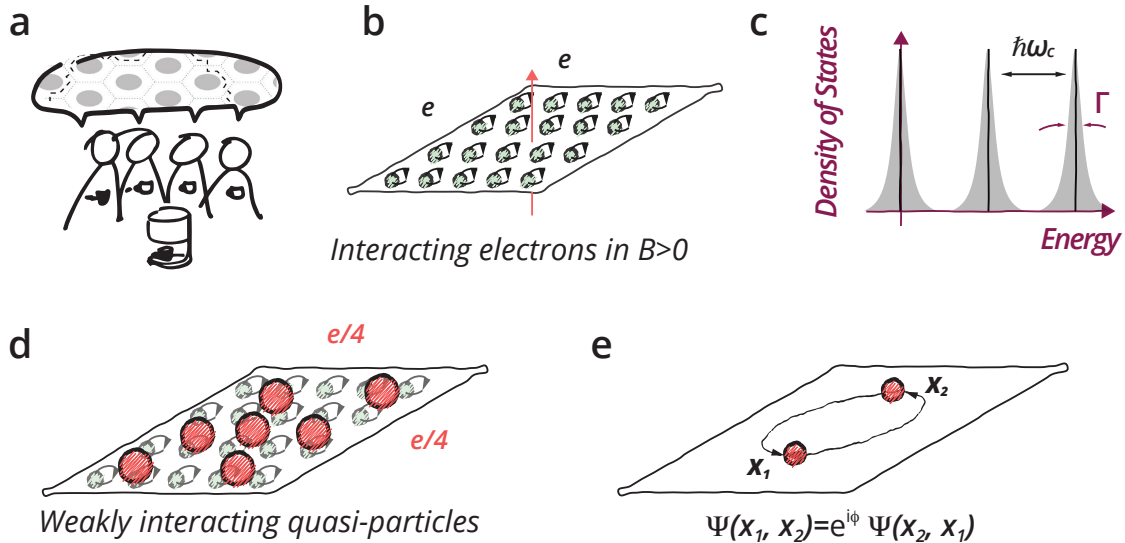



Figure 1.1: **a** Ideas emerging from social interactions at the coffee machine. **b** Electrons in a magnetic field move in cyclotron orbits. Their energies **c** are quantized to integer values of  $\hbar\omega_c$  ( $\omega_c$  is the cyclotron frequency). The spectrum of allowed energy levels is broadened by disorder  $\Gamma$ . **d** If the Coulomb interaction strength  $E_c \gg \Gamma$  the system is considered strongly interacting and is complicated to analyze, though it could be treated as a system of non- (or weakly) interacting emergent FQH quasiparticles in an effective zero magnetic field. These quasiparticles would have new quantum numbers; for example, they can have a fractional  $e/4$  charge. **e** If such quasiparticles are exchanged the wavefunction  $\Psi(x_1, x_2)$  would gain a phase  $\varphi \neq 0, \pi$ , identifying these particles as neither bosons or fermions. These particles are called *anyons*; for the  $e/4$  quasiparticles the phase  $\varphi$  is a matrix — such anyons are *non-abelian*.

order, and for that matter the focus of this thesis, is the fractional quantum Hall (FQH) state that occurs in two-dimensional (2D) electron systems (2DES) in strong magnetic fields (Fig. 1.1). In such a state, the collective motion of interacting electrons results in quasi-particle excitations with fractional charges  $e/3$ ,  $e/4$ ,  $e/5$  and so on. These quasi-particles no longer adhere to the familiar dichotomy of bosons and fermions. If two FQH quasi-particles are exchanged, the wavefunction describing the composite system would gain a phase  $\varphi$  that is different from the  $\varphi = 0$  for bosons and  $\varphi = \pi$  for fermions, these particles are named *anyons*. In fact, the gained phase is not necessarily a scalar at all, it could also be represented by a matrix — such quasi-particles are called non-abelian

anyons and have been proposed as a building block of quantum computers. The ground state of a group of non-abelian anyons is exponentially degenerate in the number of particles. The exact state from this degenerate manifold is determined by the sequence of mutual particle exchanges (*braiding* operations) — a prerequisite to quantum gate operations [1]. To date, no experiment has definitively demonstrated the non-abelian properties of anyons. At the same time, numerical studies of real strongly-interacting electron states are notoriously complicated, with studies of some FQH states limited to only a dozen electrons even with powerful modern computers, making highly controlled experimental platforms a necessity in understanding these states.

The experimental realization of strongly interacting electron systems relies on the engineering of flat potential energy bands, where the kinetic energy scale is dwarfed by that of the electron-electron interactions. Landau levels are one example of flat bands, realized by confining electrons to two dimensions and further quenching their kinetic energy by applying a large external magnetic field which drives electrons to move in cyclotron orbits [2]. Systems in which two dimensional electrons can be found include the interfaces of semiconducting heterostructures, surfaces of 3D topological insulators and, starting from the successful isolation of graphene in 2004, atomically-thin 2-dimensional materials [3, 4]. Today, the family of 2D materials includes semiconductors, insulators, magnetic materials and superconductors [5]. By assembling these materials layer-by-layer, one can create structures with designer properties leading to a slew of potential experiments to explore different interaction phenomena: FQH [6, 7, 8, 9, 10], Mott-like insulators [11, 12], superconductivity [13, 14] and others. However, the presence of disorder in a system significantly impedes observation of these phenomena. In Landau  levels, for example, the electronic bandwidth is driven solely by disorder. Realizing a low-disorder tunable Landau level system is thus the central experimental challenge for exploring interacting physics in 2D systems in a magnetic field. However, the require-

ments of tunability and cleanliness can be at odds. For instance, the Landau level electron density can be conveniently tuned by electrostatic gating; however, metallic gates can introduce enough disorder to destroy the weak FQH state. Here we present experiments enabled by advances in fabrication of extremely clean graphene heterostructures. This not only allowed us to reproduce the interacting electron phases that were the hallmark of the cleanest GaAs/AlGaAs heterostructure systems [15], but also to open up new possibilities for probing elusive emergent phenomena.

The following chapters will describe several interconnected experiments that probe strongly-interacting electron systems confined to the effectively 2D plane of several atomic-layer-thick graphite sheets (mono-, bi- and trilayer graphene). In these experiments we greatly reduced the disorder caused by the proximity of imperfect electrostatic gates. Additionally, most reported studies of the FQH effect focus on performing electron transport measurements (measuring sample resistance), where the measurements probe the *edge states* propagating along sample boundaries and are affected by the quality of the edge-state to contact coupling. In contrast, the work presented in this thesis focuses on measuring the thermodynamic *bulk* properties of graphene heterostructures by measuring the capacitance between the electrostatic gates and the 2D electrons. The signal strength from the bulk scales with the device area, and is virtually unaffected by the physics at the edge. The details of the measurement technique are presented in Chapter 3.1.

**This thesis is structured as follows:**

**Chapter 2** introduces two dimensional electron systems in high magnetic fields. The discussion starts with a semiclassical description of flat energy bands — Landau levels, where the only length scale is that set by the magnetic field, and the ef-



fects of the underlying lattice are incorporated through an electron effective mass. I then describe the single-particle (integer quantum Hall) and interaction-driven (fractional quantum Hall and symmetry broken states) effects that arise in Landau levels. I then reintroduce the lattice into the problem and describe the new states that originate from the competition of the lattice and magnetic length scales. I conclude this chapter with a description of van der Waals heterostructures with a focus on graphene and its properties.

**Chapter 3** describes the capacitance measurement technique we use to probe the thermodynamic density of states of graphene devices. I illustrate the capabilities of this technique with an example applied to trilayer graphene, where we investigate the transformations of the Fermi surface topology in response to an applied electric field.

**Chapter 4** describes experiments in high-quality dual-graphite-gated monolayer graphene devices, where we observed a multitude of odd-denominator fractional quantum Hall states, as well as even-denominator states at filling factors  $\nu = \pm 1/4, \pm 1/2$ . The presence of even-denominator fractional quantum Hall states in the zero energy Landau level of monolayer graphene came as a surprise; thus, we propose a scenario in which the observed states are multicomponent states which incorporate correlations between electrons on different carbon sublattices.

**Chapter 5** describes experiments in high-quality dual-graphite-gated monolayer graphene devices in which we observe even-denominator fractional quantum Hall states. These states are observed in regimes where the electron wavefunctions are single-component, suggesting a Pfaffian phase that is predicted to host non-Abelian anyons.

**Chapter 6** describes capacitance measurements of a bilayer graphene device subjected to a Moiré potential induced by the beating of the nearly matching boron nitride and graphene lattice constants. In a high magnetic field, this gives rise to a fractal energy band structure called the Hofstadter butterfly. The bands are topologically non-trivial generalizations of Landau levels and also show interaction-induced symmetry-breaking and emergent topologically ordered states.

**Chapter 7** concludes the thesis with an experimental proposal of how the ground state degeneracy of non-Abelian anyons could be probed by measuring the changes of the system's chemical potential in response to a varying temperature.

# Chapter 2

## van der Waals materials in high magnetic fields

### 2.1 Integer (IQHE) and fractional (FQHE) quantum Hall effects

Quantum mechanics defines the discrete energy levels electrons are allowed to occupy. If the separation between levels is negligible, we speak of continuous energy *bands* that are separated from other bands by *energy gaps*. If interactions are not included in this picture, electrons will occupy the lowest available energy state. However, if interactions via Coulomb repulsion are included, the sequence in which the energy levels are filled can be altered in order to minimize the total electron energy. Emergent phenomena require *flat bands* — an engineered environment where electron-electron interactions ( $E_c$ ) dominate over the range (or *bandwidth*  $BW$ ) of allowed kinetic energies  $E_c \gg BW$  (Fig. 2.1 a). In this case, the Coulomb energy can be minimized if the electron's degrees of freedom become strongly correlated. The most well known recipe for creating flat

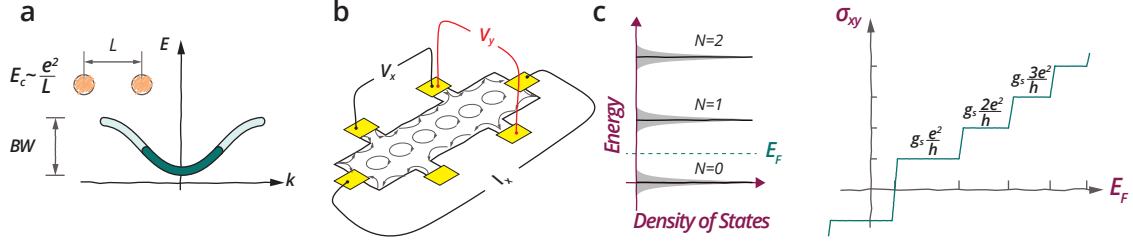


Figure 2.1: **a.** Cartoon of a flat band. If the spread of available energy states ( $BW$ ) is smaller than the energy of Coulomb repulsion between electrons, the interactions are considered strong. **b.** Typical Hall measurement: a current  $I_x$  is sourced, while voltage drops  $V_x$  and  $V_y$  are recorded. The measurement yields longitudinal  $\sigma_{xx} = R_{xx}^{-1} = V_x/I_x$  and Hall  $\sigma_{xy} = R_{xy}^{-1} = V_y/I_x$  conductivities. **c.** The energy spectrum of 2D electrons in a magnetic field is a series of highly degenerate Landau levels. If the Hall conductivity is measured as a function of the Fermi energy (e.g. tuned by electrostatic doping) then a series of quantized steps is revealed - each filled Landau level adds  $\Delta\sigma_{xy} = g_s e^2/h$  to the conductivity, where  $g_s$  accounts for spin degeneracy

bands is to place a 2DES in a perpendicular magnetic field.

In the semi-classical picture, when the magnetic field is turned on, the electrons start moving in cyclotron orbits with a characteristic length scale  $l_b = \sqrt{\frac{\hbar}{eB}} \approx 26\text{nm}/\sqrt{B[\text{Tesla}]}$  called the *magnetic length*. The electron's kinetic energy quenches to a ladder of discrete *Landau levels* separated by the cyclotron energy gap  $\hbar\omega_c$ . Each Landau level has a large degeneracy  $N = \Phi/\Phi_0$  determined by the total magnetic flux  $\Phi = B \cdot A$  passing through the 2DES of area  $A$ , where  $\Phi_0 = h/e$  is the magnetic flux quantum. With the above relations, the areal electron density of a filled Landau level is

$$n_0 = \frac{N}{A} = \frac{BA}{h/e} = (2\pi l_b^2)^{-1}, \quad (2.1)$$

where all of the electrons are occupying states with the same energy ( $BW \rightarrow 0$ ). However, Landau levels in real systems are broadened by disorder, resulting in a finite bandwidth  $BW \sim \Gamma$  (Fig. 1.1 c.). Thus the condition for strong interactions is  $E_c \sim e^2/l_b \gg \Gamma$ .

Landau levels manifest themselves most directly as the integer quantum Hall effect (IQHE) (Fig. 2.1). In experiments, a 2DES (in the X-Y plane) is subjected to a perpen-

dicular magnetic field  $B_{\perp} = |B|\hat{z}$ . A current  $I_x$  is passed through the system and parallel ( $V_x$ ) and transverse ( $V_y$ ) voltage drops are measured. If we add electrons to the 2DES<sup>1</sup>, filling the Landau levels one at a time, the measured *Hall conductivity*  $\sigma_{xy} = V_y/I_x$  would reveal a series of quantized steps separated by  $g_s e^2/h^2$ , where  $g_s$  is the spin degeneracy. The steps in conductivity occur whenever a Landau level is fully occupied. It is convenient to talk about Landau level occupation in terms of a dimensionless **filling factor**, defined as:

$$\nu = \frac{n}{n_0} = n \cdot 2\pi l_b^2 \quad \nu \in \mathbb{Z} \longrightarrow \text{IQHE} \quad (2.2)$$

At the same time, Landau levels can be thought of as a band insulator, and whenever the Fermi energy is inside the cyclotron gap, there is a large energy cost associated with adding the next electron. The longitudinal conductivity ( $\sigma_{xx}$ ) is zero inside a gap and finite inside a Landau level, where a small change in the Fermi energy is linked to a significant change in electron density. Analogously to the thermodynamic compressibility of a liquid  $\kappa = -\frac{1}{V} \frac{\partial V}{\partial P} \Big|_N$ , where  $V$  is the system's volume and  $P$  is the applied pressure, it is convenient to define *electronic compressibility*:

$$\kappa = \left( n^2 \frac{\partial \mu}{\partial n} \right)^{-1}, \quad (2.3)$$

where  $n$  is the electron density and  $\mu$  is the chemical potential. The electronic compressibility signifies the amount of charge flowing into the system if the chemical potential is slightly increased. Throughout this work the prefactor  $1/n^2$  will be omitted and  $\kappa \sim \frac{\partial n}{\partial \mu}$ , which is the *thermodynamic density of states* (DOS). The two will be used interchange-

<sup>1</sup>In most experiments on 2DES realized in semiconductor heterostructures, changing the electron density is challenging. Instead it is fixed and determined by the growth conditions, and to measure Hall resistance, the magnetic field  $B$  is swept, tuning the cyclotron energy gap. Whenever the Landau level energy lines up with the Fermi level, a change in Hall conductivity is detected.

<sup>2</sup> $h/e^2 = R_K = 25812.80745 \dots \Omega$  is called the von Klitzing constant and is used in metrology to maintain the value of electrical resistance.

ably and the observed states will be described as *compressible* (large DOS, e.g. inside a Landau level) and *incompressible* (low DOS, e.g. in a gap).

### Role of topology

Surprisingly, the *exact* quantization of the Hall conductivity stands in sharp contrast to the broad range of devices of varying quality in which it has been observed. Semiclassically, the quantized conductivity can be understood from noting that while the electrons in the bulk of the system are bound to move in cyclotron orbits (i.e. electrons are localized) and cannot contribute to the current flow, the electrons at the boundaries cannot close their orbit and *skip* along the edges of the system (Fig. 2.1b), forming extended states that each contribute  $e^2/h$ . If one imagines some depressions in the boundaries of the quantum Hall device, they would not affect the skipping orbits, and the Hall conductivity would remain unchanged. The quantum Hall effect is not dependent on the geometric details of the device, or on how disordered the sample is: the Hall conductivity always carries the same exact value of  $e^2/h$  and is a *topological invariant*.

Topological properties can be identified by examining the geometry of the band, where for every momentum value  $k$ , a local geometric curvature  $b(k)$  called *Berry curvature* can be defined. For electrons in 2D in a magnetic field, the closed path integral of  $b(k)$  over the whole band (first Brillouin zone,  $k \in BZ$ ) yields the Hall conductivity [16]:

$$\sigma_{xy} = \frac{e^2}{h} \frac{1}{2\pi} \int_{\mathbf{k}} b(\mathbf{k}) d\mathbf{k} = \frac{e^2}{h} C, \quad \text{where } C \in \mathbb{Z} \quad (2.4)$$

described by an integer  $C$  called the *Chern number*. Landau levels have  $C = 1$  and carry Hall conductivity  $1 \cdot e^2/h$ . Since the Chern number is an integer, it cannot smoothly change. At a boundary of two phases described by different Chern numbers, e.g. the boundary between a 2DES in the quantum Hall regime ( $C = 1$ ) and vacuum ( $C = 0$ ), an intermediary edge state must exist.

### Symmetry breaking and quantum Hall ferromagnetism

One of the effects interactions have on many-body electron states is the breaking of underlying symmetries. Ferromagnetism in metals is an example of spontaneously broken symmetry. Electrons are subjected to exchange and Coulomb interactions. If the interactions are strong, Coulomb energy can be minimized if the electron spins align with each other, spontaneously breaking the spin symmetry and opening an *exchange* gap between the spin- $\uparrow$  and spin- $\downarrow$  states.[17].

In a magnetic field, the Zeeman energy would break the  $g_s = 2$  spin degeneracy and, naively, would “freeze” out any spin dynamics. This turns out to not be the case. With the case of graphene in mind, the Zeeman energy splitting  $E_z = g\mu_B B = 0.115B/\text{Tesla}$  meV, where  $g = 2$  is the gyromagnetic ratio and  $\mu_B$  is the Bohr magneton. At the same time, the energy of Coulomb interactions is<sup>3</sup>  $E_c = \frac{e^2}{4\pi\epsilon l_B} \approx 8.58\sqrt{B/\text{Tesla}}$  meV. Since  $E_c \gg E_z$  for most accessible magnetic fields, the spin ordering is defined not as much by single particle Zeeman splitting but rather by the competition between the disorder broadening  $\Gamma$  and the interaction energy, which includes Coulomb and particle exchange interactions. This, just like in metallic ferromagnets, spontaneously lifts the spin degeneracy aligning the spins and opens an exchange gap  $\Delta_{\text{ex}} \gg E_z$ . Though the Zeeman energy gap is much smaller, the magnetic field chooses the spin orientation associated with a lower energy. As it will be later discussed in more detail, graphene has  $g_s = 4$  accounting for spin and *valley pseudospin* degrees of freedom. This 4-fold degeneracy can be lifted by interactions in a similar manner, which results in a complicated combined spin/valley phase ordering. These effects are collectively known as *quantum Hall ferromagnetism*, examples of which will be presented in the following chapters.

### Fractional quantum Hall effect (FQH)

---

<sup>3</sup>Specifically in the case of interactions between electrons in a graphene sheet encapsulated between two sheets of boron nitride, with a dielectric screening taken into account by the dielectric constant  $\epsilon = \epsilon_{\text{BN}}^{\parallel} = 6.6\epsilon_0$

Beyond breaking symmetries, interactions, more intriguingly, can produce new emergent states of matter. It is very fortunate that Landau levels offer a way of creating electron systems with low energy dispersion - researchers not only have a tool to force electrons to strongly interact, but they are also doing so in 2D, which is remarkably different from the 3D world we live in. In 3D, since two particles can be exchanged without their trajectories crossing, the only quantum particle exchange statistics that are allowed are either bosonic or fermionic as described by the overall phase gain  $e^{i\varphi} = \pm 1$  [2]. However, in 2D, “in-between” or *anyonic* statistics, where the phase is not limited to  $\varphi \in \{0, \pi\}$ , are allowed. These new, non-existent in 3D, particles manifest themselves in the *fractional quantum Hall effect (FQHE)*, which experimentally manifests similarly to the IQHE, but at fractional filling factors:

$$\nu = \frac{p}{q}; \quad p, q \in \mathbb{Z} \longrightarrow \text{FQHE}. \quad (2.5)$$

The Hall conductivity is quantized to  $\nu e^2/h$ . The first FQH state was experimentally observed at  $\nu = 1/3$ , with a ground state wavefunction ansatz provided by Laughlin [18]. The single particle wavefunctions in the  $n = 0$  Landau level<sup>4</sup> take the form  $\psi(x, y) \sim z^l e^{-\frac{1}{4}|z|^2}$ , where  $z = x - iy$  and  $l$  is the angular momentum, hence the many( $N$ )-particle wavefunction must be of the form  $\Psi = f(z_j) e^{-\frac{1}{4} \sum_i |z_i|^2}$ , where  $f(z_j)$  is a polynomial of degree  $N$ . The Laughlin ansatz wavefunction for filling factor  $\nu$  is

$$\Psi_{\nu=1/m} = \prod_{j < k} (z_j - z_k)^m \exp \left[ -\frac{1}{4} \sum_i |z_i|^2 \right]. \quad (2.6)$$

With cleaner devices, more and more FQHE states have been discovered, with two key observations: [19] that the FQHE states appear 1) in sequences and with 2) no even

---

<sup>4</sup>In the symmetric gauge



denominators observed. This led to the realization that the similarities of FQHE and IQHE are not accidental, and in fact, FQHE could be viewed as integer quantum Hall states of new *quasi*-particles called *composite fermions*. The proposed particle is made up of an electron and  $2p$  flux quanta attached to it, effectively absorbing flux from the external magnetic field ( $B$ ). The composite fermions then experience an effective magnetic field  $B^* = B - 2pn\varphi_0$ , where  $n$  is the electron density. When the Landau level is half-filled ( $\nu = 1/2$ ), the effective magnetic field experienced by composite fermions is then  $B_{1/2}^* = B - 2\nu n_0\varphi_0 = B - 2 \cdot 1/2 B/\varphi_0\varphi_0 = 0$ . This suggests that the composite fermions do not notice the external magnetic field and behave just like a compressible metal! In fact, like free electrons, the composite fermions at half filling form a Fermi surface that has been observed in experiments [20, 21]. Away from  $\nu = 1/2$ , the effective magnetic field  $B_\nu^* \neq 0$ , and composite fermions form Landau level-like energy bands with the filling factor defined as  $\nu^* = n\varphi_0/B^*$ ,  $\nu^* \in \mathbb{Z}$ . Expressing the magnetic fields in terms of filling factors, we obtain an expression for a sequence of odd-denominator FQH states:

$$\nu = \frac{\nu^*}{2p \cdot \nu^* \pm 1}, \quad \nu^* \in \mathbb{Z}. \quad (2.7)$$

Many states from this sequence have been observed, with denominators going as high as 16, as well as *4-flux* states with  $p = 2$ .

### Even denominator FQHE (EDFQH)

The abundance of observed odd-denominator states at filling factors predicted by eqn. 2.7 with wavefunctions similar to the Laughlin wavefunction (eqn. 2.6) made the discovery of an even-denominator state in a GaAs/AlGaAs quantum well in the  $N = 2$  Landau level at  $\nu = 5/2$  an unexpected surprise [22]. The many-body electronic wavefunctions must be anti-symmetric upon particle exchange, which in the Laughlin wavefunction is ensured by an odd power  $m$  of the polynomial. At first sight, this anti-

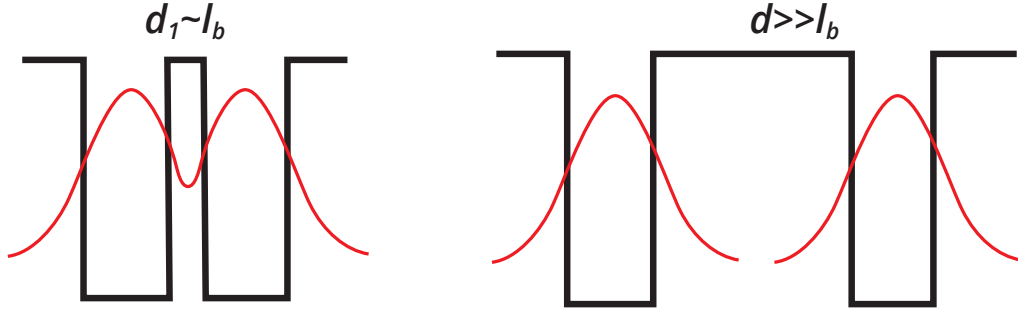


Figure 2.2: GaAs/AlGaAs double quantum wells **left**: separation barrier width  $d$  is of the order of achievable magnetic length  $l_b$  supporting finite tunneling between the two wells. The observed quantum Hall states are multi-component. **right**: the barrier width is much larger than the magnetic length; the two wells are effectively decoupled and (ignoring spin) the observed quantum Hall states are single-component.

symmetrization requirement could be satisfied by generalizing the Laughlin wavefunction to include internal degrees of freedom, i.e. spin. This is called the Halperin wavefunction [23]:

$$\Psi_{m_1, m_2, n}^H(\{z_j^\uparrow, z_j^\downarrow\}) = \prod_{k < l}^{N_\uparrow} (z_k^\uparrow - z_l^\uparrow)^{m_1} \prod_{k < l}^{N_\downarrow} (z_k^\downarrow - z_l^\downarrow)^{m_2} \prod_{k=1}^{N_\uparrow} \prod_{l=1}^{N_\downarrow} (z_k^\uparrow - z_l^\downarrow)^n \quad (2.8)$$

where the electron-electron interactions are split into inter- and intra-spin interactions. However, the  $\nu = 5/2$  EDFQH state turned out to be spin polarized[24] indicating a lack of an internal degree of freedom. Such *single-component* EDFQH states lack the multi-flavor electrons required for a Halperin-type state, and a different wavefunction was proposed by Moore and Read[25]:

$$\Psi_{\text{PF}} = \text{Pf} \left( \frac{1}{z_i - z_j} \right) \prod_{i < j} (z_i - z_j)^2, \quad (2.9)$$

where ‘‘Pf’’ stands for *Pfaffian* and is an antisymmetric matrix. The excitations from the Pfaffian ground state carry charge  $e/4$  and obey *non-Abelian statistics*, where exchange of such particles explores the vast ground state degeneracy[26]. The Pfaffian state has been extensively studied numerically, but an experimental demonstration of the exchange

properties of the  $e/4$  quasiparticles still remains an open problem.

Later, *multi-component* even-denominator states of the form shown in eqn. 2.8 were observed in double quantum wells at  $\nu = 1/2$  (Fig. 2.2). The Halperin wavefunction is applicable if the electron spin is replaced by a pseudospin that labels which of two quantum wells is considered. The intrawell interaction strength is tuned by the barrier width  $d$  and the conditions for a FQH state to form are set by the dimensionless scale  $d/l_b$ [27]. Specifically, the  $\nu = 1/2$  FQH state is defined by the Halperin wavefunction with the set of polynomial powers  $(m_1, m_2, n) = (3, 3, 1)$  (eqn. 2.8). As a side note, in order to describe multilayer FQH states in terms of composite fermions, we need to extend the picture and allow electrons to bind with flux quanta from both quantum wells [28, 29].

### What are the effects of the lattice?

In the treatment of Landau levels the magnetic vector potential ( $A(r)$ ) breaks translation invariance along one of the axes ( $x$ -axis), but the other direction ( $y$ -axis) is assumed to be translationally invariant. In most cases the lattice scale does not directly come into the problem, but instead it can be incorporated by replacing the mass of a free electron with an effective mass that takes the lattice into account. This assumption is valid as long as the magnetic length scale is much greater than the inter-atom lattice spacing  $l_b \gg a$ . But what happens if the magnetic field is large and  $l_b/a \sim 1$ ? This would of course require extremely large magnetic fields  $B \sim 10000$  Tesla, but assuming the condition is met, the electron Landau level spectrum will be modified by the periodic lattice potential. To find the energy spectrum of an electron gas in a periodic lattice potential  $V(x)$  at zero magnetic field ( $B = 0$ ), we seek eigenstates of the Hamiltonian that obey the translation symmetries of the lattice  $V(\mathbf{x} + \mathbf{a}) = V(\mathbf{x})$ , where  $\mathbf{a}$  is a lattice vector. This is done by finding the eigenstates of translation operators  $T_{\mathbf{a}}$  that, when applied to a wavefunction  $\psi(\mathbf{x})$ , translate it by  $\mathbf{a}$ :  $T_{\mathbf{a}}\psi(\mathbf{x}) = \psi(\mathbf{x} + \mathbf{a})$ . When a

magnetic field  $\mathbf{B} = |B|\hat{z}$  is applied, the vector potential  $\mathbf{A}(\mathbf{x})$  ( $\nabla \times \mathbf{A}(\mathbf{x}) = \mathbf{B}$ ) breaks the translation invariance of the lattice, and upon translation the wavefunction gains an additional phase  $\varphi_{\mathbf{a}}(\mathbf{x}) = e/\hbar \mathbf{A}(\mathbf{x}) \cdot \mathbf{a}$ . Then, the translation operators can be redefined as  $T_{\mathbf{a}}^M = e^{i\varphi_{\mathbf{a}}(\mathbf{x})} T_{\mathbf{a}}$ . These new *magnetic* translation operators will commute with each other only for a specific choice of  $\{\mathbf{a}_i\}$  which are defined by the total flux penetrating through the unit cell  $\Phi = B(\mathbf{a}_1 \times \mathbf{a}_2)$ . If

$$\frac{\Phi}{\Phi_0} = N \quad (2.10)$$

is an integer, then the problem can be mapped on to the trivial case of zero flux penetrating the unit cell. On the other hand, if  $N = p/q$  is a rational fraction, then the situation gets more interesting. In order for this condition to be satisfied, we need to consider an enlarged *magnetic* super unit cell that is  $q$ -times larger than the original cell of the potential, such that the total flux penetrating the magnetic unit cell is  $p/q \times q = p \in \mathbb{Z}$ , and the eigenstates are simultaneously eigenstates of the translation operators and the Hamiltonian. In the absence of a magnetic field, the electrons will scatter at momenta  $k \sim 1/a$ , but if the unit cell is effectively enlarged, the scattering will occur at  $k \sim 1/(q \times a)$ , which could be treated as a splitting of the original ( $B = 0$ ) Bloch band into  $q$  sub-bands. Each of these bands according to Thouless, et.al [16] carry a Chern number, that can be larger than  $C = 1$  as in the Landau level case. When  $N = p/q$  is irrational, the band is split into infinitely many bands. The resulting energy spectrum has a fractal structure and is called the *Hofstadter butterfly* after Douglas Hofstadter [30]. Hofstadter bands, unlike the dispersionless Landau levels, have a finite bandwidth. This poses the question of whether Coulomb interactions can be strong enough to form correlated states inside these finite-bandwidth Chern bands. The answer is yes, and by analogy with FQHE, we call these states *fractional Chern insulators* or FCIs (see Chapter 6).

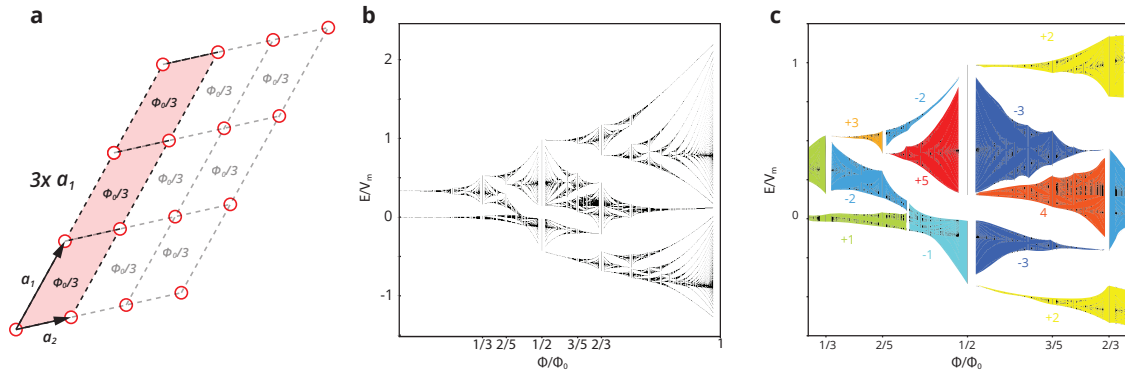


Figure 2.3: **a.** A lattice spanned by unit vectors  $\mathbf{a}_1$  and  $\mathbf{a}_2$  in a uniform magnetic field. Each unit cell is carrying flux  $\Phi = 1/3\Phi_0$ . A *magnetic* unit cell  $3\mathbf{a}_1 \times \mathbf{a}_2$  hosts an integer flux  $\Phi = \Phi_0$  and satisfies condition 2.10. **b.** Single particle energy spectrum at strong magnetic fields  $l_B \sim \mathbf{a}$  of a electrons on a hexagonal lattice called “Hofstadter butterfly”. **c.** Like Landau levels, each band is characterized by a Chern number. For LL  $C = 1$ , but Hofstadter bands can have a  $|C| >$  and carry Hall conductivity  $Ce^2/h$ . The colors represent Chern numbers.

## 2.2 van der Waals heterostructures

Historically, electrons confined to a 2D plane were first realized in heterostructures of different semiconductors (e.g. GaAs and AlGaAs) — crystals grown in high vacuum with molecular beam epitaxy. An alternative approach that emerged over the last decade is to study electrons confined to materials that are atomically thin, or in other words, 2D “by design”. One such material is *graphene*, an atom-thick ( $\sim 0.34$  nm) layer of carbon atoms on a hexagonal lattice. Graphene is a member of a family of materials called van der Waals (vdW) materials. In these materials, the binding energy between individual planes is weaker than in-plane interatomic bonds. This property makes it possible to use mechanical exfoliation to isolate nanometer-thick layers of materials. The range of materials available for exfoliation is rapidly growing, with members including semiconductors, dielectrics, superconductors and magnetic materials. The isolated thin layers can then be recombined into *stacks* with designer properties (Fig. 2.4) [5]. For example, graphene is a semi-metal with Dirac electrons and has become the workhorse

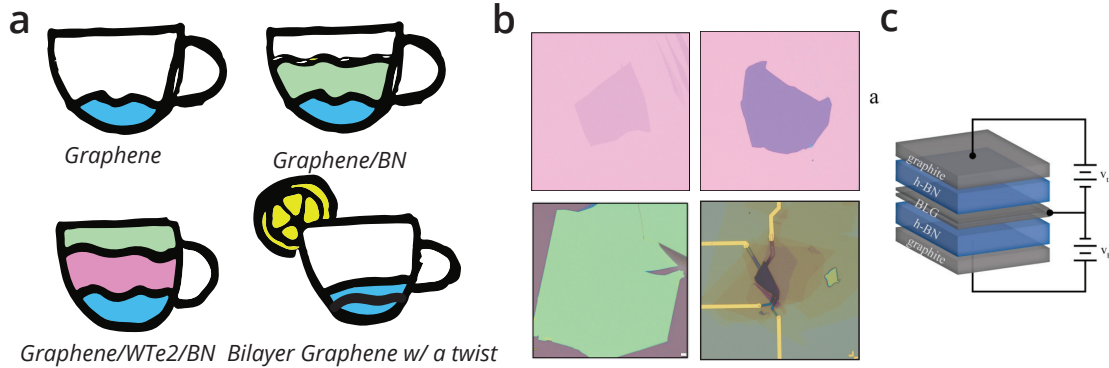


Figure 2.4: **a** 2D materials “stacked” on top of each other are held by van der Waals (vdW) forces. The choice of materials (chemical composition, thickness) and their relative orientation (angle controlled Moiré patterns) used in such vdW heterostructures can be used to tailor the character of electronic states. **b** Examples of 2D materials. Top panel: bilayer graphene (0.7 nm), graphite (15 nm). Bottom panel: hexagonal boron nitride (45 nm), an optical image of a dual gated device shown in **c**. Scale bar is 10 $\mu$ m.

for studying 2D electrons; hexagonal boron nitride (hBN) is a large bandgap semiconductor that is used as an insulator in graphene-based field effect transistors;  $\text{WTe}_2$  is a transition metal dichalcogenide (TMD) and was used to proximity-induce spin-orbit coupling in graphene electrons[31] and  $\text{CrI}_3$  [32, 33] and  $\text{Fe}_3\text{GeTe}_2$  show voltage controlled magnetism. Researchers also manipulate the crystal structure of these materials, working with metastable stacking orders; for instance, ABC-stacked trilayer graphene demonstrates Mott insulating states [12]. They also can control the relative orientation of layers; in hBN and graphene, which both have hexagonal lattices with similar atom spacing, a small rotation angle creates a Moiré pattern that acts as a periodic potential, leading to a slew of new states. A rotation angle between two graphene sheets has been shown to demonstrate superconductivity[13], zero magnetic field resistance quantization[34], and much more.

The ability to observe novel collective electron states is usually hindered by disorder in the device. For interaction-driven states to form, the disorder potential needs to be much

smaller than the other energy scales, most importantly the energy of coulomb repulsion  $E_c$ . In quantum Hall experiments, the interaction strength can be boosted by applying strong magnetic fields  $E_c \sim \sqrt{B_\perp}$ . Being able to observe the interaction phenomena (symmetry breaking and FQH) at lower magnetic fields implies that the devices must be cleaner<sup>5</sup>. Early graphene devices were made by patterning and contacting graphene directly on the underlying substrate  $\text{SiO}_2$  [3, 4, 35]; these devices showed interaction-driven symmetry breaking at fields larger  $> 20\text{T}$  [36]. Later, it was found that the  $\text{SiO}_2$  substrate traps electron puddles, creating a strong disorder potential [37, 38]. To reduce the substrate disorder, the graphene sheet was placed on top of an exfoliated 2D insulator - hexagonal boron nitride (hBN) [39, 40, 41]. With this approach, the symmetry broken quantum Hall states were observed at significantly lower magnetic fields ( $B = 8.5\text{T}$ ) and later on, fractional quantum Hall (FQH) states [42] were observed. In parallel, researchers have been working on experiments with suspending graphene[43, 44], where the  $\text{SiO}_2$  disordered substrate underneath is totally etched away. In these experiments, carefully choosing a low-disorder spot with a scanning probe, FQH states with odd-denominators have been observed, as well as signatures of the elusive even-denominator state[45, 46] which is a hallmark of the cleanest GaAs/AlGaAs semiconductor devices [22, 47].

Making graphene devices on hBN substrates required the development of a new fabrication procedure usually referred to as the “dry transfer technique” (Fig. 2.5), where the stack of 2D materials is assembled layer by layer with the help of a sticky polymer film such as polycarbonate (PC) or polypropylene carbonate (PPC). The first 2D material flake is adhered directly to the sticky film, whereas all consequent layers are held to each other by van der Waals forces. This way, the only surface that is contaminated with

---

<sup>5</sup>This is not strictly correct, as the interaction strength is also modified by the proximity of conducting gates

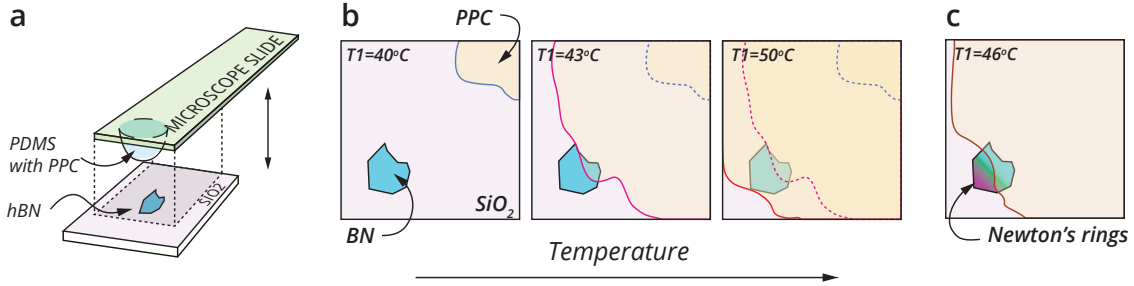


Figure 2.5: **a.** The dry assembly of vdW heterostructures starts with a “pickup” slide: a soft PDMS (polydimethylsiloxane) cushion with a sticky polymer (e.g. PPC) is mounted at the edge of a glass microscope slide. With the help of a micropositioner and a microscope the pickup slide is positioned over a 2D material flake (e.g. hBN) and brought into contact by lowering the slide. **b.** Heating the  $\text{SiO}_2$  substrate the PPC film would start flowing over until it fully covers the target flake. **c.** Reducing the temperature would cause the PPC film to retract and peel off the target flake. An interference pattern appears between the 2D flake and substrate indicating a successful pick up of a flake.

the pickup polymer is the topmost surface. After the stack is assembled on the film, it is transferred onto a clean substrate. Even though the experiments done on suspended graphene showed more fragile electronic states, the dry-stacking method is more flexible, allowing an easy assembly of dual gated devices, with the number of layers in a device limited only by the patience of the stacker.

My own contribution was to further improve on the quality of the BN-encapsulated graphene devices. I found that metallic (Au) gates, suffering from a spatially varying work function, can be easily replaced by few-layer graphite gates, with the whole process seamlessly integrating into the vdW heterostructure assembly procedure [48]. In such dual graphite-gated devices, symmetry broken states appear at fields as low as  $\sim 1.5\text{T}$  with robust even-denominator FQH at  $> 6\text{T}$ . Fig.2.6 shows a comparison of capacitive measurements of a metal-gated and a graphite-gated bilayer graphene device (See Section 3.1 and Chapter 5). The low capacitance features in panels **c,d** correspond to gapped states. Panel **c** shows gapped states in a metal-gated device appearing only at integer filling factors and a series of electric field tuned phase transitions between wavefunctions



of different spin/valley and layer “flavor” (See Fig. 2.10). In stark contrast, panel **d** additionally shows numerous finer fractional quantum Hall features at partial fillings of a Landau level, which indicates greatly reduced disorder.

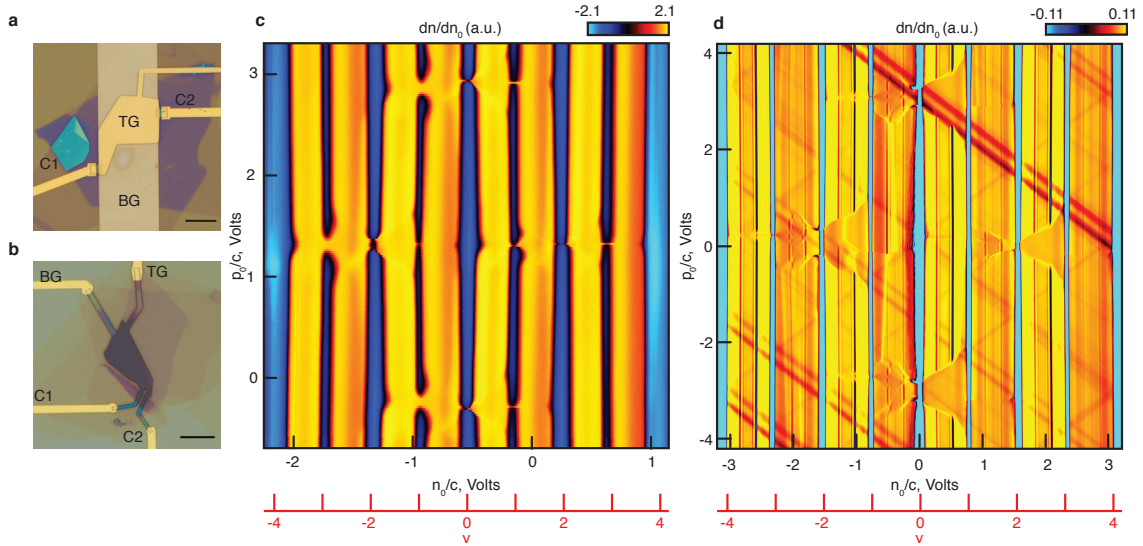


Figure 2.6: **Comparison of metal- and graphite-gated devices.** **a** Optical micrograph of a metal gated device. Scale bar corresponds to  $10 \mu\text{m}$ . **b** Optical micrograph of a graphite gated device. Scale bar corresponds to  $10 \mu\text{m}$ . **c** Symmetric capacitance (Section 3.1),  $C_S = C_T + C_B = \partial n / \partial n_0$ , for a metal gated device at  $B = 10 \text{ T}$  and  $T \approx 50 \text{ mK}$ . **d**  $C_S$  for a graphite gated device at  $B = 12 \text{ T}$ . Graphite gated devices show much narrower integer QH states, along with many fractional states. Diagonal features in **d** are features that depend on only one of the gates (top or bottom) potentials  $V_B$  or  $V_T$ , indicating either single gated regions or electronic structure within the graphite gates. Reprinted from Zibrov A.A., et. al 2017 [49]

## 2.3 Graphene

### Monolayer graphene (MLG)

Graphene is a layer of carbon atoms arranged on a hexagonal lattice; the thickness of a graphene layer is  $\sim 0.34 \text{ nm}$ . Fabricating a single graphene flake, a material closest to a real 2D system, proved to be experimentally challenging. Nonetheless, in 2004, graphene was discovered with individual flakes isolated with mind-boggling simplicity - a graphite

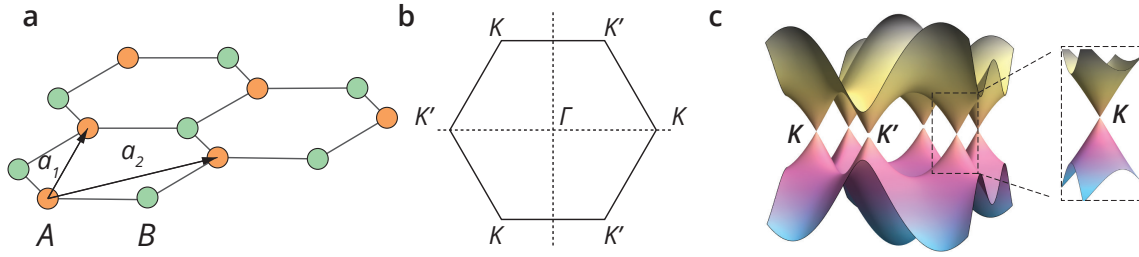


Figure 2.7: **a** Graphene is spanned by two interpenetrating triangular lattices A and B. **b** Corresponding Brillouin Zone with two distinct high-symmetry points K and K' **c** Band structure of monolayer graphene. At K and K' points of the Brillouin zone the valence and conduction bands touch and low-energy excitation follow a linear (Dirac particle) dispersion relation.

crystal was peeled apart or *exfoliated* with adhesive tape. This stands in stark contrast to the vacuum molecular beam epitaxy growth that is usually used for semiconductor heterostructures. While making graphene turned out to be as extremely easy, seeing it was much harder. To make graphene visible under white light illumination, it is usually exfoliated onto wafers with 300 nm of SiO<sub>2</sub>[50].

Today, graphene is a textbook example of a non-bravais lattice [51]. It is made from two distinct triangular sublattices labeled A and B. The full graphene sheet can be spanned by translating the two neighboring atoms (respectively belonging to A and B) by vectors  $\mathbf{a}_1$  and  $\mathbf{a}_2$  (Fig. 2.7 a). For in-depth treatments on graphene electronic properties see the reviews by Goerbig[52], McCann, et. al. [53, 54] and Castro-Neto, et.al. [55].

The most remarkable property is that the valence and conduction bands of electrons propagating through a hexagonal lattice touch at points of zero energy  $\varepsilon = 0$  at the K and K' high symmetry points of the Brillouin zone (Fig.2.7b). The Hamiltonian near the K-point is  $H_K = \hbar v_F \boldsymbol{\sigma} \cdot \mathbf{p}$ , where momentum  $\mathbf{p}$  is defined relative to the K-point,  $\sigma$  are Pauli matrices<sup>6</sup>, and  $v_F = \frac{3ta}{7} 2\hbar \approx 10^6$  m/s is the Fermi velocity and depends

<sup>6</sup>For K'-point  $H_K = H_{-K'}$

on tight binding hopping amplitude  $t$ . The energy dispersion relation depends only on the length of the momentum operator  $\varepsilon(p)_K = \hbar v_F |\mathbf{p}|$ , just like relativistic, massless Dirac particles, with the difference in the group velocity being defined by the Fermi velocity  $v_F = 10^6$  m/s (Fig. 2.7 c). The electron wavefunctions written in the basis  $\psi = (\psi_A, \psi_B)^T = 1/\sqrt{2}(1, e^{i\theta})^T$ , where  $\psi_A(B)$  refers to the component localized on A(B) sublattice, are equally spread out between the A and B sublattices. However, the phase uniquely defines if the electrons originate at K or K' points. Since K and K' are degenerate in energy, it is convenient to define a new *valley* quantum number, or a valley *isospin* ( $K/K'$ ) that mimics the real electronic  $\uparrow / \downarrow$  spin. All together, the low-energy electrons in monolayer graphene are 4-fold (spin and valley) degenerate.

In order to obtain the Landau level spectrum of graphene in a magnetic field  $B = \nabla \times \mathbf{A}(r)$ , we perform the standard (Peierls) substitution of the gauge-dependent canonical momentum with the gauge-invariant mechanical momentum:  $\mathbf{p} \rightarrow \mathbf{\Pi} = (p) + e/c \mathbf{A}(\mathbf{r})$ . With a set of ladder operators  $a, a^\dagger \sim (\Pi_x \pm i\Pi_y)$ , the Hamiltonian then reads:

$$H_{B>0} = \varepsilon \begin{pmatrix} 0 & a^\dagger \\ a & 0 \end{pmatrix}, \quad \varepsilon = \frac{\sqrt{2}\hbar v_F}{l_b}, \quad (2.11)$$

where  $l_b$  is the magnetic length. The Landau level spectrum of graphene and corresponding wavefunctions ( $\psi = (\psi_A, \psi_B)^T$ ) are then:

$$\varepsilon_n = \pm \varepsilon \sqrt{|n|} \quad (2.12)$$

$$\psi_{n=0}^K = (0, |0\rangle)^T, \quad \psi_{n>0}^K = (|n-1\rangle, |n\rangle)^T \quad (2.13)$$

$$\psi_{n=0}^{K'} = (|0\rangle, 0)^T, \quad \psi_{n>0}^{K'} = (|n\rangle, |n-1\rangle)^T, \quad (2.14)$$

where  $|n\rangle$  are harmonic oscillator eigenstates. It is evident that the  $n = 0$  Landau

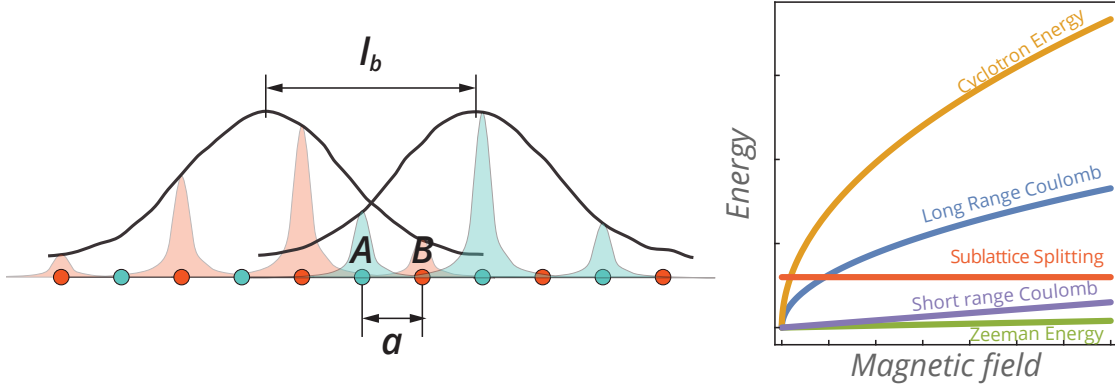


Figure 2.8: **left:** Cartoon illustrating valley-anisotropic short-range Coulomb interactions between two electron wavepackets localized on the A(B) sublattices respectively. The long-range interactions fall off as the magnetic length is  $E_c^{l.r.} \sim e^2/l_b \sim \sqrt{B}$ , while the inter-lattice repulsion scales as  $E_c^{s.r.} \sim \frac{a}{l_b} E_c^{l.r.} \sim B$ . **right:** Competing energy scales in monolayer graphene zero energy Landau level. Coulomb interactions lead to spontaneously broken Spin/Valley degeneracies, while Zeeman splitting and short-range valley anisotropies as well as single particle sublattice splitting determine the orientations of the spin and valley pseudospin.

level is special as the wavefunction in the  $K(K')$  valley is polarized to the A(B) sublattice. Since the  $n = 0$  LL has an energy  $\varepsilon_0 = 0$ , it is usually referred to as the *zero energy Landau level (ZLL)*. This connection between sublattice and valley in the ZLL leads to additional electron-electron interaction-induced valley anisotropy. Whilst long range interactions do not distinguish between the sublattice degrees of freedom, the short-range inter-sublattice repulsion biases electrons to reside on the same sublattice. The energy scale of these valley-anisotropic interactions is  $E_c^{s.r.} \sim \frac{a}{l_b} E_c^{l.r.}$  [56]. Moreover, the AB-sublattice symmetry can be explicitly broken by a choice of substrate (e.g. BN), making the ZLL particularly interesting for exploring the phases arising from interactions (Fig. 2.8).

### Bilayer graphene (BLG)

Bilayer graphene (BLG) is the next step of increasing complexity. The stable phase of BLG is called *Bernal* stacked, when the A sublattice ( $A_1$ ) of one layer is under the

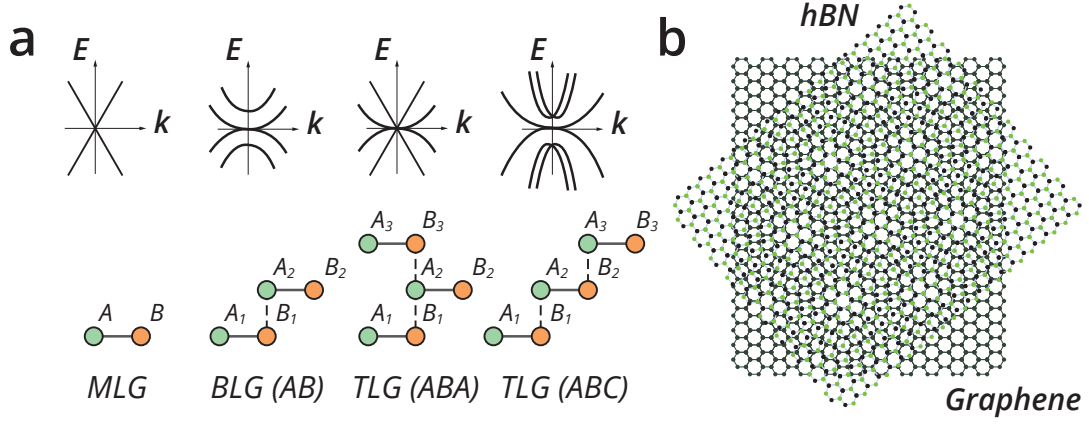


Figure 2.9: **a** Stacking order of few-layer graphite and their respective band structures. **b** Moire pattern formed between hBN and graphene.

B sublattice ( $B_2$ ) of the other (Fig. 2.9a). The low-energy band structure, just like monolayer graphene, has two special valley points  $K$  and  $K'$  where the conduction and valence bands touch. The difference lies in the dispersion relation, which is no longer linear in momentum, but instead is parabolic; therefore, bilayer graphene hosts massive chiral fermions at the  $K$  and  $K'$  points. Another major distinction is that an applied perpendicular electric field breaks the inversion symmetry of the two graphene layers, which leads to a gate-tunable gap. The tight-binding description of BLG follows closely from that of the monolayer graphene case, but here the unit cell has 4 lattice sites -  $A_1$ ,  $B_1$  and  $A_2$ ,  $B_2$ , which leads to a  $4 \times 4$  Hamiltonian. Finding the Landau spectrum at magnetic field  $B$ , after the standard Peierls substitution, the ZLL wavefunctions are (in basis the of  $(\psi_{A_1}, \psi_{B_2}, \psi_{B_1}, \psi_{A_2})$ ):

$$\psi_{n=0}^K = (|0\rangle, 0, 0, 0)^T, \quad (2.15)$$

$$\psi_{n=1}^K = (c_1 |1\rangle, 0, c_2 |0\rangle, c_3 |0\rangle), \quad \sum_i c_i^2 = 1. \quad (2.16)$$

The two different eigenstates, though they differ in energy, are nearly degenerate. In fact, if no external electric field is applied and some of the higher order tight binding

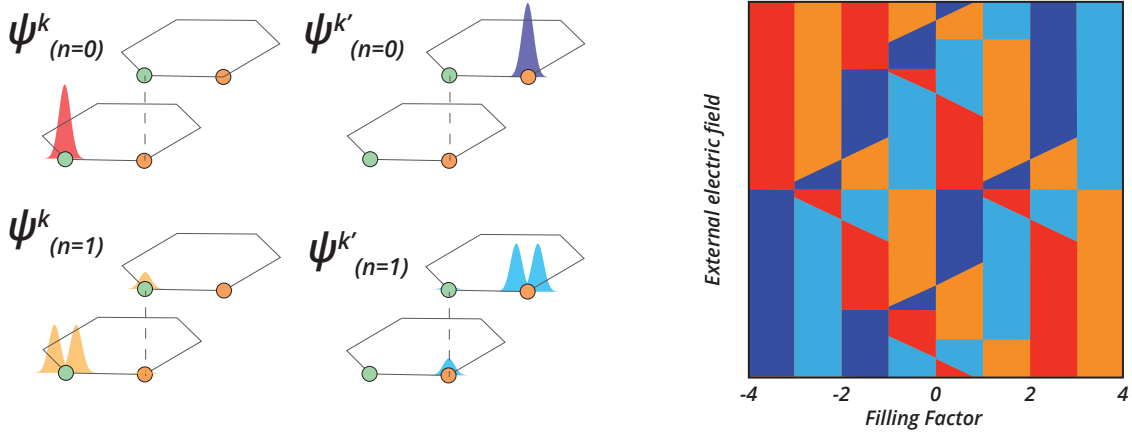


Figure 2.10: **left:** Schematic depiction of the zero energy Landau level orbital wavefunctions, shaded regions depict the relative support on the atomic sites  $A_1$ ,  $A_2$ ,  $B_1$ ,  $B_2$ . **right:** Phase diagram of ZLL as a function of filling factor and an applied external polarizing field. Different colors correspond to the 4 orbital wavefunctions  $\psi_{n=0}^K$  (red),  $\psi_{n=1}^K$  (orange),  $\psi_{n=0}^{K'}$  (blue) and  $\psi_{n=1}^{K'}$  (cyan). The figures are adopted from Hunt B.M., et.al (2017) [57]

parameters are ignored, namely  $\gamma_4$  and  $\Delta'$ , then the degeneracy is exact.  $\gamma_4$  describes the interlayer hopping between dimer and non-dimer sites  $A(B)_1 \rightarrow A(B)_2$ , while  $\Delta'$  describes the energy difference between dimer ( $A_2$  and  $B_1$ ) and non-dimer ( $A_1$  and  $B_2$ ) sites. Nonetheless, the nearly degenerate orbital wavefunctions  $\psi_{n=0}$  and  $\psi_{n=1}$  expand the standard graphene 4-fold degeneracy to 8-fold. While the  $\psi_{n=0}$  are fully layer and sublattice polarized, the  $\psi_{n=1}$  have a finite polarization, which can be tuned by an external electric field. The complicated phase structure of the 8-fold degenerate ZLL of BLG[57] is shown in Fig. 2.10.

### Stacking configurations.

Bernal stacking of BLG is the only stable configuration, though stacking faults can occur such that a graphene flake will have a domain wall between regions of AB and BA stacking orders. Trilayer graphene, on the other hand, in addition to the lowest energy Bernal stacking order, supports a metastable ABC stacking configuration. The band

structure and shape of orbital wavefunctions of the two differ greatly. ABA trilayer graphene band structure can be thought of as a monolayer-like band and a bilayer-like band that can hybridize under an applied electric field. ABC trilayer has a slowly dispersing energy spectrum at the  $K$ -points, where the conductance and valence bands touch. If a bandgap is induced near the  $K$ -point of the ABC trilayer (e.g. with a longer wavelength lattice), a flat band at zero magnetic field can form, in which correlated Mott insulator states and superconductivity have been observed [12, 14]. A more detailed discussion of ABA TLG is provided at the end of this chapter to illustrate the capabilities of capacitance measurements in clean graphene devices.

**“White” graphene, hexagonal boron nitride (hBN)** Finally, a few remarks about hexagonal boron nitride, or as it sometimes is called in the literature, “white graphene”. This name comes from the crystal’s white color and inter-atom lattice spacing exceptionally close to graphene’s (the lattice mismatch  $\delta = \frac{a_{hbn}}{a_{GR}} - 1 \approx 1.8\%$ ). This made hBN an ideal insulating partner to graphene and also hands researchers another degree of freedom. First of all, the boron(nitrogen) atoms aligning with the A(B) sublattice of the graphene layer will break the sublattice symmetry [58], which opens a gap. Second, a small angle rotation will lead to a long-wavelength (much larger than the inter-atom separation) Moiré pattern (wavelength  $\lambda \sim 14$  nm). Bragg scattering off this long-range Moiré pattern will open up additional gaps in the Brillouin zone at momentum points ( $k = \pi/\lambda$ ). This was successfully used in ABC trilayer graphene to isolate a flat band in which the electron’s kinetic energy is dwarfed by the Coulomb interactions leading to an observation of a Mott insulating state [12]. Finally, returning to the discussion of the lattice effects in high magnetic fields from the previous chapter, I want to note that  $\Phi/\Phi_0 \sim 1$  for a unit cell defined by a  $\lambda = 14$  nm Moiré pattern is satisfied at accessible magnetic fields  $B \sim h/e/\lambda^2 = 21$  T.

# Chapter 3

## Capacitive probe of the density of states of 2DEGs

### 3.1 Overview

To study 2D electron systems in a sheet of graphene, it is desirable to tune as many parameters as possible. Here, I consider devices with two electrostatic gates. Two independent voltages (Fig. 3.1) applied to the top ( $V_T$ ) and bottom ( $V_B$ ) gates allow us to electrostatically induce a net areal carrier density ( $n_0$ ), doping the graphene sheet:

$$n_0 = c_t V_T + c_b V_B, \quad (3.1)$$

where  $c_{t(b)} = \epsilon_{\text{BN}}/d_{t(b)}$  are the geometric capacitances per unit area from top(bottom) gates to the graphene sheet ( $\epsilon_{\text{BN}}$  is dielectric constant of BN,  $d_{t(b)}$  the BN thicknesses). The two voltages also allow us to set up an external electric field  $D$ :

$$D = \epsilon_{\text{BN}} \left( \frac{V_T}{d_t} - \frac{V_B}{d_b} \right). \quad (3.2)$$



When considering graphene multilayers, it is convenient to rewrite eqn. 3.2 in terms of charge polarization  $p_0$  caused by the applied electric field:

$$p_0 = c_t V_T - c_b V_B. \quad (3.3)$$

The subscript “0” in eqns. 3.1 and 3.3 implies that these values are *nominal*, which means that these equations are true if instead of a graphene sheet, we had a perfect metal. The *real* charge carrier density ( $n$ ) and polarization ( $p$ ) deviates from the nominal value due to the finite density of states (DOS) of the 2D material in question, or in other words due to the finite energy cost of adding an electron to the 2D channel that the batteries need to overcome. This observation, together with total charge conservation, allows us to directly measure the DOS of the 2D electron system.

In order to extract the density of states, we measure the charge carrier modulation on the top (bottom) gate  $\delta n_t$  ( $\delta n_b$ ) caused by a small time-varying voltage  $\delta V_B$  ( $\delta V_T$ ), which for a symmetric device with geometric capacitances from top and bottom gates to the 2D electron channel is  $c_t = c_b = c$  (eqn. A.6):

$$C_{\text{PEN}} = \frac{\delta n_{t(b)}}{\delta V_{B(T)}} = \frac{c^2}{2c + \nu}, \quad (3.4)$$

where  $\nu = \partial n / \partial \mu$  is the thermodynamic density of states of the 2DEG. This measured capacitance is called *penetration field capacitance* to emphasize that the electric field penetrates the 2DEG instead of being fully screened if the 2DEG were replaced with a metal sheet. When the Fermi level of the 2DEG lies inside a band gap, the density of states vanishes ( $\nu \rightarrow 0$ ) and the time-varying electric field penetrates the 2DEG unscreened, resulting in effectively two capacitors  $c_t = c$  and  $c_b = c$  in series, and giving a measured capacitance  $C_{\text{PEN}} = c/2$ . Hence, penetration field capacitance varies from

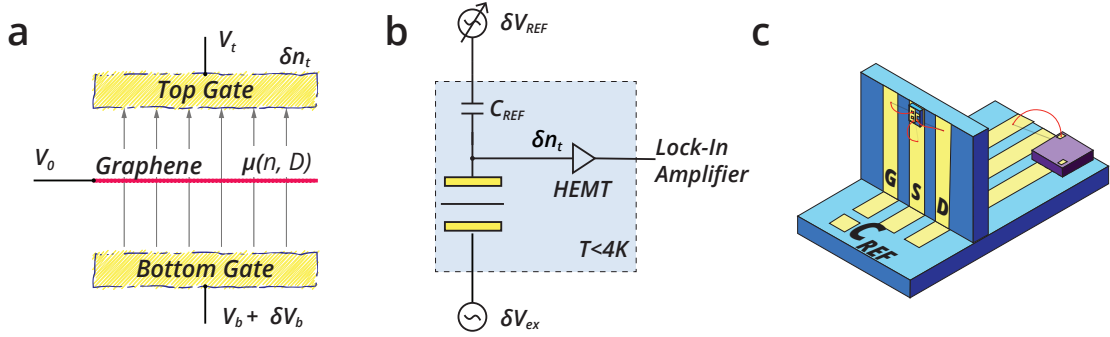


Figure 3.1: **a** A dual gated 2DES (e.g. graphene). Independent contacts to the two gates and the 2DEG allow to control the carrier density  $n$  and electric field  $D$  across the 2DES. An AC modulation  $\delta V_b$  applied to the bottom gate sets up a time varying electric field. The DOS of the 2DES can be probed by measuring the penetration field capacitance  $C_{PEN} \sim \text{DOS} = \text{DOS}(n, D)$ . **b** The device capacitance is measured by balancing against a known reference capacitor ( $C_{REF}$ ): the phase and amplitude of the AC excitation  $\delta V_{REF}$  applied to  $C_{REF}$  is adjusted until the charge modulation  $\delta n_t$  is nulled. The charge modulation is measured by a cryogenic transimpedance amplifier based on a HEMT transistor (Appendix A) **c**. A model of a transistor amplifier, the dimensions are  $\sim 4 \times 8 \times 5$  mm. The HEMT transistor is mounted on a vertical support. This way the applied magnetic field is parallel to the 2DEG in the HEMT.

0 to  $c/2$  as we modulate the DOS. If the DOS is large ( $\partial n / \partial \mu \gg c$ ), the changes in  $C_{PEN} \sim (\partial n / \partial \mu)^{-1}$  will capture the changes in the size of the Fermi surface, if  $\partial \mu / \partial n$  is monotonic, or its topology, if  $\partial \mu / \partial n$  is discontinuous.

Capacitance measurements are not limited to measuring penetration field capacitance. We can probe the capacitance from the top (bottom) gate to the 2DEG channel:

$$C_{T(B)} = \partial n / \partial V_{T(B)} \quad (3.5)$$

and their *symmetric*  $C_S = C_T + C_B$  and *antisymmetric*  $C_A = C_T - C_B$  linear combinations. In bilayer graphene, the utility of measuring the antisymmetric capacitance can be understood from Figure 3.2. If the electrons in the bilayer graphene are polarized to occupy the top (bottom) layer, then the capacitance measured from the top (bottom) gate would be enhanced. The antisymmetric capacitance is sensitive to the layer polar-

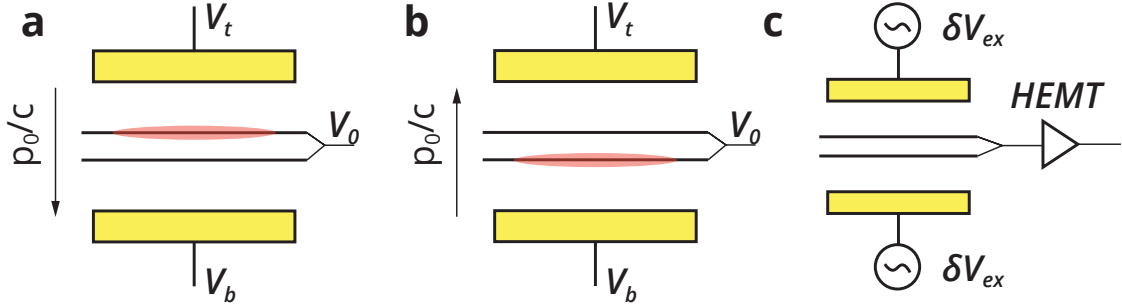


Figure 3.2: Schematic of an antisymmetric capacitance measurement in bilayer graphene **a**  $\partial n_{\text{BLG}}/\partial V_t$  is enhanced by electrons polarized to the top layer, **b**  $\partial n_{\text{BLG}}/\partial V_b$  is enhanced by electrons polarized to the bottom layer **c** Measurement layout, two out of phase AC excitations are applied to the top and bottom gates simultaneously, the cryogenic amplifier (HEMT) is connected to the BLG

ization  $p = n_1 - n_2$ , where  $n_{1,2}$  are carrier densities of the two layers. In particular, the phase diagram of the ZLL of BLG (2.10) is mapped out by measuring the antisymmetric capacitance, owing to the unique relationship between orbital wavefunction and layer polarization in ZLL BLG. See Appendix A.2 for a detailed derivation that relates the symmetric and antisymmetric capacitances to observable derivatives of layer polarization and carrier densities in bilayer graphene.

## 3.2 Example: Capacitance probe of trilayer graphene band structure

**Abstract:** In this section I illustrate the capacitance measurement technique with an example in which we probe high-quality dual-gated trilayer graphene devices. At zero applied magnetic field, we observe a number of electron density- and electrical displacement-tuned features in the electronic compressibility associated with changes in Fermi surface topology. At a high displacement field and low density, strong trigonal warping gives rise to three new emergent Dirac cones in each valley, which we term

“gullies”. The gullies are centered around the corners of a hexagonal Brillouin zone and related by threefold rotation symmetry. At low magnetic fields of  $B = 1.25$  T, the gullies manifest as a change in the degeneracy of the Landau levels from two to three. Weak incompressible states are also observed at integer filling within these triplet Landau levels, which a Hartree-Fock analysis indicates are associated with Coulomb-driven nematic phases that spontaneously break rotation symmetry.

*The contents of this section have previously appeared as Phys. Rev. Lett. 121, 167601 doi:10.1103/PhysRevLett.121.167601*

In graphene multilayers, strong trigonal warping of the electronic band structure leads to a complex evolution of Fermi surface topology within the low energy valleys located at the corners of the hexagonal Brillouin zone[59, 60]. The comparatively small energy

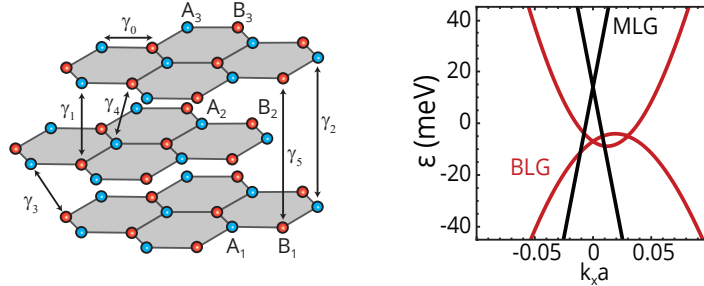


Figure 3.3: **Trilayer graphene band structure.** **left:** Lattice structure of ABA trilayer graphene with hopping parameters identified. In addition to the  $\gamma_i$ , the electronic structure is determined by the interlayer potentials  $\Delta_1 \propto D$  and the relative potential of the inner layer with respect to the outer layers,  $\Delta_2$ . **right:** Electronic band structure of trilayer graphene in the absence of an applied displacement field. The linear monolayer-like and parabolic bilayer-like bands are labeled. The momentum is relative to the  $K$  point in the  $\mathbf{k}_x \parallel \Gamma - K$  direction.

scales characterizing the underlying interlayer hopping processes ( $\sim 100$  meV) renders these transitions accessible via electrostatic gating, providing a highly tunable platform for engineering both zero- and high magnetic field electronic structure. Of particular

interest is the possibility to use band structure engineering to create novel manifolds of degenerate Landau levels (LLs), where enhanced electron-electron interaction effects can lead to novel correlated ground states. However, such control comes at the cost of requiring high sample quality to avoid smearing the subtle electronic features. In this Letter we report magnetocapacitance measurements of exceptionally high quality Bernal-stacked (ABA) trilayer graphene devices (Fig. 3.3). Absent an applied perpendicular electric field, the band structure of ABA trilayer is described by independent monolayer graphene-like (linear) and bilayer graphene-like (parabolic) bands[61, 62, 63] in each of the two valleys centered at the high symmetry  $K$  and  $K'$  points (Fig. 3.3). Applied electric displacement field  $\mathbf{D}$  strongly hybridizes these two sectors, driving the linear monolayer-like band to high energies and generating new structure in the low-energy bilayer-like bands (Fig. 3.4). For large electric fields, the strong trigonal warping is predicted to lead to the formation of new Dirac cones around three separated quasi-momentum points we term ‘gullies.’ The gully triplets are centered around each of the two original valleys[64, 65] and are related to each other by three-fold rotation symmetry. At quantizing magnetic fields, the three-fold symmetry of the gullies may lead to novel broken symmetry ground states[66], including nematic states as recently observed on the surface of high purity bismuth crystals[67].

Past experiments on ABA trilayer graphene[68, 69, 70, 71, 72, 73, 74, 75, 76, 77] have observed features associated with numerous aspects of the single particle band structure, including a variety of electric- and magnetic-field tuned LL crossings[78, 79] that tightly constrain band structure parameters[71, 74]. Recent experiments have also found evidence for interaction-induced quantum Hall ferromagnetic states at high magnetic field[73, 76, 77]. However, the high-electric field regime of the Dirac gullies has not been explored in high mobility devices where interaction driven states might be accessible. To access the high mobility, high- $D$  regime, we study ABA trilayer flakes encapsulated

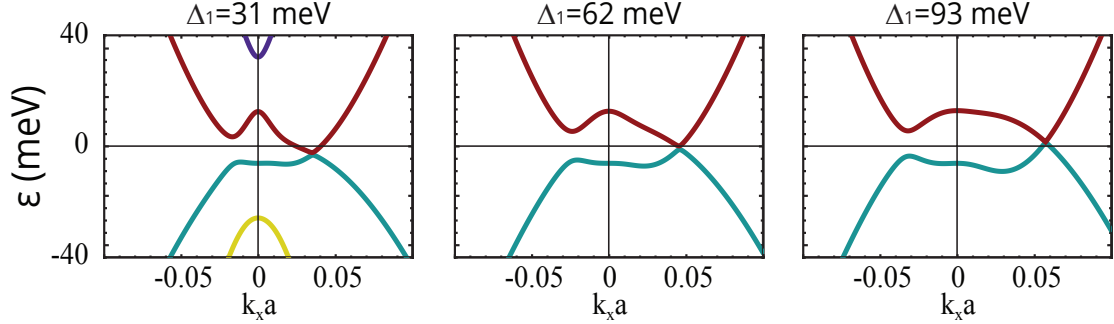


Figure 3.4: **Band structure evolution under applied electric field.** For a wide range of electric fields, the low energy structure is described by three isolated Dirac cones slightly displaced from the  $K(K')$  points.

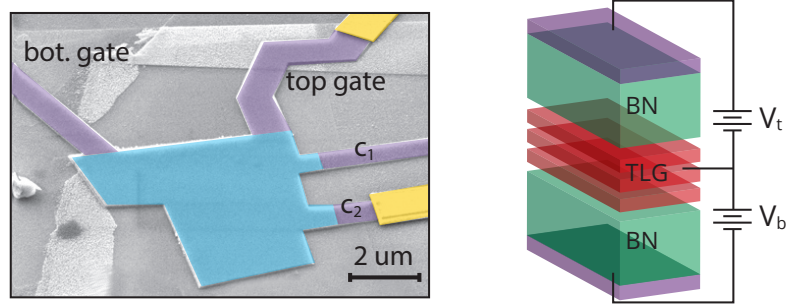


Figure 3.5: **Trilayer graphene capacitance device.** **left:** False color electron micrograph of the measured trilayer graphene device. The active region is indicated in cyan. **right:** Device schematic: trilayer graphene encapsulated in  $\sim 20$  nm BN with few layer graphite top and bottom gates. Independent contacts to the gates and graphene layer allow independent control of charge density  $n = c_t V_t + c_b V_b$  and displacement electric field  $D = \epsilon_{hBN}(V_t/d_t - V_b/d_b)$ , where  $\epsilon_{hBN} \approx 3$  and  $d_{t(b)} = 18, 20$  nm are the thicknesses of the top and bottom gates.

in hexagonal boron nitride dielectric layers and single-crystal graphite gates [49] (Fig. 3.5). We use few-layer graphite to contact the trilayer, allowing us to vary both the total charge density and displacement field  $\mathbf{D}$  across the trilayer (Fig. 3.5). We measure the penetration field capacitance  $C_P$ [80], defined as the capacitance between top and bottom gate with the graphene layer held at constant potential. The finite density of

states  $\partial n/\partial\mu$  of the trilayer only partially screens the electric field between the top and bottom gate, reducing the measured  $C_P$  so that (for symmetric top- and bottom gates with geometric capacitance  $c$ )  $C_P = c^2/(2c + \partial n/\partial\mu) \propto (\partial n/\partial\mu)^{-1}$  for  $\partial n/\partial\mu \gg c$ . Changes in  $C_P$  can then be associated with changes in the Fermi surface, with changes in topology associated with discontinuities in the density of states.

Fig. 3.6 shows  $C_P$  measured at  $B=0$  as a function of  $D$  and electron density  $n$ . A variety of  $n$  and  $D$ -tuned discontinuities are readily visible and indicated in the Figure with numeric labels (1)-(9). These include a sharp  $C_P$  maximum at charge neutrality for both positive and negative  $D$  (1); two elevated  $C_P$  features with parabolic boundaries (‘parabolas’) at negative and positive  $n$  (2-3), two low- $C_P$  regions with triangular boundary (‘triangles’) within the parabolic regions (4-5), a ‘wing’-shaped high  $C_P$  region both above and below charge neutrality (6-7), and a narrow elevated  $C_P$  region that runs parallel to the parabolic feature for negative  $n$  bounded by contours (8-9). Some of the capacitance features can be associated with the single-particle band-structure by inspection. For example, (1) is consistent with the small band gap or linear band crossing expected at charge neutrality[64]. The triangular features (4-5), meanwhile, are identified as the extrema of the linear bands (purple and yellow in Fig. 3.4) which disperse rapidly to high energy with increasing  $D$ . Additional features are thus associated with the complex band minima of the low energy bands.

To understand the remaining observed compressibility features we perform tight binding simulations of the trilayer graphene band structure. Energy eigenvalues are computed using a 6-band tight binding model (see Supplementary information). Hopping between different atoms within the unit cell is parameterized by six tight binding parameters  $\gamma_i$ ,  $i = 1..6$ , one on-site energy  $\delta$ , and two energy asymmetries  $\Delta_1$  and  $\Delta_2$ . The first describes the potential difference between the top and bottom layers and is most directly tuned by the strength of an externally applied polarizing electric field  $D$ . The second

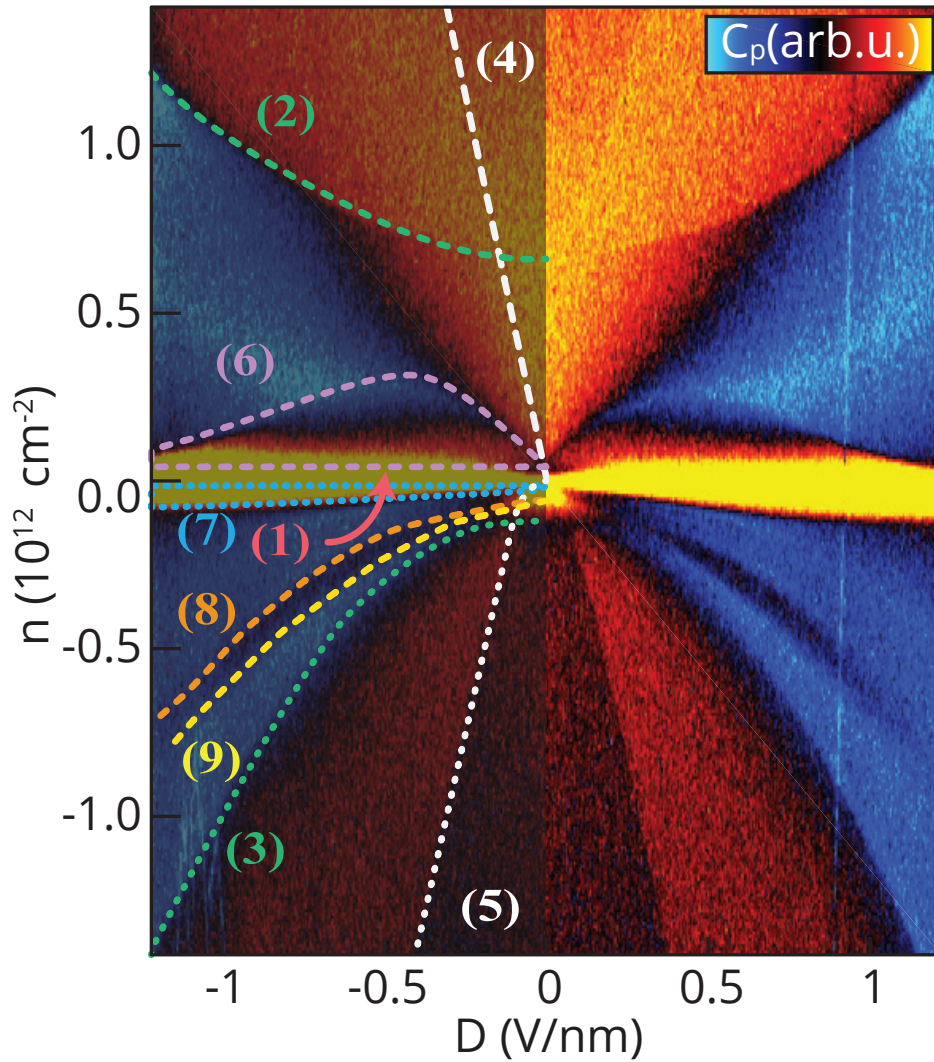


Figure 3.6: **Trilayer graphene penetration field capacitance measurements at  $B = 0$ .** Penetration field capacitance  $C_P$  at  $B = 0$  T and  $T \approx 50$  mK as a function of  $n$  and  $D$ . The applied displacement field breaks the mirror symmetry of the ABA-stacked trilayer graphene and induces a on-site energy difference  $\Delta_1$  between the top and bottom layer. Main features visible in the experimental data are highlighted by dashed lines and indexed by numerals (see main text). The  $D < 0$  region is shaded to increase the visibility of the features. Data is plotted on a saturated color scale (see Fig. S5).



measures the potential imbalance between the central layer and the two outer layers, and screening effects within the trilayer.

Figure 3.7a shows the calculated inverse compressibility within this model, as a function of the carrier density and  $\Delta_1 \propto |\mathbf{D}|$ . Both the geometric and parasitic capacitances within the device influence the mapping of  $\partial n / \partial \mu \leftrightarrow C_P$  between calculated compressibility and measured data. Moreover, interactions likely renormalize the compressibility particularly when it is high. We thus restrict ourselves to qualitative comparisons of the magnitude of the signals, and plot both in arbitrary units. We do, however, achieve quantitative agreement between data and simulation for the *position* of extrema and discontinuities for parameters  $\gamma_0 = 3.1$ ,  $\gamma_1 = .38$ ,  $\gamma_2 = -0.021(5)$ ,  $\gamma_3 = 0.29$ ,  $\gamma_4 = 0.141(40)$ ,  $\gamma_5 = 0.050(5)$ ,  $\delta = 0.0355(45)$ , and  $\Delta_2 = 0.0035$ , where all energies are expressed in eV. Notably, the model succeeds in matching the experimentally observed features only for an exceptionally narrow range of parameters, providing tighter constraints on  $\{\gamma_i\}$  and  $\{\Delta_i\}$  than previously achieved using only LL coincidences[71, 75, 81]. In addition to the parameters  $\gamma_i$  and  $\Delta_2$ , a single scale factor  $\alpha = .165$  e·nm is chosen so that  $\Delta_1 = \alpha \cdot D$ . The factor  $\alpha$  describes dielectric screening of the perpendicular electric field by the trilayer, implying an effective  $\varepsilon_{TLG}^\perp \approx 4$  for the trilayer itself. Full details of the calculations are provided in the supplementary materials.

The agreement between theory and experiment allows us to understand the connection between the observed compressibility features and the nature of the Fermi contours. Fig. 3.7b shows calculated Fermi surface contours in 11 distinct regions throughout the experimentally accessed parameter regime. Regions (i) and (xi), for example, are distinguished by the existence of a second, independent Fermi surface arising from the second electron- or hole-subband, respectively, as intuited above. All other regions are separated by Lifshitz transitions and distinguished by differences in Fermi surface topology within a single electron- or hole-band. We note that signatures of Lifshitz transitions

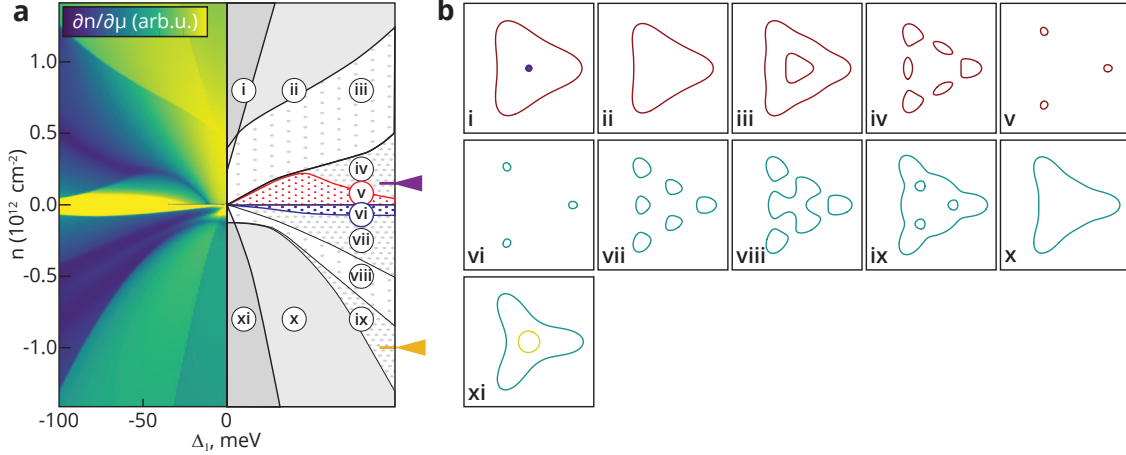


Figure 3.7: **Fermi surface topology** **a**. Left panel: Inverse electronic compressibility  $\partial n/\partial\mu$  calculated from a 6-band tight binding Hamiltonian as a function of interlayer asymmetry  $\Delta_1$  and electron density  $n$ . Right panel: schematic showing regions (indexed by the Roman numerals) separated by sharp changes in the compressibility. **b**. Fermi contours calculated at each of the points indexed by roman numerals in **a**. Color indicates the band and follows the convention of Fig. 3.4; note that panels i-v are Fermi surfaces of electrons while vi-xi are Fermi surfaces of holes.

were recently found in tetralayer graphene[60] at zero magnetic field, but no direct compressibility measurements of Lifshitz transitions have been reported. With the exception of regions iii-iv, all of the regions are bounded by experimentally observed features described in Fig. 3.6. We note that features characterized by a diverging density of states, such as the iii-iv boundary, only weakly modify the measured capacitance and are barely discernible even in Fig. 3.6.

Fig. 3.8a-b shows comparisons of traces from the measured capacitance and the numerically calculated inverse compressibility at  $n = -1.0 \times 10^{12} \text{cm}^{-2}$ . Both data and simulation show matching discontinuities associated with the band edge of the second hole subband (i.e., the xi-x transition) as well as the nucleation of three new electron pockets within the main hole-like Fermi pocket (x-ix). Of particular interest is the regime of low  $n$  and large  $D$ , where the gully Dirac points are predicted[64]. Fig. 3.8c-d show line traces at  $n = .15 \times 10^{12} \text{cm}^{-2}$ . The ‘wing’ region, bounded by sharp discontinuities

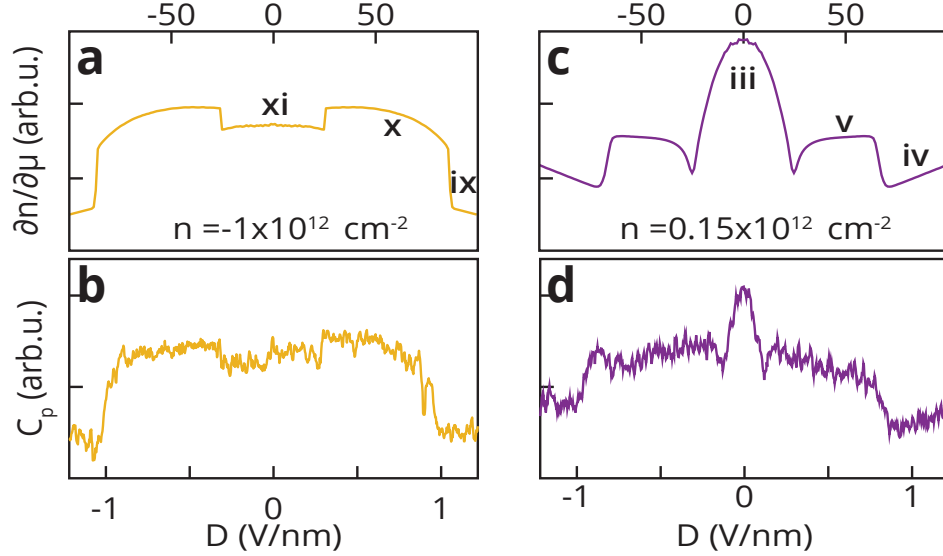


Figure 3.8: **a** Simulated  $\partial n/\partial\mu$  and **b** measured  $C_P$  at  $n = -1 \times 10^{12} \text{cm}^{-2}$ . The discontinuous jump in the data at  $D \approx \pm 3 \text{ V/nm}$  coincides with population of the 2nd hole subband (xi-x transition), while the jump at  $D \approx \pm .95 \text{ V/nm}$  coincides with the opening of internal electron-like Fermi surfaces within the main hole pocket (x-ix transition). **c** Simulated  $\partial n/\partial\mu$  and **d** measured  $C_P$  at  $n = .15 \times 10^{12} \text{cm}^{-2}$ . The sharp minimum at  $D \approx \pm .5 \text{ V/nm}$  coincides with a Lifshitz transition from one multiply connected electron pocket (iii) to three disconnected Dirac cones (v). At the discontinuity at  $D \approx \pm .9 \text{ V/nm}$ , the Dirac cones are joined by three additional auxiliary pockets.

in both the measured signal and simulated data, is readily identified with region (v), in which the Fermi surface arises from three isolated gully Dirac cones (Fig. 3.9).

In addition to its thermodynamic signatures at  $B = 0$ , the emergence of isolated Dirac cones can be expected to lead to new transport, optical, and thermodynamic phenomenology at finite magnetic fields. In monolayer graphene, for example, the two inequivalent valleys lead to four-fold internal degeneracy of the LLs, with an additional factor of two arising from electron spin. The observation of four-fold degeneracy was a critical feature of the first experimental demonstrations of the Dirac spectrum in monolayer graphene[3, 4].

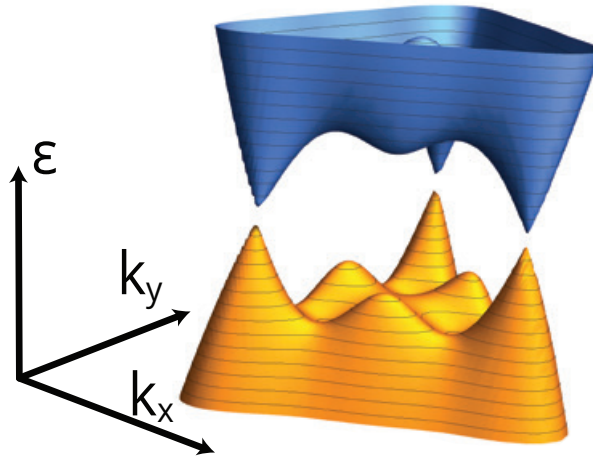


Figure 3.9: Band structure near  $K$ -point for  $\Delta_1 = 75$  meV showing the emergent Dirac gullies.

The gully Dirac cones similarly manifest as increased LL degeneracy. Figure 3.10 shows  $C_P$  data measured at  $B=1.25$  T alongside the results of diagonalizing the trilayer Hamiltonian in the presence of a magnetic field (simulations ignore spin splitting; see supplementary information for details). Larger energy gaps manifest as prominent peaks in  $C_P$  at filling factors  $\nu = eBn/h$ , spaced by integer multiples of  $g$ , the internal LL degeneracy. Near  $D = 0$ , we observe the strongest capacitance peaks spaced by  $\Delta\nu = 2$ , in agreement with the two-fold valley degeneracy ( $g = 2$ ) but lifted spin degeneracy (Fig. 3.11, top). In contrast at large displacement fields ( $D > 0.7$  V/nm) and near charge neutrality—i.e., in the regime of the Dirac gullies—this behavior changes, with the most prominent gaps spaced by  $\Delta\nu = 3$  for  $-12 < \nu < 12$  (see Fig. 3.11, bottom). The calculated single particle energy spectrum (Fig 3.12a) shows that displacement field leads to the formation of four triplets of LLs per spin projection (labeled T1, T2, T3, and T4); within each triplet, three LLs intertwine into a single three-fold quasi-degenerate band consistent with the observed LL degeneracy. We note that triplet LLs are a generic feature of trigonally warped multilayer band structures, and evidence for three-fold de-

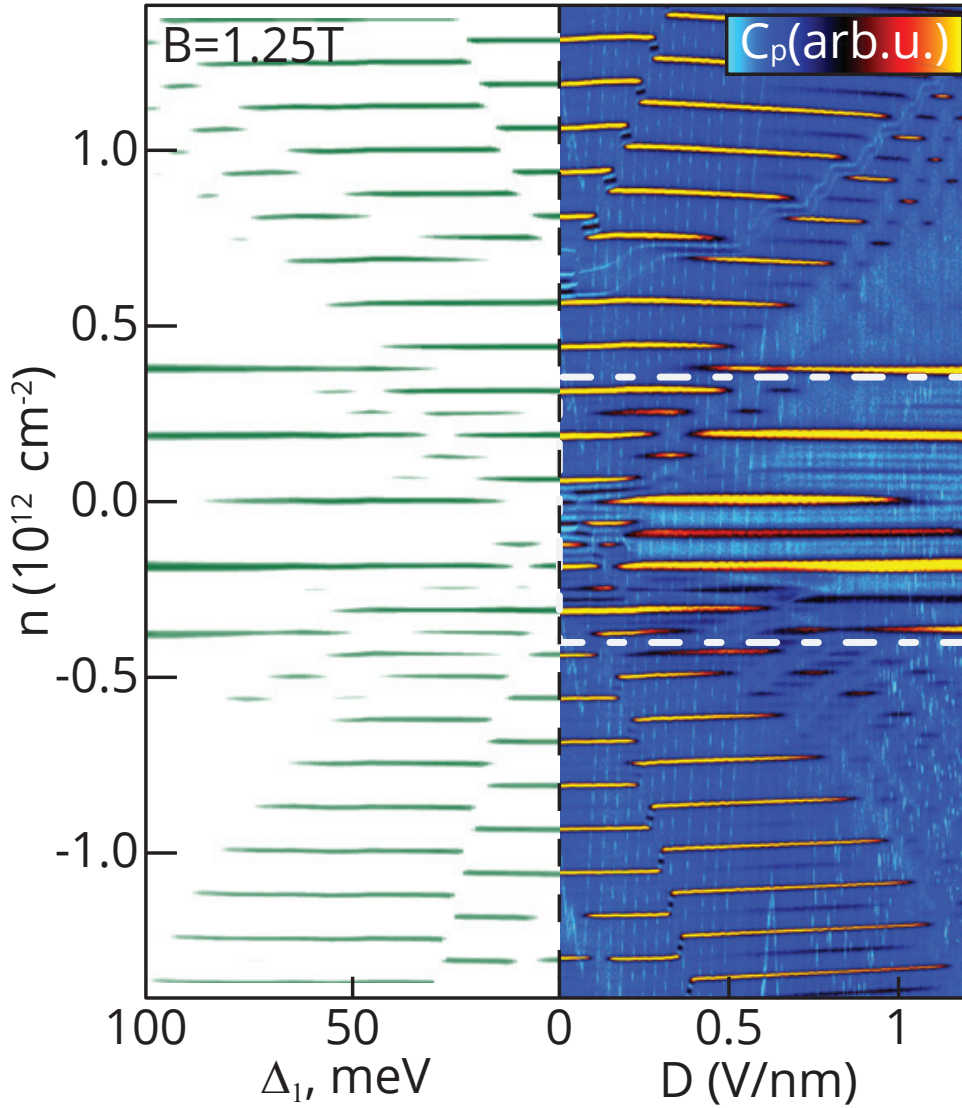


Figure 3.10: Right panel: Penetration field capacitance  $C_P$  measured at  $B=1.25$  T as a function of  $D$  and  $n$ . The dashed lines indicate the region of low carrier density near the valence and conduction band minima where trigonal warping has strongest effect and leads to a formation of new Dirac points. Left panel: simulated inverse compressibility at  $B=1.25$  T based on band structure parameters. A phenomenological thermal broadening of  $0.1\text{meV}$  is assumed to generate contrast, so that only the largest gaps are visible in green.

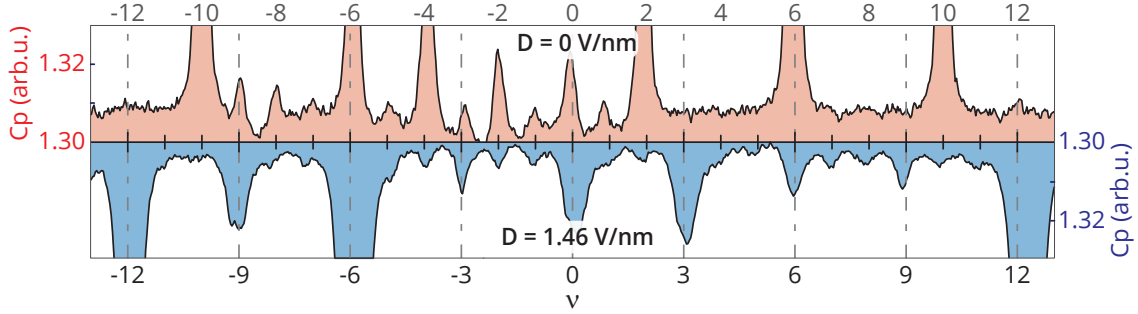


Figure 3.11:  $C_P$  traces for  $n \in [-0.5, 0.5] \times 10^{12} \text{ cm}^{-2}$  at  $D = 0$  (red) and at  $D = 1.46$  V/nm (blue). The  $D = 0$  line trace shows strong capacitance peaks at even filling factors, in contrast to the peaks at multiples of three ( $\nu = \pm 3, 6, 9, 12$ ) for  $D = 1.46$  V/nm.

generate LLs has previously been reported in suspended bilayer graphene samples[82].

While the observation of triplet LLs is consistent with expectations from our single-particle model, close examination of high displacement field data reveals departures from the noninteracting picture. In particular, we observe  $C_P$  peaks at all integer filling factors  $-6 < \nu < 12$ , corresponding to the dashed region of Fig. 3.10 (see also Fig. B.6), including weak peaks at  $(\nu \bmod 3) \neq 0$ . These gaps persist *without* closing over the whole range of  $D > 0.7$  V/nm. Such behavior is qualitatively inconsistent with the single particle spectrum, which predicts that within each triplet (denoted T1...T4 as in Fig. 3.12a) the single particle eigenstates evolve via a series of crossings with increasing  $\Delta_1$  (Fig. 3.12b). One thus expects these anomalous gaps to undergo repeated closings, in contrast to their observed persistence.

The failure of the single-particle picture is not surprising. The estimated bandwidth of each triplet (Fig. 3.12b),  $\delta\varepsilon < 0.5$  meV, is smaller than the scale of the Coulomb interactions,  $E_C = e^2/(\varepsilon\ell_B) \approx 10$  meV at  $B = 1.25$  T (here  $e$  is the elementary charge,  $\varepsilon = 6.6$  the in-plane dielectric constant of hBN[83], and  $\ell_B = \sqrt{\hbar/(eB)}$  the magnetic length). Taking these interactions into account, the individual LLs within the triplet are effectively degenerate; the ground state at integer filling must result from minimizing

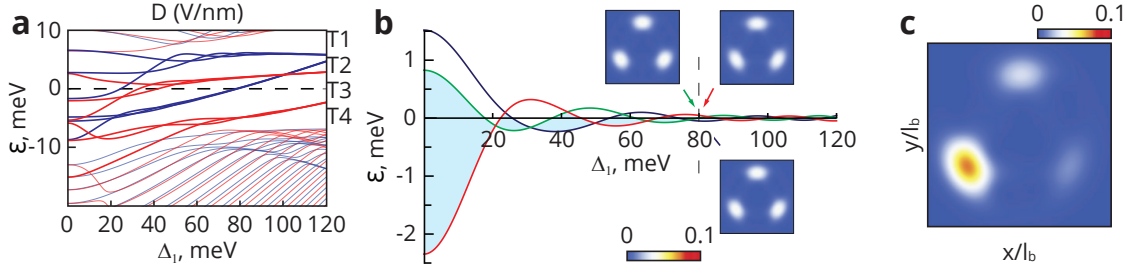


Figure 3.12: **a.** Evolution of LLs at  $B = 1.25$  T as a function of interlayer potential difference  $\Delta_1$ . As the electric potential increases, 12 distinct LLs at  $\Delta_1 \approx 0$  intertwine into 4 quasi-degenerate triplets, denoted  $T_1 \dots T_4$ , separated from a near-continuum of closely spaced LLs by energy gaps. **b.** Expanded view of the triplet T2 with the average energy of the triplet subtracted. Insets show the real-space probability distribution for a coherent state formed from wave-functions in each of the component LLs. All respect rotation symmetry. **c.** Real-space probability distribution of the Hartree-Fock ground state at  $1/3$  filling of the spin-polarized triplet T2 at  $\Delta_1 = 80$  meV, showing strongly broken three-fold rotation symmetry.

repulsive interactions and is likely to result in a gapped, symmetry breaking quantum Hall ferromagnetic state.

We investigate this quantitatively using a variational Hartree-Fock analysis (see supplementary information) of the ground state when only one out of 3 LLs within a single spin branch of triplet T2 is filled ( $1/3$  filling). The three insets to Fig. 3.12b show real space probability distributions for coherent states constructed for each of the three components of T2. Absent interactions, the ground state at  $1/3$  filling consists of the lower energy component of T2 for a given value of  $B$  and  $\Delta_1$ , and preserves rotation symmetry. In contrast, the Hartree-Fock ground state (shown in Fig. 3.12c) spontaneously breaks the  $C_3$  symmetry—it is a gully nematic. As long as  $\delta\varepsilon \ll E_C$ , the gap will be only weakly modulated by  $\Delta_1$ , making it insensitive to the single-particle level crossings, in agreement with experimental observation. The nematic ground state is merely one example of a symmetry breaking channel. Intuitively, nematics are favored by interactions when LL wave functions are localized in well separated real-space pockets, as in the case in the highly anisotropic wave functions of Fig. 3.12c. In a momentum space picture,

these pockets are associated with the main Dirac gullies represented in the contours of Fig. 3.7 v-vi. In this limit, ABA trilayer triplet LLs resemble the case of the (111) surface of SnTe recently considered theoretically. [84]. Our single-particle calculations suggest that other limiting behaviors can also be realized in ABA trilayer graphene, resulting in qualitatively different ground states. For instance, the triplet states T1 and T4 are considerably less anisotropic, being associated with multiple momentum space pockets close to the  $K(K')$  points as in Fig 3.7 vii. In these triplets, isotropic ground states constructed from a superposition of triplet wavefunctions may be favored. Notably, the relevant anisotropies within each triplet are continuously tunable by external electric and magnetic fields, making ABA trilayer graphene an remarkably versatile platform for exploring correlation effects in unusual quantum Hall ferromagnets. Cataloging the theoretical possibilities, and determining how to distinguish them experimentally, will be the topic of future work.



# Chapter 4

## Even-Denominator FQH effect in monolayer graphene

**Abstract:** In monolayer graphene, the two inequivalent sublattices of carbon atoms combine with the electron spin to give electrons a nearly fourfold degenerate internal isospin. At high magnetic fields, the isospin degeneracy increases the already large intrinsic degeneracy of the two-dimensional Landau levels, making low-disorder graphene systems a versatile platform for studying multicomponent quantum magnetism. Here, we describe magnetocapacitance experiments of ultraclean monolayer graphene devices in which a hexagonal boron nitride substrate breaks the symmetry between carbon sublattices. We observe a phase transition in the isospin system, which is marked by unusual transitions in odd-denominator fractional quantum Hall states for filling factors  $\hat{\nu}_j$  near charge neutrality and by the unexpected appearance of incompressible even-denominator fractional quantum Hall states at  $\nu = \pm 1/2$  and  $\nu = \pm 1/4$ . We propose a scenario in which the observed states are multicomponent fractional quantum Hall states incorporating correlations between electrons on different carbon sublattices, associated with a quantum Hall analogue of the Néel-to-valence bond solid transition that occurs at charge

neutrality.

*The contents of the chapter have previously appeared as Nature Physics, volume 14, pages 930-935 (2018), doi:10.1038/s41567-018-0190-0.*

Clean two dimensional electron systems in the high magnetic field limit host various correlated phenomena including Wigner crystallization of electrons, topologically ordered fractional quantum Hall liquids, and quantum Hall ferromagnets. Among such systems, monolayer graphene is distinguished by its zero energy Landau level (ZLL), which spans  $\nu \in [-2, 2]$  with  $\nu \equiv 2\pi\ell_B^2 n_e$  the Landau level filling factor. Here,  $n_e$  is the areal electron density and  $\ell_B^2 = \hbar/eB$  is the magnetic length. The four-fold degeneracy of the ZLL reflects the near-degeneracy of internal spin- and sublattice quantum numbers, while the  $\pi$ -Berry phase of the massless Dirac electrons pins the center of the ZLL to charge neutrality at  $n_e = 0$ . Within the ZLL, the dominant long-ranged Coulomb interaction does not distinguish between different spin or sublattice flavors, but favors breaking the approximate SU(4) isospin symmetry by polarizing the ground state into a single isospin component [85]. Broken isospin symmetry manifests principally as additional gapped states [86, 36] at integer fillings  $\nu = 0, \pm 1$ .

Of particular interest is the case of the charge neutral state at  $\nu = 0$ , corresponding to half-filling of the ZLL, where Pauli exclusion prevents, for example, simultaneous spin and sublattice polarization. In this case, the direction of polarization is set by competing isospin anisotropies including both single particle effects and the anisotropy of the Coulomb interactions at the scale of the honeycomb lattice. Candidate  $\nu = 0$  ground states are sketched in Fig. 4.1 and characterized by either spin or sublattice order, including a canted antiferromagnetic (CAF) state that breaks spin rotation symmetry[87] and a partially sublattice polarized (PSP) density wave featuring a Kekulé distortion that triples the size of the unit cell[88].

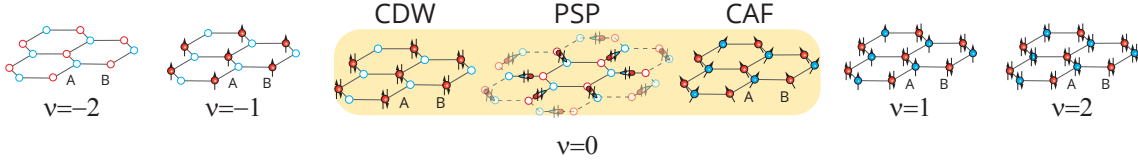


Figure 4.1: Sketches of ground state spin and sublattice polarizations at integer filling within the ZLL. At  $\nu = -2$  the ZLL is empty while at  $\nu = +2$  it is fully filled. At  $\nu = \pm 1$ , single or triple occupation permits full spin and sublattice polarization. At  $\nu = 0$ , however, corresponding to half filling, a variety of ground states are predicted[56, 87, 88, 89, 90] including charge density wave (CDW), partially sublattice polarized (PSP), and canted antiferromagnetic (CAF) phases.

The CAF and PSP states are direct analogs of the Néel and valence bond solid (VBS) states that arise in studies of two dimensional quantum magnetism, as noted in a series of recent theoretical works[91, 92, 93]. Within conventional Landau-Ginzburg-Wilson theory, incompatible symmetry breaking between the VBS and Néel phases (real-space and spin, respectively) requires a first order transition. However, unusual critical phases allowing for a continuous transition have been proposed[94], as well as first order transitions with emergent symmetry at the critical point[92]. Realizing the PSP-CAF transition in monolayer graphene could thus allow direct experimental probes of this unconventional quantum phase transition.

Here we report the observation of anomalous fractional quantum Hall features at low  $|\nu|$ , consistent with proximity to a PSP-CAF phase transition at  $\nu = 0$ . The transition is marked by the appearance—and subsequent disappearance—of even-denominator fractional quantum Hall (EDFQH) states at  $\nu = \pm 1/2$  and  $\nu = \pm 1/4$  in the vicinity of charge neutrality, coincident in magnetic field with weakening of nearby odd denominator fractional quantum Hall (ODFQH) states across the range of  $-2/3 < \nu < 2/3$ . We observe similar phenomenology in three monolayer graphene samples (A, B, and C) fabricated by encapsulating the graphene flake between single crystal hexagonal boron nitride gate dielectrics and single crystal graphite electrostatic gates[49, 95]. The mag-

netic field at which the anomalous FQH features are observed is directly correlated with the strength of an observed zero-field insulating state associated with substrate-induced sublattice splitting  $\Delta_{AB}$ , with the  $\nu = \pm 1/2$  states appearing for a narrow range of magnetic field centered on 28.3 T, 27.5 T, and 5.6 T in the three devices. We interpret the observed features within a model in which a magnetic field-dependent antiferromagnetic interaction anisotropy[96] competes with a fixed substrate-induced sublattice-symmetry breaking gap[97, 98], leading to a transition between sublattice- and spin-ordered phases at both neutrality[89, 90] and nearby fractional fillings[99].

Figure 4.2 shows penetration field capacitance ( $C_P$ ) for sample A, where  $C_P$  is defined as the differential capacitance between the top and bottom gates with the graphene held at constant electrochemical potential[80]. Data are plotted over a range spanning the ZLL as a function of magnetic field  $B$  and nominal charge carrier density  $n_0 = c(v_t + v_b - 2v_s)$ , where  $c$  is the average gate-to-sample geometric capacitance of the two (nearly symmetric) gates and  $v_t$ ,  $v_b$ , and  $v_s$  are the voltages applied to top gate, bottom gate, and sample, respectively. We observe gapped quantum Hall states, which appear as peaks in the measured signal at constant  $\nu$  (see Section ), at integer fillings  $\nu = \pm 2, \pm 1$  and 0, as well as at fractional filling factors  $|\nu - [\nu]| = \frac{p}{mp \pm 1}$ , where  $[\nu]$  is the greatest integer less than or equal to  $\nu$ . We observe states with  $m = 2, 4$  and  $p$  large as 7 (Fig. 4.2, Fig. C.1). In the absence of four terminal measurements we extract the Hall conductivity of the high  $C_P$  gapped states using the Strěda formula[100], which states that gaps following a linear trajectory in the density-magnetic field plane carry quantized Hall conductivity equivalent to their slope.

Incompressible EDFQH states appear at  $\nu = \pm 1/2$ , but only in a narrow range of magnetic fields. Similar phenomenology is also observed at  $\nu = \pm 1/4$ , with EDFQH appearing only for a small range of  $B$  (Fig. 4.3). The appearance of EDFQH states is accompanied by weakening or disappearance of adjacent ODFQH states. This is evident

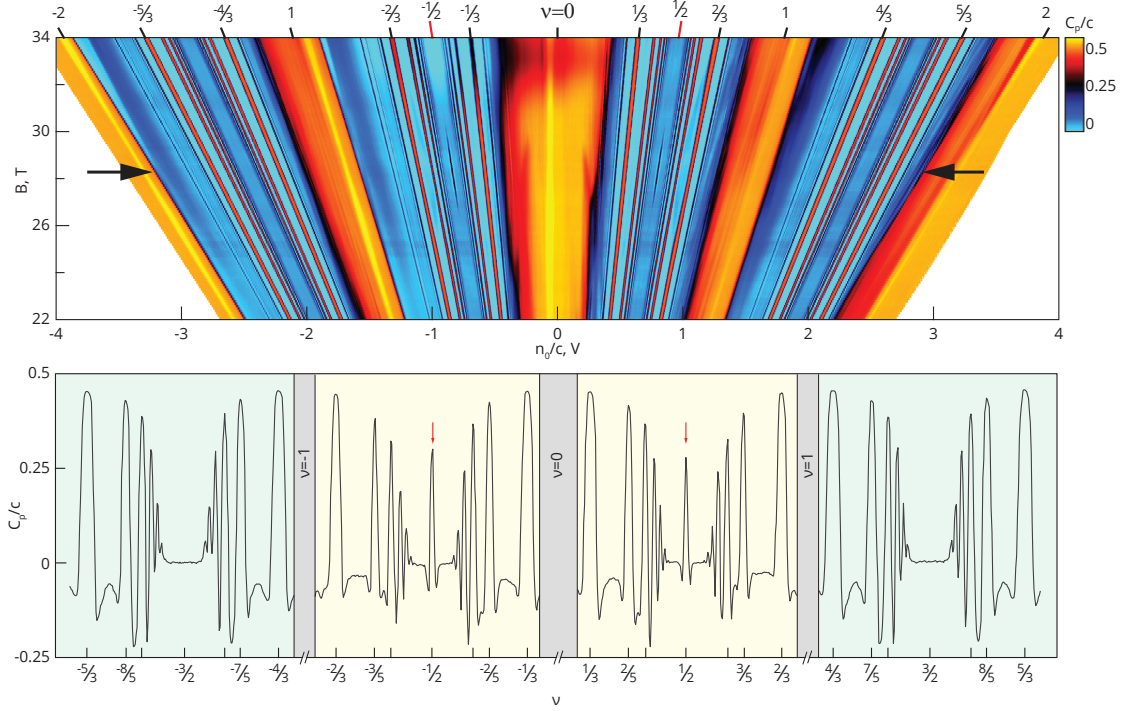


Figure 4.2: **top:** False color plot of penetration field capacitance  $C_P/c$  measured (see Methods) in sample A at  $T=300$  mK as a function of the the magnetic field,  $B$ , and the nominal charge density  $n_0 \equiv c(v_t + v_b - 2v_s)$  where  $v_t$ ,  $v_b$  and  $v_s$  are the top gate, bottom gate, and sample voltages, respectively.  $c$  is the average geometric capacitance of the two gates. Fractional quantum Hall states appear as lines of high  $C_P$  with a slope proportional to their quantized Hall conductivity[100]. The dataset spans filling factors  $\nu = [-2, 2]$ , encompassing the zero energy Landau level. **bottom:**  $C_P$  trace taken at constant  $B = 28.3$  T between filling factors  $\nu = -2$  and  $\nu = 2$ , corresponding to the black arrows in the above color plot. Incompressible states occur at  $\nu = \pm 1/2$  (red arrows), indicating an even denominator fractional quantum Hall state, while  $\nu = \pm 3/2$ , which are farther away from charge neutrality, remain compressible. Incompressible features associated with the IQH are omitted to more clearly show the FQH features.

both near  $\pm 1/4$  (Fig. 4.3 and Fig. C.3) and  $\pm 1/2$  (Fig. 4.4a,c and Fig. C.2, C.4), with weakening most evident at temperatures comparable to the ODFQH energy gaps (see Fig. C.14). In sample C, an EDFQH state at  $\nu = \pm 1/2$  and weakening/disappearance of nearby ODFQH states also occur, but at much lower  $B$  (Fig.4.4b,d). Both the appearance of the EDFQH states and the weakening of the ODFQH states occur only for fillings near

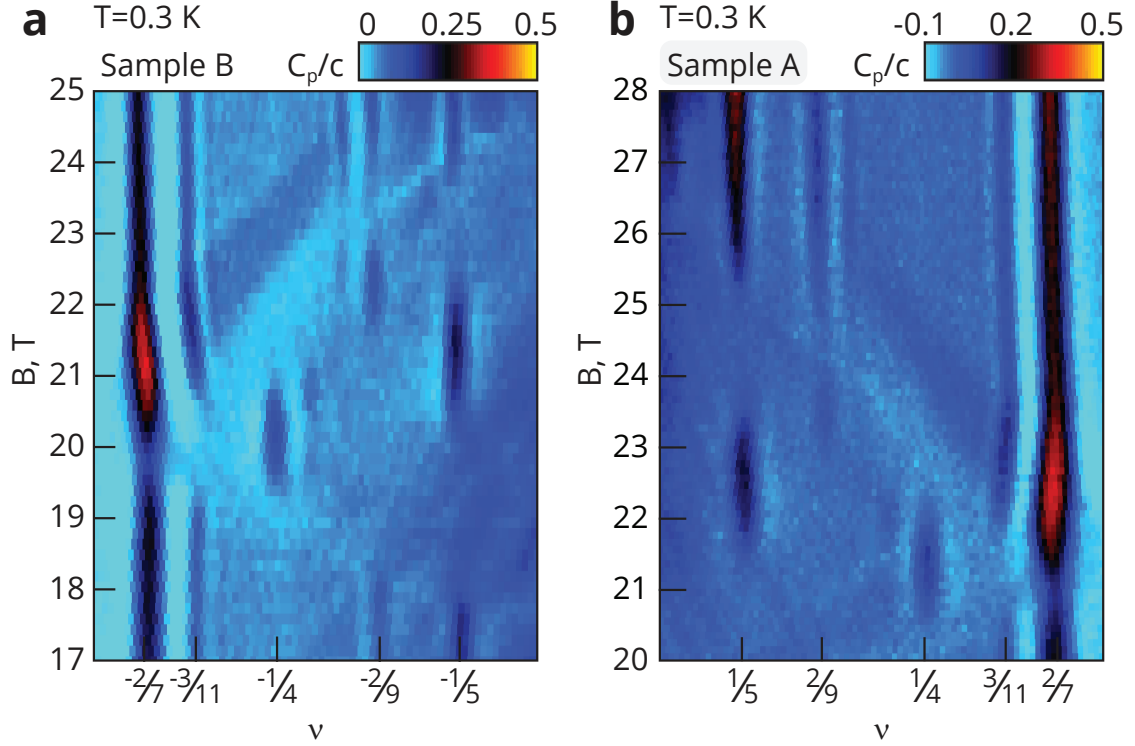


Figure 4.3: **Incompressible FQH states at  $\nu = \pm 1/4$ .** **a** False color plot of  $C_P/c$  in sample B as a function of  $\nu$  and  $B$  at  $T=300$  mK. In addition to the  $\nu = -1/4$  state, FQH states from the  $\nu = \frac{p}{4p+1}$  ODFQH sequence are visible, with  $B$ -dependent weakening associated with isospin phase transitions. **b** Similar data from sample A near  $\nu = +1/4$ .

charge neutrality,  $\nu \in [-2/3, 2/3]$ ; e.g., no EDFQH is observed at  $\nu = \pm 3/4, \pm 5/4, \pm 3/2$  or  $\pm 7/4$  throughout the experimental range of  $B$ . The magnetic field for both ODFQH weakening and EDFQH emergence occurs at lower fields for transitions closer to  $\nu = 0$ , but remains constant for  $2/3 > |\nu| > 1/2$  (Fig. 4.4e-f).

EDFQH states have not been previously reported among the many FQH states observed in monolayer graphene[7, 8, 10, 43, 101, 102], nor have they been predicted[103, 104, 105, 106, 107, 108, 109, 110]. However, previous experiments on other quantum Hall systems have revealed a variety of behaviors at even denominator fractional filling. In single layer semiconductor quantum wells, the 2D electron system is compressible

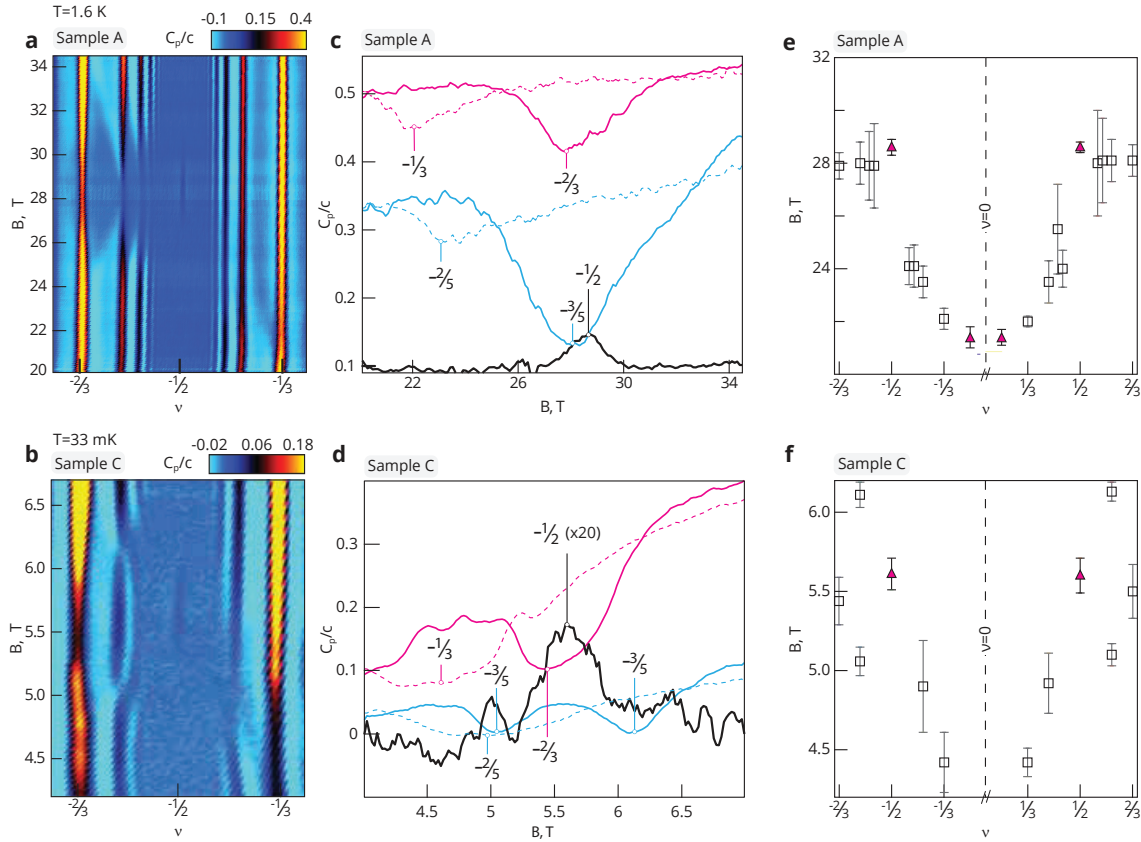


Figure 4.4: **Odd denominator fractional quantum Hall phase transitions associated with the  $\nu = -1/2$  state.** **a**  $C_P$  as a function of  $B$  and  $\nu$  in the vicinity of  $\nu = -1/2$  state for sample A, taken at  $T = 1.6$  K near  $B=28$ T. **b** Similar data from Sample C, taken at  $T = 33$  mK for  $B$  near 5.6T. **c**  $C_P$  peak height for selected FQH states  $\nu \in (-1, 0)$ , plotted as a function of  $B$ , for sample A and **d** sample C, showing the simultaneous strengthening of the even denominator state and weakening of adjacent odd-denominator states. **e** Positions of minima (maxima) of the odd (even)-denominator FQH states for  $\nu \in (-1, 1)$  in Sample A at  $T=1.6$  K. **f** Similar analysis of sample C at  $T= 33$  mK. In sample C, two gap closings are observed at  $\nu = \pm 3/5$ , while only one a single gap weakening is observed in sample A. Error bars in (e) and (f) are defined as the range of magnetic fields where the dips (peaks) are within 10% of their extremal value relative to a smooth background.

at filling factors  $\nu = 1/2$  and  $3/2$  in the lowest Landau level (corresponding to orbital quantum number  $N=0$ ) but forms incompressible FQH states at  $\nu = 5/2$  and  $7/2$  in the first excited LL (orbital quantum number  $N=1$ ) [22]. Other single-component FQH systems, including ZnO [111] and bilayer graphene [46, 49, 95], show EDFQH at different

$\nu$  but always in a regime corresponding to occupation of  $N=1$  orbital wave functions. In the MLG ZLL, orbital wave functions are identical to the  $N=0$  LL of conventional semiconductor systems, and so no single-component even denominator FQH states are anticipated[103, 104, 109, 110, 112]. Multicomponent systems, however, can host a wider variety of FQH states[23], including at even denominator filling factors. Indeed, ED-FQH states at  $\nu = 1/2$ [113, 114, 115, 116] and  $\nu = 1/4$ [117, 118] have been observed in the  $N=0$  LL for structures where electrons are confined to two spatially separated layers or electronic subbands. By analogy with such systems, it seems likely that the monolayer graphene EDFQH states are multicomponent in nature, with the role of the layer/subband quantum number replaced by isospin components within the ZLL. In this scenario, the ODFQH weakening is similarly associated with transitions between ODFQH states constructed from different isospin components[101].

The high symmetry of the ZLL permits many possible isospin polarizations at fractional filling, complicating the task of determining the components relevant for forming multicomponent FQH states. However, recent theoretical work has suggested that the isospin phase diagram of low- $|\nu|$  FQH states closely mimics that of the nearby  $\nu = 0$  integer quantum Hall state[99], which can be analyzed within a Hartree-Fock framework[89, 90]. The  $\nu = 0$  ground state is obtained by optimizing the energy of competing isospin anisotropies constrained by the Pauli exclusion principle, which prohibits double occupation of a spin- or valley component. These anisotropies include the Zeeman effect (with characteristic energy  $E_Z = g\mu_B B \approx 1.34\text{K} \times B[\text{Tesla}]$ , where  $g = 2$  and  $\mu_B$  are the  $g$ -factor of the electron and the Bohr magneton, respectively), the intrinsic sublattice-anisotropy of the Coulomb interactions themselves[56] (with characteristic energy  $E_V = \frac{a}{\ell_B} \frac{e^2}{\epsilon \ell_B} \approx .98\text{K} \times B[\text{tesla}]$ ) and substrate induced sublattice splitting (with characteristic energy  $\Delta_{AB}$ ).

A clue to the origin of the observed FQH features is provided by the observation



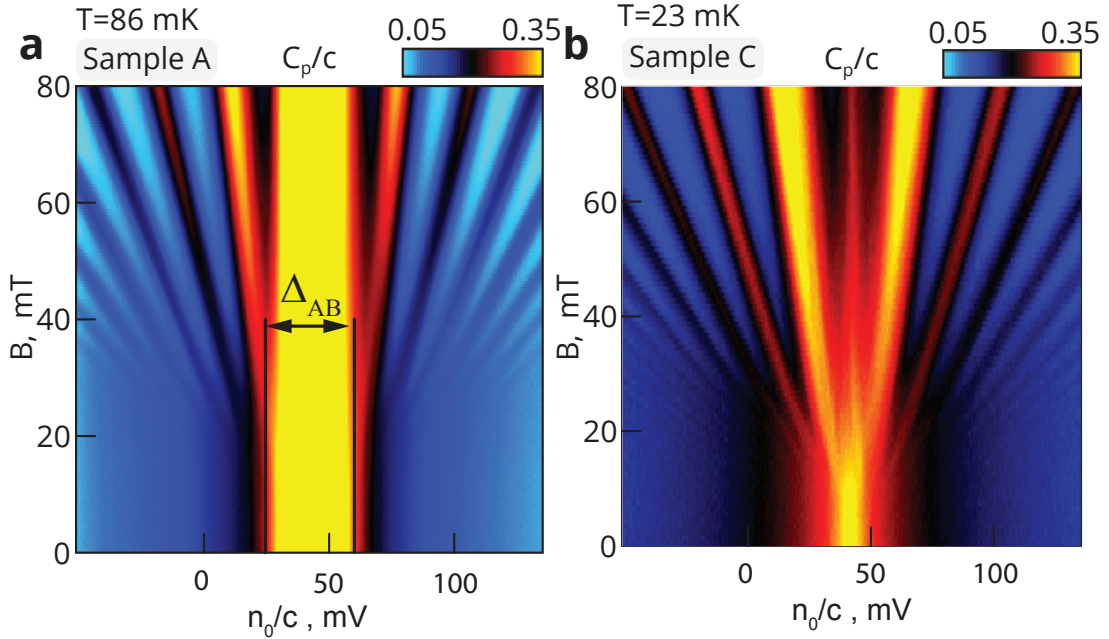


Figure 4.5: **a** Low field Landau fan in sample A, showing evidence of a large zero-field gap  $\Delta_{AB}$  induced by sublattice splitting. **b** Similar data for sample C, showing a much smaller sublattice gap.

that all the devices showing EDFQH states and ODFQH features are gapped at zero magnetic field and zero charge density, a phenomenology associated with finite  $\Delta_{AB}$ . Figs. 4.5 show low-magnetic field Landau fan plots for samples A and C. The electron system remains incompressible at  $\nu = 0$  for all magnetic fields, consistent with a single-particle  $\Delta_{AB}$ [97, 98]. The insulating nature of samples B and C is confirmed by transport measurements at zero field (Supplementary Fig. C.8; sample A did not have transport contacts). In a fourth sample showing no measurable sublattice gap, no EDFQH states were observed (Supplementary Figs. C.9-C.10). Crucially, the magnetic field at which EDFQH states appear is directly correlated with the measured  $\Delta_{AB}$  (see Fig. 4.6a and Fig. C.11), with large  $\Delta_{AB}$  corresponding to devices with a large appearance field for the FQH features.

A similar correlation between  $B$  and  $\Delta_{AB}$  arises from analyzing the phase diagram

of the  $\nu = 0$  state, where  $\Delta_{AB}$  controls the magnetic field of isospin transitions. To investigate this connection quantitatively, we analyze a mean-field model for the charge neutral state that accounts for the sublattice symmetry breaking  $\Delta_{AB}$  observed in our devices. Such a model has already been studied in the literature for bilayer graphene [89] where sublattice splitting can be actuated with applied electric field, but is equally applicable in the present scenario. Symmetry considerations permit two competing interaction anisotropies, parameterized by dimensionless couplings  $g_z$  and  $g_\perp$  which we take to be  $\Delta_{AB}$ - and  $B$ -independent constants. The resulting phase diagram [89, 90] includes both the partially sublattice polarized (PSP) and canted antiferromagnet (CAF) phases mentioned above as well as a fully sublattice polarized charge density wave (CDW) state and fully spin polarized ferromagnetic (FM) state. Among the competing isospin anisotropies, both  $E_V$  and  $E_Z$  grow with  $B$  while  $\Delta_{AB}$  is  $B$  independent. Thus the CDW phase is favored in the low- $B$  limit for  $\Delta_{AB} \neq 0$ , with phase transitions to  $E_V$ - or  $E_Z$ - driven states possible at higher  $B$ . The values of  $g_z$  and  $g_\perp$  are constrained to  $g_\perp \approx -10$  and  $g_z > -g_\perp$  from previous experiments on devices with  $\Delta_{AB} = 0$  [86, 96] (see Chapter 4). Figure 4.6b shows the calculated phase diagram as a function of  $\Delta_{AB}$  and  $B$  for fixed  $g_\perp = -10$  and  $g_z = 15$ . Two phase transitions are evident within this model: a 2nd order transition from the CDW to PSP phase, corresponding to the canting of the sublattice order parameter into the plane, and a first order transition from the PSP to CAF phase.

Associating the EDFQH states with a particular phase or phase transition of the  $\nu = 0$  ground state imposes two requirements. First, effective interactions and available components at  $\nu = \pm 1/2$  (and  $\pm 1/4$ ) should favor formation of an incompressible state. Second, these favorable conditions should only persist for a narrow range of magnetic fields. We propose that these requirements can be satisfied at the PSP-CAF phase transition. In this scenario, EDFQH states are made up of two isospin components with

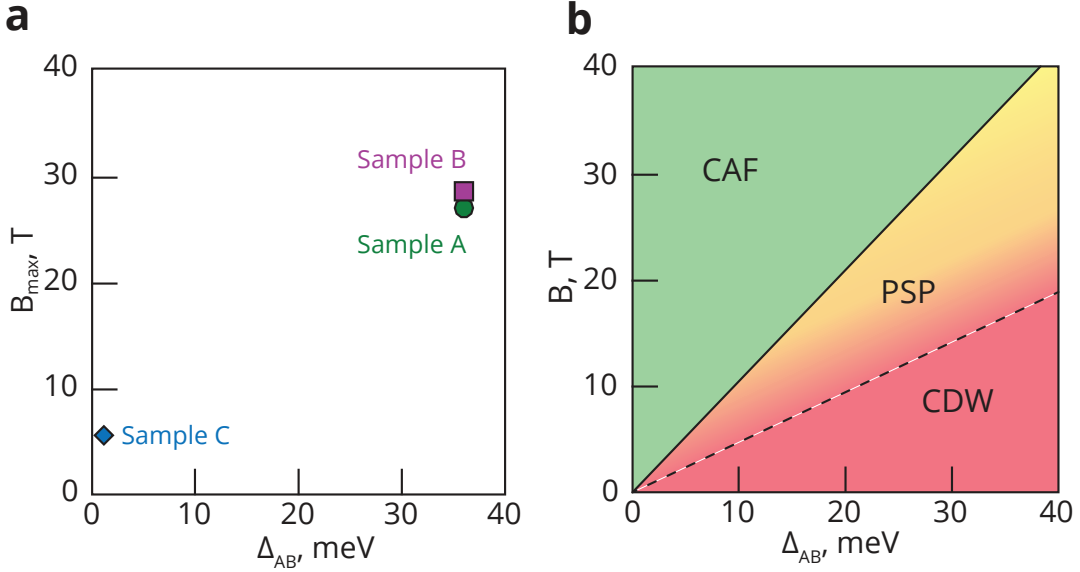


Figure 4.6: **c** The estimated gap sizes for the three measured samples ( $\Delta_{AB}$  plotted against the magnetic field at which the  $\nu = \pm 1/2$  states are maximal ( $B_{max}$ )). **d** Calculated phase diagram at  $\nu = 0$  for monolayer graphene as a function of magnetic field  $B$  and sublattice splitting  $\Delta_{AB}$ . The stability of the canted antiferromagnet (CAF), a sublattice polarized charge density wave (CDW), and a valley-coherent partially sublattice polarized phase (PSP) were calculated using anisotropy parameters  $g_{\perp} = -10$  and  $g_z = 15$  [90] (see Figs. S17-S18 and associated discussion in Supplementary information).

opposite sublattice occupation, which become degenerate in energy near the transition, thus favoring multicomponent states. Furthermore, the anisotropy of Coulomb interactions between wavefunctions on different sublattices is reminiscent of double layer systems, where asymmetry between inter- and intralayer interactions leads to the formation of a multicomponent EDFQH state [23, 113, 114]. The PSP-CAF phase transition also provides a mechanism for the concomitant weakening of ODFQH states, which are predicted to undergo isospin transitions[99]. We note that some other experimental systems have been successfully described using a picture of Zeeman-driven transitions of non-interacting composite fermion LLs[101, 119, 111]. However, such a naive picture

fails to explain a number of qualitative features of our data, most notably the observed weakening of ODFQH states at  $\nu = \pm 1/3, \pm 1/5$ . It thus appears empirically necessary to consider the full range of multicomponent FQH states allowed in the ZLL to qualitatively understand the FQH physics[99, 120].

We illustrate the mechanism for forming a multi-component incompressible state at the CAF-PSP phase transition by ignoring both the canting of spin in the CAF phase (making it a collinear antiferromagnet, denoted AF) and canting of sublattice polarization in the PSP (making it equivalent to the CDW). In this limit, CDW-AF phase transition is direct, with increasing magnetic field leading to a level crossing between single-electron LLs with identical spin but opposite sublattice polarizations, depicted schematically in Fig. 4.7. On both sides of the transition, the  $\nu = -1$  state is fully spin and sublattice polarized. Additional electrons, however, populate different sublattice orbitals in low- and high- $B$  regimes: in the CDW, electrons populate the same sublattice, while in the AF regime they populate the opposite sublattice. Far from the transition additional electrons occupy a the lower energy sublattice branch of the LL, resulting in a compressible state as observed in experiment. Near the transition, however, the two sublattice orbitals are degenerate, making inter-sublattice correlated states—which reduce the energy cost of Coulomb repulsion—energetically favorable. We interpret EDFQH at  $\nu = \pm 1/2$  and  $\nu = \pm 1/4$  as multicomponent states[23] incorporating intersublattice correlations. We note, however, that within this class of states a variety of multicomponent wavefunctions are possible[99]. Definitive resolution of the nature of the EDFQH will thus require more detailed numerical and experimental studies.

A number of experimental observations, however, are not explained even qualitatively in the simple picture described above, and warrant further study. For example, the counting of ODFQH phases is not well understood: the presence of three phases at  $\nu = 1/5$  (Fig. 4.3), and differences in the number of phases observed at  $\nu = \pm 3/5$

for samples with differing  $\Delta_{AB}$  (Fig. 4.4a,b), suggest a complex interplay of symmetry breaking and FQH physics. The nature of the transitions between ODFQH states are also open to further investigation. Some filling factors show a full closing of the gap (Fig. 4.3), while others only exhibit a weakening (e.g. Fig. 4.4a). Finally, the  $\nu$  dependence of the  $B$  at which anomalous FQH features appear is strongly dependent on  $\nu$  for  $|\nu| < 1/2$  but appears to completely flatten when  $|\nu| > 1/2$  (Fig. 4.4e,f), a phenomenon that must be accounted for quantitatively in any definitive description of the FQH transitions.

In summary, we have reported the observation of a number of sublattice-splitting tuned fractional quantum Hall phase transitions in monolayer graphene, as well as the observation of even denominator fractional quantum Hall states at  $\nu = \pm 1/2$  and  $\pm 1/4$ . While existing theoretical work has pointed out the possibility of new filling-factor dependent isospin phases[99, 121] arising from the interplay of symmetry breaking and fractional quantum Hall physics, the EDFQH was not predicted and remains to be definitively explained. We expect that future theoretical and experimental work—for example, measurements of tunneling exponents of EDFQH edge states—will be able to resolve the nature of these new phases. In addition to the obvious puzzle concerning the precise nature of the FQH states, our analysis suggests the possible existence of previously unexplored isospin phase transitions at  $\nu = 0$ . The PSP-CAF transition, in particular, remains the subject of continued study. Some authors have proposed that quantum fluctuations destroy the first order phase transition, leading to a deconfined critical point between the two phases[91, 93], while others suggest the first order phase transition survives but with an enlarged symmetry of low energy isospin rotations[92]. The most spectacular experimental manifestations of these transitions are likely to occur in the neutral sector, to which the current experiment is blind. However, future experiments can access this physics directly, for instance by probing thermal[122] or magnetic [123] transport.

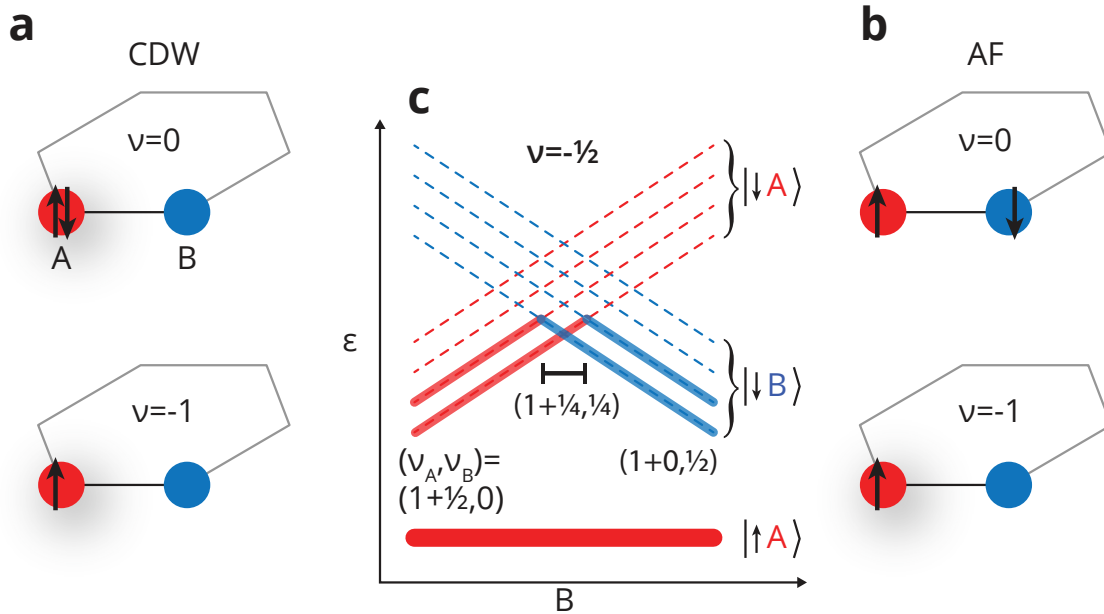


Figure 4.7: **Sublattice level crossing and multicomponent  $\nu = \pm 1/2$  states within a simplified model.** **a** Spin and sublattice polarizations of  $\nu = -1$  and  $\nu = 0$  integer quantum Hall ferromagnetic states in the low  $B$  regime where the charge neutral ground state is in the CDW phase. **b** Spin and sublattice polarizations of  $\nu = -1$  and  $\nu = 0$  integer quantum Hall ferromagnetic states in the high  $B$  regime. Within this model, which neglects spin canting, the charge neutral ground state is a collinear antiferromagnet (AF). **c** Level crossing at  $\nu = -1/2$  (an identical scenario obtains at  $\nu = +1/2$  by particle-hole conjugation across the ZLL). The  $\nu = -1$  state is identical in both cases, consisting of a single fully sublattice- and spin-polarized LL, denoted  $|\uparrow A\rangle$ . On the CDW side of the transition,  $\nu = -1/2$  consists of an additional partially-filled  $|\downarrow A\rangle$  LL, while in the AF the opposite sublattice is filled,  $|\downarrow B\rangle$ ; both cases result in compressible behavior. When the two levels are nearly degenerate, Coulomb interactions can favor a multicomponent state with equal sublattice occupation  $(\nu_A, \nu_B) = (1 + 1/4, 1/4)$ . Bold lines indicate filled levels, the  $|\downarrow A\rangle$  and  $|\downarrow B\rangle$  levels are pictured as four branches to depict partial occupation.

# Chapter 5

## Even-Denominator FQH effect in bilayer graphene

**Abstract:** Nonabelian anyons offer the prospect of storing quantum information in a topological qubit protected from decoherence[124]. Experimental systems predicted to harbor nonabelian anyons range from p-wave superfluids, to superconducting systems with strong spin orbit coupling, to paired states of interacting composite fermions that emerge at even denominators in the fractional quantum Hall (FQH) regime. While even denominator FQH states have been observed in several two dimensional systems[22, 46, 111], small energy gaps and limited tunability have stymied experimental probes of their microscopic ground state. Here, we report the observation of robust even-denominator FQH phases in a new generation of dual-gated, hexagonal boron nitride encapsulated bilayer graphene samples, with an energy gap three times larger than previously observed. We compare the observed FQH phases with numerical and theoretical models while simultaneously controlling carrier density, layer polarization, and magnetic field, providing new evidence for the paired Pfaffian phase[25] predicted to host nonabelian anyons. Electric-field controlled level crossings between states with different

Landau level index reveal a cascade of FQH phase transitions, including a continuous phase transition between the even denominator FQH state and a compressible composite fermion liquid.

*The contents of the chapter have previously appeared as Nature, volume 549, pages 360-364, (2017), doi:10.1038/nature23893.*

At high magnetic fields, two-dimensional electrons form flat bands, known as Landau levels (LLs). At finite charge density  $n$ , interactions drive the formation of ordered states depending on both the LL filling ( $\nu = 2\pi\ell_B^2 n$ , where  $\ell_B = \sqrt{\frac{\hbar}{eB}}$  is the magnetic length) as well as the spin and orbital structure of the LL wavefunctions. Of particular interest is the fate of the half-filled LL, which can be understood as a weakly interacting state of composite fermions (CFs)[125] consisting of one electron and two magnetic flux quanta. Having bound part of the external magnetic field, the CFs experience an effective field  $B_{\text{eff}} = B(1 - 2\nu)$ . At  $\nu = \frac{1}{2}$  this field vanishes and the CFs form an emergent Fermi surface[126] that manifests in both microwave and transport experiments[20, 21]. As in a conventional metal, the emergent Fermi surface can be unstable, depending on the strength and sign of the residual interactions between the CFs. Most intriguingly, CFs have been predicted to form the quantum Hall analog of a superconductor [25, 127] which, in a single component system, naturally has p-wave pairing symmetry and supports nonabelian, charge- $e/4$  quasiparticle excitations in an incompressible liquid. Numerical studies find that in the lowest LL of a conventional, massive electron system, the CF interactions are sharp and the Fermi surface is stable, while in the first LL a node in the single-particle wavefunction leads to softer CF interactions favorable to pairing.[1] An incompressible quantized Hall state was indeed observed[22] in the first LL of GaAs quantum wells, at filling  $\nu = \frac{5}{2}$ , though experiments have yet to reveal definitive evidence for nonabelian statistics.

Bernal bilayer graphene (BLG) is emerging as a new platform for exploring the half-



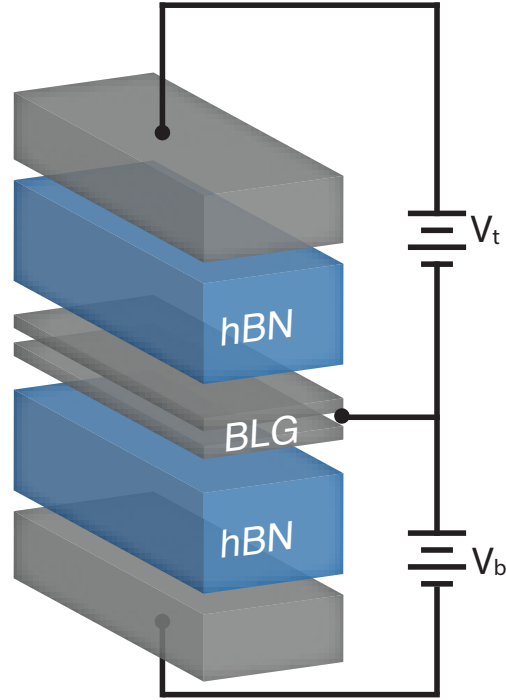


Figure 5.1: Device schematic. A BLG flake is successively encapsulated in both hexagonal boron nitride dielectric and graphite gate layers. Charge density  $n$  and layer polarization  $p$  are controlled via voltages  $n_0/c \equiv (v_t + v_b)$  and  $p_0/c \equiv (v_t - v_b)$ , where  $c$  is the average geometric capacitance of the two gates to the graphene while  $v_{t(b)}$  are the applied gate voltages.

filled LL. Comprised of two aligned graphene layers in direct contact, it has a rich phase diagram that depends on both the electron density  $n$  and layer polarization  $p$ . A fractional quantum Hall phase was observed[46] at  $\nu = -\frac{1}{2}$  in BLG devices suspended in vacuum and gated from below. The interpretation of this state[128] is complicated by the complex structure of the BLG zero energy LL (ZLL), which consists of eight quasi-degenerate components comprising electron spin, a “valley” index characteristic of honeycomb systems, and an orbital degeneracy unique to BLG. The spin and valley combine to form an approximately SU(4) isospin, while no such symmetry relates the orbital levels, which are approximately equivalent to the lowest ( $N=0$ ) and first excited ( $N=1$ )

LLs of conventional, massive electrons. While a nonabelian paired state is expected theoretically when the fractional part of the filling lies in a single  $N=1$  orbital, this is difficult to experimentally verify in a singly gated sample. In devices where the BLG is sandwiched between boron nitride, it can be gated from both above and below, and the splitting between valley and orbital degrees of freedom can then be controlled using magnetic and electric fields[42, 129]. A recent experiment[57] exploited this control to map out the valley and orbital character of the ZLL, revealing that throughout much of the accessible parameter space, the valence electrons are fully polarized within a single valley and orbital flavor. However, even denominator states have not previously been reported in dual-gated devices.

Here we report magnetocapacitance measurements from a new generation of BLG devices, depicted schematically in Fig. 5.1. Unlike previous dual-gated device architectures[42, 57, 129], the gate electrodes on both sides of the BLG are made of few-layer graphite flakes, dramatically reducing sample disorder (see Fig. D.11). The sum and difference of the two applied gate voltages,  $n_0$  and  $p_0$ , (see Fig. 5.1, caption) control the charge density  $n$  and layer polarization density  $p$  within the bilayer. Fig. 5.2a shows the penetration field capacitance,  $C_P$ , closely related to the thermodynamic compressibility[130], in a region of the  $n_0 - p_0$  plane that spans the ZLL,  $-4 < \nu < 4$ . Incompressible FQH phases manifest as peaks in  $C_P$  locked to the filling factor. We observe a plethora of new incompressible states at fractional  $\nu$  and numerous  $p_0$ -tuned phase transitions where the state becomes compressible at fixed  $\nu$ .

We group the observed FQH sequences into three categories based on the pattern of incompressible phases, indicated by red, blue, and green coloring in Fig. 5.2b. In the red regions, we observe sequences of FQH states at valence fillings  $\tilde{\nu} \equiv \nu - \lfloor \nu \rfloor = \frac{m}{2m+1}$ . In the blue regions, in contrast, we only observe robust FQH states at  $\tilde{\nu} = \frac{1}{3}, \frac{2}{3},$  and  $\frac{1}{2}$ , with weaker states observed at  $\tilde{\nu} = \frac{7}{13}$  and  $\frac{3}{5}$  (Fig. 5.3, 5.4). The red and blue regions

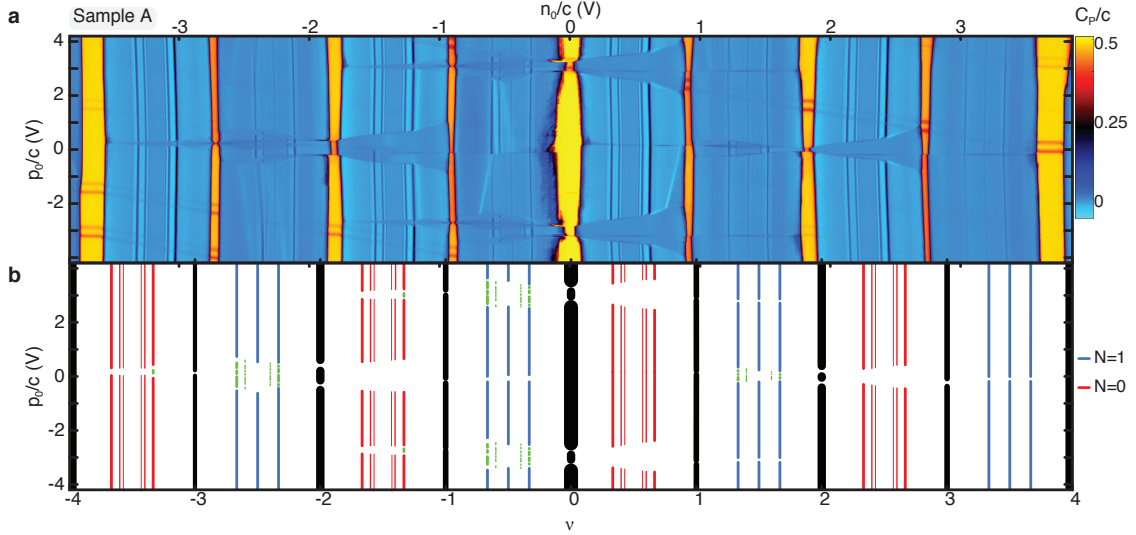


Figure 5.2: **a** Penetration field capacitance  $C_P$  at  $B = 12$  T. The plot spans the ZLL, showing incompressible quantum Hall states at all integer filling factors,  $\nu$ , as well as at a multitude of rational  $\nu = p/q$ . **b** Orbital character of observed fractional quantum Hall states. As valence electrons fill  $N=0$  orbitals (red), we observe odd-denominator fractions consistent with two-flux composite fermion hierarchy states. When filling  $N=1$  orbitals (blue), only multiples of  $\frac{1}{3}$  consistently appear from this sequence, with the second most robust state occurring at half-filling. Near orbital and valley level crossings (green), a cascade of interlayer correlated states is observed[23].

correspond to the experimentally[57] determined orbital character ( $N=0$  or  $N=1$ ) of the valence electrons, which have different effective interactions. In red regions, a single  $N=0$  component is fractionally filled and the effective interactions are sharp, stabilizing the odd denominator sequence associated with integer quantum Hall states of 2-flux CFs. We thus ascribe the compressible state at  $\tilde{\nu} = \frac{1}{2}$  to the composite Fermi liquid (CFL). In the blue regions, a single  $N=1$  component is fractionally filled and the effective interactions are softer. This suggests the incompressible state observed at  $\tilde{\nu} = \frac{1}{2}$  is a FQH state constructed from paired CFs. Finally, in the green regions,  $p_0$  induces a level crossing between the eight near-degenerate components[57], and there is a cascade of phase transitions between incompressible states with a structure that depends on the

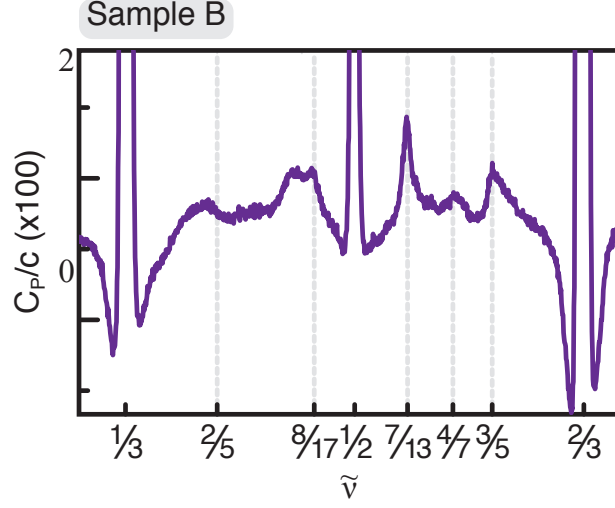


Figure 5.3: Detail of an  $N=1$  LL from a second device measured at  $B = 14\text{T}$  and base temperature, showing particle-hole asymmetric development of incompressible states at  $\tilde{\nu} = 3/5$  and  $7/13$ .

fractional filling.

We first discuss the even denominator FQH states. In an incompressible FQH state, a finite energy is required to inject an electron or hole. This “thermodynamic” gap can be determined[130] from  $C_P$ , shown in Figure 5.5a for different temperatures at  $B = 14\text{T}$ . We measure this thermodynamic gap by integrating the inverse electronic compressibility ( $\partial\mu/\partial n$ ) with respect to  $n$  (Fig. 5.5b), giving a gap of 4K at the base temperature of our dilution refrigerator (see Chapter D). Transport measurements from a second device, meanwhile, show the expected quantized Hall plateau and concomitant longitudinal resistance minimum (Fig. 5.6). Temperature dependent transport shows a lower value of the activation gap of  $1.8 \pm 0.2\text{K}$  at  $B = 14\text{T}$ . This discrepancy is not surprising[130]. The thermodynamic gap measures the energy required to add an entire electron-hole pair, while thermally activated transport measures the energy cost for injecting a fractionally charged quasiparticle-quasihole pair. For a half-filled FQH state, the quasiparticle charge is predicted to be  $e/4$ , in which case the measured activation

gap should be roughly a quarter of the thermodynamic gap at  $T=0$ [130]. In a bilayer

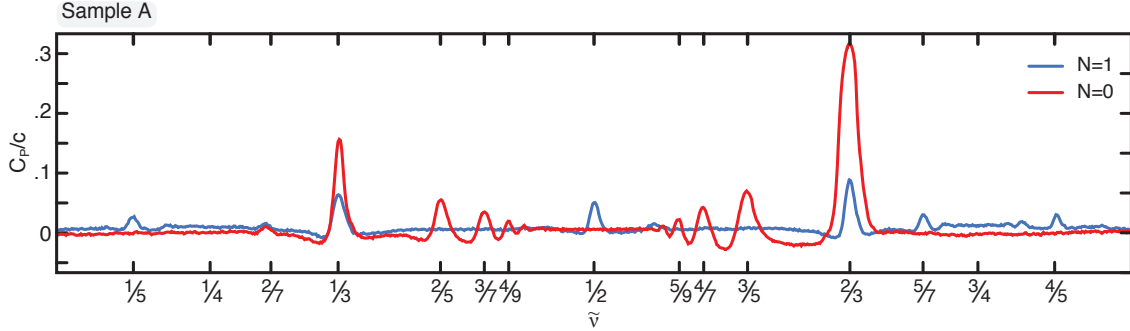


Figure 5.4: FQH sequences in valence  $N=0$  and  $N=1$  regions as a function of  $\tilde{\nu} \equiv \nu - [\nu]$  for  $1 < \nu < 2$  (blue) and  $2 < \nu < 3$  (red) measured at  $p_0/c = -2.0$  and  $-2.7$  V, respectively. The  $N=0$  levels are compressible at half-filling, while the  $N=1$  levels show incompressibility peaks.

electron system it is natural to ask whether the incompressible states observed at half-filling are single- or multi-component phases. While the leading theoretical candidates for a single-component even-denominator FQH phase, the paired Pfaffian[25] and anti-Pfaffian[131, 132] states, are nonabelian, in multi-component systems the abelian “331” phase is more likely[23]. Using the map of the valence polarization[57] (aspects of which were repeated here at higher resolution, see Methods), we find the gapped phase appears in regions where the fractional filling is polarized into a single  $N=1$  component. The situation is thus roughly analogous to the  $\nu = \frac{5}{2}$  state of GaAs,[22] where numerics have long predicted a paired phase. We note, however, that the measured activation gap is several times larger than the largest gaps measured in GaAs (558 mK[47]), ZnO (90mK[111]) or suspended BLG (600 mK[46]).

Despite the superficial similarity, the  $N=1$  orbital in BLG differs in two important ways from its counterpart in semiconductor quantum wells. First, the  $N=1$  LLs of BLG and GaAs are not strictly equivalent. The  $N=1$  LL of BLG includes a combination of the conventional  $|0\rangle$  and  $|1\rangle$  LL wavefunctions localized on the different sub-lattices of the

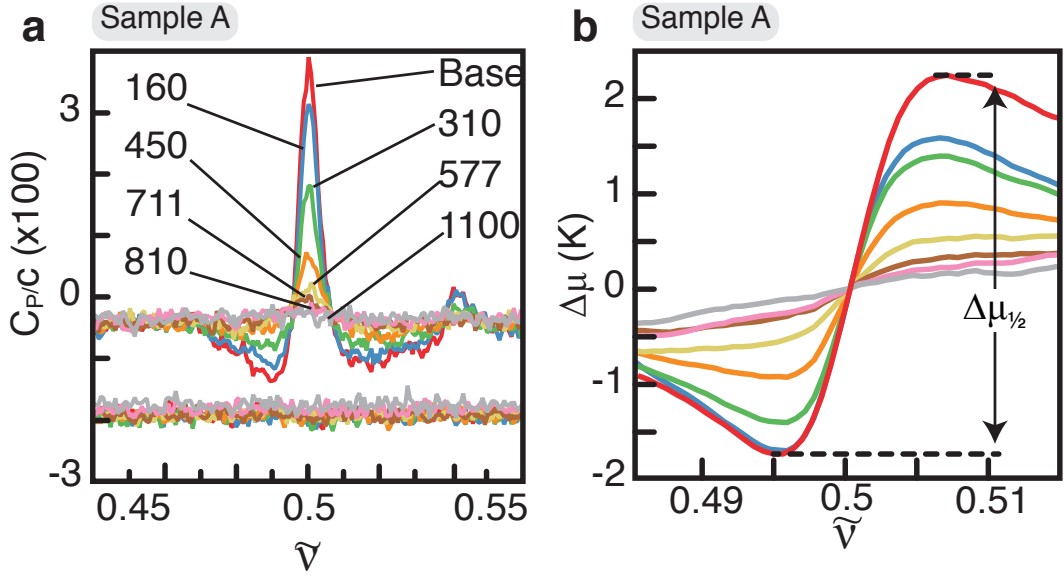


Figure 5.5: **a** Penetration field capacitance (top curves) and dissipation (bottom curves) near  $\nu = \frac{3}{2}$  at  $B = 14\text{T}$ . Labels denote probe temperature in mK. **b** Density dependence of the chemical potential,  $\Delta\mu \approx \frac{e}{k_B} \int (C_P/c) d(n_0/c)$ , obtained by integrating curves in (a).

unit cell (see Chapter D), with the relative weight of the  $|0\rangle$  wavefunction growing with  $B$ . The effective interaction depends on the orbital character, so that  $B$  continuously tunes the structure of electron-electron interactions within an  $N=1$  level. At low  $B$ , the wavefunctions are purely  $|1\rangle$ -like, with comparatively soft interactions, while at high  $B$ , they are an equal admixture of  $|0\rangle$  and  $|1\rangle$  and interactions are consequently sharper. Numerical studies predict that a nonabelian paired phase at lower  $B$  should give way to a gapless CFL at sufficiently high magnetic fields[128, 133] (Fig. 5.7 a). Indeed, we find that the  $\tilde{\nu} = \frac{1}{2}$  gap changes non-monotonically with  $B$  (Fig. 5.7b), peaking around  $B = 27\text{T}$  and then decaying up to the limit of our experiment at  $B = 35\text{T}$ . Over a similar range, we simultaneously observe the emergence of a conventional odd-denominator FQH series typical of the lowest LL, providing further evidence that the effective  $N=1$  interactions sharpen with magnetic field (see Chapter D and Fig. D.16). The decrease

of the  $\tilde{\nu} = \frac{1}{2}$  gap despite an increase in the Coulomb scale  $E_C \sim \sqrt{B}$  supports the scenario of a paired-to-CFL transition[134] at somewhat higher magnetic fields. Sec-

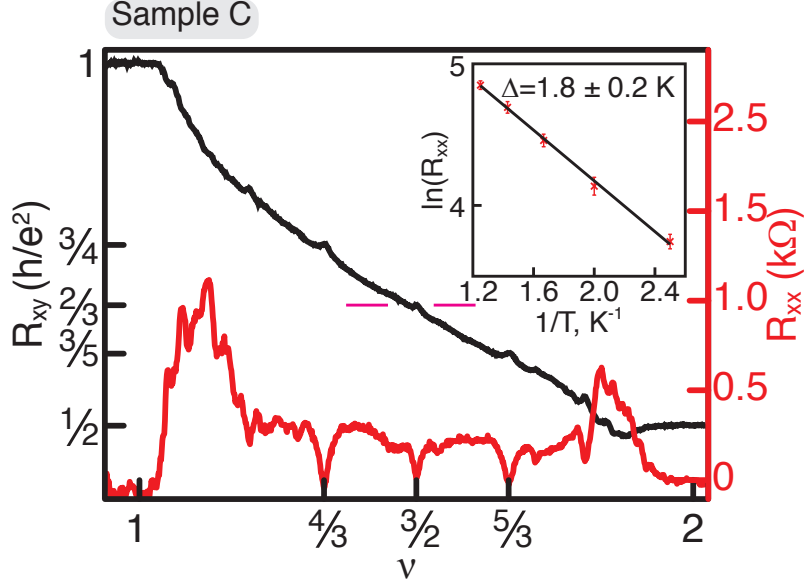


Figure 5.6: Hall (black) and longitudinal (red) resistance measured in Sample C. Inset: Arrhenius plot of  $R_{xx} \sim e^{-\Delta/(2T)}$  at  $\nu = 3/2$ , from which we obtain  $\Delta = 1.8 \pm .2\text{K}$  at  $B = 14\text{T}$ .

ond, particle-hole symmetry breaking differs in BLG as compared with GaAs. Within a single Landau level, the Pfaffian and anti-Pfaffian states, which can be understood as different pairing channels, are degenerate due to a particle-hole symmetry (effected by  $\tilde{\nu} \leftrightarrow 1 - \tilde{\nu}$ ). Including scattering between LLs breaks this symmetry and determines the ground state. Although the subject of longstanding debate, recent numerical agreement between exact diagonalization and DMRG methods suggests that the  $\nu = \frac{5}{2}$  state of GaAs is in the anti-Pfaffian phase [135, 136, 137]. However, LL scattering is dramatically different in BLG: scattering between the ZLL and the  $|N| \geq 2$  levels only breaks particle-hole symmetry weakly, while scattering within the ZLL breaks it strongly due to the small splitting ( $\Delta_{10} \approx .1E_C$ ) between  $N=0$  and  $N=1$  levels (see Chapter D). In our experiment, particle-hole symmetry breaking manifests in the fractions observed in

the  $N=1$  LL. We find incompressible states at  $\tilde{\nu} = \frac{7}{13}$  and  $\frac{3}{5}$  (Fig. 5.3), the particle-hole conjugates of what is observed in GaAs where unconventional states were observed at  $\frac{6}{13}$  and  $\frac{2}{5}$ . [47] To address these differences, we perform comprehensive DMRG calculations which account for the  $B$ -dependent mixed orbital character and screening from filled  $|N| \geq 2$  LLs, while non-perturbatively accounting for scattering between the  $N=0$  and 1 orbitals of the ZLL (Fig. 5.7, see Chapter D for computational details). We find that, in contrast to GaAs [135, 136, 137], the Pfaffian phase is strongly preferred over the anti-Pfaffian over the experimentally accessible range. Suggestively,  $\frac{7}{13}$  (as well as  $\frac{8}{17}$ , where a weaker feature is also observed) is the predicted filling of the first “daughter” state of the Pfaffian phase [138]. Our results suggest encapsulated BLG has certain advantages over

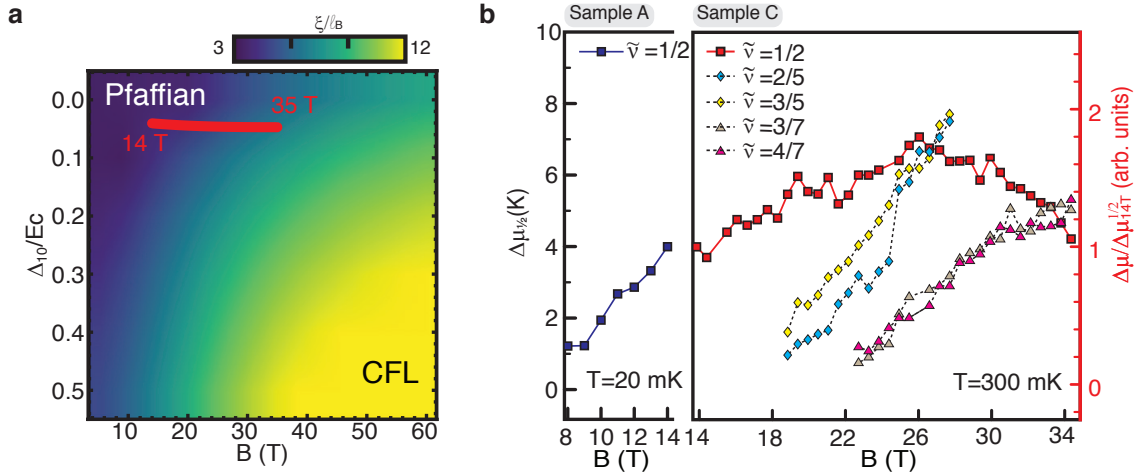


Figure 5.7: **a** Density matrix renormalization group calculation of the correlation length  $\xi$  at  $\tilde{\nu} = \frac{1}{2}$  in the  $N=1$  level as a function of the energy splitting  $\Delta_{10}$  between the  $N=0,1$  orbitals in units of Coulomb energy, and the magnetic field (see Chapter D). In the lower right corner, the system transitions to the compressible CFL phase. The red line denotes an estimate [57] of the trajectory accessed in **b**. **b** The thermodynamic gap  $\Delta\mu_{\frac{1}{2}}$  at different  $B$  in Sample A (left panel) and sample C (right panel). Data in the right panel are scaled to the  $\Delta\mu_{\frac{1}{2}}(B = 14\text{T})$  gap (see Chapter D). For energy gaps of other FQH states, see Fig. D.17 and Tables D.1-D.2.

GaAs as a platform for interferometric detection of nonabelian quasiparticles [1]. First,



the large energy gap and small correlation length relative to GaAs may reduce bulk-edge coupling that is detrimental to interferometric probes[139], while exponentially suppressing the density of thermally-activated quasiparticles. Second, hBN gate dielectrics can be made almost arbitrarily thin, allowing one to engineer edges and quantum point contacts using sharp electrostatic potentials. Recent experiments have demonstrated long coherence lengths in the quantum Hall regime along such gate-defined edges[140]. Finally, the putative Pfaffian state at  $\nu = -\frac{1}{2}$  in BLG would have fewer edge modes than the anti-Pfaffian state at  $\nu = \frac{5}{2}$  in GaAs, making the former a preferable candidate for interferometry. Even without phase coherent transport measurements, the thermodynamic measurements presented here, carried to lower temperatures, can be used to probe topological ground state degeneracy[26], providing smoking-gun evidence for non-abelian statistics in the near future. In addition to control over the total density  $n$  and

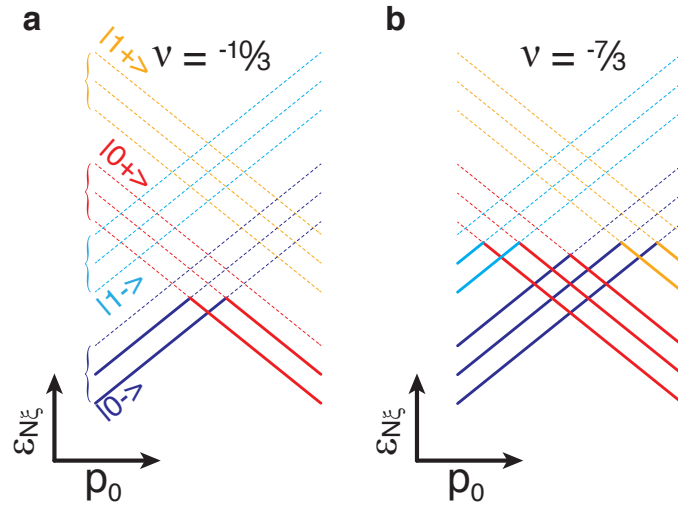


Figure 5.8: Single particle energy level ( $\varepsilon_{N\xi}$ ) crossing and level filling diagram as a function of  $p_0$ , for **a**  $\nu = -10/3 = -4 + 2/3$  and **b**  $\nu = -7/3 = -4 + 5/3$ . Occupation of the levels in increments of  $\nu = 1/3$  is represented by schematically showing each LL as divided into three branches. Three distinct phases are expected by filling the two lowest lying ‘branches’ in (a). In (b), crossings now involve both  $N=0$  and  $N=1$  levels, and 6 distinct phases are expected.

the effective interactions, the dual-gated architecture allows us to tune level crossings between the eight components of the ZLL. Within the ZLL, the two valleys are supported on opposite layers, so the electric field ( $p_0$ ) acts like a “valley Zeeman” field and the layer polarization ( $p$ ) can be used to infer valley polarization. A schematic of the single particle energies near  $p_0 \sim 0$  is shown in Figs. 5.8. Four single particle levels are involved in the crossing, which we label by their orbital ( $N = 0, 1$ ) and valley ( $\xi = \pm$ ) indices (we suppress the spin here, since tilt  $B$ -field measurements show that the spin-polarization is unchanged across the transition).

Because the two valleys are distinguished by their crystal momentum, the tunneling between them vanishes in the absence of short-range disorder and the crossing between the levels is unavoided, as supported by the sharp transition at  $\nu = -3, p_0 \sim 0$  (Fig. 35.9a). Hence, unlike the dependence on  $B$ , the  $p_0$ -dependence across the transition is not equivalent to continuously tuning the interaction potential. Indeed, when charge is separately conserved in each valley, the valley polarization cannot change continuously without closing the neutral gap: just as the charge gap vanishes in a compressible system, the neutral gap vanishes in a polarizable system. During such depolarization, the charge gap may or may not close.

Fig. 5.9a shows  $C_P$  for near  $p_0 = 0$ . For the best-developed odd-denominator  $\tilde{\nu} = \frac{m}{2m+1}$  states when  $-4 < \nu < -3$ ,  $|m| + 1$  distinct high- $C_P$  incompressible regions are visible separated by  $|m|$  low- $C_P$  transitions. Referring to Fig. 5.8a, the crossing is predicted to transfer valence filling  $\frac{m}{2m+1}$  between  $N=0$  orbitals in opposite valleys. The  $m$  compressibility spikes presumably occur when filling  $\frac{1}{2m+1}$  is transferred between valleys. This is expected from composite Fermion theory, which predicts two-component correlated states[23, 125] at fillings  $(\nu_+, \nu_-) = \frac{(m_+, m_-)}{2(m_+ + m_-) + 1}$ , (here  $\nu_{\pm}$  is the filling of valley  $\xi = \pm$ ) separated by phase transitions where the gap closes. The state at  $\nu = -4 + \frac{2}{3}, p_0 = 0$ , for instance, corresponds to  $m_{\pm} = -1$  and we ascribe it to a previ-

ously unobserved valley SU(2) singlet. For  $-3 < \nu < -2$ , states at filling  $\nu = -4 + \frac{3m+1}{2m+1}$  show  $3m + 1$  transitions. Four levels are involved in these transitions. At high  $p_0$ , one  $N=0$  level is completely filled and the fractional filling resides in the  $N=1$  level of the same valley. As  $p_0$  is decreased, occupation is transferred according to the levels shown in Fig. 5.8b, consistent with the observed strengths of the gapped phases, whose  $C_P$ -dips are strongest when only  $N=0$  orbitals are involved.

For odd denominator states, the high compressibility observed when the system changes polarization indicates that the gap for charged excitations also closes. This is not always the case at  $\tilde{\nu} = \frac{1}{2}$ , where the charge gap in the single component  $N=1$  regimes at large and small  $p_0$  fades gradually into the level crossing. We can quantify this transition by directly measuring the layer polarization (see Chapter D). Fig. 5.10a shows the layer polarizability ( $\partial p / \partial p_0$ ) over a similar region of four-level crossings. In contrast to the odd denominator fractions, where the spikes in polarizability are concentrated on the spikes in compressibility, near  $\tilde{\nu} = \frac{1}{2}$  there is a region of  $p_0$  where the polarization changes only gradually while the charge gap remains finite. Fig. 5.10b shows the measured charge gap alongside the integrated change in layer polarization across the level crossing. The charge gap persists from valley valence filling  $(\nu_+, \nu_-) = (1.5, 0)$  to  $(1.33, .17)$ .

The coexistence of polarizability and incompressibility has intriguing implications. In the clean limit where charge is conserved separately in each valley (a limit supported by the sharp transition at  $\nu = -3, p_0 \sim 0$ ), finite polarizability requires a vanishing neutral gap, implying the existence of a new phase: a gapless fractionalized insulator. Microscopically, because the layers are atomically close, the finite polarization presumably arises from a finite density of inter-valley (e.g., inter-layer) excitons, and the finite polarizability implies these neutral excitons are gapless. This is reminiscent of quantum Hall bilayers at  $\nu = 1$ , where a charge gap also coexists with a vanishing neutral gap.

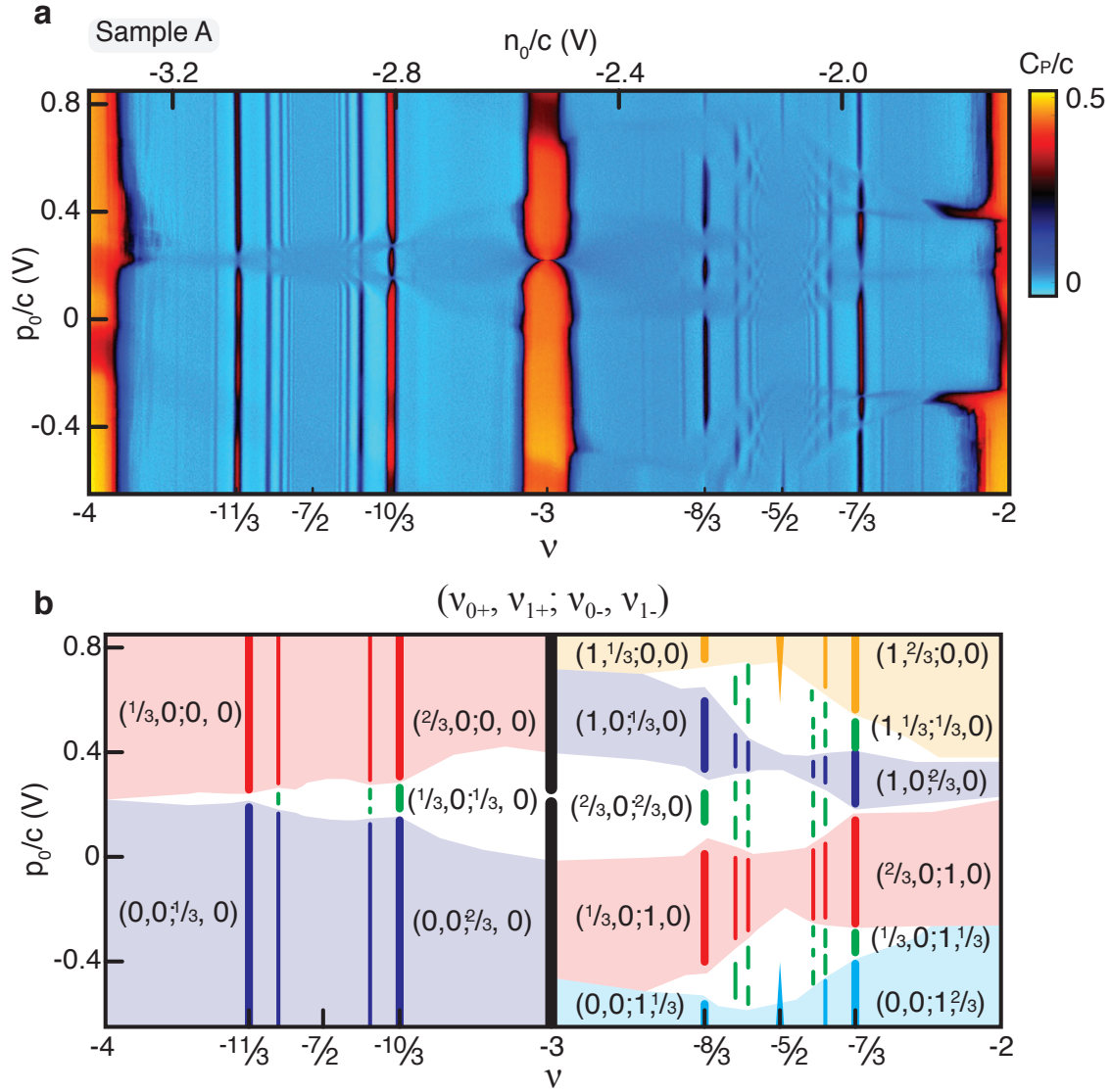


Figure 5.9: **a** Measured  $C_P$  for  $-4 < \nu < -2$  near  $p_0/c = 0$  at  $B = 12\text{T}$ . **b** Annotated phase diagram for the range depicted in (a). Occupations of the four relevant orbitals are indicated for each fractional multiple of  $1/3$ . Shaded areas correspond to regions where the fractional filling lies entirely within one orbital. Coloring follows the scheme in 5.8(a-b).

The transition is thus distinct in microscopic character from the Pfaffian-to-CFL transition predicted at high  $B$  in a single-component level (Fig. 5.7b), where the charge and neutral gap would vanish in tandem.

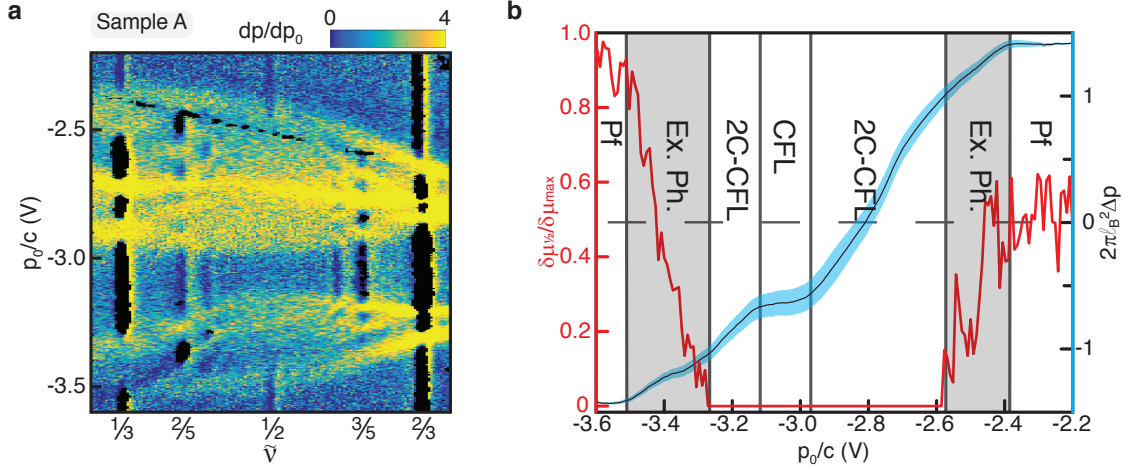


Figure 5.10: **a** Layer polarizability  $\frac{dp}{dp_0}$ , measured over an analogous quadruple level crossing at high negative  $p_0$  for  $-1 < \nu < 0$ . **b** Black curve shows the integrated change in polarization,  $2\pi\ell_B^2\Delta p = 2\pi\ell_B^2 \int \frac{\partial p}{\partial p_0} dp_0$ , measured in the regions immediately adjacent to  $\tilde{\nu} = \frac{1}{2}$ , with shading indicating  $1\sigma$  confidence interval (see Chapter D). Red curve shows the  $\tilde{\nu} = \frac{1}{2}$  charge gap. Vertical lines demarcate distinct regimes distinguished by their compressibility and polarizability. The incompressible and unpolarizable regions are the Pfaffian phase; incompressible but polarizable regions are the excitonic phase discussed in the main text; compressible but polarizable regions are presumably two-component CFLs, and the compressible and unpolarizable is a one component CFL.

Theoretically, the accompanying fractionalization at  $\tilde{\nu} = \frac{1}{2}$  leaves several possibilities for the ultimate collective ground state—and indeed even the quantum statistics—of inter-valley excitons[141]. Most simply, the incompressible exciton phase could be disorder dominated: as charge is transferred between valleys, the resulting density of excitons is trapped by local potential variations in a mechanism similar to that which stabilizes FQH plateaus over a finite range of  $\nu$ . However, as is evident in Figs. 5.5b-5.6, the even denominator state itself is only stable to pure charge doping up to  $\Delta\nu \approx .005$ , more than an order of magnitude less than the occupation change ( $\Delta\nu_+ \approx .17$ ) of the  $N=1$  orbital implied by the depolarization measurement. Absent this mechanism, the incompressible exciton phase may host such phenomena such as interlayer phase coherence or an emergent Fermi surface, which can be distinguished experimentally by probing thermal

transport or interlayer Coulomb drag.

# Chapter 6

## Fractional Chern Insulators in bilayer graphene

**Abstract:** Topologically ordered phases are characterized by long-range quantum entanglement and fractional statistics rather than by symmetry breaking. First observed in a fractionally filled continuum Landau level, topological order has since been proposed to arise more generally at fractional fillings of topologically non-trivial “Chern” bands. Here, we report the observation of gapped states at fractional fillings of Harper-Hofstadter bands arising from the interplay of a magnetic field and a superlattice potential in a bilayer graphene/hexagonal boron nitride heterostructure. We observe phases at fractional filling of bands with Chern indices  $\mathcal{C} = -1, \pm 2$ , and  $\pm 3$ . Some of these, in  $\mathcal{C} = -1$  and  $\mathcal{C} = 2$  bands, are characterized by fractional Hall conductance — that is, they are “fractional Chern insulators” and constitute an example of topological order beyond Landau levels.

*The contents of the chapter have previously appeared as Science, volume 360, issue 6384, pages 62-66, (2018), doi:10.1126/science.aan8458.*

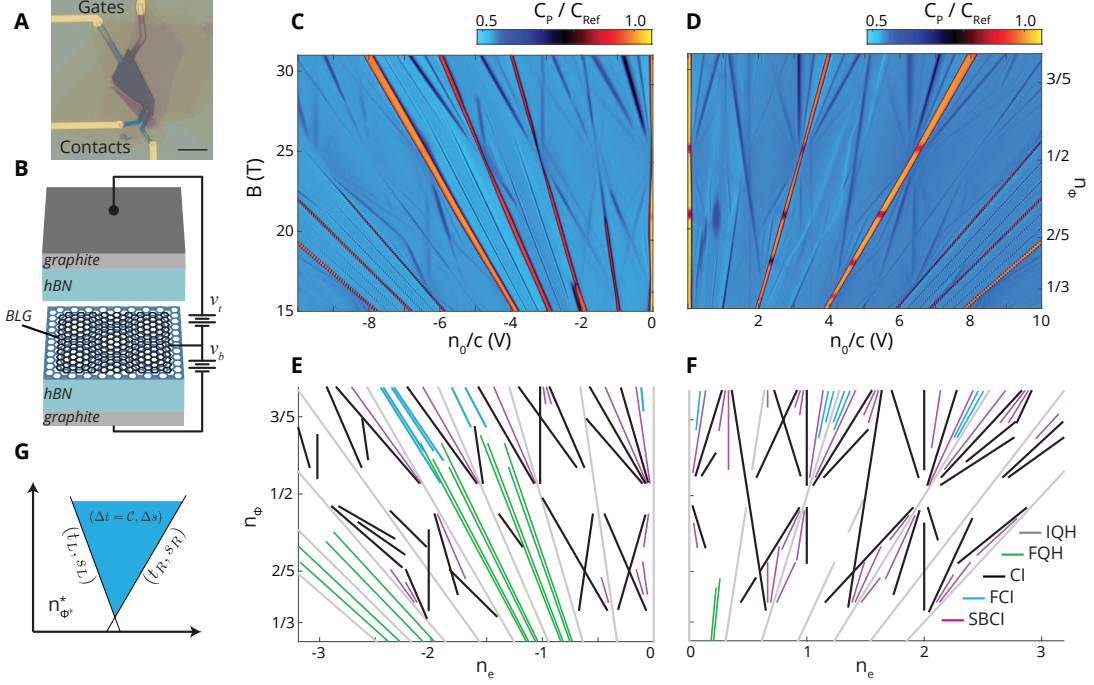


**Figure 6.1: Magnetocapacitance in a high-quality bilayer graphene moiré superlattice device.** **a** Optical micrograph of the device. Scale bar is  $10 \mu\text{m}$ . **b** Schematic of the device, with top and bottom graphite gates at potential  $v_t, v_b$ . A Moiré potential is induced by alignment of the graphene bilayer with one of the encapsulating hBN crystals. **c** Penetration field capacitance ( $C_P$ ) as a function of density  $n_e \sim n_0 \equiv c(v_t + v_b)$  and magnetic field  $B$  for  $n_0 < 0$ .  $T = 300 \text{ mK}$ , and  $C_{\text{Ref}}$  is a reference capacitance. A large electric field  $p_0/c = (v_t - v_b) = 16 \text{ V}$  is applied to force the valence electrons onto the top layer, which is in contact with the aligned hBN. **d**  $C_P$  for  $n_0 > 0$  with  $v_t - v_b = -16 \text{ V}$  at  $T = 300 \text{ mK}$ . **e-f** Linear gap trajectories observed in (C-D) parameterized by  $n_e = t \cdot n_\Phi + s$ .  $n_\Phi$  and  $n_e$  are the magnetic flux quanta and number of electrons per moiré unit cell, respectively.  $n - \Phi \equiv \frac{\sqrt{3}\lambda^2 B}{2\Phi_0} = 1/2$  when  $B = 24.3 \text{ T}$  and  $n_e = 1$  when  $n_0/c = 3.1 \text{ V}$ . Five trajectory classes are distinguished by color: integer quantum Hall (gray,  $s = 0, t \in \mathbb{Z}$ ), fractional quantum Hall (green,  $s = 0, t$  fractional), Hofstadter Chern insulators (black,  $s, t \in \mathbb{Z}, s \neq 0$ ), symmetry-broken Chern insulators (magenta, fractional  $s, t \in \mathbb{Z}$ ) and fractional Chern insulators (cyan, fractional  $s, t$ ). **g** Schematic of a  $(\Delta t, \Delta s)$  Chern band (see main text).

Bands in electronic systems can be classified by their symmetry and topology [142].

In two dimensions with no symmetries beyond charge conservation, for example, bands



are characterized by a topological “Chern” number,  $\mathcal{C}$  [16]. The Chern number determines the Hall conductance contributed by a filled band, which takes quantized integer values,  $\sigma_{xy} = t \frac{e^2}{h}$  with  $t \in \mathbb{Z}$  [16] (here  $e$  is the charge of an electron and  $h$  is the Planck constant). Systems with an integer number of filled bands with nonzero  $\mathcal{C}$  (“Chern bands”) thus show a quantized, nonzero Hall conductance, and are known as Chern Insulators (CIs). The first experimental examples of CIs are the integer quantum Hall (IQH) states, observed in isotropic two dimensional electron systems (2DES) subjected to a large magnetic fields[143]. In the case of IQH, a quantized Hall conductance is observed when an integer number of Landau levels (LLs) are filled, each with  $\mathcal{C} = 1$ .

IQH systems are very nearly translation invariant, in which case  $t$  is fixed by the magnetic field  $B$  and the electron density  $n$ , via  $t = \frac{n}{B} \frac{h}{e}$ , with some disorder required for the formation of plateaus in the Hall conductance[144]. Recently, there has been interest in a different class of CIs where continuous translation invariance is strongly broken by a lattice, decoupling the Hall conductance from the magnetic field. CIs in which  $t$  is decoupled from  $\frac{n}{B}$  have been observed in magnetically doped thin films with strong spin orbit interactions[145] and in the Harper-Hofstadter[16] bands of graphene subjected to a superlattice potential [97, 146, 147]. Haldane’s staggered flux model[148], which has non-zero quantized Hall conductance even when the net magnetic field is zero, has been engineered using ultracold atoms in an optical lattice[149].

Interactions expand the topological classification of gapped states, allowing the Hall conductance  $t$  to be quantized to a rational fraction. By Laughlin’s flux-threading argument, an insulator with  $t = \frac{p}{q}$  ( $p, q \in \mathbb{Z}$ ) must have a fractionalized excitation with charge  $\frac{e}{q}$  [18]. A fractionally quantized Hall conductance in a bulk insulator is thus a smoking-gun signature of topological order, and fractional quantum Hall (FQH) effects have been observed in partially-filled continuum LLs in a variety of experimental systems [6, 7, 150, 151]. Can a “fractional Chern insulator” (FCI) arise from fractionally filling a

more general Chern band<sup>1</sup>? Although a FQH effect in a LL may be considered a special case of a FCI, in this work we focus on FCIs that require a lattice for their existence.

The phenomenology of lattice FCIs differs from that of continuum LLs. Chern bands with  $\mathcal{C} \neq 1$  can arise, leading to different ground states than are allowed in  $\mathcal{C} = 1$  LLs. In addition, unlike LLs, Chern bands generically have a finite, tunable bandwidth that competes with interactions, providing a new setting for the study of quantum phase transitions. Finally, FCIs might be found in experimental systems where Chern bands, but not LLs, are realizable. A large body of theoretical work has begun to investigate these issues [152, 153, 154, 155, 156, 157, 158, 159].

Here, we report the experimental discovery of FCIs in a bilayer graphene (BLG) heterostructure at high magnetic fields. The requirements to realize an FCI in an experimental system are, first, the existence of a Chern band, and, second, electron-electron interactions strong enough to overcome both disorder and band dispersion. We satisfy these requirements by using a high quality bilayer graphene heterostructure, in which the bilayer is encapsulated between hexagonal boron nitride (hBN) gate dielectrics and graphite top- and bottom gates (Fig. 6.1, A and B). This geometry was recently demonstrated to significantly decrease disorder, permitting the observation of delicate FQH states[49]. We generate Chern bands by close rotational alignment ( $\sim 1^\circ$ ) between the bilayer graphene and one of the two encapsulating hBN crystals. Beating between the mismatched crystal lattices leads to a long-wavelength ( $\sim 10$  nm) moiré pattern that the electrons in the closest layer experience as a periodic superlattice potential (Fig. 6.1B) (See Appendix E). At high magnetic fields, the single particle spectrum of an electron in a periodic potential forms the Chern bands of the Hofstadter butterfly[97, 146, 147]. These bands are formally equivalent to Chern bands proposed to occur in zero magnetic

---

<sup>1</sup>We use the term “fractional Chern insulator” to denote any non-FQH, topologically ordered state at fractional filling of a Chern band, rather than a more restrictive definition requiring the states to occur at zero field.

field lattice models; at any fractional flux, a finite-field lattice model can be converted to an equivalent zero-field model using gauge invariance[152].

We measure the penetration field capacitance[80] ( $C_P$ ), which distinguishes between gapped (incompressible) and ungapped (compressible) states (See Appendix E). Figure 6.1, C and D, shows  $C_P$  measured as a function of  $B$  and the electron density,  $n \sim n_0 \equiv c(v_t + v_b)$ , where  $v_t$  and  $v_b$  are the applied top and bottom gate voltages and  $c$  denotes the geometric capacitance to either of the two symmetric gates. We used a perpendicular electric field, parameterized by  $p_0/c = v_t - v_b$  (where  $p_0$  is the electron density imbalance between layers in the absence of screening), to localize the charge carriers onto the layer with a superlattice potential, e.g., adjacent to the aligned hBN flake. High- $C_P$  features, corresponding to gapped electronic states, are evident throughout the experimentally accessed parameter space (Fig. 6.1, C and D), following linear trajectories in the  $nB$  plane. We estimate the area of the superlattice unit cell from zero-field capacitance data (See Appendix E), and defined the electron density  $n_e = N_e/N_S$  and flux density  $n_\Phi = N_\Phi/N_S$  per unit cell. Here  $N_e$ ,  $N_s$ , and  $N_\Phi$  are the number of electrons, superlattice cells, and magnetic flux quanta in the sample, respectively. The trajectories are parameterized by their inverse slope  $t$  and  $n$ -intercept  $s$  in the  $nB$  plane,

$$N_e = tN_\Phi + sN_s, \quad n_e = tn_\Phi + s. \quad (6.1)$$

The Středa[160] formula,  $t = \frac{\partial n_e}{\partial n_\Phi}|_{N_S} = \frac{h}{e^2} \sigma_{xy}$ , shows that the Hall conductance of a gapped phase is exactly  $t$ . The invariant  $s = \frac{\partial N_e}{\partial N_S}|_{N_\Phi}$  encodes the amount of charge “glued” to the unit cell, i.e., the charge which is transported if the lattice is dragged adiabatically[161]. Non-zero  $s$  indicates that strong lattice effects have decoupled the Hall conductance from the electron density. Within band theory, the invariants of a gap arise from summing the invariants  $(\Delta t_j, \Delta s_j)$  of the occupied bands,  $(t, s) = \sum_{j \in \text{occ}} (\Delta t_j, \Delta s_j)$

— in particular, the Hall conductance  $t$  is the sum of the occupied band Chern indices,  $\Delta t_j = C_j$ .

On the basis of the properties of  $t$  and  $s$ , we observe five classes of high- $C_P$  trajectories, each of which correspond to a distinct class of gapped state (Fig. 6.1, E and F). Free-fermion band gaps must have integer  $t$  and  $s$ : trajectories with  $s = 0$  correspond to gaps between LLs, i.e., IQH states. Trajectories with  $s \neq 0$  indicate the formation of the non-LL Chern bands of the Hofstadter butterfly [97, 146, 147]. Trajectories with fractional  $t$  or  $s$  are beyond the single particle picture and thus indicate interaction-driven gapped phases. The conventional FQH states follow trajectories with fractional  $t$  and  $s = 0$ . Gap trajectories with integer  $t$  and fractional  $s$  (previously observed in monolayer graphene [162]) must be either topologically ordered or have interaction-driven spontaneous symmetry breaking of the superlattice symmetry. The theoretical analysis below suggests the latter case is most likely, so we refer to this class as symmetry-broken Chern insulators (SBCIs). Finally, there are gapped trajectories with fractional  $t$  and fractional  $s$ , which are the previously unreported class of topologically-ordered FCI phases.

To better understand states with fractional  $t$  or  $s$ , we first identify the single-particle Chern bands in our experimental data by identifying all integer- $t$ , integer- $s$  gapped states. We focus on adjacent pairs of gapped states with integer  $(t_L, s_L)$  and  $(t_R, s_R)$ , which form the boundaries of a finite range of  $n_e$  in which no other single-particle gapped states appear (Fig. 6.1G). Adding charge to the left gapped state corresponds to filling a Chern band with invariants  $(\Delta t, \Delta s) = (t_R - t_L, s_R - s_L)$ . From this criterion we find a variety of Chern bands with  $\Delta t = \pm 1, \pm 2, \pm 3$  and  $\pm 5$  in the experimental data (See Appendix E), each of which appear as a triangle between adjacent single-particle gapped states. These Chern bands are observed to obey certain rules expected from the Hofstadter problem: for example,  $\Delta t$  and  $\Delta s$  are always coprime, and Chern bands with

$\Delta t$  always emanate from a flux  $n_{\Phi}^* = p/\Delta t$ .

Interaction-driven phases occur at fractional filling  $\nu_C$  of a Chern band, following trajectories  $(t_{\nu_C}, s_{\nu_C}) = (t_L, s_L) + \nu_C \mathcal{C}(\Delta t, \Delta s)$ . The Chern numbers of the bands in which some of the observed interaction-driven phases appear (Figs. 6.2, A to C) are depicted schematically in Figs. 6.2, D to F.

By combining a phenomenological description of the moiré potential with knowledge of orbital symmetry breaking in bilayer graphene[57], we are able to construct a single particle model that closely matches the majority of the experimentally observed single-particle Chern bands (See Appendix E). The calculated energy spectra of the bands relevant to Figs. 6.2, A to C are shown in Fig. 6.2, G to I. As is clear from the band structure, stable phases at fractional  $\nu_C$  are not expected within the single particle picture: instead, the encompassing Chern band splits indefinitely into finer Chern bands at lower levels of the fractal butterfly that depend sensitively on  $n_{\Phi}$ .

The three columns of Fig. 6.2 represent instances of three general classes of fractional  $\nu_c$  states observed in our experiment. Fig. 6.2A shows two gapped states within a  $\Delta t = -1$  band at  $\nu_C = 1/3$  and  $2/3$ . These gapped states extend from  $n_{\Phi} = 0.55$  to at least  $n_{\Phi} = 0.8$  (See Appendix E). Both are characterized by fractional  $t$  and  $s$ , and we identify them as FCI states. As with FQH states, the fractionally quantized Hall conductance implies that the system has a charge  $e/3$  excitation[18]. The fractional  $s$  values of these states, being multiples of this fractional charge, do not require broken superlattice symmetry. Gapped states at  $\nu_C = 1/3, 2/3$  in a  $\Delta t = -1$  band are accompanied by comparatively weaker states at  $\nu_C = 2/5, 3/5$  (Fig. 6.3B). These fillings match the odd-denominator composite fermion sequence observed for FQH states (Fig. 6.3C), in agreement with theoretical predictions [163]).

Figure 6.2 shows gapped states with fractional  $s$  and integer  $t$  at  $\nu_C = 1/3, 2/3$  in a  $\Delta t = +3$  band (Fig. 6.2B) and at  $\nu_C = 1/2$  in a  $\Delta t = +2$  band (Fig. 6.2C). Filling a

Chern- $\Delta t$  band to a multiple of  $\nu_C = \frac{1}{|\Delta t|}$  corresponds to integer  $t$  but fractional  $s$ . These states are unlikely to admit a simple interpretation as FCIs; however, we cannot exclude exotic fractionalized states. Absent fractional excitations, a gapped state with fractional  $s = \frac{x}{y}$  implies broken superlattice symmetry: the unit cell of such a phase must contain an integral number of electrons, and the smallest such cell contains  $y$  superlattice sites. Theoretically, such symmetry breaking is expected to arise spontaneously as a result of electronic interactions, in a lattice analog of quantum Hall ferromagnetism[164]. A  $\Delta t$  Chern band is similar to a  $\Delta t$ -component LL, but in contrast to an internal spin, translation acts by cyclically permuting the components[164, 165, 166]. Spontaneous polarization into one of these components thus leads to a  $t$ -fold increase of the unit cell[164]. The observation of SBCIs is thus analogous to the observation of strong odd-integer IQHEs that break spin-rotational invariance. Some of the “fractional fractal” features recently described in monolayer graphene appear to be consistent with this explanation[162].

Further, we also observe fractional- $t$  states within a  $\Delta t = +2$  band (Fig. 6.3C); for example at  $\nu_C = 1/3$  ( $t = 8/3$  and  $s = -1/3$ ) and  $\nu_C = 1/6$  ( $t = 7/3, s = -1/6$ ). FCIs in Chern- $\Delta t \neq \pm 1$  bands can either preserve or break the underlying lattice symmetry. Symmetry preserving FCIs are expected [156, 163, 167] at fillings  $\nu_c = \frac{m}{2lm\Delta t+1}$  for integers  $l, m$ . The state observed  $\nu_C = 1/3$  is consistent with this sequence ( $l = 1, m = -1$ ); in contrast, the weaker state at  $\nu_1/6$  is not. For the  $\nu_C = 1/6$  state, the observed  $t = 7/3$  suggests a fundamental charge of  $e/3$ . As for SBCIs, the observed  $s = -1/6$  implies that each unit cell binds only half a fundamental charge — i.e., the moiré unit cell is doubled and the  $\nu_C = 1/6$  state is a “SB-FCI” state. A  $\Delta t = 2$  Hofstadter band is similar to a spin degenerate LL, with lattice symmetry taking the place of spin symmetry. In a spin degenerate LL at  $\nu_C = 1/6$  (i.e., LL filling  $\nu = 1/3$ ) the system spontaneously spin polarizes, forming a single component Laughlin state. In contrast, at

$\nu_C = 1/3$  ( $\nu = 2/3$ ) the system can either spin polarize (observed only for large Zeeman energy) or form a multicomponent FQH state that preserves spin rotation symmetry. The absence of an obvious analogue of the Zeeman effect in our Hofstadter band makes a multicomponent state a more likely candidate for the feature observed at  $\nu_C = 1/3$ .

To assess the plausibility of FCI and SBCI ground states, we use the infinite density matrix renormalization group (iDMRG) to numerically compute the many body ground state within a minimal model of the BLG[136]. We first consider Coulomb interactions and a triangular moiré potential of amplitude  $V_M$  projected into a BLG  $N = 0$  LL[168], matching the parameter regime in Fig. 6.2A (See Appendix E). We focus on  $n_\Phi = 2/3$  at a density corresponding to  $\nu_C = 1/3$  filling of the  $\Delta t = -1$  band.

If interactions are too weak compared to the periodic potential (as parameterized by  $V_M/E_C$ , where  $E_C = e^2/(\epsilon l_B)$  is the Coulomb energy,  $l_B = \sqrt{\frac{\hbar}{eB}}$  is the magnetic length, and  $\epsilon$  the dielectric constant, and  $\hbar$  is the reduced Planck constant), the ground state at  $n_\Phi = 2/3$  is gapless, corresponding to a partially filled Chern band. If the interactions are too strong, the system forms a Wigner crystal which is pinned by the moiré potential. In the intermediate regime, however, the numerical ground state of this model has a fractional  $t$  and  $s$  that match the experiment, and hence is an FCI, with entanglement signatures that indicate a Laughlin-type topological order (See Appendix E). The FCI is stable across a range of  $V_M/E_C$  (Fig. 6.4A) corresponding to  $|V_M| \approx 14 - 38$  meV, consistent with recent[169] experiments that suggest  $|V_M| \sim 25$  meV. Fig. 6.4B shows that the real-space density of an FCI is strongly modulated by the potential, but preserves all the symmetries of the superlattice.

We next conduct iDMRG calculations to assess the plausibility of the SBCI hypothesis. We focus on the well developed Chern-3 band of Fig. 6.2, B,E and H. As a minimal model, we project the moiré and Coulomb interactions into the  $N = 1$  LL of the BLG, fixing  $V_M = 21$  meV and  $E_C(B = 17\text{T}) = 35$  meV, and take  $n_\Phi = 3/8$ .

At  $\nu_C = 1/3$  filling, the electron density exhibits a modulation that spontaneously triples the superlattice unit cell (Fig. 6.4C). A similar tripling is observed at  $\nu_C = 2/3$ . These are not merely density waves, however, as they have finite  $(t, s)$  invariants, in agreement with experiment.

We note that the SBCI states are distinct from a second class of integer- $t$ , fractional- $s$  features, the moiré-pinned Wigner crystals[162, 170]. In the latter case, starting from a LL-gap at  $t, s = t_L, 0$ , additional electrons form a Wigner crystal pinned by the moiré; the added electrons are electrically inert, leading to a state at  $t, s = t_L, \frac{x}{y}$  that can't be ascribed to fixed  $\nu_C$  of an encompassing band. These states are thus analogous to reentrant IQH effects, with the moiré playing the role of disorder. In contrast, although the electrons added to the SBCI spontaneously increase the unit cell, they also contribute an integer Hall conductance, which together correspond to some  $\nu_C$ .

In summary, we find that instead of a self-repeating fractal structure, interactions mix Hofstadter-band wavefunctions to form stable, interaction-driven states at fractional filling of a Chern band. Among these are both symmetry-broken Chern insulators and topologically-ordered fractional Chern insulators, the latter of which constitute a lattice analog of the FQH effect. Lattice engineering can lead to increased experimental control. For example, multicomponent FCI states in higher Chern number bands - as may be responsible for the  $\nu_C = 1/3$  feature in Fig. 6.3C - have been predicted to host non-abelian defects at engineered lattice dislocations[165]. A pressing experimental question, then, is thus whether FCI states can be realized in microscopically engineered superlattices.



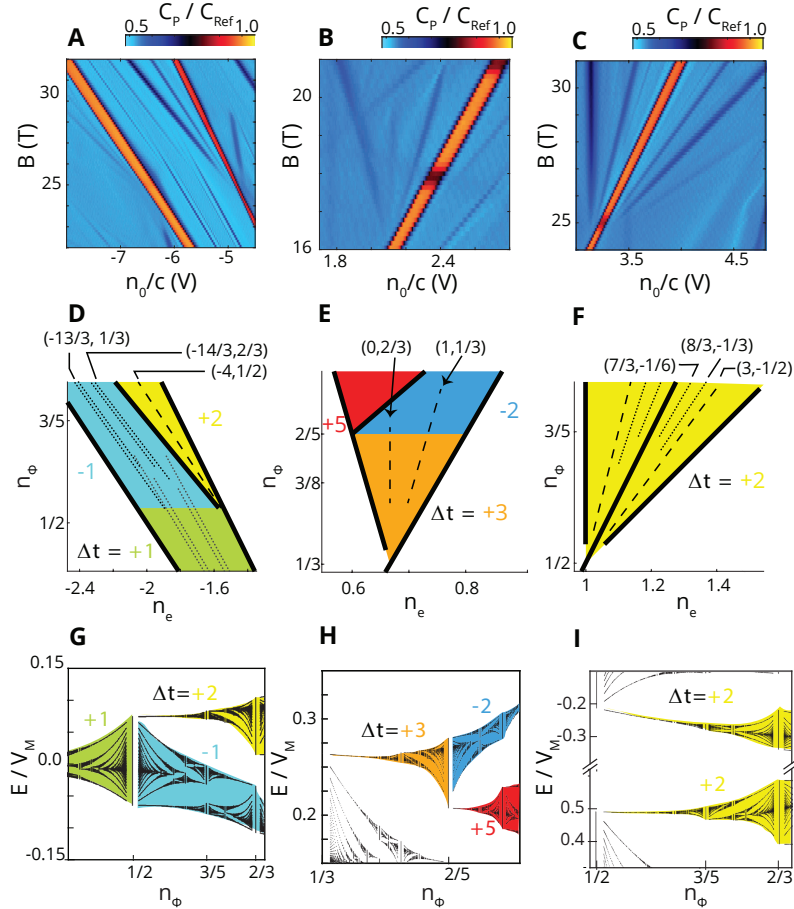


Figure 6.2: **Interaction driven states at partial Chern-band filling.** **a-c** Details of Fig. 6.1, **C** and **D** showing (a) FCI states in a  $\Delta t = -1$  band, (b) SBCI states in a  $\Delta t = +3$  band, and (c) FCI and SBCI states in  $\Delta t = 2$  bands. **d** Schematic of (a). FCI states (black dotted lines) with  $(t, s) = (-13/3, 1/3)$ ,  $(-22/5, 2/5)$ ,  $(-23/5, 3/5)$ , and  $(-14/3, 2/3)$  occur at fractional filling of a  $\Delta t = -1$  band (light blue). FQH states (gray dotted lines) occur at fractional filling of a conventional LL ( $\Delta t = +1$ , green) at low fields. **e** Schematic of (b). SBCI states (dashed lines) at  $(t, s) = (0, 2/3)$  and  $(1, 1/3)$  occur at  $1/3$  and  $2/3$  fractional filling of a  $\Delta t = 3$  band (orange). **f** Schematic of (c). Both FCI and SBCI states (dotted and dashed lines) occur in the  $\Delta t = 2$  bands. **g** Calculated Hofstadter energy spectrum  $E$  in the regime of (a), matching the observation that the LL splits into  $\mathcal{C} = -1, 2$  bands. **h** Calculated Hofstadter spectrum in the regime of (b), matching the observed splitting of a  $\mathcal{C} = 3$  band into  $\mathcal{C} = 5, -2$  bands. **i** Calculated Hofstadter spectrum in the regime of (c). The IQH gap at  $\nu = 2$  separates the two single-particle bands and is much larger than  $V_M$ .

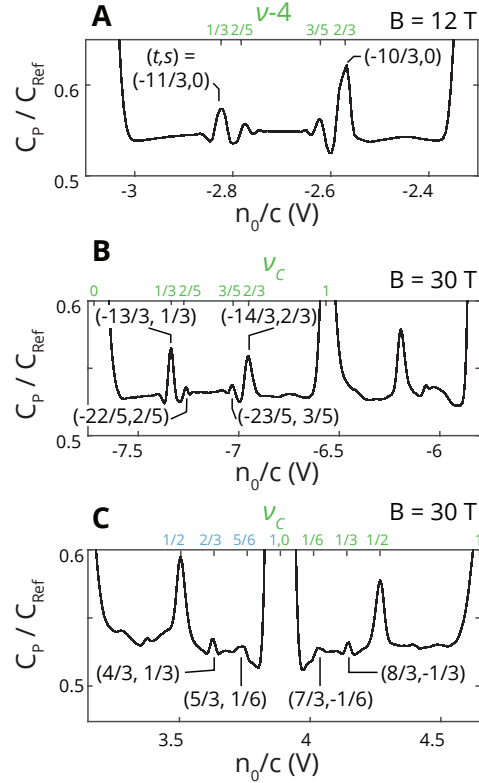


Figure 6.3: **Line cuts of  $C_P$  comparing FCI and FQH states.** **a** Line cut of  $C_P$  vs.  $n_0/c$  (bottom axis) and Chern band filling factor ( $\nu_C$ , top axis). The data is averaged over  $p_0/c \sim 1.0 - 4.0$  V at  $B = 12$  T, showing FQH states in a conventional LL. At low fields, the effective moiré potential is weak, and FQH states are observed at filling factors  $\nu - 4 = 1/3, 2/3$  as well as  $2/5, 3/5$  of the  $\Delta t = +1$  LL. **b** Line cut averaged over  $p_0/c \sim 4.0 - 14.0$  V at  $B = 30$  T, showing FCI in the a  $\Delta t = -1$  band (also shown in Fig. 6.2a). Weaker features appear at  $\nu_C = 2/5, 3/5$ , similar to the composite fermion sequence in (a). **c** Line cut averaged over  $p_0/c \sim -14.0$  to  $-9.0$  V at  $B = 30$  T, showing FCI in two  $\Delta t = 2$  bands (also shown in Fig. 6.2c). Blue and green  $\nu_C$  values indicate filling of two distinct  $\Delta t = 2$  bands. The relative strength of the  $\nu_C = 1/3$  state compared to the  $\nu_C = 1/6$  state in the right  $\Delta t = 2$  band is consistent with the former preserving the lattice symmetry.

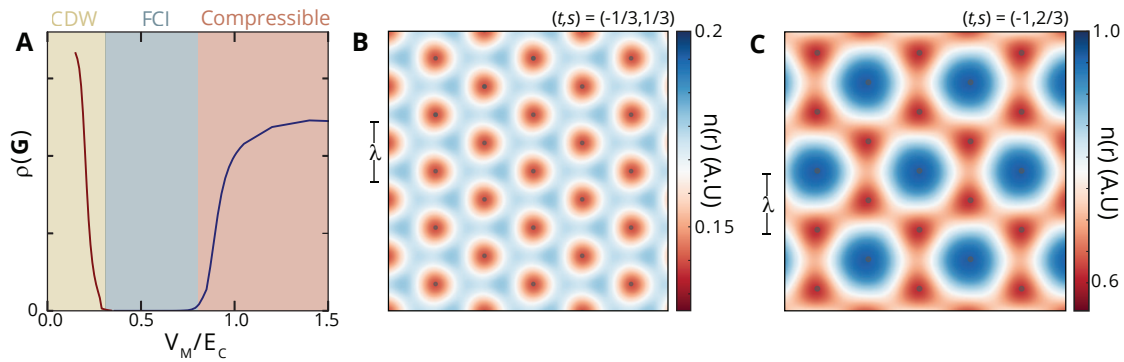


Figure 6.4: **iDMRG calculations showing the stability of FCI and SBCI states.** **a** Calculated iDMRG phase diagram at  $\nu_C = 1/3$  filling of the  $\Delta_t = -1$  band shown in Fig. 6.2a,d,g ( $n_\Phi = 2/3$ ).  $|V_M|$  is the moiré potential amplitude,  $E_C$  is the Coulomb energy, and  $\rho(\mathbf{G})$  is the charge density at Bragg vector  $\mathbf{G}$ . The FCI competes with two other phases: a charge density wave (CDW) at low  $|V_M|$ , and a compressible phase at high  $|V_M|$ . The competing phases are diagnosed by symmetry breaking density waves at wavevector  $\mathbf{G} = \mathbf{G}_0/3$  (red) and  $\mathbf{G} = \mathbf{G}_0/2$  (blue), where  $\mathbf{G}_0$  is a reciprocal vector of the moiré E. **b** Calculated real-space electron density  $n(r)$  of the FCI found in (A).  $n(r)$  preserves the symmetry of the moiré potential, whose periodicity is indicated by the gray circles. Here  $V_M/E_C = 0.7$ . **c** Calculated real-space electron density  $n(r)$  at  $\nu_C = 2/3$  filling of the  $\Delta t = 3$  band shown in Fig. 6.2B,E,H ( $n_\Phi = 3/8$ ). The result is consistent with an SBCI phase;  $(t, s) = (-1, 2/3)$ , and  $n(r)$  spontaneously triples the unit cell of the underlying moiré potential, indicated by gray circles. Here  $V_M/E_C = 0.6$  and  $\theta_M = \pi/8$ .

# Chapter 7

## Outlook

“Never meant to copy, only to surpass.” *Chongqing Meiquan, Advertisement slogan*<sup>1</sup>

“We plan, God laughs.” *Yiddish proverb*

Most of the experiments presented in this thesis are observations of new fractional quantum Hall states in *graphene* that were made possible by greatly reducing disorder. This was achieved by replacing metallic gates with few-layer graphite. However, the majority of the observed states have ancestral counterparts in semiconductor and thin oxide heterostructures, dating to work done in the 1980s. Many publications of ever-increasing complexity that deepened our understanding of interacting electron states in 2DES have paved the way for the experiments presented here. While fabrication of graphene devices is not as extensively developed as that of GaAs/AlGaAs heterostructures, graphene has already distinguished itself. In monolayer graphene, we have observed an

---

<sup>1</sup>A rebuttal to plagiarism claims from Zaha Hadid Architects accusing a Chinese development company of copying a building design

unconventional phase transition between a canted antiferromagnet state and a partially sublattice polarized state, which some authors suggest to be an example of a deconfined critical point[91, 92, 93]. While EDFQH in bilayer graphene is the direct analog of the  $5/2$  state in GaAs/AlGaAs, it has several key differences, including: 1) the  $\nu = -1/2$  Pfaffian state in BLG would contain fewer edge states than the anti-Pfaffian  $\nu = 5/2$  state in GaAs<sup>2</sup>, thus making it more preferable for interferometry experiments to detect non-Abelian statistics[1], and 2) the polarizability measurements at half Landau level filling reveal a potentially new phase: a gapless fractionalized insulator. Moreover, in bilayer graphene, we have observed fractional Chern insulator states that can coexist with conventional quantum Hall states, enabling the investigation of phase transitions between states of different topological order. Additionally, other research groups have observed multicomponent states in double layer graphene systems [28, 29] and even denominator “221-parton” state [172] in monolayer graphene that lack counterparts in GaAs/AlGaAs heterostructures. Beyond quantum Hall physics, the flexibility in manufacturing graphene heterostructures has made graphene a platform for studying unconventional superconductivity[13, 14].

To conclude, I will describe a potential experimental path that extends the bulk capacitive measurements towards probing the ground state degeneracy of  $e/4$  quasi-particle excitation with a Pfaffian ground state that may reveal their non-Abelian properties. The foundation for this experiment is outlined in Cooper,et al [26] (A similar experiment in GaAs has been proposed in [173]). Theory predicts that excitations from the ground state at  $\nu = -1/2$  of BLG would be quasiparticles with charge  $e/4$ , so for a charge

---

<sup>2</sup>Numerics suggest that the  $\nu = 5/2$  state in GaAs is described by an anti-Pfaffian state. However, this is still a subject of debate: recent thermal Hall measurements done by Banerjee, et.al. [171] do not agree with the predictions for either Pfaffian or anti-Pfaffian states.

carrier density  $n$  next to the gap, the quasiparticle carrier density would be:

$$n_{e/4} = 4 \times \left| n - \frac{1}{2}n_0 \right|, \quad (7.1)$$

where  $n_0 = (2\pi l_b^2)^{-1}$  is the Landau level degeneracy. The Pfaffian state will have  $g = 2^{n_{e/4}/2-1}$  ground states with an associated entropy per unit area:

$$s_{e/4} = k_B \ln g = k_B \frac{n_{e/4}}{2} \ln 2. \quad (7.2)$$

In turn, Maxwell relations allows one to relate the entropy density to a measurable quantity:

$$\left( \frac{\partial \mu}{\partial T} \right)_n = - \left( \frac{\partial s}{\partial n} \right)_T = - \frac{ds_{e/4}}{dn_{e/4}} \left( \frac{\partial n_{e/4}}{\partial n} \right)_T = \mp 2k_B \ln 2. \quad (7.3)$$

Therefore, by measuring  $\partial\mu/\partial T$  as a function of filling factor, the states with Abelian statistics should not contribute a signal in the limit of  $T \rightarrow 0$ ; on the contrary, the non-Abelian states would have a finite contribution. A potential realization of such a measurement is shown in Figure 7.1. The device in this experiment is a 4 plate capacitor, with two gates and two graphene layers. The first graphene layer is the BLG, tuned to a half filled Landau level  $\nu = -1/2$ , where non-Abelian excitations are expected. The second layer, is a monolayer graphene sheet that acts as a sensor (Similar experiment was proposed by Zhang et.al. [174]). Both mono and bilayer graphene sheets are in electro-chemical equilibrium with their respective contacts  $\varphi_i + \mu_i = v_i$ , where  $\varphi_i$  are electric potentials,  $\mu_i$  are chemical potentials,  $v_i$  applied voltages, and  $i = \text{BLG, MLG}$ . This implies that any changes in  $\mu_{\text{BLG}}$  would cause a change in the electric potentials doping the monolayer graphene  $n_{\text{MLG}} \rightarrow n_{\text{MLG}} + \delta n$ . A capacitance measurement from the top gate to the MLG would capture the charge variation  $\delta n$ . Using a feedback control loop we can restore the MLG to the initial state (carrier density), with the control signal

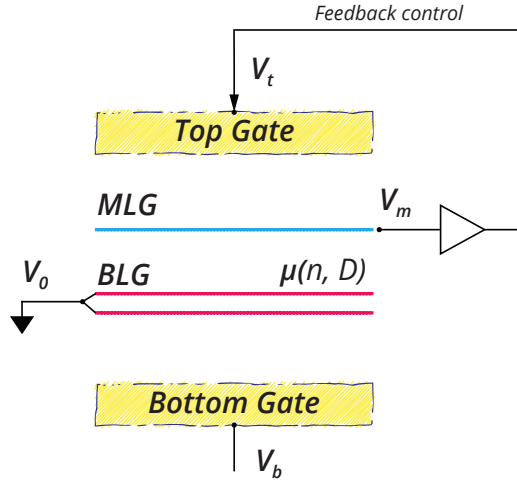


Figure 7.1: Measurement layout for entropy measurements. The device is dual-gated with two active layers separated by an hBN dielectric: 1) the monolayer graphene acts as a sensor layer and 2) the bilayer graphene is the layer we probe for non-Abelian statistics. Since both layers are in electro-chemical equilibrium with their contacts, any changes in the chemical potential of the bilayer graphene would result in a change to electric potentials in the device, which in turn modulate the MLG carrier density. If the variations of the MLG density are detected by a cryogenic HEMT amplifier, we can form a feedback control signal to the top gate returning the monolayer carrier density to the initial state. The feedback control voltage is proportional to the change in BLG chemical potential.

$V_{FB} \sim \delta\mu_{BLG}$ . Practically speaking, modulation of the BLG chemical potential can be done by passing a time-varying current through a heater connected to the BLG. In this case, the a measured time varying feedback voltage would be the desired derivative  $\partial\mu/\partial T$ . Though in this scenario, care needs to be taken to keep the electric potential of the BLG fixed. This can be achieved by using superconducting (e.g. NbN) leads to short the BLG to an electrical ground: the electric potential will be always  $v_{BLG} = 0$ , but heat would still be injected into the system.

This is just one of the many exciting possibilities offered by investigating 2DES in graphene. One could imagine an extension of this technique in which three graphene layers are used, with two monolayers acting as sensors on both sides of the bilayer

---

graphene devices. In such an experiment one could potentially probe the difference in chemical potential of the BLG's top and bottom layers; mapping this out as a function of temperature would allow to detect states with charge neutral excitation, but finite layer polarizability, like the exciton metal proposed in Chapter 5. The high degree of control offered by dual-gated graphene devices and the configurability of the heterostructure composition are a fruitful venue for studying correlated electron systems with many amazing results to come.



# Appendix A

## Capacitance Bridge

### A.1 Penetration field capacitance

Consider a truly 2-dimensional electron gas (2DEG) with an ohmic contact placed between two metallic gates. Metals have an extremely large density of states making the quantum-mechanical energy cost of adding an electron negligible compared to the electrostatic charging energy. The case is different for the 2DEG. The 2DEG is in electrochemical equilibrium with the contact:

$$V_0 = \varphi + \mu, \tag{A.1}$$

where  $V_0$ ,  $\varphi$  and  $\mu$  are the applied voltage, electric and chemical potentials respectively.

The electrostatic equations for the three plate capacitor are:

$$n_t = c_t(v_t - \varphi), \tag{A.2}$$

$$n_b = -c_b(\varphi - v_b), \tag{A.3}$$

$$0 = n_t + n_b + n_0 \tag{A.4}$$

Replacing the values with their differentials and noting that  $\delta\varphi = \delta V_0 - \delta n/\nu$  ( $\nu = \partial n/\partial\mu$  is the thermodynamic density of states) we find the expression for the differential capacitance matrix  $C_{ij} = \partial n_i/\partial V_j$ , with  $i, j = (t, b)$  and setting  $V_0$  and  $\delta V_0 = 0$  to define the “zero” potential:

$$\mathcal{C} = C_{ij} = \frac{1}{c_b + c_t + \nu} \begin{pmatrix} c_t(c_b + \nu) & -c_b c_t \\ -c_b c_t & c_b(c_t + \nu) \end{pmatrix} \quad (\text{A.5})$$

The penetration field capacitance for a symmetric device ( $c_b = c_t = c$ ) is then

$$C_{\text{PEN}} = C_{tb} = \frac{c^2}{2c + \nu}. \quad (\text{A.6})$$

## A.2 Symmetric and anti-symmetric capacitances in BLG

*The contents of the chapter have previously appeared in the supplementary materials of Hunt B. et.al, “Direct measurement of discrete valley and orbital quantum numbers in bilayer graphene”, Nature Communications, volume 8, article 948 (2017), doi: 10.1038/s41467-017-00824-w.*

The electrostatic model presented in the previous chapter can be extended to bilayer graphene if we consider a four-plate capacitor: top and bottom gates, and two layers of the bilayer graphene. As before, the geometric capacitances from top and bottom gates are denoted as  $c_t(b)$ , while a new interlayer capacitance  $c_0$  is introduced to describe the bilayer. Both of the graphene layers are in electrochemical equilibrium with the same

contact at voltage  $v_0$ . The electric potentials  $\varphi_{1,2}$  are given by:

$$\varphi_1 = v_0 - \mu_1, \quad (\text{A.7})$$

$$\varphi_2 = v_0 - \mu_2, \quad (\text{A.8})$$

where  $\mu_i = \mu_i(n_1, n_2)$  are the chemical potentials of the two layer of BLG, and  $n_i$  are the respective carrier densities. Capacitance measurements are differential, so we are interested in the variations of  $\varphi_i$ :

$$\delta\varphi_1 = \delta v_0 - \frac{\partial\mu_1}{\partial n_1}\delta n_1 - \frac{\partial\mu_1}{\partial n_2}\delta n_2, \quad (\text{A.9})$$

$$\delta\varphi_2 = \delta v_0 - \frac{\partial\mu_2}{\partial n_1}\delta n_1 - \frac{\partial\mu_2}{\partial n_2}\delta n_2 \quad (\text{A.10})$$

$$(\text{A.11})$$

Note, from Maxwell relations  $\partial\mu_2/\partial n_1 = \partial\mu_1/\partial n_2$ .

The experimentally relevant capacitances are: 1) penetration field capacitance

$$C_P = \frac{\partial n_{T(B)}}{\partial v_{B(T)}} \quad (\text{A.12})$$

and 2) capacitances from the top and bottom gates to the graphene bilayer

$$C_{T(B)} = \frac{n_0}{v_{T(B)}}. \quad (\text{A.13})$$

Eliminating the electric potentials  $\varphi_{1,2}$ :

$$C_P = \frac{c_b c_t (c_0 \kappa_{11} \kappa_{22} - \kappa_{12} - c_0 \kappa_{12}^2)}{1 - (c_0 - c_t) \kappa_{11} - (c_0 + c_b) \kappa_{22} + (c_b c_t + c_0 c_b + c_0 c_t) (\kappa_{11} \kappa_{22} - \kappa_{12}^2) + 2c_0 \kappa_{12}} \quad (\text{A.14})$$

$$C_B = \frac{c_b (1 + c_t (\kappa_{11} - \kappa_{12}) + c_0 (\kappa_{11} + \kappa_{22} - 2\kappa_{12}))}{1 - (c_0 - c_t) \kappa_{11} - (c_0 + c_b) \kappa_{22} + (c_b c_t + c_0 c_b + c_0 c_t) (\kappa_{11} \kappa_{22} - \kappa_{12}^2) + 2c_0 \kappa_{12}} \quad (\text{A.15})$$

$$C_T = \frac{c_t (1 + c_b (\kappa_{11} - \kappa_{12}) + c_0 (\kappa_{11} + \kappa_{22} - 2\kappa_{12}))}{1 - (c_0 - c_t) \kappa_{11} - (c_0 + c_b) \kappa_{22} + (c_b c_t + c_0 c_b + c_0 c_t) (\kappa_{11} \kappa_{22} - \kappa_{12}^2) + 2c_0 \kappa_{12}} \quad (\text{A.16})$$

The physical quantities (Chapter 3.1) we are interested in are  $n \equiv n_1 + n_2$  and  $p \equiv n_1 - n_2$ , while the control parameters are  $n_0 = c_t v_t + c_b v_b$  and  $p_0 = c_t v_t - c_b v_b$ . Then the partial derivatives of  $n$  are:

$$\frac{\partial n}{\partial n_0} = \frac{\partial n}{\partial v_t} \frac{\partial v_t}{\partial n_0} + \frac{\partial n}{\partial v_b} \frac{\partial v_b}{\partial n_0} = \frac{1}{2} \left( \frac{C_T}{c_t} + \frac{C_B}{c_b} \right) = \frac{1}{2} \frac{C_S}{c} \quad (\text{A.17})$$

$$\frac{\partial n}{\partial p_0} = \frac{\partial n}{\partial v_t} \frac{\partial v_t}{\partial p_0} + \frac{\partial n}{\partial v_b} \frac{\partial v_b}{\partial p_0} = \frac{1}{2} \left( \frac{C_T}{c_t} - \frac{C_B}{c_b} \right) = \frac{1}{2} \frac{C_A}{c}, \quad (\text{A.18})$$

where  $c = 0.5(c_b + c_t)$  is the average geometric capacitance. With geometric capacitance asymmetry defined as  $\delta = (c_b - c_t)/(c_b + c_t)$ , the symmetric(antisymmetric) capacitance is given by:

$$C_{S(A)} \equiv \frac{C_B}{1 - \delta} \pm \frac{C_B}{1 + \delta} \quad (\text{A.19})$$

The partial derivative of layer polarization  $p$ :

$$\frac{\partial p}{\partial n_0} = \frac{\partial n_1}{\partial v_t} \frac{\partial v_t}{\partial n_0} + \frac{\partial n_1}{\partial v_b} \frac{\partial v_b}{\partial n_0} - \frac{\partial n_2}{\partial v_t} \frac{\partial v_t}{\partial n_0} - \frac{\partial n_2}{\partial v_b} \frac{\partial v_b}{\partial n_0} \quad (\text{A.20})$$

$$= \frac{1}{2} \left( \frac{\partial n_1}{\partial v_t} \frac{1}{c_t} + \frac{\partial n_1}{\partial v_b} \frac{1}{c_b} - \frac{\partial n_2}{\partial v_t} \frac{1}{c_t} - \frac{\partial n_2}{\partial v_b} \frac{1}{c_b} \right) \quad (\text{A.21})$$

$$= \frac{1}{2} \left( \frac{c_t(\kappa_{11} + \kappa_{12}) + 2c_0(\kappa_{11} - \kappa_{22}) - c_b(\kappa_{12} + \kappa_{22})}{1 - (c_0 + c_t)\kappa_{11} - (c_0 + c_b)\kappa_{22} + (c_b c_t + c_0 c_b + c_0 c_t)(\kappa_{11}\kappa_{22} - \kappa_{12}^2) + 2c_0\kappa_{12}} \right) \quad (\text{A.22})$$

$$= \frac{-c_0}{c(1 - \delta^2)} \left( \frac{C_A(1 - \delta^2) + \delta((C_S - 2c)(1 - \delta^2) + 4C_P)}{c(1 - \delta^2)} \right) - \frac{4C_P\delta + C_A(1 - \delta^2)}{c(1 - \delta^2)} \quad (\text{A.23})$$

$$\frac{\partial p}{\partial p_0} = \frac{\partial n_1}{\partial v_t} \frac{\partial v_t}{\partial p_0} + \frac{\partial n_1}{\partial v_b} \frac{\partial v_b}{\partial p_0} - \frac{\partial n_2}{\partial v_t} \frac{\partial v_t}{\partial p_0} - \frac{\partial n_2}{\partial v_b} \frac{\partial v_b}{\partial p_0} \quad (\text{A.24})$$

$$= \frac{1}{2} \left( \frac{\partial n_1}{\partial v_t} \frac{1}{c_t} - \frac{\partial n_1}{\partial v_b} \frac{1}{c_b} - \frac{\partial n_2}{\partial v_t} \frac{1}{c_t} + \frac{\partial n_2}{\partial v_b} \frac{1}{c_b} \right) \quad (\text{A.25})$$

$$= \frac{1}{2} \left( \frac{2 + c_t(\kappa_{11} + \kappa_{12}) + c_b(\kappa_{12} + \kappa_{22})}{1 - (c_0 + c_t)\kappa_{11} - (c_0 + c_b)\kappa_{22} + (c_b c_t + c_0 c_b + c_0 c_t)(\kappa_{11}\kappa_{22} - \kappa_{12}^2) + 2c_0\kappa_{12}} \right) \quad (\text{A.26})$$

$$= \frac{c_0}{c(1 - \delta^2)} \left( \frac{4C_P + (C_S - 2c)(1 - \delta^2) + \delta C_A(1 - \delta^2)}{c(1 - \delta^2)} \right) - \frac{4C_P + C_S(1 - \delta^2)}{2c(1 - \delta^2)} \quad (\text{A.27})$$

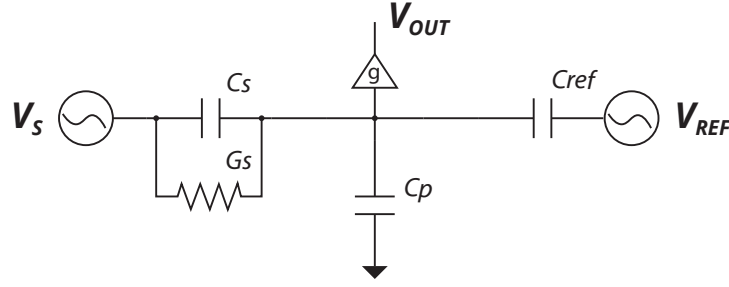


Figure A.1: Lumped element model of the capacitance bridge

For a symmetric device  $\delta \approx 0$ , and  $c_0 \gg c/2$ :

$$\frac{\partial n}{\partial n_0} \approx \frac{C_S}{2c}, \quad (\text{A.28})$$

$$\frac{\partial n}{\partial p_0} \approx -\frac{C_A}{2c}, \quad (\text{A.29})$$

$$\frac{\partial p}{\partial p_0} \approx \frac{\partial c_0}{c} \frac{4C_P + C_S - 2c}{c}, \quad (\text{A.30})$$

$$\frac{\partial p}{\partial n_0} \approx -\frac{c_0}{c} \frac{C_A}{c} \quad (\text{A.31})$$

### A.3 Lumped model

We measure the unknown capacitance  $C_s$  by comparing it with a known reference capacitor  $C_{\text{ref}}$  (Fig. A.1). During the capacitance measurement we apply a fixed AC excitation  $V_s$  to modulate the sample's carrier density, the voltage drop at the input of the amplifier is then zeroed out by adjusting the phase and magnitude of the reference capacitor excitation  $V_{\text{ref}}$ .

The output of the amplifier with gain  $g$  would then read:

$$V_{\text{out}}(Z_{\text{par}}^{-1} + Z_{\text{ref}}^{-1} + Z_s^{-1}) = V_s Z_s^{-1} + V_{\text{ref}} Z_{\text{ref}}^{-1}, \quad (\text{A.32})$$

where  $Z_i$  are the complex impedances of the sample, reference and parasitic capacitors.

We treat the sample as a “leaky” capacitor with capacitance  $C_s$  and bulk conductivity  $G_s$  connected in parallel. Its inverse impedance at excitation frequency  $\omega$  is then:

$$G_s + j\omega C_s = Z_s^{-1}. \quad (\text{A.33})$$

It is convenient to redefine the phase delays to be measured relative to the capacitors and to introduce a complex *dissipation* quantity  $D_s = G_s/\omega$ :

$$C_s - jD_s = Z_s^{-1} \quad (\text{A.34})$$

Rewriting eqn. A.32:

$$V_{\text{out}} = \left[ \frac{C_s C_\Sigma + D_s D_\Sigma}{C_\Sigma^2 + D_\Sigma^2} + j \frac{C_s D_\Sigma - C_\Sigma D_s}{C_\Sigma^2 + D_\Sigma^2} \right] V_s + \frac{C_{\text{ref}}}{C_\Sigma^2 + D_\Sigma^2} (C_\Sigma + jD_\Sigma) V_{\text{ref}}, \quad (\text{A.35})$$

Where:

$$D_\Sigma = D_s + D_p, \quad (\text{A.36})$$

$$C_\Sigma = C_s + C_p + C_{\text{ref}}, \quad (\text{A.37})$$

are the total dissipation (including parasitics) and capacitance. As a reference capacitor we are using a break in a thin gold lead with negligible leakage.

In order to relate this equation with the measured by a lock-in amplifier quadratures, it is convenient to rewrite eqn. A.35 in matrix form:  $V_{\text{out}} = \mathbf{M} \cdot V_{\text{ref}} + V_{\text{offset}}$ , where  $V_i = (V_i^x, V_i^y)^T$  are two-component quadrature vectors. In this notation, balancing the

bridge determines the transfer matrix  $\mathbf{M}$  and the offset  $V_{\text{offset}}$ :

$$\mathbf{M} = \frac{gC_{\text{ref}}}{C_{\Sigma}^2 + D_{\Sigma}^2} \begin{pmatrix} C_{\Sigma} & -D_{\Sigma} \\ D_{\Sigma} & C_{\Sigma} \end{pmatrix} \quad (\text{A.38})$$

$$V_{\text{offset}} = V_s \frac{g}{C_{\Sigma}^2 + D_{\Sigma}^2} \begin{pmatrix} C_s C_{\Sigma} + D_s D_{\Sigma} \\ C_s D_{\Sigma} - D_s C_{\Sigma} \end{pmatrix} \quad (\text{A.39})$$

The bridge is balanced ( $V_{\text{out}} = 0$ ) when the reference capacitor excitation is set to:

$$\begin{pmatrix} V^x \\ V^y \end{pmatrix}_{\text{ref}} = \frac{V_s}{C_{\text{ref}}} \begin{pmatrix} -C_s \\ D_s \end{pmatrix} \quad (\text{A.40})$$

which immediately provides the sample capacitance and dissipation at balance point. In order to speed up measurements we avoid rebalancing the capacitance bridge for every point of the parameter space and assume the amplifier to be in the linear regime. The assumption is incorrect only in the largest quantum Hall gapped states, where the sample becomes incompressible and the capacitance signal changes a lot. However, in the regime of an incompressible sample, quantitative measurements are, in either case, complicated by the long RC charging time of the sample. Expanding the output signal  $V_{\text{out}} = (V_x, V_y)^T$  in  $C_s$  and  $D_s$ , assuming  $C_{\Sigma}$  and  $D_{\Sigma}$  constant, we obtain the values for the off balance capacitance  $\delta C_s$  and dissipation  $\delta D_s$ :

$$\delta C_s^{\text{off}} = \frac{C_{\Sigma} V_x + D_{\Sigma} V_y}{g V_s} \quad (\text{A.41})$$

$$\delta D_s^{\text{off}} = \frac{D_{\Sigma} V_x - C_{\Sigma} V_y}{g V_s} \quad (\text{A.42})$$



## A.4 How to make a transistor mount?

### Materials and Components:

1. GaAs 4 in. wafers from AXT, polished, undoped, prime grade, 625um thick
2. Insulating epoxy: LOCTITE Stycast 2850FT and CAT 23LV catalyst
3. Conducting silver epoxy: EPO-TEK H20E
4. HEMT transistors Sumitomo FHX14X or FHX35X
5. 100MOhm Resistors (MSHR-6-S-S-10005-K-G) from Mini Systems INC
6. Chip carrier

### Prepare in advance:

1. First, we pattern Ti/Au (2/300 nm) leads on a GaAs wafer using standard optical mask lithography. Then, we cleave in small pieces of two types, labeled “top” and “bottom” (see Fig. A.2), using a diamond scribe.
2. Prepare an insulating chip carrier. We use a PCB board with dimensions matching a 16pin DIP socket. The PCB boards are ordered from OSHPark, we use a small end mill to remove the protective coating.

### Assembling a transistor mount:

1. Fix GaAs pieces onto a microscope glass slide with a droplet of PMMA.
2. Under a wire-bonder microscope, use a thin wire to place a droplet of silver epoxy onto a “top” GaAs piece and glue a transistor; let it dry. You can gently push on the transistor with wirebonder wire to position it. Note, the transistors are small and are easy to lose, so use small, sharp tweezers to manipulate them.

3. Bond the gate, source and drain of the transistor to the gold leads.
4. On a probe station check that the transistor responds to a change in gate voltage, be aware that the effect at room temperature is very small. Check if a biased transistor responds to light intensity.
5. On the “bottom” piece, using insulating epoxy glue the 100 MOhm resistor; let it dry. Make a “capacitor” by adding a small scratch in the gold lead. Be careful not to scratch the surface of the resistor.
6. This is the tricky part: using tweezers the “top” piece needs to be positioned perpendicular to the “bottom piece”. The top piece can be secured by a small droplet of insulating epoxy at the corner. Dry the transistor mount in an oven.
7. Now you can connect the leads of the “top” and “bottom” parts by carefully placing small droplets of silver epoxy at the joints.
8. Bond the resistor to the gate. Bond the drain, source, remaining resistor pad and capacitor to chip carrier pins.

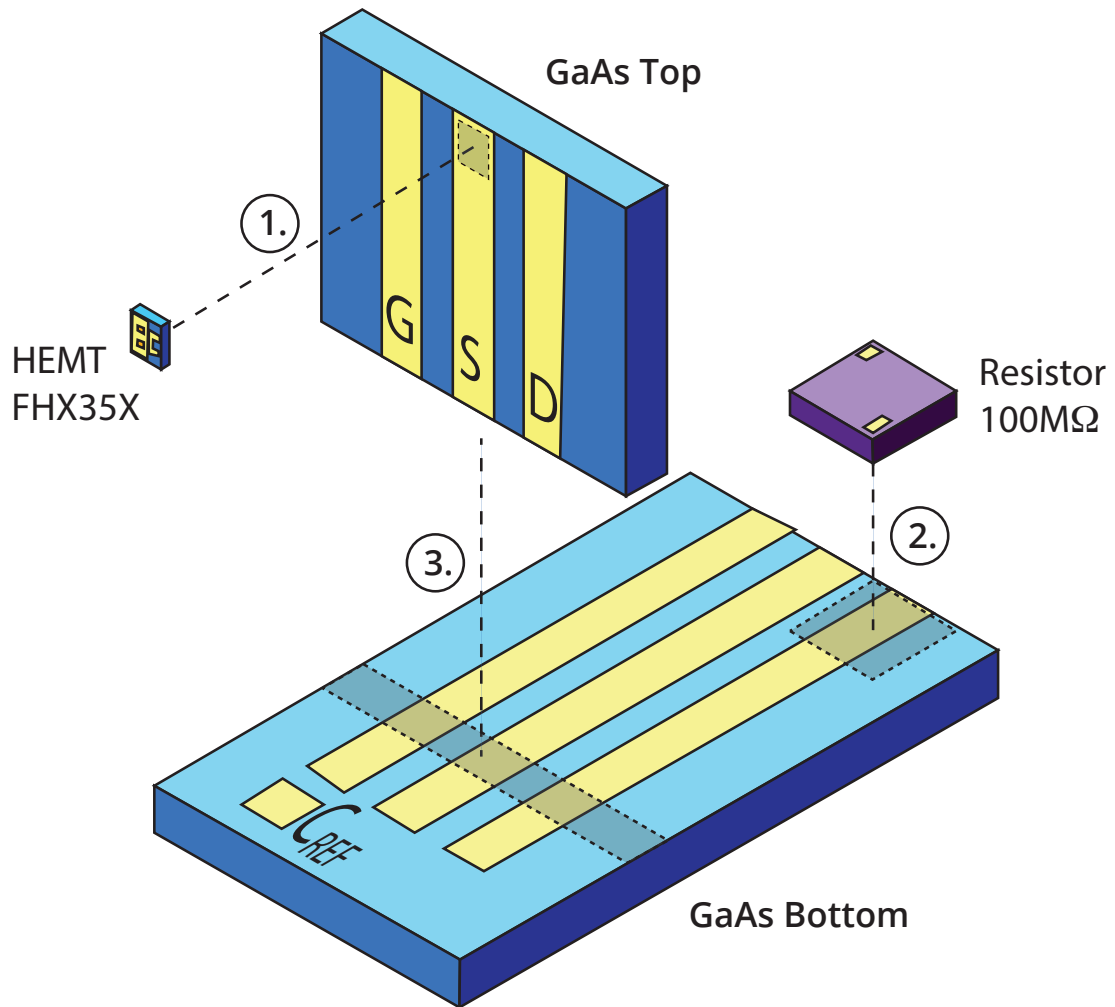


Figure A.2: Exploded view of a transistor mount.

# Appendix B

## Supplementary materials for Chapter 3

**Abstract:** In these supplementary materials we summarize the tight-binding description of ABA-stacked trilayer graphene and outline the procedure used to simulate the density of states. In addition, we discuss how we constrain and refine the tight-binding parameters using zero field and Landau level data. Finally, we provide details on the self-consistent Hartree-Fock calculation of symmetry broken states in Landau levels and discuss their visualization. Supplementary figure B.5.

### B.1 Model and Methods

#### B.1.1 Hamiltonian and bandstructure

To describe the band structure of ABA trilayer graphene we use the Slonczewski-Weiss-McClure parametrization of the tight-binding model [175]. This parametrization uses six tight-binding parameters  $\gamma_0 \dots \gamma_5$  to describe hopping matrix elements between

different atoms:

$$A_i \leftrightarrow B_i : \gamma_0, \quad B_{1,3} \leftrightarrow A_2 : \gamma_1, \quad (\text{B.1})$$

$$A_1 \leftrightarrow A_3 : \frac{1}{2}\gamma_2, \quad A_{1,3} \leftrightarrow B_2 : \gamma_3, \quad (\text{B.2})$$

$$\begin{aligned} A_{1,3} \leftrightarrow A_2 & : -\gamma_4, \\ B_{1,3} \leftrightarrow B_2 & : \frac{1}{2}\gamma_5, \end{aligned} \quad (\text{B.3})$$

where  $A_i$  ( $B_i$ ) refers to an atom from  $A$  ( $B$ ) sublattice, and index  $i = 1 \dots 3$  labels three layers (see Fig. 3.3 in the main text). In addition, parameter  $\delta$  accounts for an extra on-site potential for  $B_1$ ,  $A_2$ , and  $B_3$  sites, which are on top of each other. Finally, we use two additional parameters  $\Delta_{1,2}$  to capture the effect of external electric field and charge asymmetry between internal and external layers of ABA graphene. Parameters  $\Delta_{1,2}$  are related to layer potentials  $U_1 \dots U_3$  as: [176, 177, 178, 61]

$$\Delta_1 = (-e)\frac{U_1 - U_2}{2}, \quad \Delta_2 = (-e)\frac{U_1 - 2U_2 + U_3}{6}. \quad (\text{B.4})$$

We note that the above parameterization is spin-independent. As we shall see below, spin-degenerate simulations fully capture experimental features at zero magnetic field, and adequately describe Landau level data except in vicinity of neutrality point. Effects that break spin degeneracy, i.e. Zeeman splitting and electron interactions, are included only in Section C where we address symmetry broken states in Landau levels.

Via rotation of basis, the tight-binding Hamiltonian for ABA-stacking trilayer graphene can be decoupled into monolayer-graphene-like (SLG) and bilayer-graphene-like (BLG) sectors which are coupled due to presence of displacement field  $\Delta_1$ :

$$H = \begin{pmatrix} H_{SLG} & V_{\Delta_1} \\ V_{\Delta_1}^T & H_{BLG} \end{pmatrix}, \quad (\text{B.5})$$

where the matrix blocks are defined as:

$$H_{\text{SLG}} = \begin{pmatrix} \Delta_2 - \frac{\gamma_2}{2} & v_0\pi^\dagger \\ v_0\pi & -\frac{\gamma_5}{2} + \delta + \Delta_2 \end{pmatrix}, \quad (\text{B.6})$$

$$H_{\text{BLG}} = \begin{pmatrix} \frac{\gamma_2}{2} + \Delta_2 & \sqrt{2}v_3\pi & -\sqrt{2}v_4\pi^\dagger & v_0\pi^\dagger \\ \sqrt{2}v_3\pi^\dagger & -2\Delta_2 & v_0\pi & -\sqrt{2}v_4\pi \\ -\sqrt{2}v_4\pi & v_0\pi^\dagger & \delta - 2\Delta_2 & \sqrt{2}\gamma_1 \\ v_0\pi & -\sqrt{2}v_4\pi^\dagger & \sqrt{2}\gamma_1 & \frac{\gamma_5}{2} + \delta + \Delta_2 \end{pmatrix}, \quad (\text{B.7})$$

$$V_{\Delta_1} = \begin{pmatrix} \Delta_1 & 0 & 0 & 0 \\ 0 & 0 & 0 & \Delta_1 \end{pmatrix}. \quad (\text{B.8})$$

Here we introduced velocities  $v_i = \sqrt{3}a\gamma_i/2\hbar$  corresponding to some of the tight-binding hopping matrix elements, where  $a = 0.246$  nm is the lattice constant. These notations coincide with those used in Ref. [64]. At zero magnetic field  $B$ , the operator  $\pi$  in Eqs. (B.6)-(B.7) can be written as  $\pi = \xi k_x + ik_y$ , where  $k$  is crystal momentum measured with respect to corresponding  $K^\pm$  point labeled by  $\xi = \pm 1$ . For finite magnetic field,  $\pi$  can be replaced with the annihilation (creation) operator acting in the basis of Landau level states in the  $K^-$  ( $K^+$ ) valley.

The capacitance measurements presented in this paper are sensitive to the band structure within a range  $\sim 10$  meV from neutrality point. Within this energy range one can obtain additional insights into effects of TB parameters by deriving  $2 \times 2$  low energy effective Hamiltonian of  $H_{\text{BLG}}$ . This Hamiltonian is obtained by projecting out 2 bands

which are split by energies of order 0.5 eV away from neutrality point:

$$\begin{aligned}
 H_{\text{BLG}}^{\text{eff}} = & -\frac{1}{2m} \begin{pmatrix} 0 & \pi^{\dagger 2} \\ \pi^2 & 0 \end{pmatrix} + \sqrt{2}v_3 \begin{pmatrix} 0 & \pi \\ \pi^{\dagger} & 0 \end{pmatrix} + \\
 & + \begin{pmatrix} \frac{\gamma_2}{2} + \Delta_2 & 0 \\ 0 & -2\Delta_2 \end{pmatrix} + \dots
 \end{aligned} \tag{B.9}$$

where  $1/2m = v_0^2/(\sqrt{2}\gamma_1)[1 + O(\gamma_4/\gamma_0)^2]$ . We see that, to first order,  $\gamma_4$  doesn't appear in the effective Hamiltonian and its effect on the band structure is small.

From explicit form of  $2 \times 2$  Hamiltonians for monolayer and bilayer blocks, Eqs. (B.6) and (B.9) one can qualitatively understand the effects of tight-binding parameters on the band structure. The nearest neighbor hopping  $\gamma_0$  gives the fermi-velocity of the massless monolayer sector fermions. Interlayer hopping  $\gamma_1$  influences to the effective mass of the bilayer graphene. The trigonal warping term  $\gamma_3$  determines the behavior of bilayer bands at small momenta. Finally, small parameters  $\Delta_2$ ,  $\gamma_2$ ,  $\delta$  and  $\gamma_5$  located on the diagonal of Hamiltonians (B.6) and (B.9) determine the magnitude of band gap and relative displacement of BLG and SLG bands.

### B.1.2 Simulation method

At zero magnetic field, we numerically calculate the charge density  $n(\mu)$  and density of states (DOS)  $\nu(\mu)$  as a function of the external potential  $\Delta_1$  and chemical potential  $\mu$ . We discretize the crystal momentum in vicinity of a given  $K$  point. For a fixed value of  $\Delta_1$  we calculate single particle energies for each point of the momentum grid by numerically diagonalizing the Hamiltonian (B.5). Density  $n(\mu)$  (density of states  $\nu(\mu)$ ) is calculated by summing the Fermi-distribution  $n_F(\varepsilon_{\mathbf{k}} - \mu)$  (derivative of Fermi function

Data set	$\gamma_0$	$\gamma_1$	$\gamma_2$	$\gamma_3$	$\gamma_4$	$\gamma_5$	$\delta$	$\Delta_2$
[71] (Graphite)	3.16	0.39	-0.02	0.315	0.044	0.038	0.037	n/a
[179] (Graphite)	3.0121	0.3077	-0.0154	0.2583	0.1735	0.0294	0.0214	n/a
[75]	3.1	0.39	-0.028	0.315	0.041	0.05	0.034	0
[81]	3.1	0.39	-0.02 to -0.016	0.315	0.04 to 0.14	0.005 to 0.015	0.012 to 0.018	n/a
[77]	3.1	0.39	-0.028	n/a	n/a	0.01	0.021	n/a
[180]	3.1	0.39	-0.02	0.315	0.12	0.018	0.02	0.0043 to 0.0044
This paper	3.1	$0.38 \pm 0.003$	$-0.021 \pm 0.005$	0.29	$0.141 \pm 0.04$	$0.05 \pm 0.005$	$0.0355 \pm 0.0045$	0.0035

Table B.1: Different sets of tight-binding parameters from the literature are compared to the set of parameters determined in this work. All parameters are given in units of eV, “n/a” means that corresponding reference did not consider the corresponding parameter.

$n'_F(\varepsilon_{\mathbf{k}} - \mu)$  over all points in the grid,

$$n(\mu) = 4g_{\text{sym}} \frac{S_k}{(2\pi)^2} \frac{1}{N} \sum_{\mathbf{k}} n_F(\varepsilon_{\mathbf{k}} - \mu), \quad (\text{B.10})$$

$$\nu(\mu) = 4g_{\text{sym}} \frac{S_k}{(2\pi)^2} \frac{1}{N} \sum_{\mathbf{k}} n'_F(\varepsilon_{\mathbf{k}} - \mu), \quad (\text{B.11})$$

where  $N = \sum_{\mathbf{k}} 1$  is the total number of momentum points in the considered portion of the Brillouin zone with area  $S_k$ , and factor of 4 accommodates for spin and valley degeneracies. Finally,  $g_{\text{sym}}$  takes into account the symmetry of the BZ: for example,  $g_{\text{sym}} = 6$  for our simulations where we use the triangular grid covering 1/6 of vicinity of  $K$  point. The normalization constant in Eqs. (B.10)-(B.11) is chosen so that  $n(\mu)$  and  $\nu(\mu)$  have physical units  $\text{m}^{-2}$  and  $\text{m}^{-2} \text{eV}^{-1}$  respectively.

Simulations of DOS  $\nu(\mu)$  in the presence of magnetic field  $B = 1.25$  T are carried out in two steps. First, we determine the Landau level spectrum  $\varepsilon_n(\Delta_1)$  in each of the valleys,  $K^+$  and  $K^-$ , as a function of displacement field. The LL spectrum is calculated via exact diagonalization of the Hamiltonian (B.5) with operators  $\pi$ ,  $\pi^\dagger$  replaced by properly truncated ladder operators (see e.g. Ref. [64] for additional details).

Next, we assume that each Landau level (LL) contributes a Lorentzian-shaped DOS



centered at its energy. The total DOS is calculated as a sum of DOS from all LLs:

$$\nu(\mu) = \sum_n \nu_n(\mu), \quad (\text{B.12})$$

$$\nu_n(\mu) = 2 \frac{eB}{2\pi\hbar c} \frac{\Gamma}{[\mu - \varepsilon_n(\Delta_1)]^2 + \Gamma^2}, \quad (\text{B.13})$$

where factor  $eB/(2\pi\hbar c)$  accounts for the LL degeneracy and  $\Gamma$  is the LL broadening. Due to the small value of Zeeman splitting, we do not incorporate it in our calculation and treat all LLs as spin-degenerate. In order to account for this degeneracy, we include additional factor of 2 in Eq. (B.13). Density  $n(\mu)$  and density of states  $\nu(\mu)$  are then calculated by summing individual contributions from all filled LLs for a grid in space of parameters  $(\Delta_1, \mu)$ . We used value of  $\Gamma = 0.1$  meV for our simulations.

## B.2 Refinement of tight-binding parameters

The determination of tight-binding parameters for ABA trilayer graphene was performed by a number of earlier works [64, 71, 75, 77, 81, 179, 180]. The resulting sets of tight-binding parameters are summarized in the Table B.1. This table shows that despite overall consensus, values of some parameters differ quite significantly between different references.

We use our zero field data and LL data to refine the existing parameter sets. We perform refinement of tight-binding parameters starting with values established in Ref. [64]. The tight-binding parameters are divided in two classes:

- (i) Parameters  $\gamma_0, \gamma_3, \gamma_4$  and  $\Delta_2$  which influence  $\nu(\mu)$  (measured via penetration field capacitance) at zero magnetic field.
- (ii) Parameters  $\gamma_2, \delta$  and  $\gamma_5$ , which determine gaps in bilayer/monolayer sectors and

thus can be constrained using Landau levels.

After determining constraints from experimental data for the Landau levels, we refine parameters in the set (i) using our simulations at zero magnetic field.

Magnetic field data imposes strict conditions on the tight-binding parameters  $\gamma_2$ ,  $\delta$  and  $\gamma_5$ . They must be chosen to satisfy the requirements that prominent LLs have the correct positions corresponding to experimental data. Figure B.1 illustrates the positions of special LLs which are used to deduce the constraints on the tight-binding parameters. The LLs in Fig. B.1 are labeled as  $S_n^\pm$  or  $B_n^\pm$  for  $n = 0, 1$  and for  $n \geq 2$  on the electron side, where letter specifies if the given LL belongs to SLG (S) or BLG (B) sector when the displacement field is vanishing,  $\Delta_1 = 0$ . We use bar above LL indices to distinguish the LL on the hole-doped side. For example  $B3^+$  ( $\bar{B}3^+$ ) stands for the LL with  $n = 3$  from bilayer sector on the electron (hole) doped side in  $K^+$  valley. From comparing LL fan diagram to experimental data in Fig. B.1 we obtain the following requirements:

- (i) At  $\Delta_1 = 0$ , there should be 9 (spin-degenerate) LLs between neutrality point (NP) and  $S0^+$ . Likewise, there are 5 (spin-degenerate) LLs between NP and  $\bar{B}3^-$ . In addition, LLs  $S0^\pm$  and  $B6^\pm$  are almost four-fold degenerate.
- (ii) Gap at neutrality point should vanish as a function of displacement field  $\Delta_1$ . The most natural scenario for this is the touching of new emergent Dirac points, see Ref. [64].
- (iii) LLs  $\bar{B}8^\pm$  and  $S\bar{1}^\pm$  are degenerate at  $\Delta_1 = 0$ ; in addition there are 10 (spin degenerate) BLG LLs between  $\bar{B}3^\pm$  and  $\bar{B}8^\pm$ .

In order to use condition (i) we calculate the energies of relevant LLs. From Eqs. (B.6) and (B.9) we find that the energies of  $S0^-$  and  $B0^-$  are given by  $\pm\gamma_2/2 + \Delta_2$  respectively. Thus the number of LLs between  $S0^-$  and NP, which is close to  $B0^-$ , is controlled

by parameter  $\gamma_2$ . To satisfy condition (i), this parameter should take the value  $\gamma_2 = 0.02 \pm 0.005$  eV which also results in the correct counting for  $B\bar{3}^-$ . In order to determine the associated error bars, we fix the value of all other parameters as their final values (see Table B.1), determine the range of  $\gamma_2$  where condition (1) is still satisfied. The values of  $\gamma_2$  in the range  $-0.016 \leq \gamma_2 \leq -0.025$  eV give the correct total 14 LLs between  $B\bar{3}^-$  and  $S0^-$ . Thus, we determine

$$\gamma_2 = -0.02 \pm 0.005 \text{ eV.} \quad (\text{B.14})$$

Next, we determine parameter  $\gamma_5$  from condition (ii) which implies the triplet crossing (see the main text). Increasing parameter  $\gamma_5$  shifts the this crossing to smaller values of electric fields  $\Delta_1$ . In order to satisfy condition (2), we adjust

$$\gamma_5 = 0.05 \pm 0.005 \text{ eV,} \quad (\text{B.15})$$

where error bar is estimated by comparing the position of triplet crossing relative to crossings between LL  $S0^+$  with  $B12^\pm$  and  $B11^\pm$ .

After we fix parameters  $\gamma_{2,5}$ ,  $\delta$  must be chosen to satisfy the second part of condition (i). We see from Eq. (B.6) that energies of  $S0^\pm$  LLs are  $-\gamma_5/2 + \delta + \Delta_2$  and  $\Delta_2 - \gamma_2/2$  respectively. Thus, we obtain one condition which allows us to express  $\delta$  via  $\gamma_{2,5}$ :  $-\gamma_5/2 + \delta = -\gamma_2/2$ . From here we determine

$$\delta = 0.0355 \pm 0.0045 \text{ eV,} \quad (\text{B.16})$$

where we estimated error bars from known error bars for parameters  $\gamma_{2,5}$ .

Finally, to satisfy condition (iii), we need to adjust the parameter  $\gamma_1$  by the small amount compared to its value in the literature. Decreasing  $\gamma_1$  to be  $\gamma_1 = 0.38$  eV increases

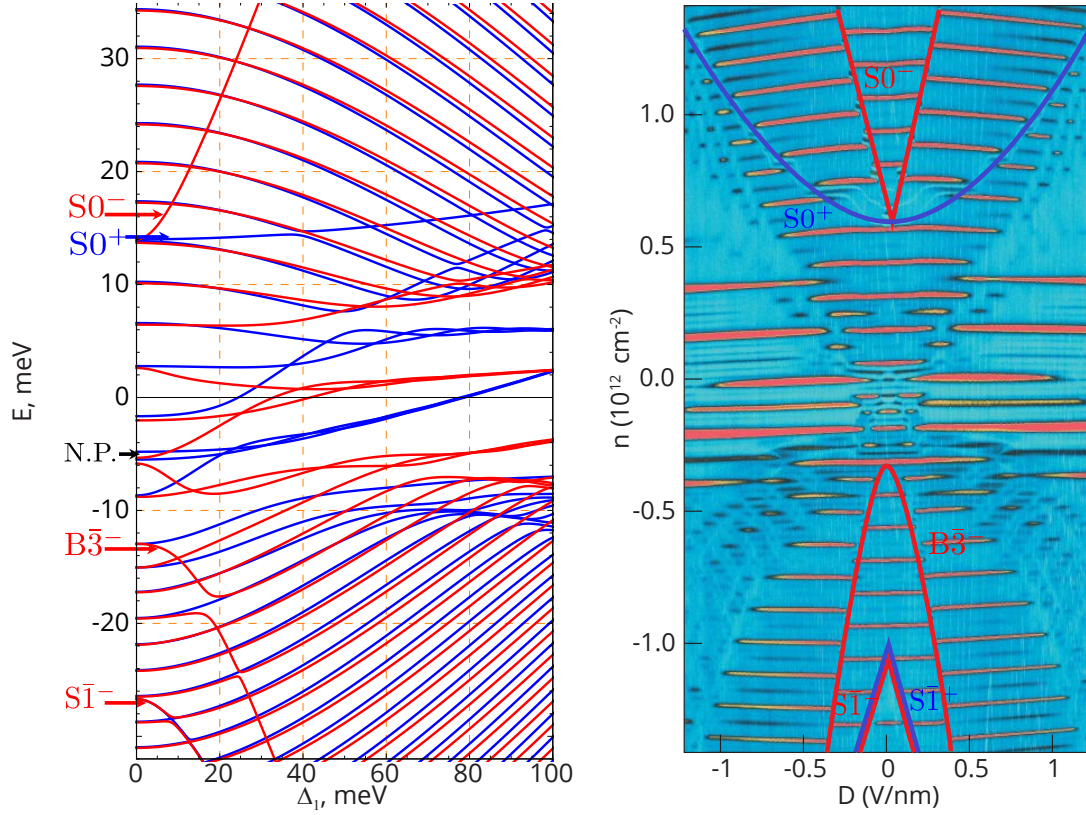


Figure B.1: (left) LL fan diagram shows energies of LLs as a function of displacement field  $\Delta_1$  at  $B = 1.25$  T. Blue (red) lines denote LLs from  $K^+$  ( $K^-$ ) valley. (right) Experimental data from the main text. The LL responsible for most prominent crossings are labeled explicitly.

the cyclotron frequency of the bilayer sector, resulting in the correct counts of LL number between  $B\bar{3}^\pm$  and  $S\bar{1}^\pm$ . By checking the range of  $\gamma_1$  which gives correct crossing pattern between  $S\bar{1}^\pm$  and  $B\bar{8}^\pm$ , and assuming LL width of 0.1 meV, we determine the error bar as

$$\gamma_1 = 0.38 \pm 0.003 \text{ eV}. \quad (\text{B.17})$$

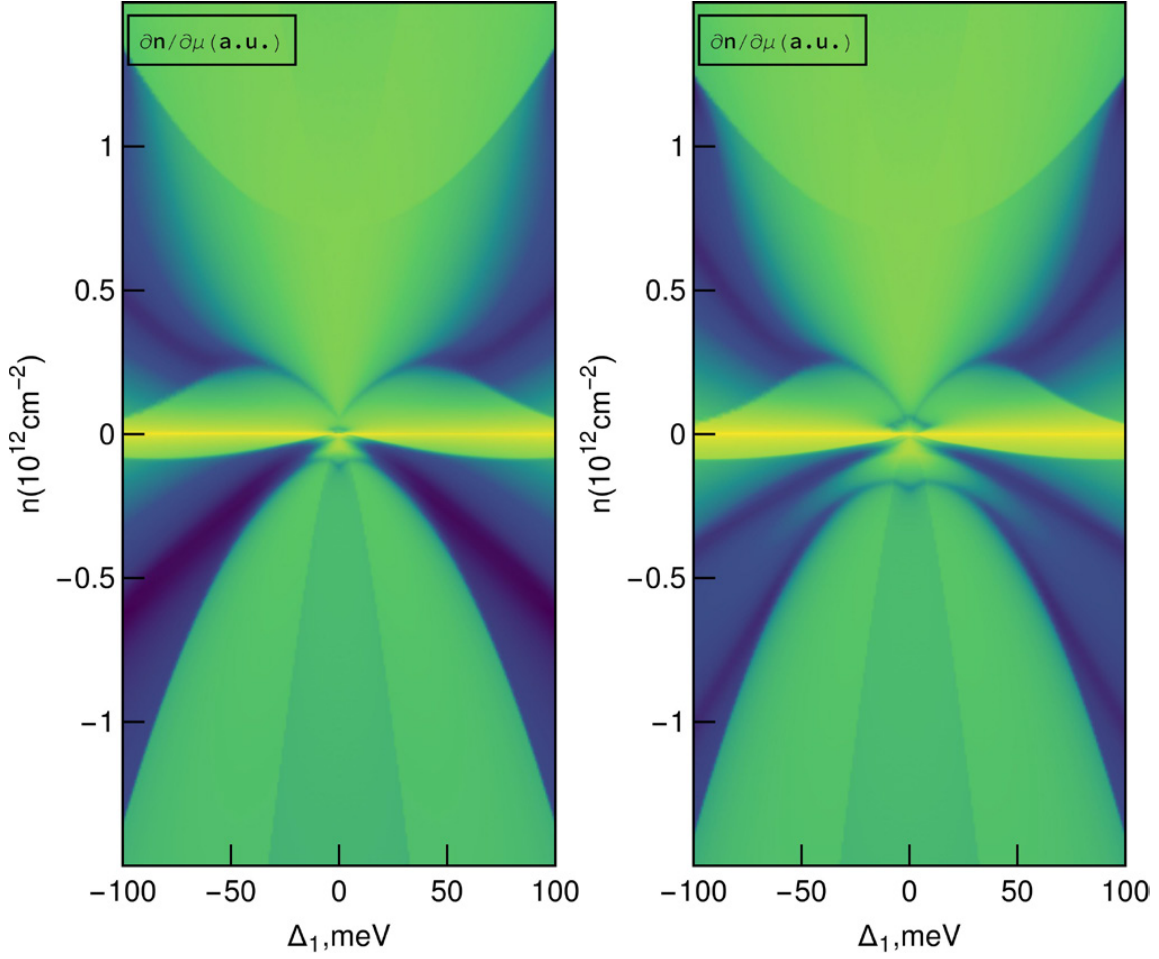


Figure B.2: Increasing  $\gamma_3$  from 0.25 eV (left) to 0.35 eV (right) increases the distance between the tip of feature (3) and the origin in the simulations, and also reduces the DOS near Lifshitz transitions at (8) and (9). Here the features are labeled in the same way as in the main text Fig. 3.6.

After determining parameters  $\gamma_2$ ,  $\gamma_5$ ,  $\delta$ , and adjusting parameter  $\gamma_1$  using LL data, we fix the remaining parameters  $\gamma_3$ ,  $\gamma_4$  and  $\Delta_2$  by matching features in the DOS at zero magnetic field. Here we label the qualitative band features with the same notation as Fig. 3.6 in the main text. We keep parameter  $\gamma_0$  fixed, given overall agreement in the literature. Let us first discuss the qualitative effect of these parameters on the band structure and resulting DOS pattern. Decreasing  $\gamma_3$  decreases the curvatures of bilayer bands at small momenta. This decreases the distance between the tip of feature (3),

which is due to BLG-like band extrema, (see the main text) and the origin, see Fig. B.2. Parameter  $\Delta_2$  shifts most of the features on the electron doped side (and also Lifshits transitions at negative fillings, given roughly by (8) and (9)) away from the NP, see Fig. B.3. Finally, Fig. B.4 illustrates the effect of changing  $\gamma_4$ . We observe that DOS is not very sensitive to  $\gamma_4$  which has the most pronounced effect on the positions of Lifshits points (8) and (9) on the hole-doped side.

The above intuition suggests that parameters  $\Delta_2$  and  $\gamma_3$  has to be respectively increased and decreased compared to their values in Ref. [64]. We determine the values of  $\Delta_2$  and  $\gamma_3$  which give the closest agreement between our simulation and experimental data to be

$$\gamma_3 = 0.29 \text{ eV}, \quad \Delta_2 = 3.5 \pm 0.2 \text{ meV}, \quad (\text{B.18})$$

where we estimated error bar for  $\Delta_2$  from the sensitivity of Landau levels plot. Due to very weak effect of  $\gamma_3$  on LL crossing pattern, we could not quantify the associated error bars. However, Fig. B.2 suggests that changing  $\gamma_3$  by 0.05 eV visibly degrades agreement of our simulations with experimental data.

Finally, Fig. B.4 shows the effect of changing  $\gamma_4$ . Increase in  $\gamma_4$  brings Lifshits transitions on the hole doped side closer to each other. This removes the dip in the DOS that would be present otherwise between Lifshits transition at small values of  $\gamma_4$ , and which is not observed in the experiment. Since the experimental data does not allow for a very precise determination of Lifshits points, it is hard to estimate the error bar on our value  $\gamma_4 = 0.141 \text{ eV}$ . At the same time, we can estimate error bar for  $\gamma_4$  using its effect on the position of the triplet crossing, in a way similar to the estimates for  $\gamma_5$ . This gives us

$$\gamma_4 = 0.141 \pm 0.04 \text{ eV}. \quad (\text{B.19})$$

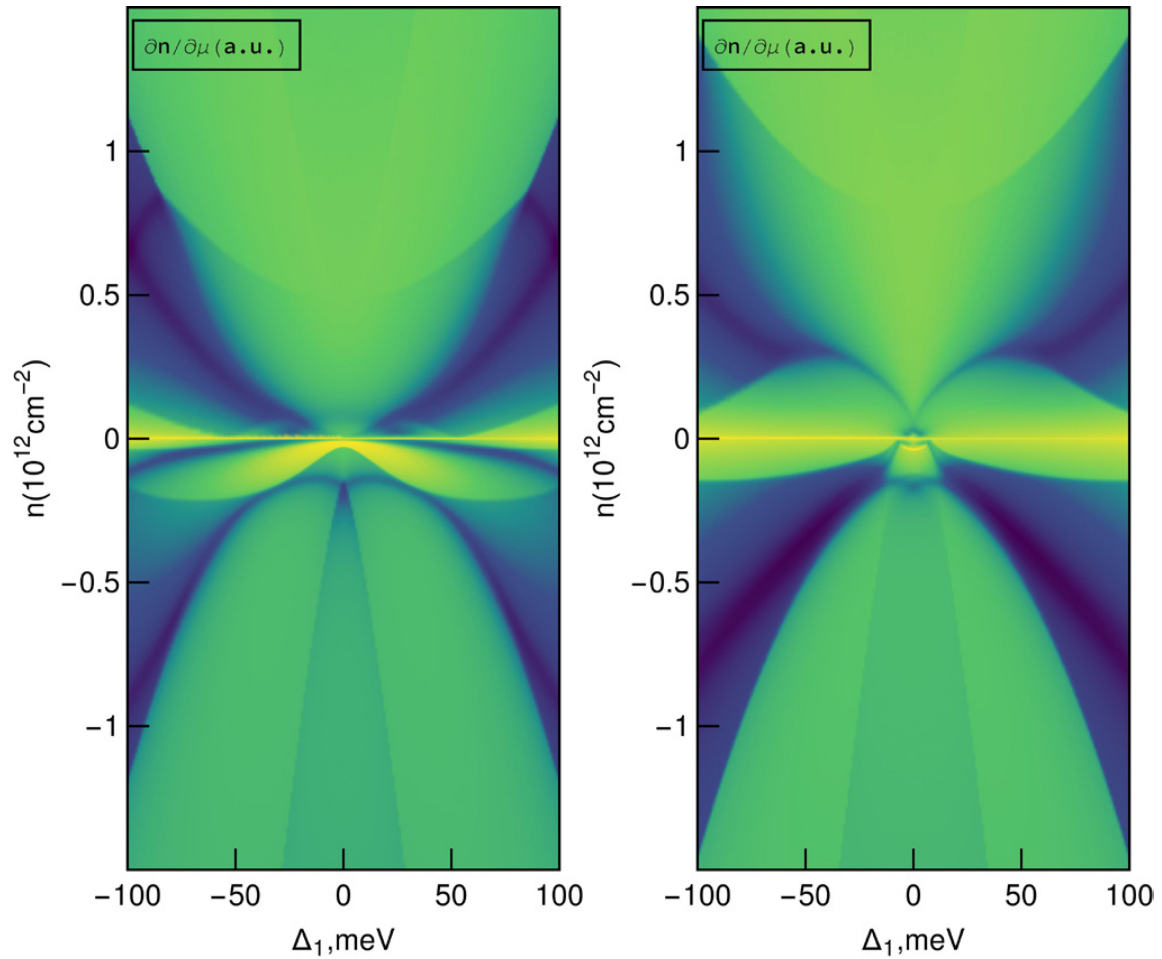


Figure B.3: Increasing  $\Delta_2$  from 0 (left) to 5 meV (right) pulls almost all features on the electron-doped side away from the neutrality point. In addition, upon increasing  $\Delta_2$  the first Lifshits transition on the hole side (8) is displaced away from the neutrality point towards more negative fillings.

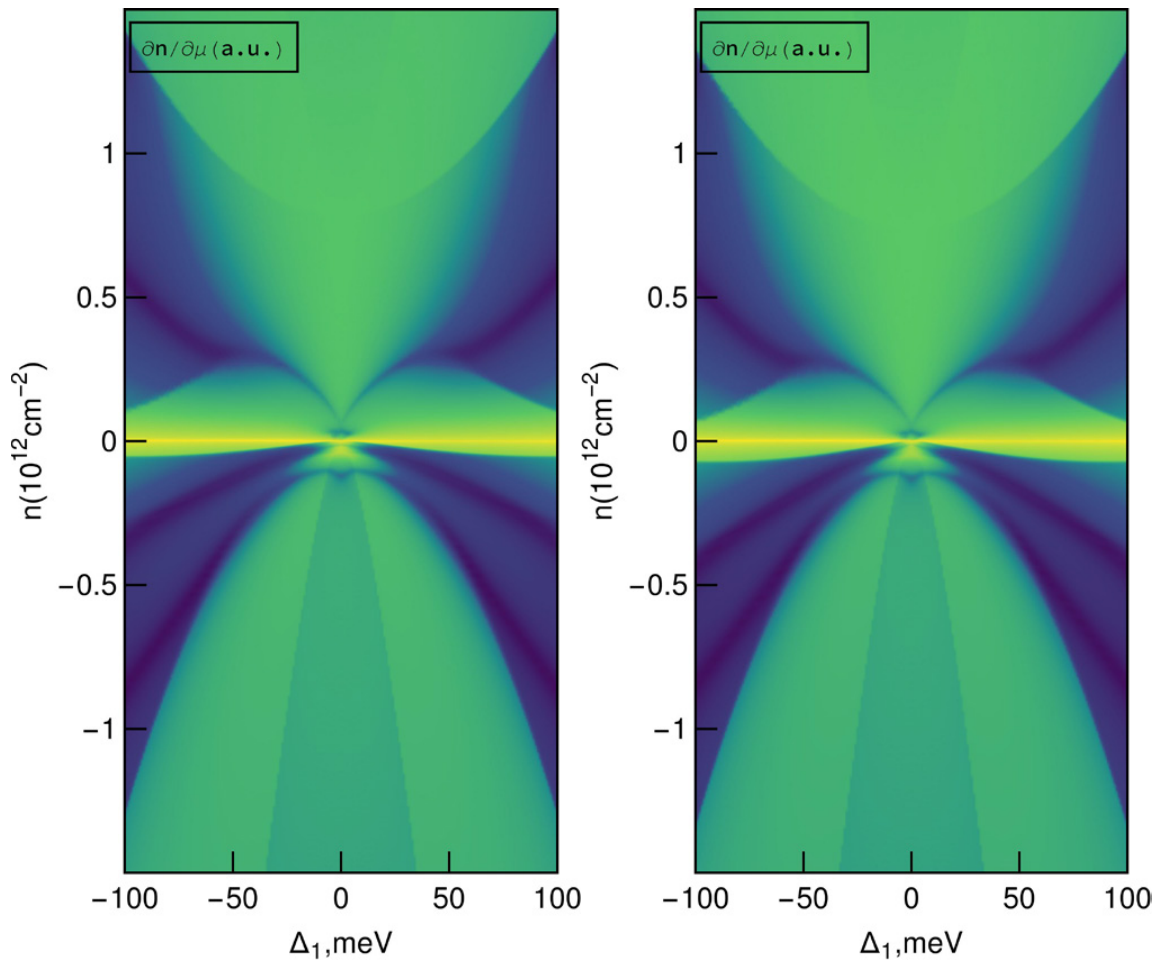


Figure B.4: Upon increasing  $\gamma_4$  from  $\gamma_4 = 0.041$  eV (left) to 0.1 eV (right) Lifshits transitions (8) and (9) move closer to each other.



Collecting together value ranges of tight-binding parameters in Eqs. (B.14)-(B.19) we arrive to the tight-binding parameter set

$$\gamma_1 = 0.380 \pm 0.003 \text{ eV}, \quad (\text{B.20a})$$

$$\gamma_2 = -0.020 \pm 0.005 \text{ eV}, \quad (\text{B.20b})$$

$$\gamma_3 = 0.29 \text{ eV}, \quad (\text{B.20c})$$

$$\gamma_4 = 0.141 \pm 0.04 \text{ eV}, \quad (\text{B.20d})$$

$$\gamma_5 = 0.050 \pm 0.005 \text{ eV}, \quad (\text{B.20e})$$

$$\delta = 0.0355 \pm 0.0045 \text{ eV}, \quad (\text{B.20f})$$

$$\Delta_2 = 3.5 \pm 0.2 \text{ meV}. \quad (\text{B.20g})$$

as the best set of parameters satisfying all constraints. listed in the last row of Table B.1. Finally, we would like to point out that despite the overall agreement in positions of all features between experiment and our simulations, we were unable to obtain the correct *magnitude* of DOS  $\nu(\mu)$  between the two LPs at negative densities. The simulation values of DOS far exceed the experimentally observed values. We attribute this disagreement to possible interaction effects which may be enhanced due to the proximity of two Lifshits points.

## B.3 Effect of interactions: Hartree Fock approximation

### B.3.1 Symmetry broken states in emergent triplets

In this Section we describe the Hartree-Fock (HF) approximation for completely filled Landau Levels (LL) originally proposed in Ref. [181]. The essence of the method is a variational optimization of the energy over a trial set of wave functions (Slater determinants). In this work we largely follow approach of Ref. [182]. We aim to capture the interactions-induced splitting of emergent (nearly) three-fold degenerate Landau levels formed at large  $\Delta_1$ . In what follows we refer to such states as “triplets”, where three-fold degeneracy originates from the set of three Dirac cones related to each other via  $C_3$  rotation symmetry, see Fig. 3.9 in the main text. Hence, we restrict our set of variational states to an arbitrary superpositions of single-particle triplet wave functions.

More specifically, we start with the set of six Landau level wave functions denoted as  $\psi_{\text{tri}}^{(ms)}$ ,  $m = 1, 2, 3$ . Index  $s$  labels spin projection onto  $z$ -axis, so that  $\psi_{\text{tri}}^{(m\uparrow)} = \psi_{\text{tri}}^{(m)} \otimes |\uparrow\rangle$  and  $\psi_{\text{tri}}^{(m,\downarrow)} = \psi_{\text{tri}}^{(m)} \otimes |\downarrow\rangle$ , with the wave function  $\psi_{\text{tri}}^{(m)}$  obtained from exact diagonalization of Hamiltonian (B.5). Three states  $\psi_{\text{tri}}^{(m)}$  with  $m = 1, 2, 3$  can be distinguished by their transformation under  $C_3$  rotations which can be intuitively seen as a proxy of “angular momentum”. Due to presence of discrete rotational symmetry, this “angular momentum” is defined moduloe 3 and takes values 0, 1, and 2, corresponding to phase of 0,  $2\pi/3$  and  $4\pi/3$  acquired from rotation by angle of  $2\pi/3$ .

The wave functions  $\psi_{\text{tri}}^{(m)}$  are vectors in the basis of Landau level indices and sublattices. Note, that the valley indices are omitted since all 3 Landau level forming the triplet belong to the same valley. In addition, we introduce a LL index cut-off  $\Lambda_{\text{max}} = 12$  which allows to represent triplet vector norm of about  $\sim 0.9$ , thus incorporating most of

the triplets weight.

Projecting Hamiltonian on the manifold of 6 triplet states, we get the following expression for the projected Hamiltonian:

$$\begin{aligned} \langle m, s | H | m', s' \rangle = & E_0(m) \delta_{m,m'} \delta_{s,s'} - E_{ZM} \sigma_{ss'}^z \\ & + (U_H)_{m's'}^{ms} + J_{m's'}^{ms}. \end{aligned} \quad (\text{B.21})$$

In this Hamiltonian,  $E_0(m)$  represents the diagonal spin-degenerate single-particle Hamiltonian. The second term is the Zeemann energy which retains its standard form after projection onto the triplet states. The last two terms in Eq. (B.21) originated from the interactions and account for Hartree and exchange terms respectively. These terms can be obtained from the rotation of conventional Hartree and exchange terms by the wave functions of triplet states, and they depend on the density matrix in the basis of sublattices ( $\alpha, \alpha'$ ) and Landau levels ( $n, n'$ ),  $\Delta_{\alpha n s}^{\alpha' n' s'}$ . This density matrix can be straightforwardly obtained from the density matrix in the triplet basis,  $\Delta_{m_k s_k}^{m_i s_i}$  via change of basis:

$$\Delta_{\alpha n s}^{\beta n' s'} = \sum_{m_i, m_k, s_i, s_k} \Delta_{m_k s_k}^{m_i s_i} \psi_{\alpha n s}^{(m_i s_i)} \otimes \psi_{\beta n' s'}^{(m_k s_k) \dagger}. \quad (\text{B.22})$$

Using density matrix in the basis of Landau levels,  $\Delta_{\alpha n s}^{\beta n' s'}$ , we can write standard expressions for Hartree and exchange terms, following Ref. [182]:

$$\langle \alpha n s | U_H | \beta n' s' \rangle = \frac{E_H}{2} \Delta_{\text{mid}} (2\delta_{B_2, \alpha} + 2\delta_{A_2, \alpha} - 1), \quad (\text{B.23})$$

$$\langle \alpha n s | U_{ex} | \beta n' s' \rangle = J_{n, n_1, n_2, n'}^{\alpha \beta s s'} \Delta_{\alpha n_1 s}^{\beta n_2 s'}. \quad (\text{B.24})$$

where parameter  $E_H$ ,

$$E_H = \frac{e^2 d}{2l_B^2 \kappa}, \quad (\text{B.25})$$

characterises the scale of the Hartree energy.  $\kappa$  is the effective screening constant,  $l_B = \sqrt{\hbar c/(eB)}$  is the magnetic length and  $d = 0.335$  nm measures the distance between adjacent graphene layers. Density matrix projection  $\Delta_{\text{mid}} = \sum_{n,s} (\Delta_{A_2ns}^{A_2ns} + \Delta_{B_2ns}^{B_2ns})$  corresponds to the electron density on the middle layer. The exchange integral is defined as:

$$J_{n,n_1,n_2,n'}^{\alpha\beta ss'} = \int \frac{d^2q}{(2\pi)^2} U_{\alpha\beta}(q) F_{n,n_1}(-q) F_{n_2,n'}(q) \delta_{ss'}. \quad (\text{B.26})$$

The explicit form of the form factors  $F_{nn'}(q)$  is listed in Ref. [181], and the interaction potential in the exchange integral is given by:

$$U_{\alpha\beta}(q) = \frac{2\pi e}{q\varepsilon(q)} T_{\alpha\beta} \quad (\text{B.27})$$

where  $\varepsilon(q)$  is the dielectric function.  $T_{\alpha\beta} = 1, \exp(-qd)$  or  $\exp(-2qd)$  for  $\alpha, \beta$  in the same, adjacent or different outer layers.

The projection of the exchange interaction matrix onto the triplet basis is given by:

$$J_{m_k s_k}^{m_i s_i} = \sum \psi_{\beta n' s'}^{(m_k s_k)} \langle \alpha, n, s | U_{ex} | \beta, n', s' \rangle \psi_{\alpha n s}^{(m_i s_i) \dagger}, \quad (\text{B.28})$$

where the summation is taken over repeated indices. The same procedure must be applied to the Hartree term to obtain  $(U_H)_{m_k s_k}^{m_i s_i}$ .

The self-consistent solution of HF equations is implemented as follows. For instance, fixing filling at  $N = 1$ , we start with the trial density matrix in the triplet basis,  $\Delta_{m_i s_i, m_k s_k} = (c_1, c_2, c_3) \times (c_1, c_2, c_3)^T | \uparrow \rangle \langle \uparrow |$ , where  $c_i$  are random normalized coefficients,  $\sum_{i=1}^3 |c_i|^2 = 1$ . Using this density matrix, we calculate the density matrix in LL basis and exchange integrals according to Eqs. (B.22)-(B.27). Finally, by diagonalizing projected Hamiltonian in Eq. (B.21) we calculate updated eigenstates  $|n\rangle$  and produce

a new density matrix  $\Delta_{m_k s_k}^{m_i s_i}$  by filling the lowest  $N$  of them,

$$\Delta_{m_k s_k}^{m_i s_i} = \sum_{n=1}^N |n\rangle \langle n|.$$

The above procedure is repeated until the eigenvalues converge.

We apply the above self-consistent HF procedure to the case of filling  $N = 1$  of the triplet T2 (see Fig. 3.12b in the main text). We use the constant dielectric function  $\varepsilon(q) = 6.6$  and  $\kappa = \varepsilon$ . The calculation yields the symmetry broken state as the one which has the lowest variational energy. This symmetry broken states consists of superposition of all three single-particle triplet wave functions  $\psi_{\text{tri}}^{(m)}$ . Since each of the single-particle triplet wave functions acquires a different phase under  $C_3$  rotation, such superposition of single particle wave functions breaks rotational symmetry.

Intuitively, one can easily understand why the interactions favor the symmetry broken state at  $N = 1$ . Each of the single-particle wave functions  $\psi_{\text{tri}}^{(m)}$ ,  $m = 1, 2, 3$  lives on all three Dirac points (see Fig. 3.12b in the main text). In fact, in the limit of weak magnetic field (or large separation between emergent Dirac gulleys), these single particle wave-functions become the proper combination of wave-functions localized on each of the Dirac cones  $\varphi_i$  with an additional phase factors

$$\psi_{\text{tri}}^{(1)} = \frac{1}{\sqrt{3}}(\varphi_1 + \varphi_2 + \varphi_3), \quad (\text{B.29})$$

$$\psi_{\text{tri}}^{(2)} = \frac{1}{\sqrt{3}}(\varphi_1 + e^{2\pi i/3}\varphi_2 + e^{4\pi i/3}\varphi_3), \quad (\text{B.30})$$

$$\psi_{\text{tri}}^{(3)} = \frac{1}{\sqrt{3}}(\varphi_1 + e^{4\pi i/3}\varphi_2 + e^{2\pi i/3}\varphi_3). \quad (\text{B.31})$$

The  $C_3$  rotations simply permutes  $\varphi_i$  between themselves. This results in the function  $\psi_{\text{tri}}^{(1)}$  being invariant under rotation, and remaining two states  $\psi_{\text{tri}}^{(2,3)}$  acquiring a phase factor  $e^{\pm 2\pi i/3}$ . Now, since support of wave functions  $\varphi_i$  and  $\varphi_j$  are weakly overlapping for

$i \neq j$ , exchanges favor the state where all weight of the wave function is located in one of the Dirac gulleys. In the basis of  $\psi_{\text{tri}}^{(m)}$  such state corresponds to a coherent superposition of all three single-particle wave functions and it breaks  $C_3$  rotation symmetry.

### B.3.2 Visualizing symmetry broken states

In order to visualize the form of the symmetry broken states in real space, we transform the LL wave functions into the maximally localized “wave packet”. This is done via convolving the single particle LL wave function in the Landau gauge with the Gaussian envelope function,

$$\Psi_n(x, y) = \int_{-\infty}^{\infty} C_X \exp(iXy/l_B^2) \psi_n\left(\frac{x-X}{l_B}\right) dX$$

where  $\psi_n$  is the  $n$ -th eigenstate of the Hamiltonian. In order to get the maximally localized wave packet in both directions, we choose  $C_X = (2\pi l_B^2)^{-\frac{1}{2}} \exp(-X^2/2l_B^2)$ . We calculate the integral using explicit expression for  $\psi_n$ ,

$$\psi_n(x) = \frac{1}{\pi^{\frac{1}{4}} \sqrt{2^n n!} l_B} \exp(-x^2/2) H_n(x),$$

where  $H_n(x)$  is the  $n$ -th Hermite polynomial. This gives the following wave function describing LL “wave packet” centered at the origin:

$$\Psi_n(x, y) = \frac{1}{\sqrt{n!}} \left(\frac{x-iy}{\sqrt{2}l_B}\right)^n \times \exp\left(-\frac{x^2+y^2}{4l_B^2}\right) \exp\left(i\frac{xy}{2l_B^2}\right). \quad (\text{B.32})$$

We numerically simulate the probability distribution for the triplet eigenstates  $\psi_{\text{tri}}^{(m)}$ ,  $m = 1, 2, 3$  at  $B = 1.25$  T and compare them with the momentum band structure. More

specifically, we plot probability density  $p(x, y)$  for the wave function in the basis of LL and sublattices,  $\psi^{\alpha n}$ , is calculated as

$$p(x, y) = \sum_{\alpha=1}^6 \left| \sum_{n=1}^{\Lambda_{\max}} \psi^{\alpha n} \Psi_n(x, y) \right|^2, \quad (\text{B.33})$$

where the inner sum goes over LL and outer sum sums probability density for each of the sublattices. The probability density calculated for the single-particle triplet wave functions is shown in Fig. 3.12c in the main text. Indeed, as expected we observe that maximas of  $p(x, y)$  are centered around their spatial semiclassical trajectories which coincide with the position of Dirac gullies in momentum space after  $\pi/2$  rotation.

Figure 3.12c in the main text shows  $p(x, y)$  for the self-consistent eigenstate at  $B = 1.25$  T and  $\Delta_1 = 0.08$ . From this plot it is clear that the HF state breaks  $C_3$  symmetry as it is strongly localized in a single Dirac gully.

## Supplementary figures

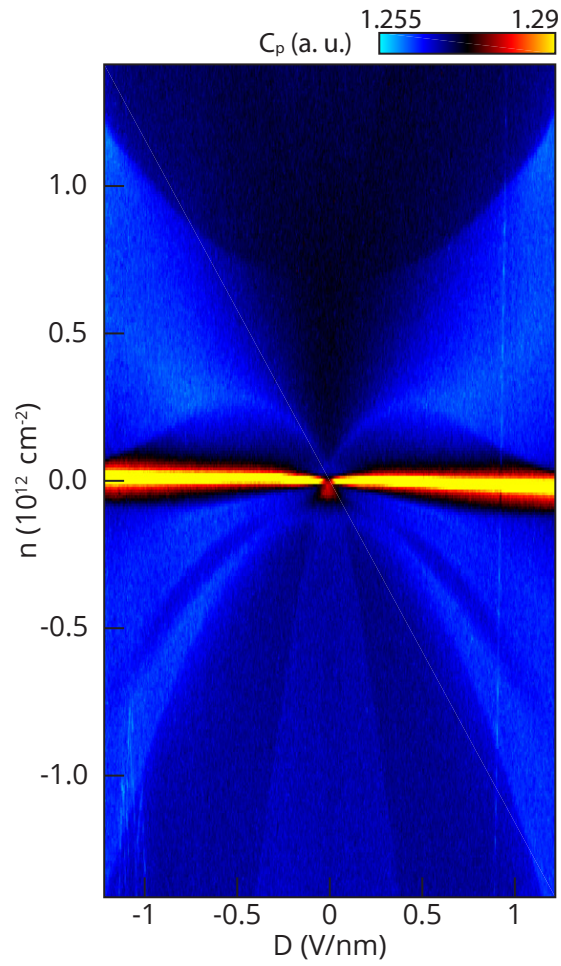


Figure B.5: Penetration field capacitance  $C_p$  at  $B = 0$  T and  $T \approx 50$  mK as a function of  $n$  and  $D$ .



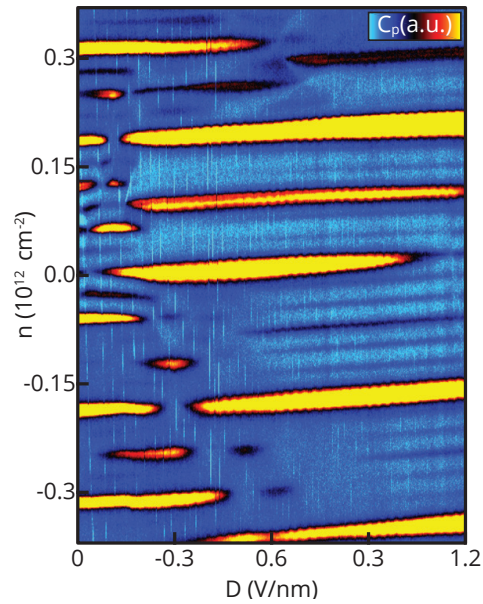


Figure B.6: Penetration field capacitance  $C_p$  at  $B = 1.25$  T inside the dashed region of Fig 3.10 of main text showing symmetry broken quantum Hall states in the 'gully' regime

# Appendix C

## Supplementary materials for Chapter 4

### C.1 Materials and Methods

We used the van der Waals dry transfer method to assemble graphite/ hBN/ MLG/ hBN/ graphite heterostructures. Graphite contact(s) were incorporated in the stack to contact the dual-gated monolayer. hBN thicknesses of 40-60 nm were used, while graphite contacts and gates were between 3 nm and 10 nm thick. In samples A-C, windows to the graphite contacts and gates were etched in a Xetch-X3 xenon difluoride etching system, a selective hBN etch, and defluorinated with a 400°C anneal in forming gas. The gates and contacts were then contacted Ti/Au (5nm/100nm) contacts. In sample D, edge contacts [48] to the graphite were made with Cr/Pd/Au (3nm/15nm/80nm). Optical images of the four measured devices are shown in Fig. C.16.

Measurements below  $B = 14$  T were performed in a top-loading Bluefors dry dilution refrigerator. Reported temperatures were measured using a ruthenium oxide thermometer attached to the cold finger. Higher magnetic field measurements were performed at the National High Magnetic Field Lab in Tallahassee in a 35 T resistive magnet and 45 T hybrid magnet, in He-3 fridges with a nominal base temperature of 0.3 K. We performed

measurements of the penetration field capacitance ( $C_P$ ) as a function of magnetic field and gate voltages to probe incompressible/insulating states. This measurement technique is outlined in Fig. C.15 and described in detail in Ref. [49] and references therein. Unless otherwise noted, measurements were performed *above* the low frequency limit (at  $f = 60\text{-}100$  kHz), i.e. there is an out of phase dissipative signal associated with many of the observed gapped states. In this frequency regime, an elevated  $C_P$  indicates a combination of incompressibility and bulk insulating behavior, both are an indication of gapped states[183]. We focus on gapped states at fixed filling factor, which, by arguments first proven by Strěda[100], have quantized Hall conductance equal to their slope in the  $n$ - $B$  plane.

In. Fig.2a, a fixed filling factor running average of 3 pixels was used to remove line noise which obscured some weaker features. In Fig.3 c-d, a fixed filling factor running average of 5 pixels was used to remove line noise.

## C.2 Supplementary Figures

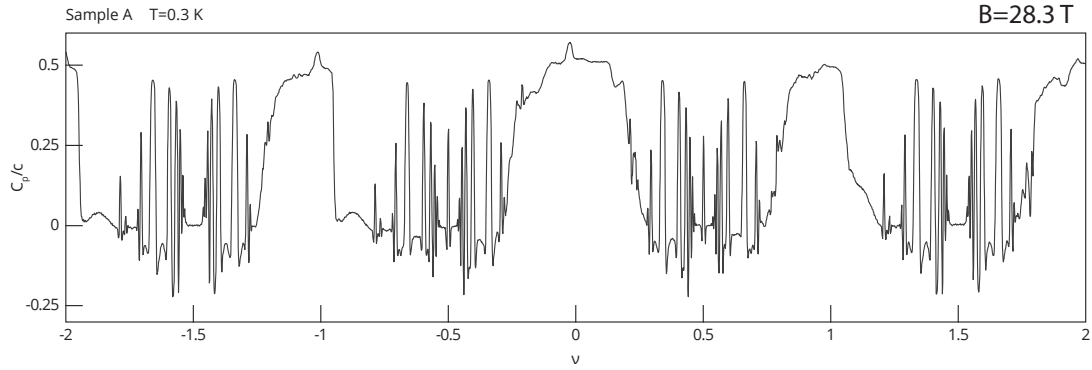


Figure C.1:  $C_P$  at  $B = 28.3 \text{ T}$  taken between the filling factors  $\nu = -2$  and  $\nu = 2$  in Sample A,  $T=0.3\text{K}$ .

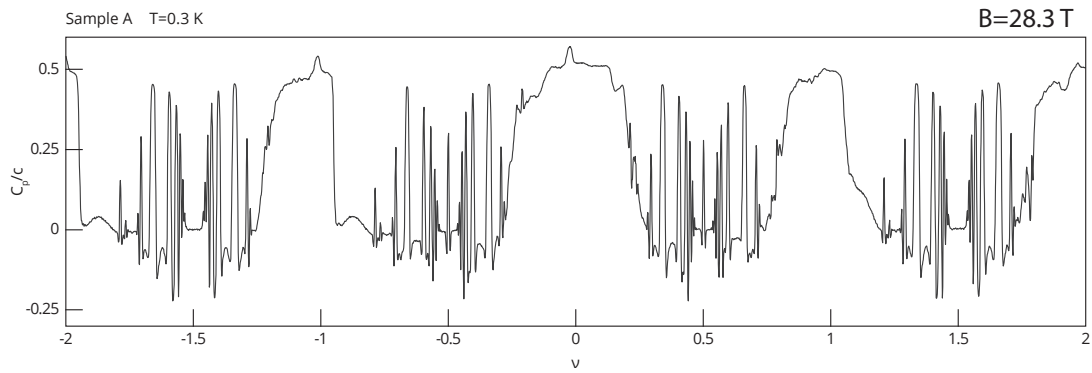


Figure C.2:  $C_P$  vs  $B$  at different LL filling factors  $C_P$  peak height as a function of magnetic field plotted for selected FQH states  $\nu \in (-1, 0)$  for sample A **a** and  $\nu \in (-1, 1)$  for sample C **b**, showing the simultaneous strengthening of the even-denominator state and weakening of the adjacent odd-denominator states.

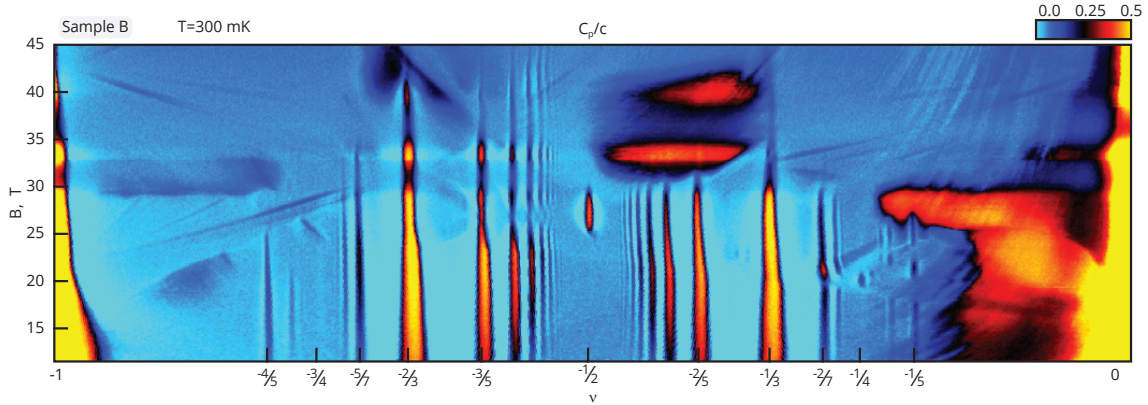


Figure C.3:  $C_P$  from  $\nu = -1$  to  $0$  in sample B.  $C_P$  vs. filling factor and field, showing the relationship between the  $\nu = -1/2$  and  $\nu = -1/4$  states and their associated phase transitions. Above 30 T, all FQH states are suppressed by the features associated with the Hofstadter butterfly, which follow linear trajectories but not constant  $\nu$ . Despite the similarity of the estimated zero-field gaps and magnetic field of  $\nu = \pm 1/2$  states, Sample A shows no sign of a moiré pattern up to  $B = 45$  T.

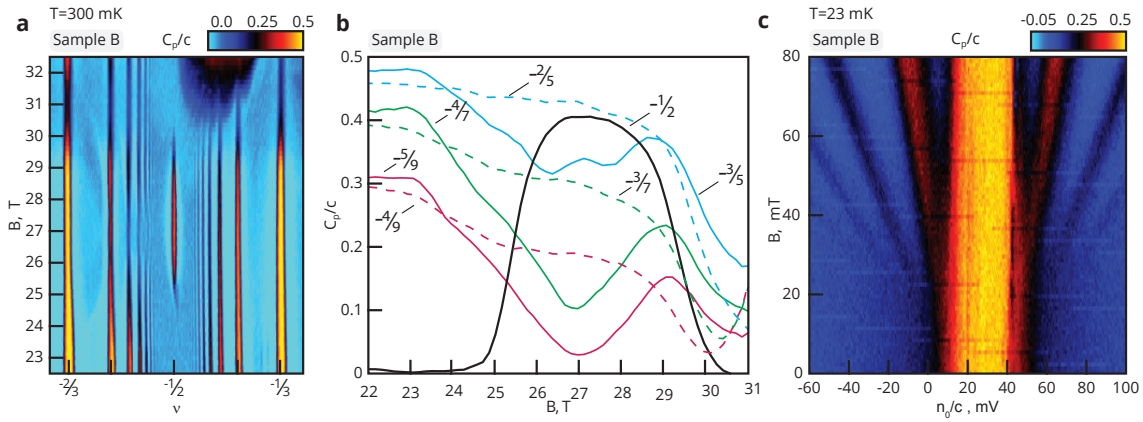


Figure C.4: **Phenomenology of the  $\nu = -1/2$  state in sample B.** (a)  $C_P$  as a function of  $B$  and  $\nu$  in the vicinity of  $\nu = -1/2$  state for Sample B, taken at  $T = 300$  K (b)  $C_p$  peak height as a function of magnetic field plotted for selected FQH states  $\nu \in (-1, 0)$  for Sample B. (c) Low field Landau fan in Sample B, showing evidence of a large zero-field gap  $\Delta_{AB}$  induced by sublattice splitting.

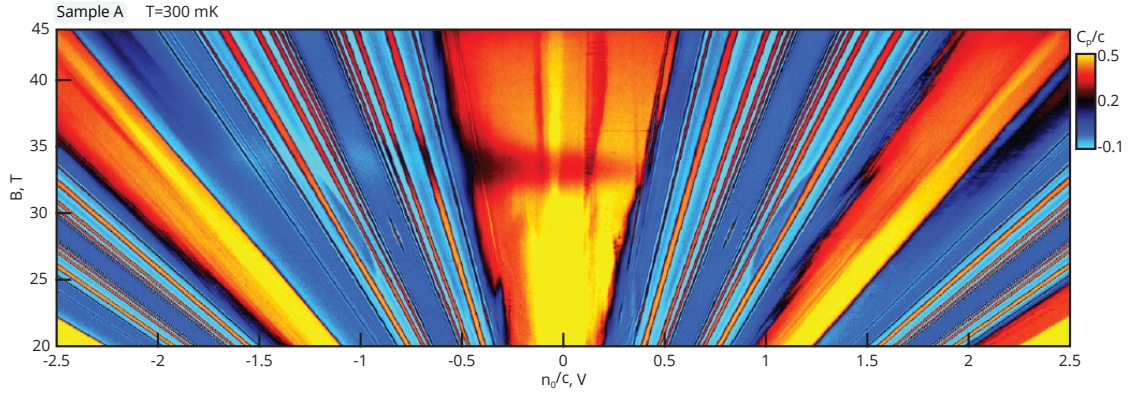


Figure C.5: **Expanded Landau Fan in sample A up to 45 T.** Penetration field capacitance ( $C_P$ ) as a function of charge carrier density ( $n_0/c$ ) and magnetic field ( $B$ ) in sample A.

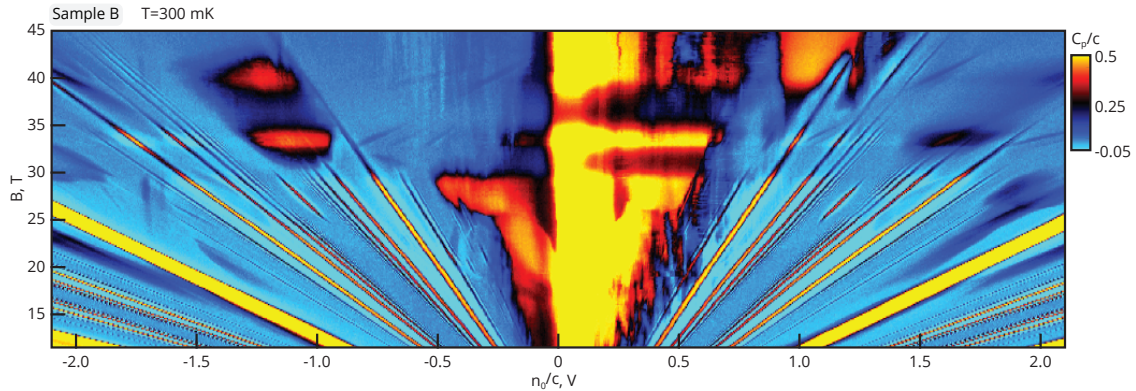


Figure C.6: **Expanded Landau Fan in sample B up to 45 T.** Penetration field capacitance ( $C_P$ ) as a function of charge carrier density ( $n_0/c$ ) and magnetic field ( $B$ ) in sample B. Despite similarities in the estimated zero field gap ( $\Delta$ ) between sample A and sample B, sample B exhibits a weakening of the fractions and Hofstadter features with a full flux quantum per unit cell at  $B = 43T$ , while sample A does not show any strong Hofstadter features.

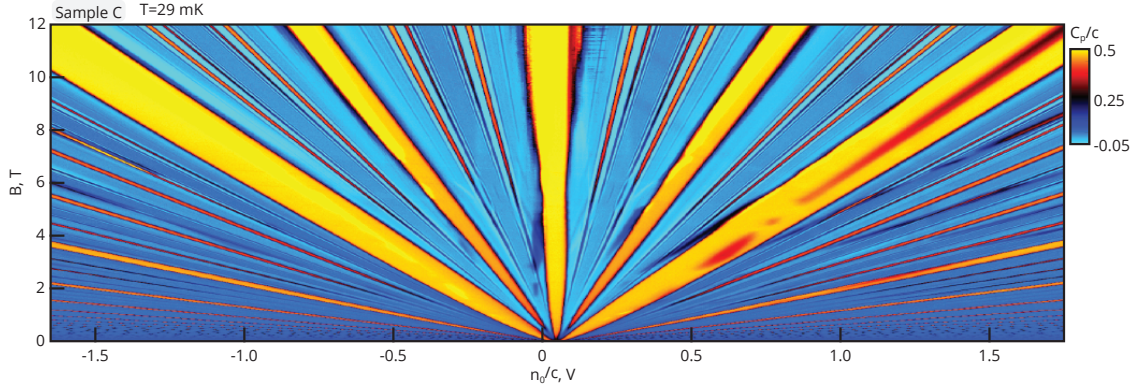


Figure C.7: **Expanded Landau Fan in sample C up to 12 T.** Penetration field capacitance ( $C_P$ ) as a function of charge carrier density ( $n_0/c$ ) and magnetic field ( $B$ ) in sample C. The four flux FQH states are not well developed by  $B = 6$  T, most likely preventing the observation of  $\nu = \pm 1/4$  states in this device.

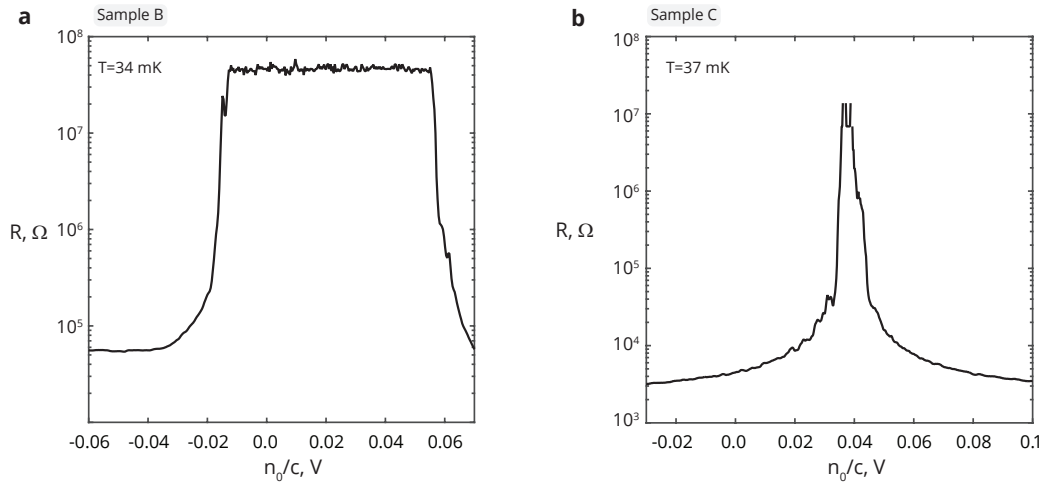


Figure C.8: **Two terminal transport in sample B and C.** Samples were voltage biased with an RMS amplitude of  $100 \mu V$  and the current was measured. (a) Two-terminal resistance as a function of  $n_0$  in sample B at  $T = 34$  mK. The high resistance regime is cut off by the input impedance of our lock-in amplifier. (b) Two-terminal resistance as a function of  $n_0$  in sample C at  $T = 37$  mK, showing a much narrower insulating regime than sample B.

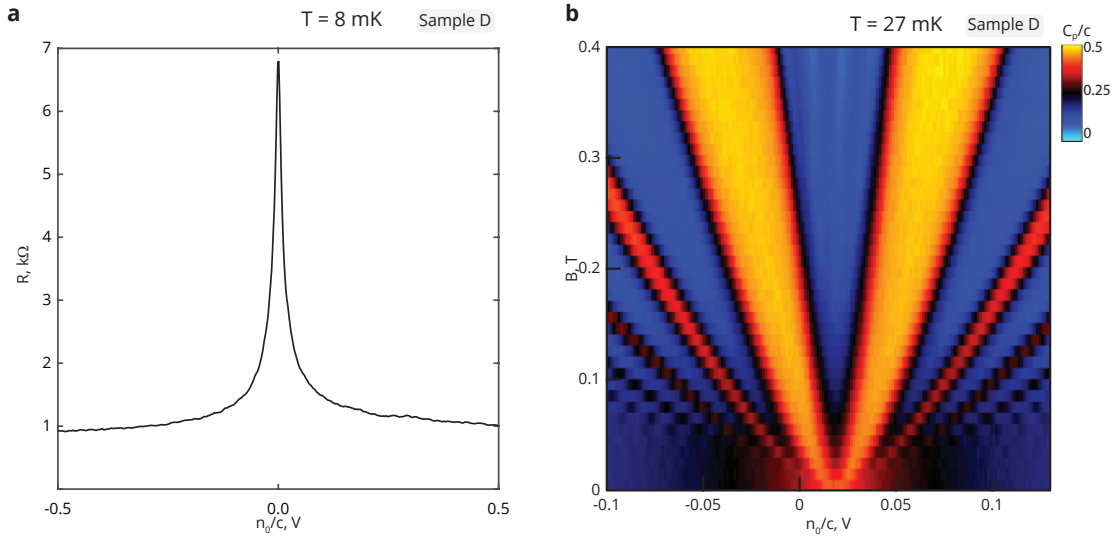


Figure C.9: **Evidence of the absence of a sublattice gap in sample D.** (a) Two terminal transport in sample D at zero applied magnetic field. The device was voltage biased at  $100 \mu V$  and the induced current was measured. (b) Low field  $C_P$  Landau fan in sample D, showing the absence of an incompressible peak at  $\nu = 0$  just above  $B = 0$ , in contrast with the behavior of gapped samples (Fig. 4a,b).

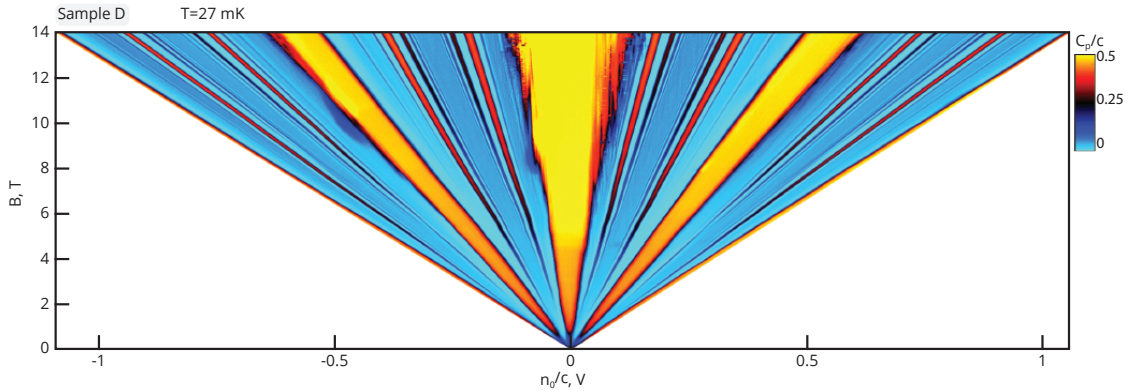


Figure C.10:  **$C_P$  Landau fan in sample D.**  $C_P$  as a function of gate voltage ( $V_G$ ) and applied magnetic field ( $B$ ). This monolayer sample shows no zero-field insulating gap, and exhibits phase transitions in FQH states in  $\nu \in [-2, -1]$  and  $\nu \in [1, 2]$  which are not observed in any of the zero-field gapped samples.  $\nu = \pm 1/2$  states are not observed up to 14 T.



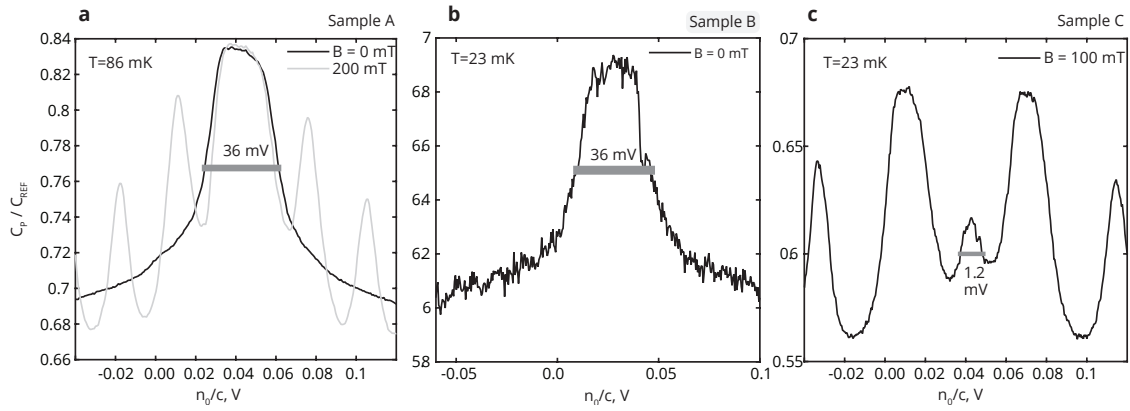


Figure C.11: **Estimation of zero-field gaps ( $\Delta$ ) from capacitance.** (a) Line cuts of  $C_P/C_{REF}$ , where  $C_{REF}$  is an external reference capacitor, as a function of  $n_0$  at  $B=0$  mT (black) and 200 mT (gray) in sample A extracted from Fig. 2e in the main text. The gap is estimated to be  $\Delta = 36$  mV by the observed width of the peak in  $C_P$ , which is mainly determined by the quantum capacitance. (b) Line cut of  $C_P$  at  $B = 100$  mT for sample B, extracted from Fig. 4a in the main text. Here, the estimation of the gap is made difficult by the presence of density of states effects at zero field and the presence of LLs at finite field. An estimate of the gap is shown in gray, and a similar scale of gap is estimated from transport (see Fig. S6). (c) Line cut at  $B=0$  mT in sample C extracted from Fig. 4b of the main text. The gap is estimated to be  $\Delta = 36$  mV, similar to sample A.

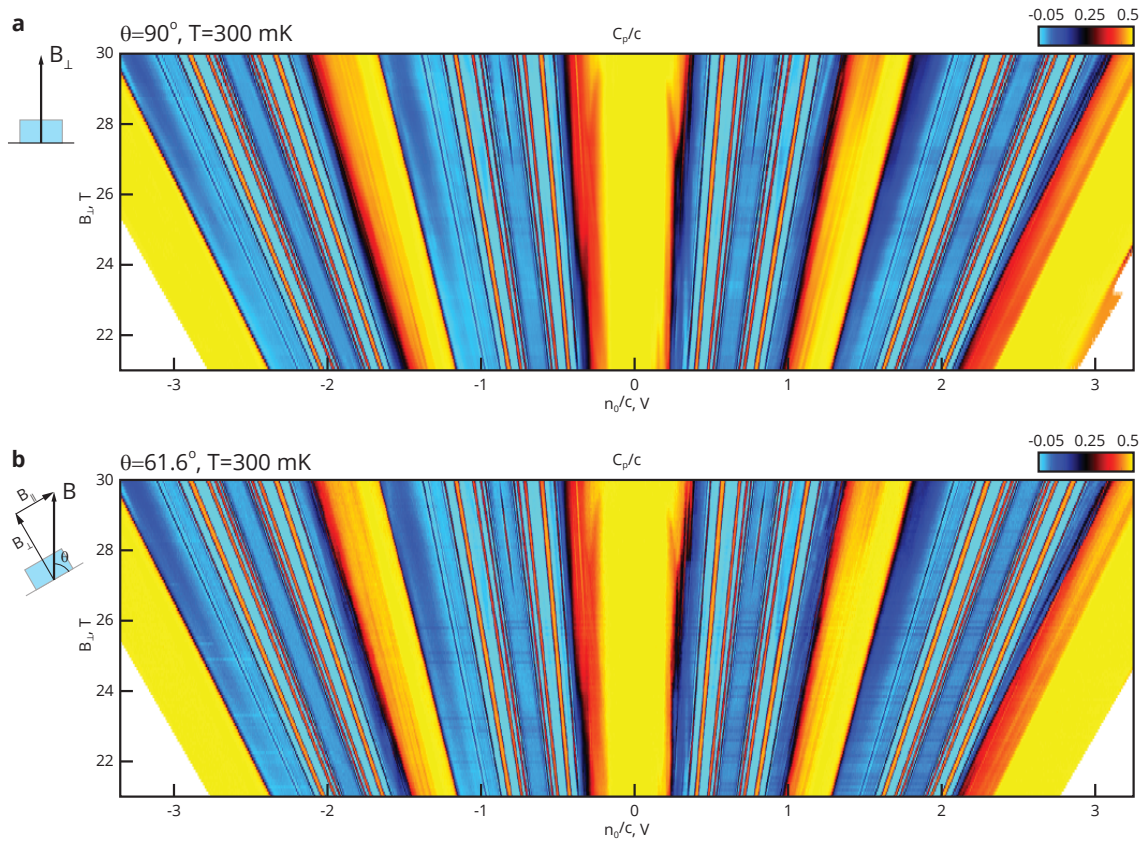


Figure C.12: **Dependence of  $\nu = \pm 1/2$  on tilted magnetic field in Sample A.**  $C_P$  as a function of density ( $n_0/c$ ) and applied perpendicular magnetic field ( $B$ ) with (a) the sample fully perpendicular to the field ( $\theta = 90^\circ$ ) and (b) tilted to  $\theta = 61.6^\circ$ . The  $\nu = \pm 1/2$  FQH states do not change with an applied in-plane magnetic field.

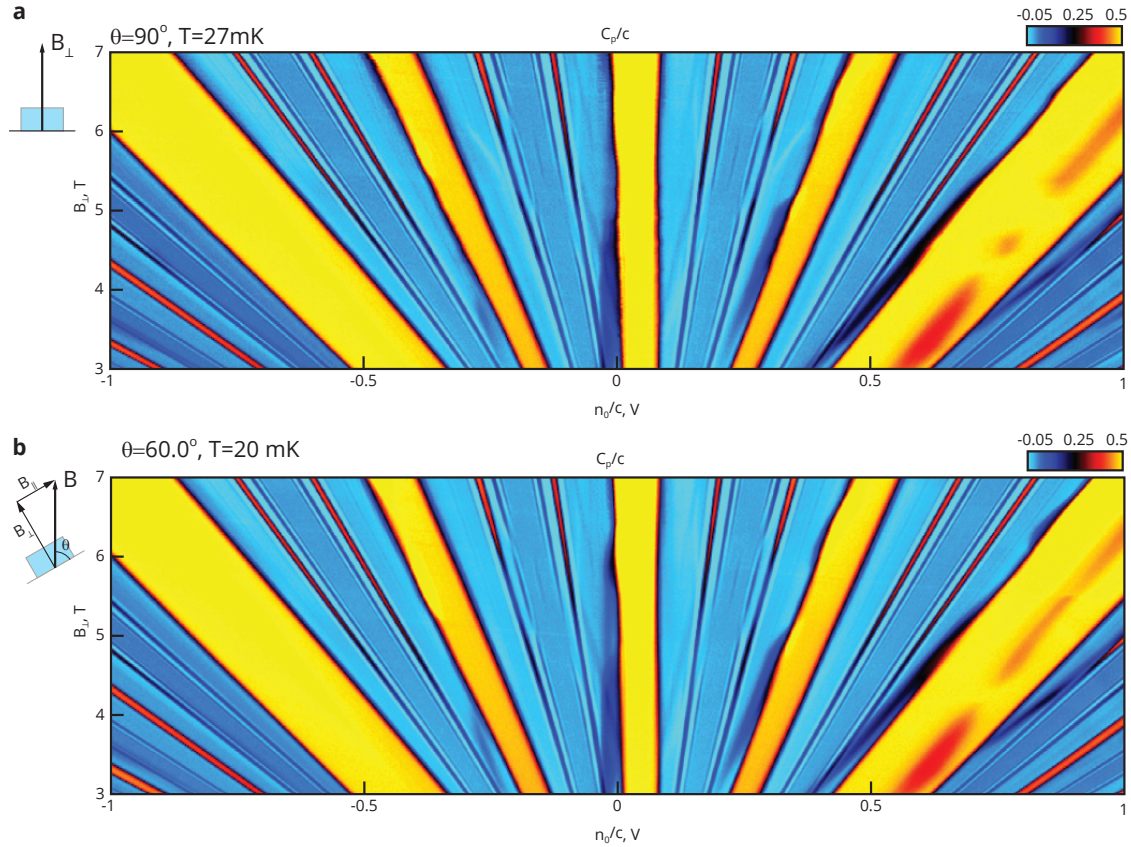


Figure C.13: **Dependence of  $\nu = \pm 1/2$  and FQH transitions on tilted magnetic field in Sample C.**  $C_P$  as a function of density ( $n_0/c$ ) and applied perpendicular magnetic field ( $B$ ) with (a) the sample fully perpendicular to the field ( $\theta = 90^\circ$ ) and (b) tilted to  $\theta = 60.0^\circ$ . The  $\nu = \pm 1/2$  FQH states and the transitions in odd denominator FQH states do not change with an applied in plane magnetic field, suggesting that spin polarization does not play a significant role in the phase transition associated with both phenomena.

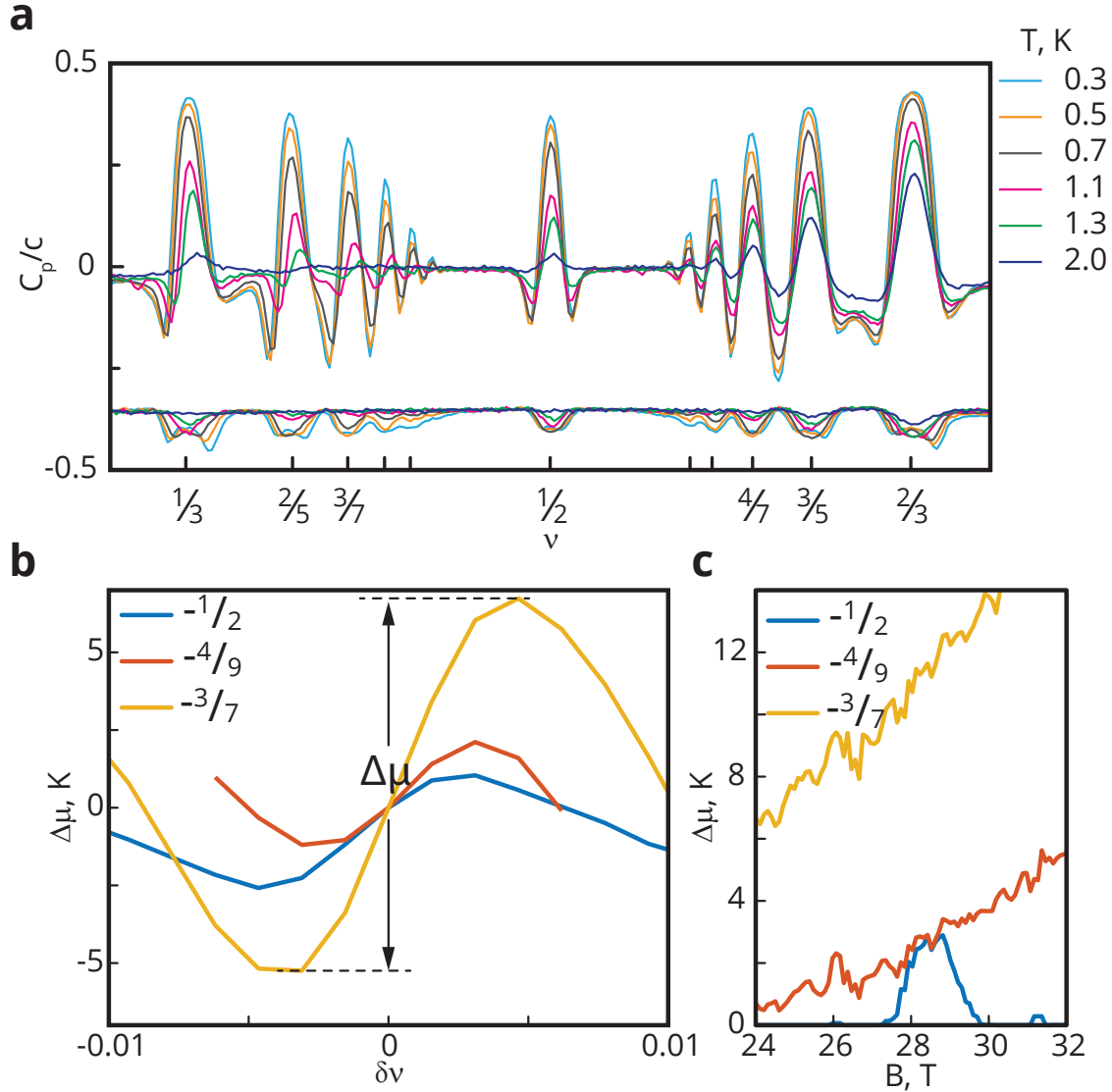


Figure C.14: **Temperature dependence and thermodynamic gap measurements in sample A.** (a) Penetration field capacitance  $C_p/c$  (upper curves) and dissipation (lower curves) at  $B = 28.3$  T,  $\nu = [1/3, 2/3]$  as a function of temperature (measured in K). The incompressible state at  $\nu = 1/2$  is still present at  $T = 2$  K. (b) Thermodynamic gap  $\Delta\mu \sim \frac{e}{k_B} \int \frac{C_p}{c} d(n_0/c)$  at  $T = 1.6$  K. The comparatively high temperature is chosen to ensure sufficient conductivity to reach the low-frequency regime[183]: as  $T \rightarrow 0$  the gapped bulk becomes exponentially insulating and the measured penetration field capacitance is no longer an accurate probe of density of states (see Methods). (c) Thermodynamic gap as a function of magnetic field for  $\nu = -1/2$ ,  $\nu = -3/7$  and  $\nu = -4/9$  at  $T=1.6$  K. At its largest  $\Delta\mu_{-1/2} = 2.8\text{K} \approx \Delta\mu_{-4/9}$ .

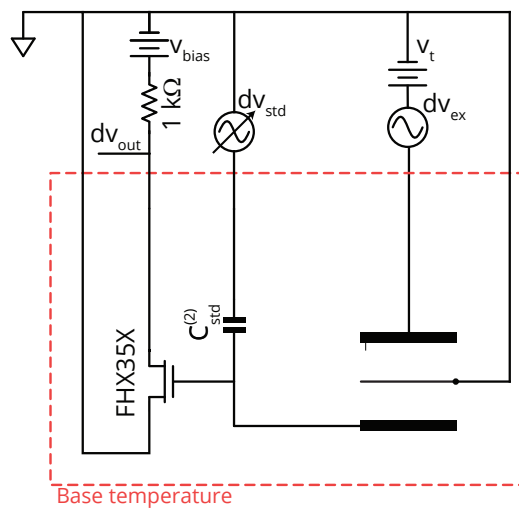


Figure C.15: **Measurement schematic.** The penetration field capacitance  $C_P$  is measured in a capacitance bridge configuration against a fixed, on-chip reference capacitor  $C_{std}$ . A fixed AC excitation is applied to the sample ( $dv_{exc}$ ) and a variable phase and amplitude ac excitation of the same frequency ( $dv_{std}$ ) is applied to the reference capacitor to balance the capacitance bridge. The voltage at the balance point is amplified by a low temperature transistor (FHX35X) which is biased with a  $1\text{ k}\Omega$  resistor. In the measurements presented here, the bridge is balanced at the beginning of a measurement at a fixed location and deviations from balance are measured as the dc voltages of the sample and/or gate are swept.

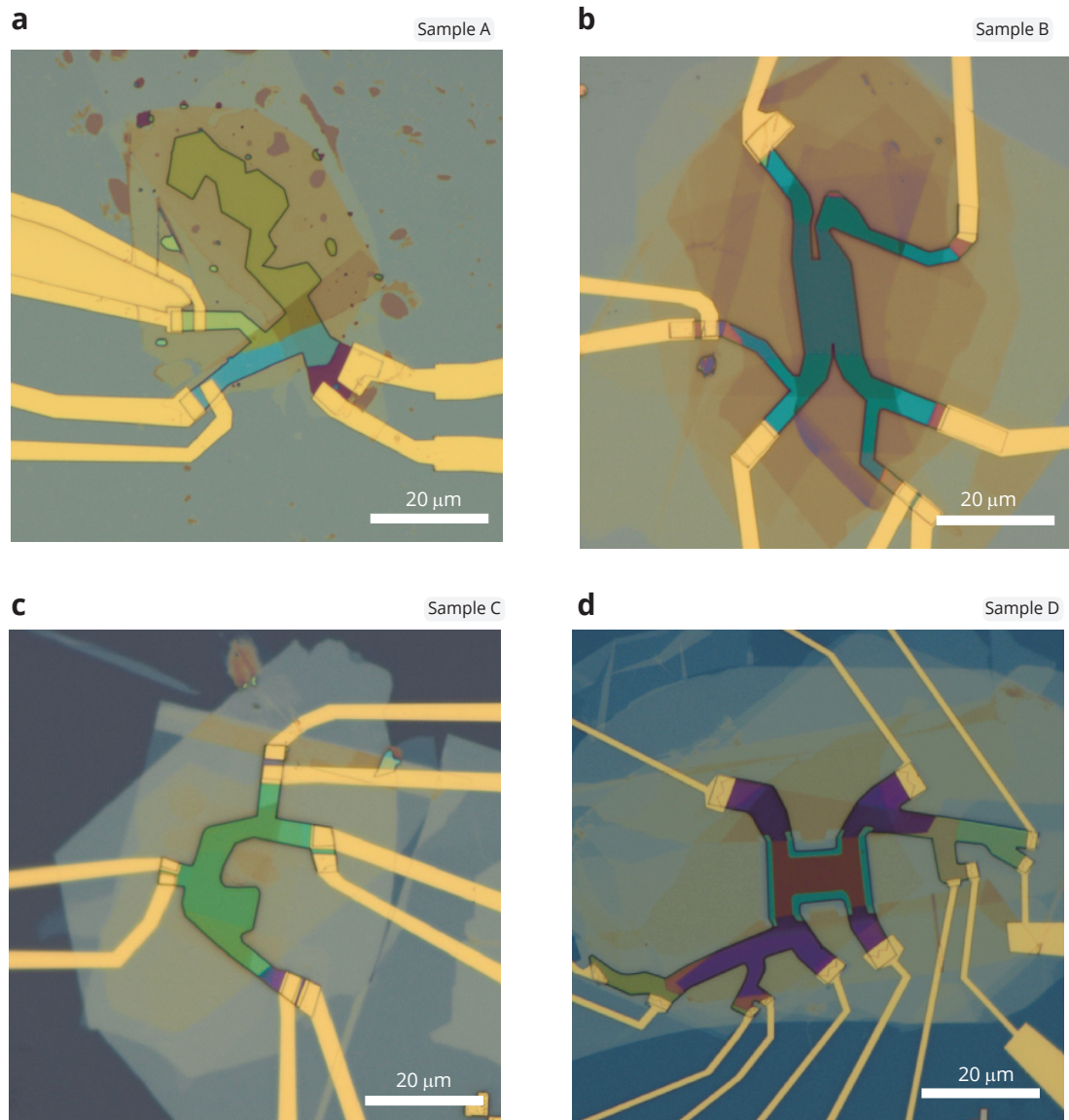


Figure C.16: **Optical images of the measured samples.** a-d. Optical images of samples A-D, respectively. Scale bar is 20  $\mu\text{m}$ .

### C.3 Calculation of $\nu = 0$ phase diagram

Here we describe the calculation of the  $\nu = 0$  phase diagram, based on the model outlined in [90]. This model, originally intended for bilayer graphene, is in fact a generalization of a monolayer model[89] to include a valley Zeeman that neglects bilayer physics, such as the orbital degeneracy, that would make it inapplicable to monolayer. Within this model, there are four phases: a spin polarized, valley-singlet Ferromagnet (F), a valley polarized, spin-singlet lattice-scale charge density wave (CDW), a canted antiferromagnet that is partially spin polarized and valley unpolarized (CAF), and a spin-singlet partially sublattice polarized phase (PSP), in which the valley polarization lies somewhere between the z-axis and the xy-plane. In the limit of  $\Delta_{AB} = 0$ , the PSP phase becomes full sublattice unpolarized (with valley polarization lying in the plane). This phase is known as the Kekule distorted phase (KD) in the literature, and in this limit, the KD-CDW phase transition is also first order. Following the terminology of reference [90], the PSP phase is analogous to the partially layer polarized phase (PLP) while the CDW phase is analogous to the Fully Layer Polarized (FLP) phase.

The energies of the different phases, and their phase boundaries, are obtained by calculating the energy expressions for explicit forms of the isospin wavefunctions in the expressions provided in [90]. They are:

phase	energy	condition
F	$-2\varepsilon_Z - 2u_{\perp} - u_z$	
CDW	$u_z - 2\Delta_{AB}$	
CAF	$-u_z - \frac{\varepsilon_Z^2}{2 u_{\perp} }$	$0 < -\frac{\varepsilon_Z}{2u_{\perp}} < 1$
PSP	$u_{\perp} - \frac{\Delta_{AB}^2}{u_z +  u_{\perp} }$	$\frac{\Delta_{AB}}{u_z +  u_{\perp} } < 1$

(C.1)

Here  $\Delta_{AB}$  is the single particle AB sublattice splitting;  $\varepsilon_Z$  is the Zeeman energy, and

$u_{z,\perp} = g_{z,\perp} \frac{a}{\ell_B} \frac{2^2}{\varepsilon \ell_B}$  are the anisotropic interaction energies as described in the main text.

The energies depend on four parameters:  $g_z$ ,  $g_\perp$ ,  $\varepsilon_Z$ , and  $\Delta_{AB}$ .  $\varepsilon_Z = g\mu_B B_T$  follows from the fact that spin-orbit coupling is exceptionally weak in graphene, so that  $g = 2$ .  $\Delta_{AB}$  we estimate from the low field behavior in each device, giving  $\sim 25$ meV for device A and  $\sim 2$  meV for device B, and  $\sim 0$ meV for device C. Phase diagrams in the  $g_\perp - g_z$  plane for different values of  $\Delta_{AB}$  are shown in Fig. C.17.

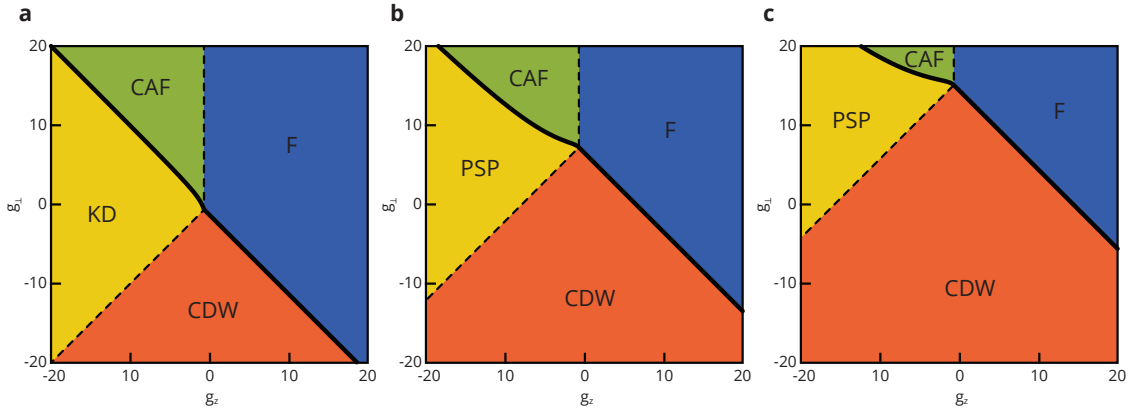


Figure C.17: **Phase diagram for different values of  $\Delta_{AB}$ .** (a) For  $\Delta_{AB} = 0$ , the phase diagram is magnetic field independent and the CDW-KD transition is first order. (b) Finite  $\Delta_{AB} = 10$  meV stabilizes the CDW phase while transforming the CDW-KD phase transition to 2nd order. (c)  $\Delta_{AB} = 20$  meV.

The interaction anisotropy parameters are more difficult to estimate, and follow from knowledge of the  $\nu = 0$  phase diagram. For example the phase transition from the CAF to the F occurs at  $u_p = -\varepsilon_Z/2$ , and can thus be tuned by varying the total- and in-plane magnetic fields independently. Notably, these are determined at high energies, and are unlikely to be affected significantly by low energy band structure effects such as the presence of a  $\Delta_{AB}$  gap, allowing us to estimate them from experiments on  $\Delta_{AB} = 0$  samples. Reference [96] reported this crossover at out-of-plane magnetic fields of  $B_\perp \approx 1T$  and total magnetic field  $B_T \approx 25T$  in single-gated graphene devices. From this



measurement, we estimate

$$u_{\perp} = \frac{\varepsilon_Z}{2} \quad (\text{C.2})$$

$$g_{\perp} \frac{a}{\ell_{B_{\perp}}} \frac{e^2}{\frac{\varepsilon_{hBN} + \varepsilon_{vac}}{2} \ell_{B_{\perp}}} = -\frac{g\mu_B B_T}{2} \quad (\text{C.3})$$

$$g_{\perp} \approx -10 \quad (\text{C.4})$$

where we use the in-plane dielectric constant of hBN,  $\varepsilon_{hBN} = 6.6$ , most relevant for screening of Coulomb interactions.

This leaves  $g_z$  as a free parameter. We assume that gapless ( $\Delta_{AB} = 0$ ), neutral graphene at high field is in the CAF state. The evidence for this is somewhat circumstantial: based solely on [96], the KD phase cannot be excluded. However, as will be evident below, if this is not the case then no phase transition to the CAF in the current experiment would be possible, inconsistent with our observation of first-order phase transitions in the FQH regime. From Eq. C.1, we can derive the following constraints:

$$\mathcal{E}_{CAF} < \mathcal{E}_F \quad \mathcal{E}_{CAF} < \mathcal{E}_{KD} \quad (\text{C.5})$$

$$-u_z - \frac{\varepsilon_Z^2}{2|u_{\perp}|} < -2\varepsilon_Z - 2u_{\perp} - u_z \quad -u_z - \frac{\varepsilon_Z^2}{2|u_{\perp}|} < u_{\perp} \quad (\text{C.6})$$

$$u_{\perp} < -\frac{1 + \sqrt{2}}{2}\varepsilon_Z \quad u_z > \frac{\varepsilon_Z^2 - 2u_{\perp}^2}{2u_{\perp}} \quad (\text{C.7})$$

$$g_{\perp} \lesssim -1.7 \quad g_z \gtrsim -g_{\perp} + \frac{.93}{g_{\perp}} \quad (\text{C.8})$$

As described in the main text, with the exception of  $\Delta_{AB}$ , all the anisotropy energies are linear in  $B$ . Thus the low  $B$  limit is equivalent to very large  $\Delta_{AB}$ , where we expect the CDW ground state to prevail. Conversely, the high  $B$  limit in our device is equivalent to the low  $\Delta_{AB}$  limit in [90]. Figure C.18 shows the phase diagram for different values of  $g_z$ . For choices of  $g_z$  such that the ‘natural’ state is indeed the CAF, this state will

obtain at the highest magnetic field, with the magnetic field required tuned by  $g_z$  as well as  $\Delta_{AB}$ .

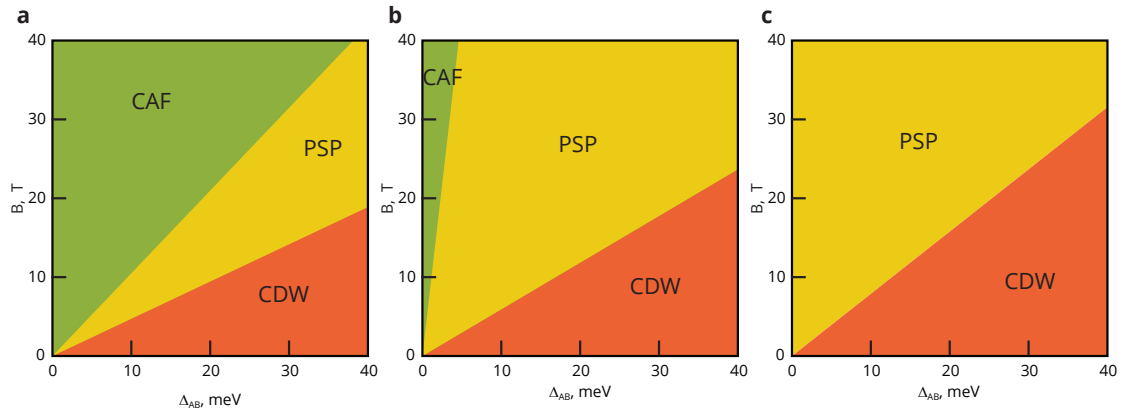


Figure C.18: **Phase diagram in the  $B$ - $\Delta_{AB}$  plane.** Theoretically calculated phase diagram for (a)  $g_z=15$ , (b)  $g_z=10$ , and (c)  $g_z=5$ .

# Appendix D

## Supplementary materials for Chapter 5

### D.1 Device fabrication

Devices were assembled using a dry transfer method based on van der Waals adhesion [48], with top and bottom gates as well as the electrical contacts to the hBN-encapsulated Bernal stacked BLG device made from  $\sim 10$  nm-thick graphite flakes. As shown in Figs. S1-S4, this leads to a significant improvement in sample quality as compared to samples with evaporated metal gates. Care was taken in order to match the top and bottom hBN thicknesses, which were approximately 40-50 nm for all three devices. The resulting mismatch in geometric capacitance was determined to be  $\delta \equiv (c_t - c_b)/(c_t + c_b) = 0.018$  for Device A, and was  $< .05$  for all devices. Despite efforts to rotationally misalign the hBN crystals proximate to the graphene bilayer, the effects of an intermediate wavelength moire pattern[97, 146, 147] are visible on one of the layers at high density in device A (Fig. D.12). The resulting staggered sublattice potential is responsible for the asymmetry upon inversion of  $p_0$  in some of the transitions visible in Fig. 1 of the main text. While no secondary fans were observed in devices B and C, similar offsets (albeit of differing magnitudes and signs) were observed in these devices as well, indicating that coupling

to one or more of the hBN layers remains relevant (See Figs. D.13, D.14, and D.15). Devices A and C were patterned by using a dry ICP etch in a mixture of  $\text{CHF}_3 + \text{O}_2$ , and the graphite contacts were themselves contacted along the edge with a Cr/Pd/Au metal stack. Device B was first exposed to a  $\text{XeF}_2$  atmosphere to remove a sacrificial top hBN layer used for stack assembly, annealed at  $400^\circ\text{C}$  in forming gas, and the graphite contacts and gates were area contacted with a Ti/Au metal stack.

## D.2 Capacitance circuit

To measure the small capacitances of our device with high sensitivity, we utilize a cryogenic impedance transformer based on an FHX35X high electron mobility transistor [184] in a bridge configuration. This measurement works by effectively disconnecting the sample capacitance from the large capacitance of the cryostat cabling: the BLG device is connected only to the gate of the HEMT (with input capacitance of a few hundred fF) and a large resistor ( $100\text{ M}\Omega$ ), with additional  $\sim 1\text{pF}$  of stray capacitance. While the HEMT is operated at or below unity voltage gain to minimize power dissipation, it effectively transforms the picofarad sample impedance into a  $1\text{k}\Omega$  output impedance. At  $50\text{ kHz}$ , and assuming cryostat cable capacitances of  $\approx 1\text{nF}$ , this translates to a power gain of approximated 1000.

As described in detail in references [185] and [57], measurements of three distinct capacitances—the top gate, bottom gate, and penetration field capacitance—provide a complete reconstruction of both the charge and layer polarization in the bilayer as a function of applied voltages. For devices in which top and bottom gate geometric capacitances are symmetric ( $\delta \equiv \frac{c_t - c_b}{c_t + c_b} \rightarrow 0$ , see supplementary information of [57] for a detailed derivation), one accesses the derivatives of the total density ( $n$ ) and layer polarization ( $p$ ) with respect to the applied voltages  $n_0$  and  $p_0$  through the relations

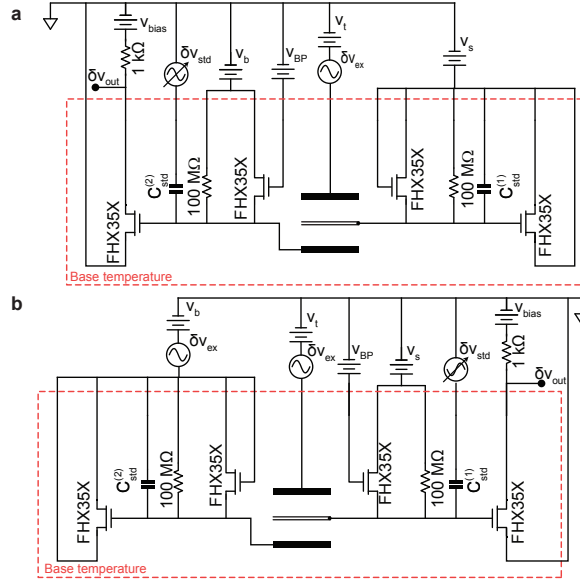


Figure D.1: **Simplified measurement schematics.** (a) Measurement of penetration field capacitance,  $C_P$ . (b) Measurement of symmetric capacitance,  $C_S$ . Here DC voltages are denoted  $v_i$  while AC voltages are denoted  $\delta v_i$ .  $v_{BP} \approx -0.5$  V pinches off the multiplexing transistor (on bottom gate or sample, respectively for the two measurement schemes), tuning the input impedance of the measurement transistor on that terminal.  $\delta v_{ex}$  is the AC excitation applied across the relevant capacitor to be measured, and  $\delta v_{std}$  is chosen to balance the bridge such that  $\delta v_{out} = 0$ .  $v_t$ ,  $v_s$ , and  $v_b$  in combination control  $p_0$  and  $n_0$ , with one of the three fixed to control the working point of the measurement transistor.  $n_0$  and  $p_0$  are swept and  $\delta v_{out}$  is monitored to extract the capacitance. In all measurements, the measurement transistor bias  $v_{bias} \approx 20$  mV was limited to prevent excessive heating of the sample.

$$\frac{\partial n}{\partial n_0} \approx \frac{C_S}{2c} \quad (\text{D.1})$$

$$\frac{\partial n}{\partial p_0} \approx -\frac{C_A}{2c} \quad (\text{D.2})$$

$$\frac{\partial p}{\partial p_0} \approx \frac{c_0}{c} \frac{4C_P + C_S - 2c}{c} \quad (\text{D.3})$$

$$\frac{\partial p}{\partial n_0} \approx -\frac{c_0}{c} \frac{C_A}{c}, \quad (\text{D.4})$$

where  $c = (c_t + c_b)/2$  is the average of the top and bottom gate geometric capaci-

tances,  $c_0 \gg c$  is the interlayer capacitance of the bilayer itself, and  $C_{S(A)} = C_T \pm C_B$  are the symmetric and antisymmetric measured gate capacitances per unit area. The approximation is well justified as  $\delta = .018$  for Device A and is similarly small for the other devices.

In order to measure all three quantities without warming up the sample, low-impedance access to all three terminals of the device must be possible in situ, in apparent conflict with the desire to maintain the amplifier input at high impedance. This problem is solved using a cryogenic multiplexer constructed out of two additional HEMTs, which allows either the bottom gate or the bilayer graphene flake to be brought to a high impedance. Figure D.1a shows a simplified electrical schematic for measuring  $C_P \equiv \partial n_T / \partial v_b$ , where  $n_T$  is the charge on the top gate while  $v_b$  is the bottom gate voltage.  $v_b \approx -.3V$  is fixed to set the transistor operating point,  $v_{bias} \approx 25mV$  is chosen so that no heating of the probe is observed (see the next subsection on likely electron temperature). Additional DC voltages on the top gate ( $v_t$ ) and applied to the ohmic contacts of the graphene ( $v_s$ ) are varied to control  $n_0$  and  $p_0$ , defined as

$$n_0 = c_t(v_t - v_s) + c_b(v_b - v_s) \approx c(v_t + v_b - 2v_s) \quad (D.5)$$

$$p_0 = c_t(v_t - v_s) - c_b(v_b - v_s) \approx c(v_t - v_b). \quad (D.6)$$

To measure the differential capacitance, a fixed AC excitation is applied to top gate ( $\delta v_{ex}$ ). A second AC excitation at the same frequency is applied to a standard capacitor  $\delta v_{std}$ , with phase and amplitude chosen to balance the bridge ( $\delta v_{out} = 0$ ). Crucially, for the  $C_P$  measurement the ‘bypass’ HEMT attached to the bottom gate is driven deep into depletion ( $v_{BP} \approx v_b - .6V$ ), maintaining the high impedance of the measurement transistor input. A final DC voltage is applied to all pins of the second amplifier ( $v_s$ ). Because the FHX35X is depletion mode, in this configuration it shorts out the 100

M $\Omega$  resistor, providing a low impedance connection to the sample. To measure  $C_S$ , the situation is reversed (Figure D.1b), with the transistor amplifier on the sample now active and the bypass transistor on the bottom gate short circuited, providing a low impedance path for the bottom gate voltage excitation. Although not focus of the current work,  $C_A$  can also be measured by applying opposite phase excitation signals to the top and bottom gate[57]. The frequency and excitation voltages for data shown in all figures are shown in Table S3.

All measurements below 14T were performed in a dry dilution refrigerator with a base temperature of  $\approx 10$  mK. However, the sample temperature was likely higher due to heating from the cryogenic amplifiers, which were directly connected to the sample and only a few millimeters away. While we do not have a thermometer for the electron temperature in our devices, recent tunneling experiments, which use an identical amplification scheme in a dilution fridge with a similar base temperature, do allow for in situ thermometry[186]. In these experiments, electron temperatures below 100 mK are possible only with careful thermal isolation and heat sinking of the HEMT, which is a heat source directly tied to the sample[187]. Because we have not taken these precautions in our setup, our electron temperature is likely no less than 100mK for the capacitance measurements. Indeed, data taken at the NHMFL in Tallahassee in a 3He system with a base temperature of 300mK do not look qualitatively different.

### D.3 Measurement of electronic compressibility and thermodynamic energy gaps

Most of the experimental data presented in the main text are  $C_P$ , which we interpret as proportional to electronic compressibility. As is clear from Eqs. D.1-D.3, this is not

generally true: solving those equations for  $C_P$  gives

$$C_P = \frac{c}{2} \left( 1 - \frac{\partial n}{\partial n_0} \right) + \frac{c^2}{4c_0} \frac{\partial p}{\partial p_0}. \quad (\text{D.7})$$

The third term in this equation is unique to multilayers, denoting the layer polarizability. Near layer polarization phase transitions, where the layer occupation changes rapidly over a small range of  $p_0$ , this term can be large; however, in the single component regimes where, for example, we perform our measurements of the thermodynamic gaps, this term is tiny. In these regimes, charge cannot move easily between the layers, and the bilayer system behaves as a single layer system (measurements of  $\partial p / \partial p_0$ , discussed below, are featureless in this regime). In this case, the conventional quantum capacitance[188] formula applies, so that

$$\frac{\partial n}{\partial n_0} = \frac{1}{1 + 2c \frac{\partial \mu}{\partial n}} \quad (\text{D.8})$$

$$C_P = \frac{c}{2} - \frac{1}{4} \left( \frac{1}{2c} + \frac{1}{\partial n / \partial \mu} \right)^{-1} \quad (\text{D.9})$$

$$= \frac{c^2}{2c + \partial n / \partial \mu} \quad (\text{D.10})$$



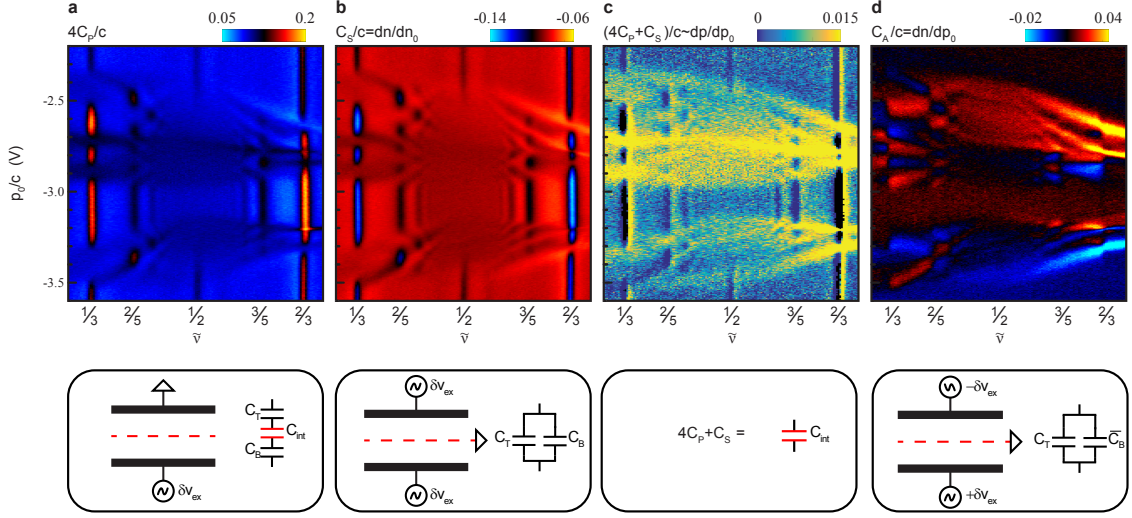


Figure D.2: **Thermodynamic properties of interlayer correlated states.** (a) Penetration field capacitance  $4 \times C_P/c$ . (b) Symmetric capacitance  $C_S/c$ . (c)  $4C_P + C_S$ , proportional to the polarizability. (d) anti-symmetric capacitance  $C_A$ . As presented,  $C_P/c$  and  $C_S/c$  were offset by constant parasitic capacitance levels  $C_{\text{par}}/c = -0.55$  and  $C_{\text{par}}/c = -2.84$  respectively. The lower panels illustrate the effective geometric capacitance measured in each case, as would be applicable for a classical four plate capacitor.  $C_P$  measures top, bottom, and interlayer capacitance in series, while  $C_S$  measures the sum of the top and bottom capacitance.  $4C_P + C_S$  thus gives the interlayer capacitance,  $C_{\text{int}}$ , which is  $dp/du \sim dp/dp_0$ .  $C_A$ , discussed extensively elsewhere[57], measures the difference between top and bottom capacitances.

From the above formulas, the change in chemical potential follows as

$$\Delta\mu_{12} = \int_{n^{(1)}}^{n^{(2)}} \frac{\partial\mu}{\partial n} dn = \int_{n_0^{(1)}}^{n_0^{(2)}} \frac{\partial\mu}{\partial n} \frac{\partial n}{\partial n_0} dn_0 \quad (\text{D.11})$$

$$= \int_{n_0^{(1)}}^{n_0^{(2)}} \frac{C_P}{c} d(n_0/c) \quad (\text{D.12})$$

We take the gap as the difference between the maximum and minimum in  $\Delta\mu$  near a FQH state, as shown in Fig. 5.5b of the main text. As can be seen from Eq. D.12, quantitative measurement of  $\Delta\mu$  requires accurate knowledge of  $c$ . This is calibrated in situ from the capacitance in an integer quantum Hall gap (where the full  $c/2$  penetration

capacitance obtains). Unfortunately, this data was not be acquired in the limited time available at the National high magnetic field lab. For this reason, the gaps in Fig. 5.4 of the main text (right panel) are presented only in relative units, normalized to their value at  $B=14\text{T}$ .

Interpretation of any measured capacitance as a thermodynamic derivative requires that the sample is sufficiently conductive to fully charge over a time scale comparable to the inverse measurement frequency[183]. At low temperature and high magnetic fields, our sample becomes strongly insulating at all integer and many fractional filling factors, precluding this condition being satisfied at high frequency. This is unimportant for identifying the existence of fractional quantum Hall phases, which manifest as  $C_P$  peaks regardless of whether the contrast mechanism is due to low electronic compressibility or low bulk conductivity; however, it is critical to be in the low frequency limit for any quantitative analysis of energy gaps following Eq. D.12. Failure to charge manifests as an increase in the out of phase, dissipative signal in the complex capacitance,  $\tilde{C} = C + iD$ , where we have plotted ‘C’ throughout the text. We can monitor charging across the parameter range by plotting ‘D’. In order to measure energy gaps, we decrease the frequency until no features are visible in D. In this limit, it is justified to integrate  $C_P$  to extract energy gaps.

## D.4 Measurement of layer polarizability, $\partial p/\partial p_0$

To measure  $\partial p/\partial p_0$ , as shown in Fig. 5.10b of the main text, we measure penetration field ( $C_P$ ) and symmetric capacitance ( $C_S$ ) over a range of  $n_0$  and  $p_0$  corresponding to the four-level crossing described in the main text Figs. 5.8. As can be seen in Fig. D.11, there are diagonal features in  $C_S$  within the  $n_0 - p_0$  plane that correspond to constant gate voltage. We ascribe these features either to incompressible LL gaps in the graphite

gates themselves. To avoid them, we perform the measurement in the nearly identical level crossing at  $p_0/c \approx -3V$  for  $-1 < \nu < 0$ , where diagonal features are not observed in the regime of the phase transition.  $C_P$  and  $C_S$  in this regime are shown in Fig D.2, along with their weighted sum,  $4C_P + C_S$  as per Eq. D.3. The two measurements were calibrated against each other by measuring  $C_T$ , the top gate capacitance, accessible in either configuration.

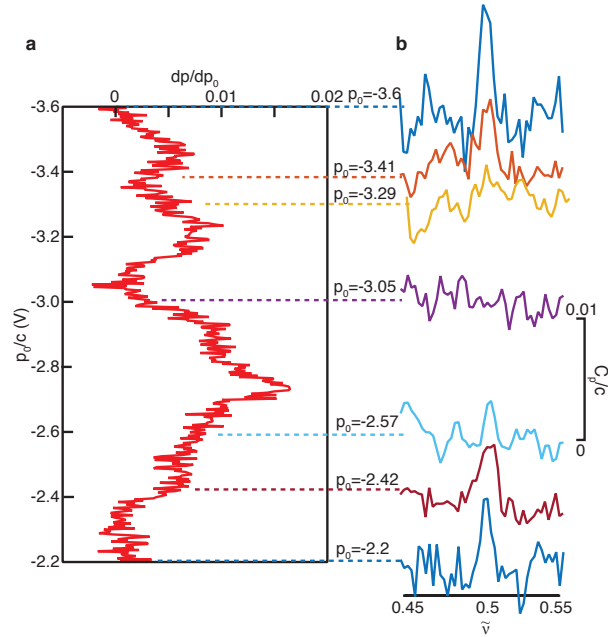


Figure D.3: **Qualitative comparison of incompressibility and depolarization at  $\nu=1/2$**  **a**  $C_P + 4C_S \sim dp/dp_0$  near  $\tilde{\nu} = 1/2$  as a function of  $p_0$  and **(b)**  $C_P$  as a function of  $\tilde{\nu}$  showing the incompressible peak at  $\tilde{\nu} = 1/2$ . The gap persists despite finite depolarization, fading with increasing  $p$  but vanishing only between  $p_0/c \approx -3.3$  and  $p_0/c \approx -2.6$ .

FQH gaps show strong features in the  $\partial p/\partial p_0$  data. This is spurious: digital subtraction of the two data sets measured with different amplifiers leads to systematic errors where  $C_P$  and  $C_S$  have large gradients, for example in FQH gaps. There, small offsets in  $n_0$  and nonlinearities in the amplifier chain can lead to incomplete cancellation of the two signals, leading to the visibility of the gaps themselves in Fig. 5.10a of the main

text. This is confirmed by the measurement of  $\frac{dp}{dn_0}$ : if the changes in polarization were real, they would manifest in this quantity as well.  $\frac{\partial p}{\partial n_0}$  is shown in Fig. D.2d. Because  $\frac{\partial p}{\partial n_0}$  can be measured directly with a single amplifier(see, for example, [57]), subtraction-induced systematic errors are automatically canceled. We find no change in polarization of the  $\tilde{\nu} = \frac{1}{2}$  state relative to its immediate background, indicating that the features in  $\partial p/\partial p_0$  at fractional filling are indeed spurious. We thus integrate  $\frac{\partial p}{\partial p_0}$  at  $\tilde{\nu} = 0.495$  and  $\tilde{\nu} = 0.505$  and average the results to determine .

To determine the layer polarization change for arbitrary  $\nu$  and  $p_0$ , we integrate the measured  $C_S + 4C_P$  signal, as

$$\Delta p_{12} = 2\pi\ell_B^2 \int_{p_0^{(1)}}^{p_0^{(2)}} \frac{\partial p}{\partial p_0} dp_0 \quad (\text{D.13})$$

$$= 2\pi\ell_B^2 \frac{2c_0}{c} \int_{p_0^{(1)}}^{p_0^{(2)}} \left( \frac{C_S + 4C_P - 2c}{c} \right) dp_0 \quad (\text{D.14})$$

$$= 2\pi\ell_B^2 2c_0 \int_{p_0^{(1)}}^{p_0^{(2)}} \left( \frac{C_S + 4C_P - 2c}{c} \right) d(p_0/c) \quad (\text{D.15})$$

where  $\Delta p$  is expressed in filling factor units and all capacitances are understood to be in units of particle number per area per volt.

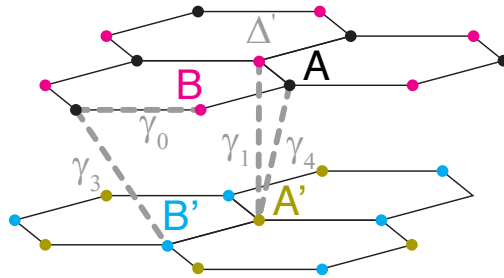


Figure D.4: **Bilayer graphene hopping parameters used in the single particle model for the wavefunctions.** In the calculations,  $\gamma_0=-2.61$  eV,  $\gamma_1=.361$  eV,  $\gamma_3=0$ ,  $\gamma_4=.138$  eV, and  $\Delta'=.015$  eV.

The measured data may be subject to an arbitrary offset due to differing parasitic

capacitances in the  $C_S$  and  $C_P$  measurements which need not cancel. In addition, an overall magnitude error can lead to a systematic under- or over estimate of the change in polarization. To compensate these errors, we take advantage of the fact that we know, from band structure, the total layer polarization change that must occur between the two extremes in Fig. 5.10a (and Fig. D.2a-d). At the bottom of these plots, an  $N=0$  orbital on the bottom layer is fully occupied, while an  $N = 1$  orbital on the bottom layer has occupation  $\tilde{\nu}$ . At the top, these orbitals are empty while an  $N=0$  orbital on the top layer is fully occupied while the  $N = 1$  orbital on the top layer has occupation  $\tilde{\nu}$ . Thus, for a given  $\tilde{\nu}$  in this regime, we expect a total occupation transfer of  $\Delta\nu = 2(1 + \alpha\nu)$ , where  $\alpha = .84$  is the layer polarization of the  $N = 1$  orbitals at 12T determined from tight binding calculations. We use this to fit two constants to the integrated data,  $a$  and  $b$ , so that

$$a \int_{-3.6}^{-2.2} \left( \frac{C_S + 4C_P}{c} - b \right) d \left( \frac{p_0}{c} \right) = 2(1 + \alpha\nu) \quad (\text{D.16})$$

where the contour of integration is at constant  $\tilde{\nu}$  from the bottom to the top of Fig. D.2c. The constant  $b$  can be determined directly by measuring the background level in a single component region, where we expect  $\partial p/\partial p_0 = 0$ , and this background is subtracted from the  $4C_P + C_S$  data set shown in Fig. D.2c. The error with which this background can be determined is  $\sigma_b = 2.3 \times 10^{-4}$ . We then calculate  $a$  from Eq. D.16 by performing this integration for 35 combinations of 7 different regions of  $\tilde{\nu}$ , from which we find  $a = (422 \pm 22) \text{ V}^{-1}$ . Following Eq. D.15 allows us to extract the interlayer dielectric constant of the graphene bilayer,  $\varepsilon_{BLG}$  since,

$$a = 4\pi c_0 \ell_B^2 \quad (\text{D.17})$$

$$= 4\pi \frac{\varepsilon_{BLG} \varepsilon_0}{d_{BLG} e} \ell_B^2 \quad (\text{D.18})$$

$$\therefore \varepsilon_{BLG} = \frac{a}{113.6 \text{ V}^{-1}} = 3.71 \pm .19 \quad (\text{D.19})$$

for  $d_{BLG} = .335\text{nm}$ ,  $B = 12\text{T}$ . This is roughly consistent (to within 25%) with  $\varepsilon_{BLG} = 2.8$  determined in recent experiments at higher magnetic fields[57]. We note that  $\varepsilon_{BLG}$  receives contributions from filled Landau levels, and may well be field dependent. To generate Fig. 5.10b of the main text, we integrate along  $p_0/c$ , for example

$$\Delta p(p_0) = a \int_{-3.6}^{p_0/c} \left( \frac{C_S + 4C_P}{c} - b \right) d \left( \frac{p_0}{c} \right) \quad (\text{D.20})$$

$$\sigma_{\Delta p}(p_0) = \frac{\sigma_a}{a} \Delta p(p_0) + \sigma_b(p_0/c + 3.6) \quad (\text{D.21})$$

Because the layer polarization is known also for  $p_0/c = -2.2$  V, either the increasing or decreasing integral are equivalent, and error bars are defined by the lesser of the two. The largest uncertainty thus obtains approximately midway between the extremes near  $p_0/c = -2.9$  V.

This analysis provides a quantitative view of the correlation of depolarization with gap size, the existence of a gapped phase despite depolarization is visible in the raw data. This is evident in Fig. D.3, where a finite incompressibility peak is visible after considerable polarization has been transferred.

## D.5 Single particle model

We use the same single-particle model for bilayer graphene as described in the supplementary information of [57], which includes tight binding parameters  $\gamma_0$ ,  $\gamma_1$ ,  $\gamma_4$ , and  $\Delta'$  (see Fig. D.4). The single-particle spectrum at  $B = 14\text{T}$  is shown in Fig. D.6, with a level ordering which is typical for all the  $B$ -fields used in the experiment. Within this model, the ZLL wavefunctions in the different valleys (written in the lattice basis

$\psi_{N\xi} = (\varphi_A, \varphi_{B'}, \varphi_{A'}, \varphi_B)$  are

$$\psi_{0+} = \begin{pmatrix} |0\rangle \\ 0 \\ 0 \\ 0 \end{pmatrix} \quad \psi_{0-} = \begin{pmatrix} 0 \\ |0\rangle \\ 0 \\ 0 \end{pmatrix} \quad \psi_{1+} = \begin{pmatrix} \cos \Theta |1\rangle \\ 0 \\ \cos \Phi \sin \Theta |0\rangle \\ \sin \Phi \sin \Theta |0\rangle \end{pmatrix} \quad \psi_{1-} = \begin{pmatrix} 0 \\ \cos \Theta |1\rangle \\ \sin \Phi \sin \Theta |0\rangle \\ \cos \Phi \sin \Theta |0\rangle \end{pmatrix} \quad (\text{D.22})$$

$|0\rangle$  and  $|1\rangle$  denote the  $n = 0, 1$  magnetic oscillator states of a conventional parabolically dispersing system. The layer polarization of the  $|1\rangle$  orbitals is then  $\alpha = \cos^2 \Theta - \sin^2 \Theta (\cos^2 \Phi - \sin^2 \Phi)$ . However,  $\Phi$  is very small ( $< .033$  for fields below 35T). Thus  $\Phi$  does not shift the balance between  $|0\rangle$  and  $|1\rangle$  oscillator states, and so does not enter calculations of long range Coulomb effects such as fractional quantum Hall.  $\Theta$  controls the degree to which  $N=1$  orbitals are strictly analogous to a parabolic electron system, i.e., purely composed of  $|1\rangle$  oscillator states. A plot of  $\Theta(B)$  is shown in Fig. D.5.

## D.6 Numerical simulations

The phase diagram of Fig. 5.7a of the main text was calculated using the density matrix renormalization group (DMRG) for multicomponent quantum Hall systems[189, 136]. For a detailed exposition and justification of the approach used here, we refer to Ref.[57], which benchmarked similar numerical computations against the experimentally determined layer polarization data.

The splitting  $\Delta_{10}$  between the  $N = 0, 1$  orbitals of the ZLL is small, while the splitting between the ZLL and the higher LLs is large, of order  $\hbar\omega_c$ . Our approach is based on the hierarchy  $\Delta_{10} < E_C < \hbar\omega_c$ , where  $E_C$  is the Coulomb scale, which holds throughout the

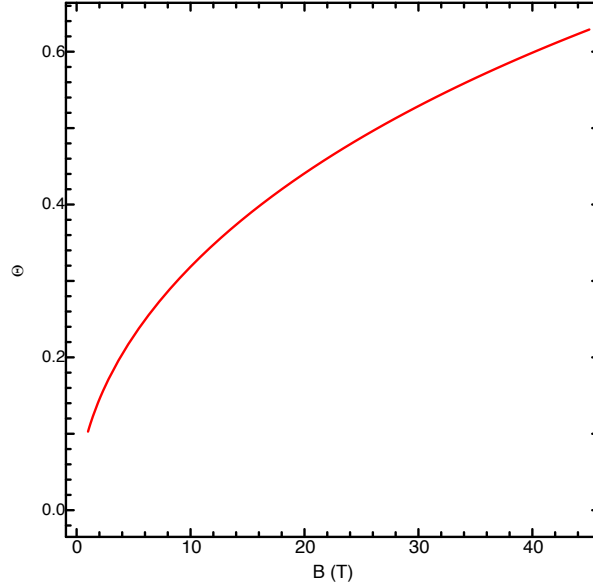


Figure D.5: **Band structure parameter**  $\Theta$ , as calculated from the tight binding model as a function of magnetic field.

experimental range of  $B$  and  $p_0$  (see Fig D.6). Because of the large splitting between the ZLL and the  $N \geq 2$  LLs, we project the problem into the ZLL, though will account for screening from the filled LLs through an effective interaction  $V_{\text{eff}}$  we will discuss shortly. The ZLL projected Hamiltonian takes the form

$$H = \int d^2q n_{\text{ZLL}}(q) V_{\text{eff}}(q) n_{\text{ZLL}}(-q) + \Delta_{10} \hat{N}_1 + [\text{isospin splittings}] + \quad (\text{D.23})$$

$$+ [\text{SU}(4)\text{-interaction anisotropies}] \quad (\text{D.24})$$

Here  $n_{\text{ZLL}}(q)$  is the Fourier transform of the 2D electron density projected into the ZLL,  $V_{\text{eff}}$  is the effective interaction,  $\hat{N}_1$  is the electron number in the  $N = 1$  orbital, and  $\Delta_{10}$  is the splitting between the  $N = 0, 1$  orbitals. There are also single-particle isospin (spin-valley) splittings and small SU(4) interaction anisotropies, but since our interest is in regions where the valence electrons partially occupy a single isospin, while all other



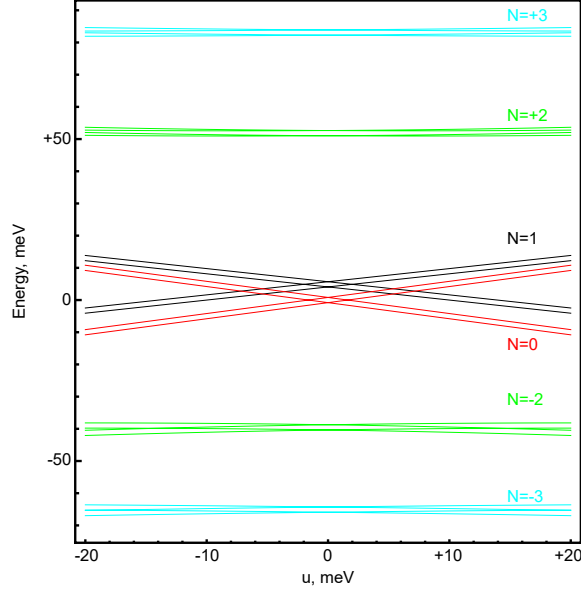


Figure D.6: **Single particle energy spectrum of bilayer graphene at  $B = 14\text{T}$** , calculated from a tight binding model and including the Zeeman splitting and inter-layer potential. The interlayer potential difference  $u \approx \frac{p_0}{c} \frac{c}{2c_0} \approx 3.3 \times 10^{-3} \frac{p_0}{c}$ , does not exceed 15 meV in the data presented. For reference, the bare Coulomb energy at 14T is  $e^2/\varepsilon_{\text{hBN}}^{\parallel} \ell_B \approx 31$  meV, where we have taken  $\varepsilon_{\text{hBN}}^{\parallel} = 6.6$ [83]. Interactions thus strongly mix the  $N=0$  and  $N=1$  levels (and in fact change the order of level filling within the ZLL, as shown in Ref. [57]), while mixing of the 0-1 manifold with the  $|N| \geq 2$  levels is comparatively weak.

isospins are either full or empty, these can be dropped from the problem.

The bare Coulomb interaction is screened by the encapsulating hBN, the graphite gates at a distance  $d/2$  from the sample, and the filled LLs below the ZLL. Screening from the hBN is accounted for in the Coulomb scale  $E_C = \frac{e^2}{4\pi\ell_B\varepsilon_{\text{hBN}}}$ , where  $\varepsilon_{\text{hBN}} \sim 6.6$  is the dielectric constant of the hBN[83]. We assume the graphite behaves as a metal, so in units of  $\ell_B, E_C$ , the gate screened interaction is  $V(q) = \frac{2\pi}{q} \tanh(qd)$ . The phase diagram here is presented for device A,  $d = 40\text{nm}$ ,  $d/\ell_B = 1.56\sqrt{B/\text{T}}$ , but the results are largely insensitive to  $d$  at these fields since  $d/\ell_B \gg 1$ .

The residual response of the filled LLs below the ZLL is controlled by the ratio  $\frac{E_C}{\hbar\omega_c} \approx 0.5 - .8$ . We account for it within a phenomenological RPA-type treatment discussed in

Refs.[128, 57], taking

$$V_{\text{eff}}(q) = \frac{V(q)}{1 + a_{\text{scr}} V(q) \tanh(0.62q^2 \ell_B^2) 4 \log(4) / 2\pi}. \quad (\text{D.25})$$

Within the two-band model of BLG at  $\nu = 0$ , RPA calculations give  $a_{\text{scr}} = \frac{E_C}{\hbar\omega_c} \equiv a_*$ . However, this value will not be quantitatively correct due to 4-band corrections and the filling of the isospins within the ZLL. For this reason, we treat  $a_{\text{scr}}$  as a phenomenological parameter. In Ref.[57], quantitative agreement between numerics and experiment at 31T was obtained for  $a_{\text{scr}} \sim 0.38a_*$ , which is the value used in the phase diagram of the main text. To check that our conclusions are qualitatively insensitive to screening, the calculations below will be repeated for  $a_{\text{scr}} = 0, 0.25a_*, 0.5a_*$  and  $0.75a_*$ .

We note that the RPA treatment only renormalizes the two-body Hamiltonian, while in principle higher-body terms are also generated. However, the two-body screening diagrams are larger by a factor of  $N_f = 4$  relative to three-body corrections, and three-body corrections actually vanish within the “standard” model of graphene, which only accounts for the nearest neighbor hoppings, due to particle-hole symmetry. When accounting for the further-neighbor hoppings, there is a small amount of particle-hole symmetry breaking, but taken together this suggests the effective three-body interactions from outside the ZLL are much smaller than those which will be generated (and fully accounted for) from LL-mixing within the ZLL itself.

Under the assumption of isospin polarization, the  $n_{\text{ZLL}}(q)$  can be restricted to the contribution from a single isospin, which contains the two LLs  $N = 0, 1$ . In this study we keep the full Hilbert space of both, since the splitting  $\Delta_{10}$  between them is small and mixing between them plays a crucial role in stabilizing the Pfaffian. As discussed, within the four-band model of graphene, the  $N = 0$  orbital has the character of a conventional  $n=0$  LL of GaAs, while the  $N = 1$  orbital is an admixture of the conventional  $n=0$  and

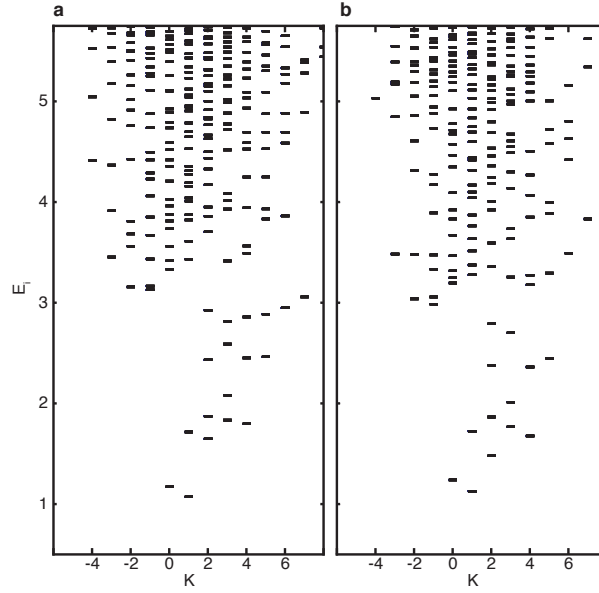


Figure D.7: **Entanglement spectrum from cylinder DMRG simulations of the incompressible half-filled Landau level.**  $E_i$  is the spectrum of the reduced density matrix for one half of the cylinder,  $E_i = -\log(\rho_L)$ , plotted against the momentum  $k$  around the cylinder. The counting of low lying levels,  $1, 2, 4, \dots$ , mimics the energy spectrum of the chiral edge theory of the Pfaffian phase, which we use to identify the state as the Pfaffian. The spectrum is shown for BLG model parameters  $\Delta_{10} = 0.1E_C, B = 12\text{T}$  on a circumference  $L = 19\ell_B$  cylinder. We repeat the calculations for two different values of the screening length **(a)**  $a_{scr} = 0$  and **(b)**  $a_{scr} = .75a_*$ , where  $a_* = \frac{E_C}{\hbar\omega_c}$ . We find that the Pfaffian is stable over a wide range.

$n=1$  LLs. Letting  $\bar{\rho}_{NN'}(q) \equiv \sum_k e^{-ikqy\ell_B^2} c_{N,k+q_x/2}^\dagger c_{N',k-q_x/2}$  denote the “guiding center” density operator projected into orbitals  $N, N'$ , [190] the density operator is

$$n_{\text{ZLL}}(q) = \sum_{N,N'} \mathcal{F}_{N,N'}(q) \bar{\rho}_{NN'}(q) \quad (\text{D.26})$$

where  $\mathcal{F}$  are the BLG “form factors” for LL projection, which depend on the lattice structure of the wavefunctions, Eq.D.22. Up to small corrections at the lattice scale of order  $\frac{a_0}{\ell_B}$ , the BLG form factors  $\mathcal{F}_{MN}$  can be expressed as linear combinations of the

conventional form factors  $F_{mn}$  as

$$\mathcal{F}_{00} = F_{00} \quad (\text{D.27})$$

$$\mathcal{F}_{11} = \cos^2(\Theta)F_{11} + \sin^2(\Theta)F_{00} \quad (\text{D.28})$$

$$\mathcal{F}_{01} = \cos(\Theta)F_{01}. \quad (\text{D.29})$$

where  $\Theta$  is determined from the  $B$ -dependent band structure, Eq.D.22 and

$$F_{mn}(q_x, q_y) = e^{-q^2/4} \sqrt{\frac{m!}{n!}} \left( \frac{q_x + iq_y}{\sqrt{2}} \right)^{n-m} L_m^{(n-m)}(q^2/2). \quad (\text{D.30})$$

The two-band model is recovered in the limit  $\Theta \rightarrow 0$ , while in the four-band model of bilayer graphene,  $\Theta$  grows with perpendicular magnetic field  $B$ , Fig.D.5 [57, 191].

Having defined the Hamiltonian, which depends on  $B$ ,  $\Delta_{10}/E_C$ , and  $a$ , infinite-DMRG was used to obtain the ground state of an infinitely long, circumference  $L_y = 19\ell_B$  cylinder. In the main text, the ground state was found on a  $6 \times 16$  grid of points in the  $\Delta_{10}/E_C, B$  plane at screening strength  $a_{\text{scr}} = 0.38a_*$ , keeping  $m = 12000$  DMRG states, with truncation errors less than  $10^{-6}$ . The computations required around 32000 cpu-hours. The Pfaffian ground state is identified by a finite correlation length ( $\xi \sim 3\ell_B$  in the most robust regions) and distinctive entanglement spectrum characteristic of the associated edge chiral CFT [192, 193] (see Fig. D.7). The anti-Pfaffian, in contrast, would have an entanglement spectrum with the opposite chirality. Unlike GaAs, scattering between the  $N = 0$  and  $N = 1$  orbitals strongly breaks particle-hole symmetry, unambiguously stabilizing the Pfaffian order over the particle-hole conjugated anti-Pfaffian. For the reader more interested in how we have distinguished between the Pfaffian and anti-Pfaffian, we refer to the detailed DMRG study of this question described in Ref. [136], which studied a cut equivalent to  $a_{\text{scr}} = 0, \Theta = 0, \Delta_{10}$ .

Larger  $\Theta$  (possibly achievable at the very highest  $B$  fields) increases the correlation length of the Pfaffian and drives a transition into the compressible CFL phase, which is to be expected since sharper interactions favor the CFL phase.[195, 196, 109] Since the competing CFL phase is gapless, computing the precise location of the Pfaffian-CFL phase boundary is extremely difficult; finite size or finite entanglement effects turn the continuous transition into a crossover. In particular, because DMRG simulations at bond dimension  $\chi$  can only capture at most  $S = \log(\chi)$  entanglement, while the CFL has a log-divergent entanglement, it is impossible to exactly capture the CFL in DMRG. As discussed in detail in Ref.[194], the DMRG thus induces a “finite-entanglement” correlation length  $\xi$ . In the CFL phase,  $\xi \sim \chi^\kappa$  diverges with increasing bond dimension, while in the Pfaffian phase,  $\xi$  should converge to its physical value. Furthermore, in the CFL, the entanglement should scale with the finite-entanglement correlation length as  $S(\chi) = \frac{c}{6} \log(\xi(\chi)) + s_0$ , where  $c = 5$  at circumference  $L = 19$ .

In Fig. D.8, we plot both  $S(\chi)$  and  $S(\xi)$  at  $L = 19$ ,  $\Delta_{10}/E_C = 0.5$ ,  $a_{\text{scr}} = 0.5a_*$  as the field increases from  $B = 5 \cdots 60\text{T}$ . There is a regime where the simulations are clearly converging with  $\chi$ , indicating that the state is the gapped Pfaffian, and regions where the scaling is consistent with the CFL up to the largest  $\chi$ . Precisely pinpointing the transition is clearly difficult, since we can’t really distinguish between a Pfaffian phase of correlation length  $\xi > 13$  and the CFL.

Further insight is provided by the guiding-center density-density structure factor  $\bar{D}(q)$  shown in Fig. D.9. As discussed in Ref.[194], in the CFL phase  $\bar{D}(q)$  is predicted to have non-analyticities at wave vectors associated with scattering a composite Fermion across the Fermi surface. At low  $B$ , there is only a broad bump, consistent with a Pfaffian, while at high  $B$  three kinks develop close to the positions predicted for a circular Fermi surface. These kinks are brought into sharper relief by plotting “ $\partial_{|q|}\bar{D}(q)$ ,”[194] which is defined by multiplying the real-space correlations by  $|x|$  before Fourier transforming to

$q_x$ . Like the scaling of the entropy, the structure factor is consistent with a Pfaffian to CFL transition.

We note that a third competing phase is a striped phase, which breaks translation invariance. We have checked for this possibility by initializing the DMRG simulations with a charge density wave state close to the known wavelength of the stripe.[196] Throughout the phase diagram studied here, the stripes melt and form a liquid at sufficiently high DMRG accuracy. However, we do find that there is a critical  $\Delta_{10} < 0$  where the Pfaffian phase is destroyed in favor of a stripe. Potentially, experiments could reach this regime by tuning  $\Delta_{10}$  with very large electric fields (since the  $N = 0, 1$  orbitals have slightly different layer polarization), but none of our experiments are in this regime.

To address the uncertainty in the screening strength, we present calculations ( $m=6000$ , truncation error less than  $10^{-5}$ ) for a variety of screening strengths  $a_{\text{scr}}$ . Again, the Pfaffian is preferred throughout most of the phase diagram. The screening has some quantitative effect on the growth of the correlation length, and hence presumably the precise location of the Pfaffian to CFL transition.

While we computed a phase diagram in the  $\Delta_{10}/E_C, B$  plane, we do have a microscopic estimate of the splitting  $\Delta_{10}$ . As discussed in detail in Ref.[57], it has three contributions: a  $B$ -dependent single particle splitting due to four-band corrections, a single particle splitting proportional the applied electric field  $p_0$ , and a ‘‘Lamb-shift’’ contribution arising from the exchange interaction with the levels below the ZLL. The data from Sample C shown in Fig. 5.7b of the main text were taken at  $p_0=6.0V$ . The trajectory shown in Fig. 5.7a of the main text is calculated including the effects of  $B$ - and  $p_0$  induced orbital splitting for  $p_0 = 6V$  within the tight binding model described above, and also include the Lamb shift. The  $p_0$  dependence of  $\Delta_{10}$  is an interesting feature, since it can be used to tune the strength of the LL-mixing in-situ.

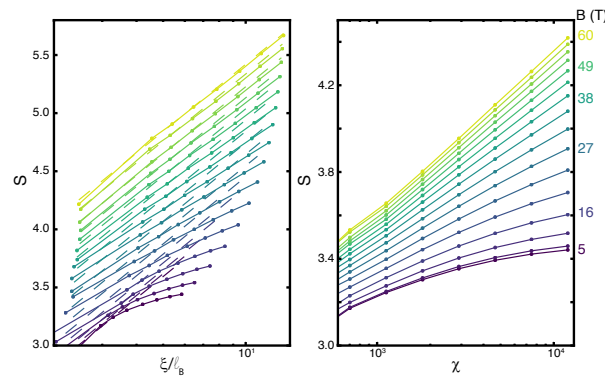


Figure D.8: **Finite entanglement scaling for the Pfaffian to CFL transition.** Data is shown for  $L = 19$ ,  $a_{\text{scr}} = 0.5a_*$ ,  $\Delta_{10}/E_C = 0.5$  over a range of  $B$ . For each  $B$ , the DMRG simulations are repeated with increasing bond dimension (e.g., accuracy)  $\chi = 600, \dots, 12000$ . The bipartite entanglement  $S$  and correlation length  $\xi$  are measured at each point. **a)** Numerically calculated  $S(\xi)$  (solid) compared with the theoretical prediction for a CFL,  $S = \frac{c}{6} \log(\xi) + s_0$ ,  $c = 5$  (dashed). The log-linear scaling at high  $B$  is consistent with a CFL, while the behavior at low  $B$  is not, indicating a Pfaffian. **Right)**  $S(\chi)$ . For low  $B$ , the entanglement is converging with bond dimension, indicating the state is the gapped Pfaffian. For high  $B$ , the scaling is log-linear up to the largest  $\chi$ , consistent with the log-divergent entanglement of the CFL. Arguably the entanglement shows signs of saturating up  $B \sim 34 - 38\text{T}$ , beyond which we can't tell, suggesting the Pfaffian is stable up to at least this range.

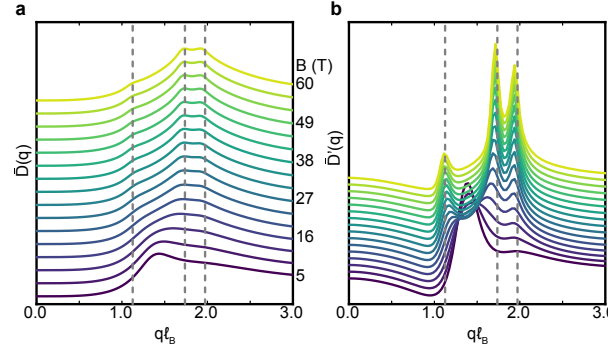


Figure D.9: **Structure factor across the Pfaffian-composite fermi liquid transition.** The guiding center density-density structure factor  $\bar{D}(q) = \langle : n(q_x = q, q_y = 0)n(q_x = -q, q_y = 0) : \rangle$  (a) and its derivative,  $\bar{D}'(q)$  (b). The gray vertical lines indicate the location of predicted kinks for a perfectly circular composite Fermi surface. At low  $B$ , where the state is a Pfaffian, there is only a single broad peak unattached to these locations. At high  $B$ , where the state is transiting to a CFL, three sharp peaks develop. They are slightly displaced from the naive prediction because the circular Fermi deforms slightly when it is placed on a cylinder.[194]

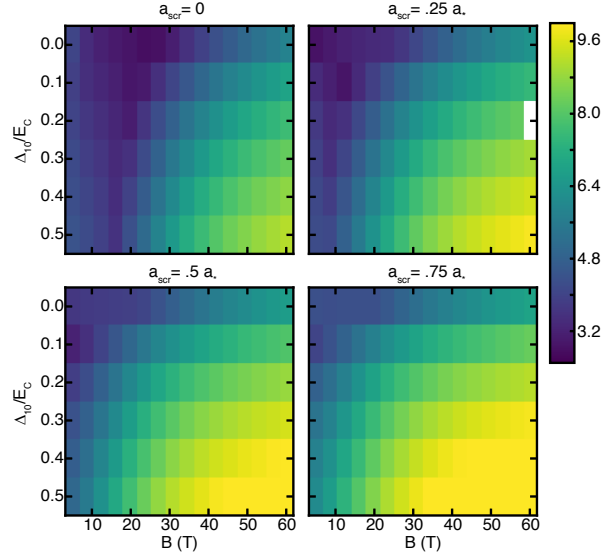


Figure D.10: **Correlation length in the  $B - \Delta_{10}/E_C$  plane.** The computed DMRG correlation length  $\xi/\ell_B$  is computed for four values of the screening strength  $a_{scr}$ . The plots are analogous to that in Fig. 2d of the main text. Computations are performed on an  $L = 19\ell_B$  cylinder, with  $\chi = 6000$  DMRG states. Larger screening increases the correlation length somewhat, but the general features are changed (e.g. the entanglement spectrum is consistent with the Pfaffian in the low- $\xi$  regime, Fig.D.7)



## D.7 Additional data

Table D.1: Thermodynamic energy gaps in the single component N=0 orbital regime (Sample A). Gaps are measured at B=14T and expressed in Kelvin.

$\tilde{\nu}$	Temperature, mK								
	20	160	310	450	577	711	810	1000	1150
2/7	0.63	0.77	0.59	0.38	0.3	0.2	-	-	-
1/3	-	-	-	-	-	-	-	3.77	3.1
2/5	-	-	-	3.85	3.25	2.63	2.25	1.4	1.15
3/7	-	-	1.89	1.46	1.03	0.625	0.53	0.31	-
4/9	0.83	0.8	0.62	0.40	0.29	0.15	-	-	-
5/11	0.345	0.22	0.13	0.11	-	-	-	-	-
6/13	0.12	0.07	-	-	-	-	-	-	-
7/13	0.07	0.06	0.04	-	-	-	-	-	-
6/11	0.35	0.22	0.18	0.13	-	-	-	-	-
5/9	0.96	0.98	0.79	0.57	0.38	0.2	0.18	-	-
4/7	2.9	2.67	2.34	1.83	1.36	0.87	0.89	0.48	0.34
3/5	-	-	-	6.0	5.23	4.36	3.8	2.7	2.1
2/3	-	-	-	-	-	-	-	10.5	9.56

Table D.2: Thermodynamic energy gaps in the single component N=1 orbital regime. Gaps are measured at B=14T and expressed in Kelvin.

$\tilde{\nu}$	Temperature, mK								
	20	160	310	450	577	711	810	1000	1150
1/5	1.3	0.9	0.94	0.51	0.3	-	-	-	-
2/7	0.9	0.39	0.33	0.15	0.1	-	-	-	-
1/3	-	-	-	3.15	2.94	2.4	1.76	0.78	0.63
1/2	3.99	3.17	2.68	1.7	1.01	0.57	0.46	-	-
7/13	0.9	0.44	0.4	0.28	-	-	-	-	-
2/3	-	-	-	4.35	3.79	3.12	2.6	1.7	1.1
5/7	1.73	1.02	0.8	0.53	0.43	0.2	0.18	-	-
4/5	1.14	0.98	0.81	0.57	0.43	0.21	0.16	-	-

Table D.3: Frequency and excitation voltages used in capacitance data presented in main text, methods, and supplementary figures.

Figure	$\delta V_{ex}$ (mV)	$f$ (kHz)
1b	1.4	71.77
1d	0.22	85.77
1e	0.9	2.48
2a,b	0.9	2.48
2e (L)	0.9	2.48
2e (R)	1.6	17.7
3c	0.9	71.77
3e	2.96	8.17
S2a-c	2.96	8.17
S2d	0.9	8.17
S11	2.96	71.77
S12	2.1	81.7
S13	1	71.77
S14	.2	87.77
S15	4.7	84.77
S16	1.6	17.7
S17	0.9	2.48

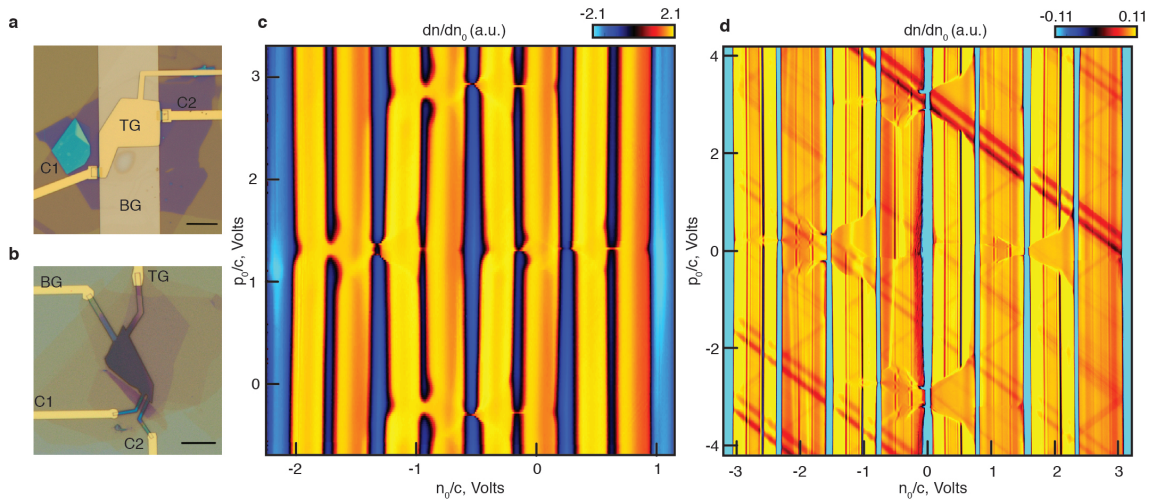


Figure D.11: **Comparison of metal- and graphite-gated devices.** (a) Optical micrograph of a metal gated device. Scale bar corresponds to  $10 \mu\text{m}$ . (b) Optical micrograph of a graphite gated device. Scale bar corresponds to  $10 \mu\text{m}$ . (c) Symmetric capacitance,  $C_S = C_T + C_B = \partial n / \partial n_0$ , for a metal gated device at  $B=10 \text{ T}$  and  $T \approx 50 \text{ mK}$ . (d)  $C_S$  for a graphite gated device at  $B=12 \text{ T}$ . Graphite gated devices show much narrower integer QH states, along with many fractional states. Diagonal features in (d) are features that depend on only one of the gates (top or bottom) potentials  $V_B$  or  $V_T$ , indicating either single gated regions or electronic structure within the graphite gates.

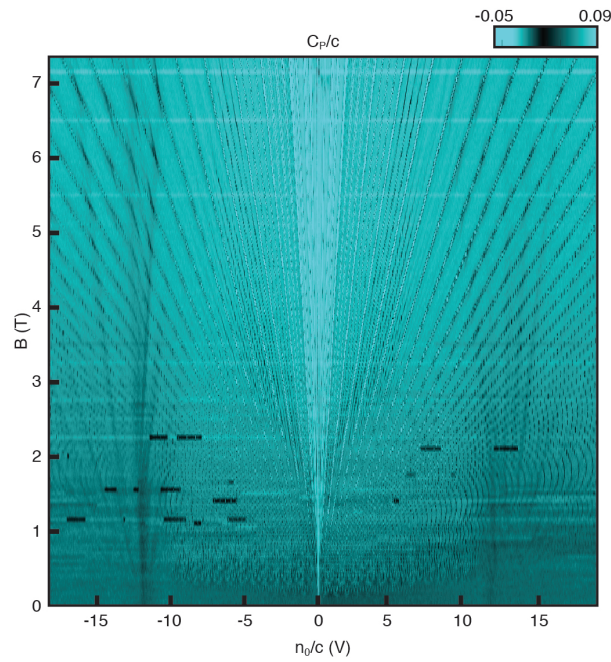


Figure D.12: **Moire features in Sample A.** Landau fan plot of  $C_p/c$  in Sample A. The main fan centered at charge neutrality is visible, along with satellite fans originating from superlattice zone boundary at  $n_0/c = \pm 11.8$  V. The location of the satellite peaks imply a superlattice constant  $\lambda \approx 13.3$  nm, corresponding to near-perfect (within experimental error) angular alignment of the Bernal bilayer to the underlying boron nitride.

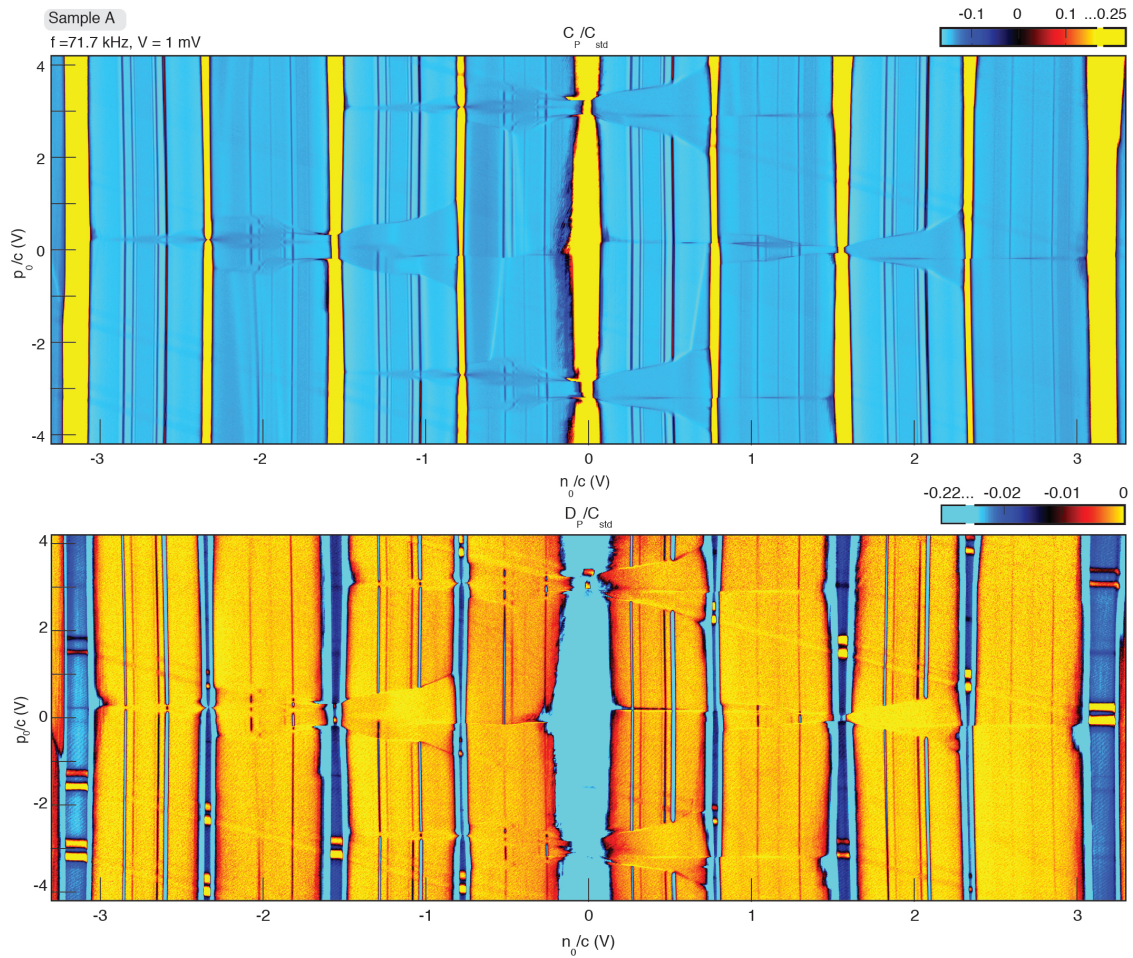


Figure D.13: **Additional data from Device A.** Penetration field capacitance and dissipation for the data set shown in Figure 1 of the main text from Device A (#SZ13), taken at base temperature and  $B=12\text{T}$ . Data was taken with a 1 mV AC excitation at 71.77 kHz applied to the top gate, and is shown in units of an arbitrary fixed reference capacitor.

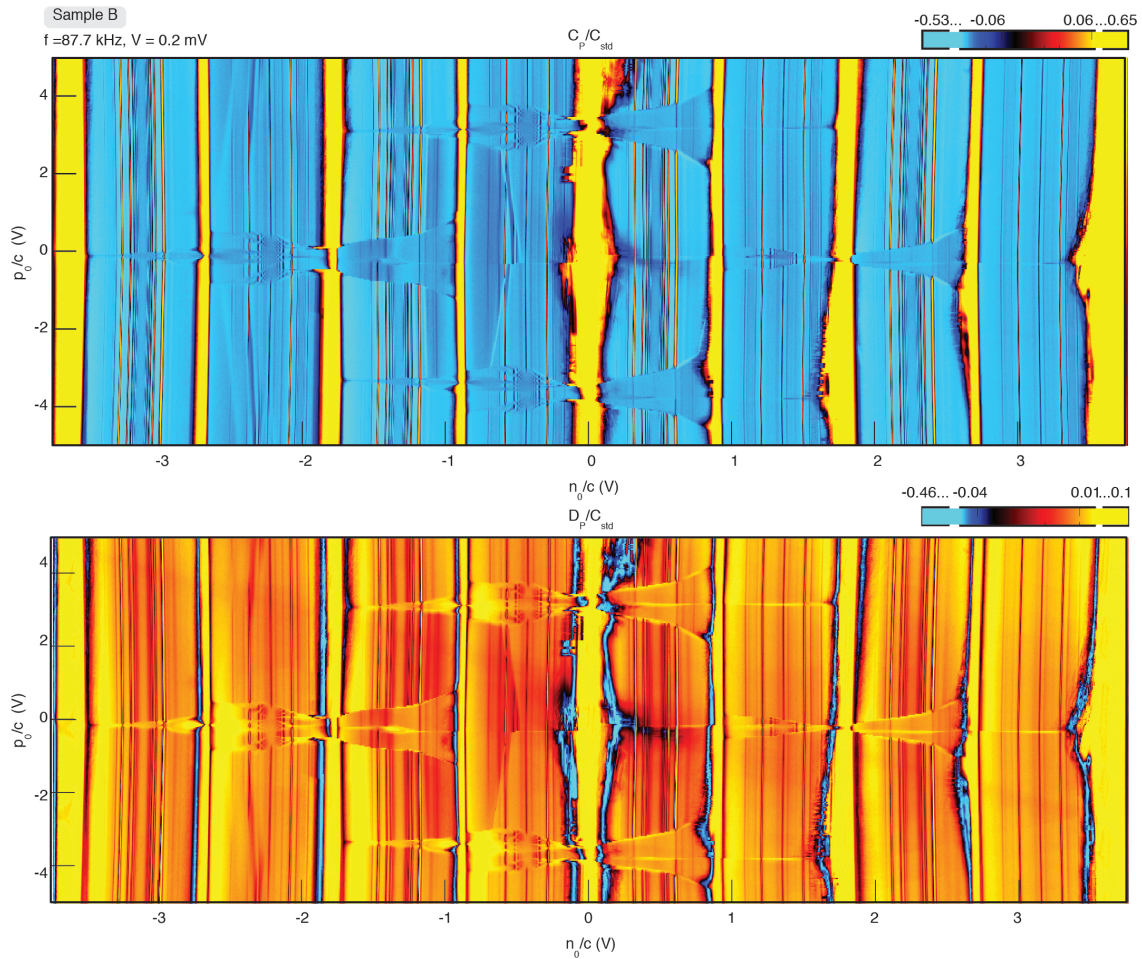


Figure D.14: **Additional data from Device B.** Penetration field capacitance and dissipation for Device B (#EMS13), taken at base temperature and  $B=14\text{T}$ . Data was taken with a  $0.2 \text{ mV}$  AC excitation at  $87.77 \text{ kHz}$  applied to the top gate, and is shown in units of an arbitrary fixed reference capacitor.

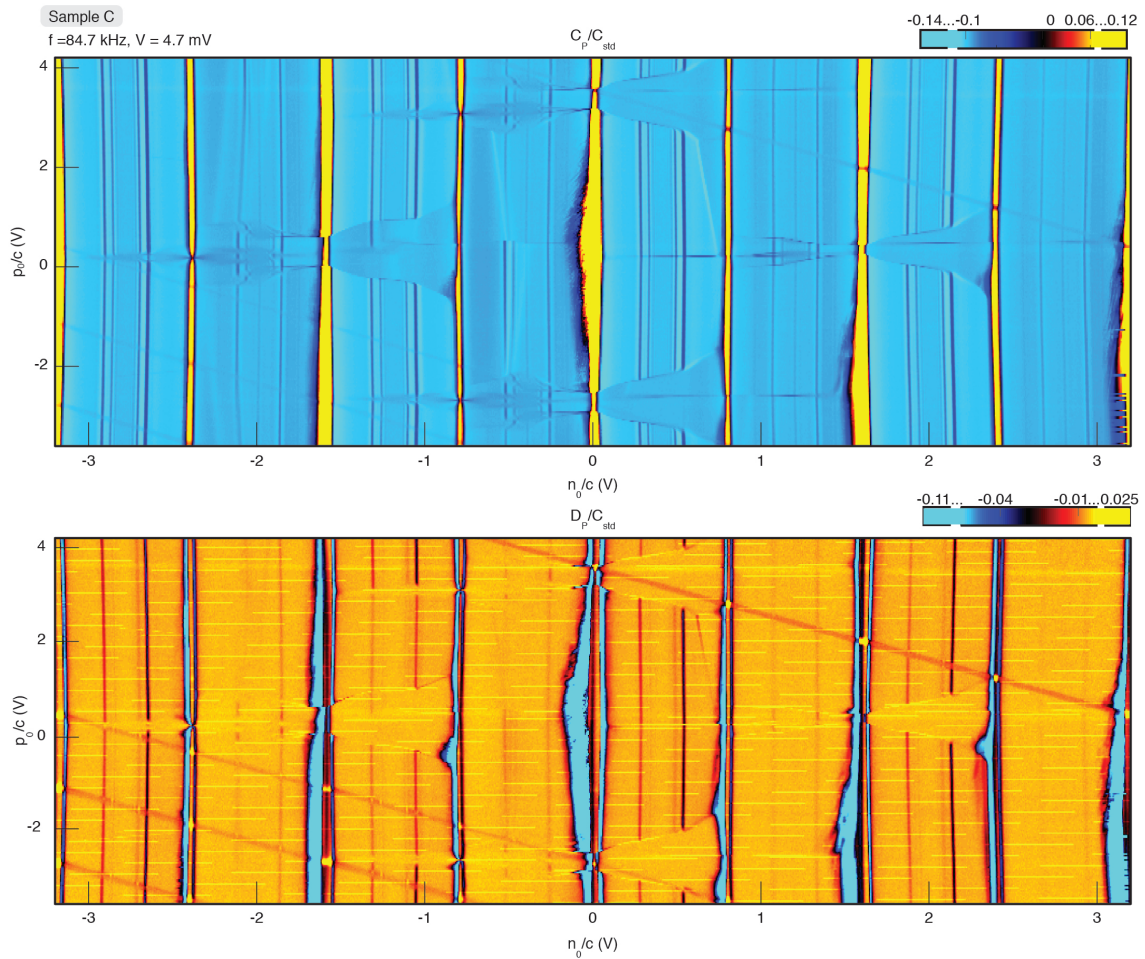


Figure D.15: **Additional data from Device C.** Penetration field capacitance and dissipation for Device C (#HZS63), taken at base temperature and  $B=14\text{T}$ . Data was taken with a 4.7 mV AC excitation at 84.77 kHz applied to the top gate, and is shown in units of an arbitrary fixed reference capacitor.

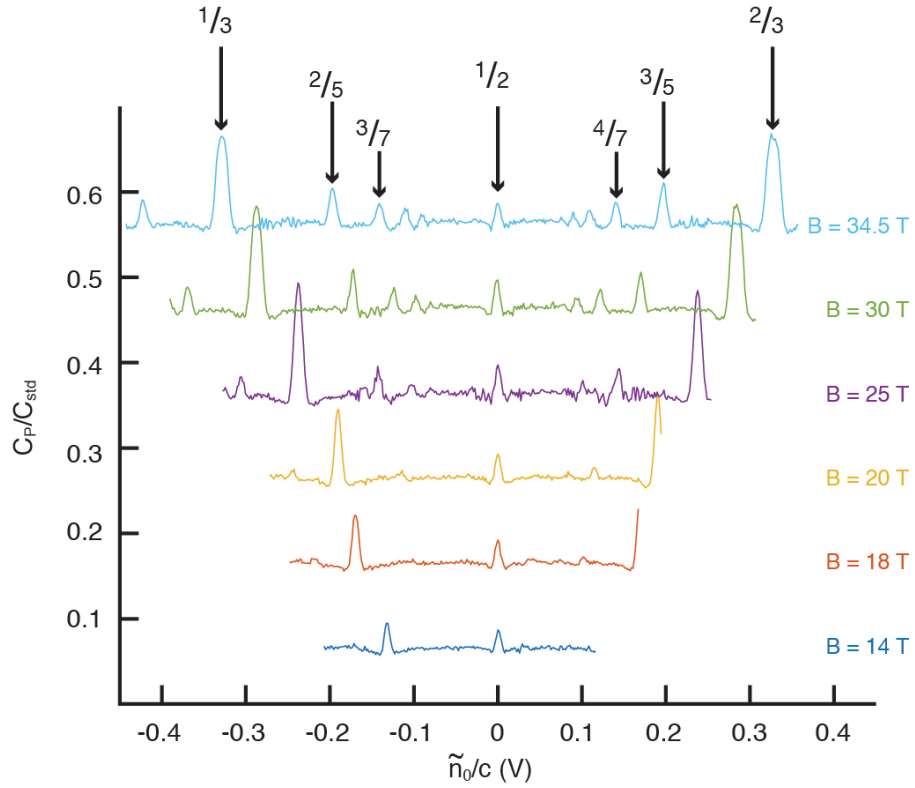


Figure D.16: **Pseudopotential tuning.**  $C_{pen}$  at different magnetic fields in Device C. Data are taken between  $\nu = 1$  and  $\nu = 2$  at  $p_0/c = 6$  V, corresponding to partial occupation of an  $N=1$  orbital level. The line-traces are offset for visibility. As the magnetic field is increased the structure of the wavefunction is tuned from  $N=0$ -like to  $N=1$ -like, and a hierarchy sequence of odd denominator states appears.



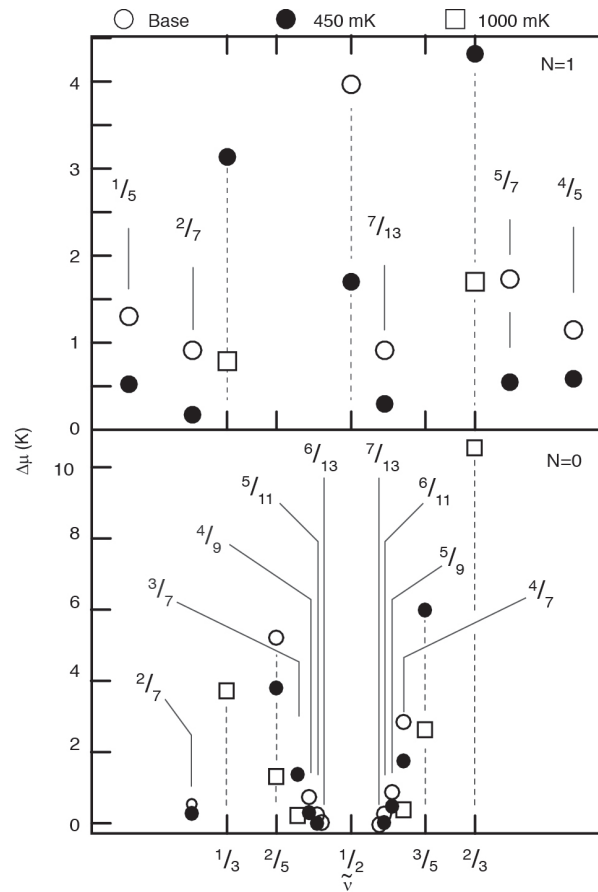


Figure D.17: **Measured gaps of fractional quantum Hall states** Data are taken from Device A at  $B=14$  T, within one of the single component regimes between  $\nu = 0$  and  $\nu = 1$  (for the  $N=0$  orbital) and  $\nu = 1$  and  $\nu = 2$  (for the  $N=1$  orbital). Measurements are taken at temperatures from 20 mK to 1.1 K

# Appendix E

## Supplementary materials for Chapter 6

### E.1 Materials and methods

The device fabrication and measurement techniques presented in Chapter 6 are identical to those presented in Chapter 5, and the device we study here is Sample A in that manuscript. A more comprehensive discussion of fabrication and experimental methods is found in the supplementary material D. We assembled the heterostructure using a dry transfer method which utilizes the van der Waals force to fabricate layered structures consisting of hBN, graphite, and graphene. We contacted the bilayer graphene directly with a thin graphite contact, which in turn was edge contacted with Cr/Pd/Au metallic leads [48]. The top and bottom gates are also thin graphite, which results in devices with significantly less disorder than similar heterostructures with metal gates made using standard deposition techniques[49]. We performed magnetocapacitance measurements to identify bulk gapped states as described in Ref. [49] and references therein. In this work we measure the penetration field capacitance ( $C_P$ ) and the symmetric capacitance ( $C_S$ ), both of which primarily access whether the bulk of the device is gapped or not.  $C_P$  is the capacitance between the top and bottom gate, and it is suppressed when the bi-

layer can screen electric fields (i.e. when the bilayer is compressible and conducting). Gapped states, therefore, appear as peaks of enhanced  $C_P$ .  $C_S$  is the sum of the capacitances of the bilayer to the top and bottom gates, is suppressed when the bilayer is more insulating/incompressible, and therefore gaps appear as dips in  $C_S$ . We have chosen the color scale for both  $C_S$  and  $C_P$  such that gaps appear as warmer colors, despite the sign difference of the gapped features. Due to a small asymmetry between the top and bottom hBN thicknesses, we observed a corresponding asymmetry between top and bottom gate capacitances  $\delta = \frac{c_t - c_b}{c_t + c_b} = 0.018$  which was taken into account when applying  $n_0/c$  and  $p_0/c$  to the device. The full expressions including this asymmetry are  $n_0/c = (1 - \delta)v_t + (1 + \delta)v_b$  and  $p_0/c = (1 - \delta)v_t - (1 + \delta)v_b$ , where  $v_t$  and  $v_b$  are the applied top and bottom gate voltages. The data presented here was taken at relatively high frequencies (between 60 and 100 kHz), where an out of phase dissipative signal is present in many of the gapped states we observe. This arises because the measurement time is not sufficient to fully charge the sample. In this regime, measured capacitance is a convolution of both conductivity and compressibility [183]; however because both low conductivity and low compressibility are hallmarks of gapped states, this does not affect the interpretation of high  $C_P$  or low  $C_S$  as indicative of a gapped state. We performed the magnetocapacitance measurements at the National High Magnetic Field Lab in He-3 refrigerators at their base temperature of  $T \sim 300$  mK. In both measurements, we ramped the field continuously while performing the measurements and were unable to concurrently record the magnetic field. There are systematic errors in the reported field up to  $\sim 0.5$ T between different data sets due to errors in timing between data acquisition and the field sweep. We identify  $t, s$  of linear trajectories of high- $C_P$  features in the main text by visually comparing slopes to known features such as IQH gaps and identifying fields at which multiple features intersect. To more robustly confirm the finding of fractional  $t, s$  states, we used a peak finding algorithm to identify peaks in each horizontal

line scan of  $C_P$  (Fig. E.1), manually grouped the peaks belonging to a single trajectory and then fit their slope and intercept in the  $n_0 - B$  plane. Quantum capacitance prevents a direct conversion from the fitted slope and intercept to quantitative  $t, s$  for the full range of measured voltages and fields. Therefore we used the fitted slopes and intercepts of nearby CI and FQH features to obtain the local conversion to  $t, s$ . These local conversions also give a quantitative check on the conversions from  $B$  to  $n_\Phi$  and  $n_0/c$  to  $n_e$  used in the main text. For Fig. E.1A, we find that  $B_{\Phi_0} = 48.6$  T and  $n_0/c = 3.08$  V at  $n_e = 1$  and for Fig. E.1B we find  $B_{\Phi_0} = 48.3$ T and  $n_0/c = 3.10$  V at  $n_e = 1$ . Both of these conversions are consistent with the values used in Figs. 16.1, E-F.

## E.2 Supplementary text

### Estimating the moiré periodicity

The encapsulated nature of our device does not allow direct scanned probes of the moiré pattern, so we must rely on electronic signatures of the superlattice. First, we estimate the periodicity from zero field features in the density of states and the geometry of our device. We observe satellite peaks in  $C_P$  at approximately  $\left| \frac{n_0^{SAT}}{c} = 11.8 \right|$  V, which do not vary strongly with  $p_0$  (Fig. E.2). These peaks are a direct consequence of the moiré periodicity and occur at  $n_e = \pm 4$  in bilayer graphene, e.g. when there is one of electron of each spin-valley flavor per moiré unit cell [146, 147, 97]. For a triangular lattice

$$\frac{eg_s g_v 2}{\sqrt{3}\lambda^2} = \frac{\varepsilon n_0^{SAT}/c}{d} \quad (\text{E.1})$$

where  $g_s = 2$  and  $g_v = 2$  are the spin and valley degeneracies,  $\lambda$  is the moiré wavelength,  $\varepsilon = (3 \pm 0.15)\varepsilon_0$  is the dielectric constant for hBN[57],  $\varepsilon_0$  is the vacuum permittivity,  $d = 45$  nm is the average thickness of the hBN dielectrics, and  $n_0^{SAT}/c$  is the value of

$v_t + v_b$  at which satellite peaks appear. We estimate, therefore, that  $\lambda = 10.3 \pm 0.3\text{nm}$  and predict  $n_\Phi = 1$  should occur at  $B = \frac{\Phi_0}{(3\lambda^2)/2} = 42.5 - 47.5$  T.

A more accurate method for determining the moiré potential is by noting the crossing of many trajectories around  $B = 24.3 \pm .2\text{T}$ , and associating this field with as  $n_\Phi = 1/2$ . This implies a moiré periodicity of  $\lambda = 9.92 \pm .03$  nm, consistent with the zero-field assessment but considerably more precise. Unlike the zero field assessment, the latter estimate is less susceptible to quantum capacitance corrections to the realized density. Note that for analysis of the observed trajectories in  $C_P$  described in the main text,  $t$  (the inverse slope) is unaffected by the choice of  $\lambda$ , as both  $n_e$  and  $n_\Phi$  go as  $\lambda^{-2}$ .

### **A Minimal model for BLG with a single-layer moiré potential**

The interplay between the moiré potential and the complex high-field physics of bilayer graphene is non-trivial. There are a large number of degrees of freedom (spin, valley, and LL-level index) and competing energy scales (the cyclotron energy  $\omega_c$ , the Coulomb scale  $E_C = \frac{e^2}{\epsilon l_B}$ , the potential bias across the bilayer  $u$ , the Zeeman energy  $E_Z$ , the amplitude of the moiré potential  $V_M$ , and various small interaction anisotropies). In particular, interactions are essential, and even integer gaps cannot be understood based on a single-particle model[57]. While a complete understanding at the microscopic level is not required to demonstrate fractional filling of Chern bands, which follows purely from the observation of quantized fractional  $s$  and  $t$ , in this section we motivate an approximate model for the system which is the starting point for our DMRG simulations. A number of features of our data can be accounted for in this model, including the dominant single-particle CI features.

### **The ZLL in the absence of a moiré potential**

The LLs of graphene are labeled by the electron spin ( $\sigma = \pm 1/2$ ), the graphene valley index ( $\xi = \pm$ ), and the integer LL index ( $N \in \mathbb{Z}$ ). The spin and valley combine to form an approximately SU(4)-symmetric “isospin”, and so the order in which the levels fill depends

on various competing anisotropies. Of particular interest are the eight components of the zeroth Landau level (ZLL), which includes both  $N = 0, 1$  and fills for  $4 < \nu < 4$ , the regime of our experiment. A detailed experimental and theoretical account of the ZLL in the absence of a moiré was provided in Ref. [57], to which we refer the interested reader. Here, we summarize those results at a qualitative level in order to argue the following:

1. it is a reasonable starting point to project the problem into the eight degrees of freedom of the ZLL
2. because of the large interlayer potential difference  $u$  applied in the current experiment, it is further justified to restrict to the four ZLL levels in valley  $+$ , i.e.,  $|\xi N \sigma\rangle \in | +0 \uparrow \rangle, | +0 \downarrow \rangle, | +1 \uparrow \rangle, | +1 \downarrow \rangle$
3. these levels fill in a different order depending on whether  $u < 0$  or  $u > 0$ , leading to different Chern bands and fractional states in these two regimes.

### ZLL projection

To a good approximation, the cyclotron energies of BLG scale as  $E_N^{\omega_c} \approx \hbar\omega_c \sqrt{N(N-1)}$ . The  $N = 0, 1$  levels are near degenerate, so together with spin and valley combine to give the eight components of the “zeroth Landau level” (ZLL). In our experiment, the cyclotron splitting is  $\hbar\omega_c \sim 45 - 120$  meV across the range  $B \sim 1744$ T, the Coulomb interactions are at scale  $E_C \sim 35 - 57$  meV. Earlier electron focusing experiments[169] on encapsulated monolayer graphene estimated the moiré potential magnitude as  $|V_M| \sim 10 - 20$  meV. Given the hierarchy of scales  $E_C, V_M < \hbar\omega_c$ , it is reasonable to project the problem into the eight components of the ZLL. Note that even with the large bias  $u$  (controlled by the experimental parameter  $p_0$ [57]) applied in our experiment, we do not observed crossings between the ZLL and higher LLs.

Focusing on the ZLL, which fills from  $4 < \nu < 4$ , the single particle energies take the

form[57]

$$E_{\text{ZLL}}^{(1)} = N\Delta_{10} - \sigma E^{(Z)} - \xi \frac{u}{2} \alpha_N \quad (\text{E.2})$$

$$\approx B \left[ \frac{\text{meV}}{\text{T}} \right] N \left( 0.3 + 0.013 \xi \frac{u}{2} \right) - 0.116\sigma - \xi \frac{u}{2} \quad (\text{E.3})$$

Here  $1 = \alpha_{N=0} > \alpha_{N=1} > 0$  and  $\Delta_{10} > 0$  are B-dependent factors which can be computed numerically from the band structure of bilayer graphene,  $u$  is the potential difference between the two layers due to a perpendicular electric field (in meV), and  $E^{(Z)}$  is the Zeeman splitting.

*Restriction to valley +.* The effect of the bias  $u$  depends directly on the valley  $\xi = \pm$ ; this is because the ZLL wavefunctions have the property that valley + is largely localized on the top layer, while valley - is largely localized on the bottom layer. Within the ZLL, then, valley  $\approx$  layer and the bias  $u$  splits the valley degeneracy. In our experiment, the top and bottom gates are approximately 100nm apart and at a voltage difference of  $\pm 16\text{V}$ . The layer separation of BLG is 0.335 nm, so we expect a large bias  $u/2 \sim \pm 16 \frac{0.335}{100} \text{eV} = \pm 27 \text{meV}$  across the bilayer, though the precise value of  $u$  is modified somewhat due to the relative dielectric constant of the BLG and hBN. Regardless,  $|u|$  is large enough to ensure that for  $u > 0$ , valley  $\xi = +$  fills before valley  $\xi = -$ , while for  $u < 0$  the reverse occurs[57]. Since the moiré potential couples dominantly to the top layer (a consequence of the near perfect crystallographic alignment of the BLG with the top hBN, but misalignment with the bottom hBN), we expect the Hofstadter features to appear most strongly when valley + is filling. This is confirmed by the Landau fan at  $u > 0$ , shown in Fig. E.3. For  $n_0 < 0$ , the top layer (+) is filling and we see very strong Hofstadter features, while for  $n_0 > 0$ , the bottom layer (-) is filling and the Hofstadter features are absent or weak. For  $u < 0$  (not shown), the opposite is observed. For this reason, in the main text we present data for  $n_0 < 0, u > 0$ , and  $n_0 > 0, u < 0$ , in order

to focus on the electrons affected by the moiré. We thus restrict our attention to the four components  $+N\sigma$  of the ZLL.

*u-dependence of the filling order.* For valley  $+$ , the splitting between the  $N = 0, 1$  orbitals is

$$\varepsilon_{10} \sim B \left[ \frac{\text{meV}}{\text{T}} \right] \left( \frac{u}{2} 0.013 + 0.3 \right) \quad (\text{E.4})$$

Comparing with the small Zeeman energy, at the non-interacting level (for moderate  $u$ ) we expect the levels  $|\sigma N\rangle$  to fill in the order  $|\uparrow 0\rangle, |\downarrow 0\rangle, |\uparrow 1\rangle, |\downarrow 1\rangle$ . However, Coulomb interactions rearrange this order, because filling two orbitals of the same spin, e.g.  $|\uparrow 0\rangle, |\uparrow 1\rangle$ , has much more favorable Coulomb energy than filling two orbitals of opposite spin, e.g.,  $|\uparrow 0\rangle, |\downarrow 0\rangle$ . Having filled  $|\uparrow 0\rangle$ , this effectively reduces the energy of the  $|\uparrow 1\rangle$  level by an amount  $\xi_{10} \propto \sqrt{B}$  (at the level of Hartree-Fock, this is the difference in “exchange energy”). If  $\varepsilon_{10} - \xi_{10} < 0$ , the orbitals will instead fill in order  $|\uparrow 0\rangle, |\uparrow 1\rangle, |\downarrow 0\rangle, |\downarrow 1\rangle$ , an effect which was confirmed experimentally in Ref. [57]. However, because  $\varepsilon_{10} \propto B$  while  $\xi_{10} \propto \sqrt{B}$ , there is a critical  $B$  where  $\varepsilon_{10}$  wins out and the ordering should revert to that expected from the non-interacting picture. For  $u \gg 0$  (e.g. region  $n_0 < 0$ )  $\varepsilon_{10}$  is large and this transition should occur at moderate  $B$ ; for  $u \ll 0$  (e.g. region  $n_0 > 0$ ),  $\varepsilon_{10}$  is small and the transition does not occur until much larger  $B$ . While quantitatively predicting the location of the transition requires accounting for some additional interaction effects (e.g. the Lamb shift and inter-layer capacitance[57]), such a transition is clearly seen in our experiment. Fig. E.3 shows that for  $u > 0$ , there is a transition at  $\nu = 4 + 2$  around  $B \sim 17$  T (indicated by the white arrow). This is the transition between filling  $|\uparrow 0\rangle, |\uparrow 1\rangle$  (low B) and filling  $|\uparrow 0\rangle, |\downarrow 0\rangle$  (high B). No analogous transition is observed for  $u < 0$  at  $\nu = 2$ , at least up to  $B = 44$ T.

The analysis, then, can be summarized as follows. For the  $n_0 < 0, u > 0$  side of the experiment, at high  $B$  there is a large splitting  $\varepsilon_{10}$  between  $|+\sigma 0\rangle$  and  $|+\sigma 1\rangle$ , and



the levels fill in order  $|+\uparrow 0\rangle, |+\downarrow 0\rangle, |+\uparrow 1\rangle, |+\downarrow 1\rangle$   $-4 < \nu < 0$ . In contrast, for the  $n_0 > 0, u < 0$  side of the experiment, the splitting  $\varepsilon_{10}$  between  $|+\sigma 0\rangle$  and  $|+\sigma 1\rangle$  is much smaller, and the levels fill in order  $|+\uparrow 0\rangle, |+\uparrow 1\rangle, |+\downarrow 0\rangle, |+\downarrow 1\rangle$  for  $0 < \nu < 4$ , at least in the absence of a moiré potential. The moiré will “mix” the  $N = 0, 1$  LLs in this regime, as we will see.

### Effect of the moiré potential on the ZLL

Following the existing literature, and the absence of Hofstadter features in states localized on the bottom layer, we assume that the moiré pattern affects only the top layer of the BLG, leading to a six-parameter phenomenological model whose effective two-band Hamiltonian for BLG is given in Ref. [168]. Because the amplitude  $V_M$  of the moiré is small compared to  $\hbar\omega_c$ , we project the moiré Hamiltonian into the ZLL. This assumption is supported by the experimental observation that the cyclotron gaps at  $\nu = \dots - 8, -4, 4, 8, \dots$  remain robust up to  $n_\Phi \sim 1$ , which implies the moiré potential is weak compared to the cyclotron energy. The effective moiré Hamiltonian [168] simplifies drastically when projected into the ZLL, consisting of only a scalar potential. The simplest form of the moiré which is C3 symmetric is of the form

$$V_M(\mathbf{r}) = V_M \sum_{m=0,1,2} e^{i\mathbf{G}_m \cdot \mathbf{r}} + h.c., V_M = |V_M| e^{i\Theta_M}, \quad (\text{E.5})$$

here  $G_m = \hat{R}_{\frac{2\pi m}{3}} \mathbf{G}_0$  are the minimal reciprocal vectors of the moiré pattern.

Taking  $\Theta_M \rightarrow \Theta_M + 2\pi/3$  leaves the model invariant up to a translation, while under inversion  $\Theta_M \rightarrow -\Theta_M$ . We note three special cases: (a)  $\Theta_M = 0 (V_M > 0)$ : an inversion-symmetric triangular lattice in which sites are repulsive (b)  $\Theta_M = 2\pi/6$  (equivalent to  $V_M < 0$ ): an inversion symmetric triangular lattice in which sites are attractive (c)  $\Theta_M = \pm\pi/6 (V_M = \pm i)$ : an inversion anti-symmetric lattice. Cases (a-c) are shown in Fig. E.4. Microscopically, there is no inversion symmetry, and no consensus exists on

the more realistic choice of  $\Theta_M$ .

### Hamiltonian of minimal model

Projecting into the +-valley of the ZLL, a minimal model for the system is then

$$H = \frac{1}{2} \int d^2q \rho_{ZLL+}(-\mathbf{q}) V_c(q) \rho_{ZLL+}(-\mathbf{q}) + \int d^2r V_M(r) \rho_{ZLL+}(\mathbf{r}) + \varepsilon_{10} \hat{N}_{N=1} + E^Z \sigma^Z, \quad (\text{E.6})$$

where  $\rho_{ZLL+}(\mathbf{q})$  is the projected 2D density operator, which requires the use of BLG “form factors” as reviewed in Ref. [57]. The model includes (1) a spin-SU(2) symmetric Coulomb interaction; (2) a moiré potential parameterized by complex amplitude  $V_M$  (Eq. (E.5)); (3) a splitting  $\varepsilon_{10}$  between the  $N = 1$  and  $N = 0$  orbitals, which depends on  $B$  and  $u$  (4) a Zeeman splitting. We ignore the small SU(4)-breaking valley interaction anisotropies; they are unlikely to play a role here due to the large valley splitting  $u$ .

### Single particle analysis

We begin with a single-particle analysis to compare the non-interacting (integer  $t, s$ ) features we observe to the expected Hofstadter spectrum. Given  $E_C > V_M$ , interactions may change the observed Hofstadter spectrum significantly, and we do not necessarily expect quantitative agreement with experiment.

While the limit in which the lattice potential is the largest scale has received the most attention of late, leading to a tight-binding problem with complex hopping amplitudes, [148, 197, 198, 30] in our experiment the lattice is weak compared with the cyclotron gap. In this limit it is appropriate to consider the Hamiltonian of Eq. (E.6), where the lattice potential is projected into the continuum Landau levels, as analyzed in Refs. [199] and [200]. Hints of this physics were observed in semiconducting quantum wells with patterned superlattice [201, 202].

At the single-particle level, the two spins decouple and the phase diagram depends only on the complex ratio  $V_M/\varepsilon_{10}$ . Two illustrative Hofstadter spectra are shown in

Fig. E.5. At low  $n_\Phi$ , the energy spectrum collapses into two flat bands separated by  $\varepsilon_{10}$ ; these are the  $N = 0, 1$  continuum LLs. This is consistent with experiment, where Hofstadter features only begin appearing around  $n_\Phi > 1/3$ . This can be qualitatively understood because potentials which vary faster than  $l_B$  are invisible to the low LLs. Quantitatively, when potential  $V_M(\mathbf{G})$  is projected into LL  $N = 0, 1$ , it is scaled by the factor  $\mathcal{F}_{00}(G) = e^{-\frac{(Gl_B)^2}{4}}$  and  $\mathcal{F}_{11} = e^{-\frac{(Gl_B)^2}{4}}(1 - \frac{(Gl_B)^2}{2})$  respectively. As  $\frac{(Gl_B)^2}{4} = \frac{\pi}{\sqrt{3}n_\Phi}$ , the potential vanishes at low  $n_\Phi$ . The  $N = 1$  level also develops bandwidth faster than the  $N = 0$  level, because of the factor  $(1 - \frac{(Gl_B)^2}{2}) < -1$  in the effective  $N = 1$  potential.

Interestingly, when  $|V_M|/\varepsilon_{10} \gtrsim 1$ , bands with different Chern number can be realized for different values of  $\varepsilon_{10}$ , which can be tuned with  $u$  (i.e.  $p_0$ ) in our measurements. This is evident in the differences in single-particle gaps which appear in our measurements at positive and negative  $p_0$  (Figs. 6.1C-F). In the future, this could be used to engineer the butterfly spectrum in-situ. To compare this model with experiment, we analyze the  $u > 0$  and  $u < 0$  cases separately, as they have very different  $|V_M|/\varepsilon_{10}$  ratios. We recover many of the single-particle features we observe by fine tuning  $|V_M|/\varepsilon_{10}$  and  $\Theta_M$  of the model moiré pattern.

**Case I:**  $n_0 < 0, u > 0$ . In this regime, several observations are consistent with our assertion that  $u$  leads to a large splitting  $\varepsilon_{10}$  between the  $N = 0, 1$  orbitals. For large  $\varepsilon_{10}$ , we expect the filling order is  $|+\uparrow 0\rangle, |+\downarrow 0\rangle, |+\uparrow 1\rangle, |+\downarrow 1\rangle$ . This order is supported by the presence of a feature at  $\nu = -3$ , indicated by an arrow in Fig.E.3, which presumably marks a phase transition from the previously reported [162] lower- $u$  filling order  $(|+\uparrow 0\rangle, |+\uparrow 1\rangle, |+\downarrow 0\rangle, |+\downarrow 1\rangle)$ .

The  $|V_M|/\varepsilon_{10} < 1$  limit is also consistent with several other experimental observations: (1) the LL gaps at  $\nu = 4, 3, 2, 1$  persist across  $n_\Phi = 1/2$ , indicating  $V_M$  is too weak to overcome  $\varepsilon_{10}$  at this magnetic field; (2) filling  $4 < \nu < 3$  looks similar to  $3 < \nu < 2$  (both are dominated by  $\mathcal{C} = -1, 2$  Chern-bands, with FCIs in the first  $\mathcal{C} = -1$  band),

while  $2 < \nu < 1$  looks more similar to  $1 < \nu < 0$ . This again supports the filling order  $\sigma N = |\uparrow 0\rangle, |\downarrow 0\rangle, |\uparrow 1\rangle, |\downarrow 1\rangle$ . (3) The Hofstadter features begin appearing at  $n_\Phi \sim 1/2$  for filling  $4 < \nu < 2$ , while they appear earlier, around  $n_\Phi \sim 1/3$ , for  $2 < \nu < 0$ . This is consistent with the expected broader moiré-induced bandwidth of the  $N = 1$  levels, which fill after the  $N = 0$  orbitals.

To compare our single particle model with experiment, we calculated the single-particle Hofstadter butterfly for  $V_M$  with different  $\Theta_M$  in the limit of  $|V_M|/\varepsilon_{10} \rightarrow 0$ . (the result is qualitatively unchanged for small but finite  $|V_M|/\varepsilon_{10}$ ). In Fig. E.6, we plot the calculated single particle gaps on a Wannier plot for the three cases shown in Fig. 6.1C, assuming the  $|N\rangle = |0\rangle, |0\rangle, |1\rangle, |1\rangle$  filling order described previously. In the  $N = 0$  orbital,  $\delta t = -1, 2$  bands are prominent in the data, and theoretically are predicted for  $\Theta_M = 0, \pi/6$  but not  $\pi/3$ . The inversion-odd case ( $\pi/6$ , Fig. E.6C) favors features which are more particle-hole symmetric within a LL, and lead to crossing features at low  $n\hat{\eta}e$  which are observed in the data (Fig. 6.1C). Comparing with our data in this regime, we thus conclude that  $\theta_M$  is somewhere between 0 and  $\pi/6$ .

By setting  $\Theta_M = \pi/8$ , we observe good agreement between the calculated Chern band structure and the observed bands (Fig. E.7). We used the calculated Hofstadter spectrum (Fig. E.7A) to generate a Wannier plot (Fig. E.7B) which matches the filling order of orbitals observed in the data. The color of the points encodes the size of the single particle gap ( $\Delta/|V_M|$ ), and we only plot gaps above a threshold, in effect cutting off the fractal nature of the Hofstadter spectrum. We color the bands of the energy spectrum and Wannier plot based on their Chern numbers, using the rules outlined in the main text.

In Fig. E.7C we generate a qualitatively equivalent plot from the data (from Fig. 6.1C) by plotting the height of peaks in  $C_P$  as a function of density ( $n_0/c$ ) and magnetic field ( $B$ ). We again color the Chern bands, now ignoring gapped trajectories which we

know to be outside of the single-particle picture.

In  $N = 0$  orbitals, we observe  $\Delta t = -1, 2$  bands filling above  $n_\Phi = 1/2$  in both the calculation and experiment. Additionally, the appearance of  $\Delta t = -2, 3, 5$  bands below  $n_\Phi = 1/2$  in  $N = 1$  bands is consistent. Some features, e.g. the differences in filling order of Chern bands in  $N = 1$  orbitals above  $n_\Phi = 1/2$ , cannot be reproduced without invoking mixing between spin species, which is not allowed in the single particle model we present. Details of  $\mathcal{C} = -1$  band hosting FCI states. The  $\nu_C = 1/3, 2/3$  FCI states discussed in the main text occur in a  $\mathcal{C} = -1$  band of the  $n_0 > 0, u < 0$  region, which, as discussed above, arises in a model of a moiré potential with  $0 < \Theta_M < \pi/6$  projected into a single  $|+0\sigma\rangle$  level. In our DMRG calculations (see next section) we choose  $\Theta_M = \pi/8$ , which reproduces most of the large single-particle gaps in the  $n_0 < 0, u > 0$  side of the data as well.

In Fig. E.8, we show the real-space charge density profile and energy dispersion of this band at  $n_\Phi = 2/3$ , assuming  $V_M/\varepsilon_{10} = 1/6$  and  $\Theta_M = \pi/8$ . From the density profile, we see that the  $\mathcal{C} = 1$  band is localized on a triangular lattice.

**Case II:**  $n_0 > 0, u < 0$ . In this regime, we expect  $\varepsilon_{10}$  is smaller and, in the absence of a moiré potential, the levels would fill in order  $|+\uparrow 0\rangle, |+\uparrow 1\rangle, |+\downarrow 0\rangle, |+\downarrow 1\rangle$ . This is consistent with experiment: the  $\nu = 2$  LL gap is robust, and the  $0 < \nu < 2$  physics looks very similar to the  $2 < \nu < 4$  physics. Strikingly, we see that the  $\nu = 1, 3$  LL gaps are destroyed near  $n_\Phi = 1/2$ . For  $n_\Phi = 1.2, 0 < \nu < 2$ , the system has rearranged from  $\mathcal{C} = 1, 1$  LLs into  $\mathcal{C} = -1, 3$  Chern-bands, which requires  $V_M$  comparable to  $\varepsilon_{10}$ .

The calculated Wannier plots with  $|V_M|/\varepsilon_{10} = 6.0$  shows the dependence on the moiré parameter  $\Theta_M$ , where the strength of the moiré now strongly mixes  $N = 0$  and  $N = 1$  orbitals of the same spin (Fig. E.9).

At the single particle level, we can ask which values of  $|V_M|/\varepsilon_{10}$  and  $\Theta_M$  rearrange filling  $0 < \nu < 2$  at  $n_\Phi = 1/2$  into  $\mathcal{C} = -1, 3$  bands. We find that  $\Theta_M = 0, \pi/6$

both reproduce this behavior, while  $\Theta_M = \pi/3$  does not. Weaker features, such as the presence of  $\mathcal{C} = 5$  bands around  $n_\Phi = 2/5$  favor a more antisymmetric form of the moiré potential (e.g.  $\Theta_M$  close to  $\pi/6$ ). The value  $\pi/8$  used in our DMRG numerics satisfies these constraints.

As before, tuning  $\Theta_M$  generates good agreement between the calculated Chern band structure and the observed bands (Fig. E.10). We find that  $\Theta_M = 0.5$ ,  $|V_M|/\varepsilon_{10} = 6.0$  gives slightly better agreement for some weaker gaps above  $n_\Phi = 1/2$  than  $\Theta_M = \pi/8$  (which is used in the iDMRG calculations), but the  $\Delta t = +3$  band where we performed the calculation is robust in both cases.

We color both the calculated and experimental Wannier plots (Fig. E.10, B-C) in the same way as before. Here, we replicated the entire mixed Hofstadter spectrum to reproduce  $2 < \nu < 4$  and a large  $\nu = 2$  gap is assumed. This matches the observed filling order of  $|+\uparrow 0\rangle, |+\uparrow 1\rangle, |+\downarrow 0\rangle, |+\downarrow 1\rangle$ .

Focusing on  $0 < \nu < 2$  in the experimental data, we find a very close match between the observed Chern bands. Many features of the data are reproduced, including the  $n_\Phi$  onset of Hofstadter features in  $N = 0$  and  $N = 1$  orbitals, disappearance of the  $\nu = 1$  gap at  $n_\Phi = 1/2$ , presence of a  $\Delta t = 5$  band above  $n_\Phi = 2/5$  and the first and last filled  $\Delta t = +2$  bands above  $n_\Phi = 1/2$ .

Deviations between the theory and experiment are primarily in smaller gap features. For example, the calculated spectrum shows low field  $\delta t = +3, -5$  bands, which are a single  $\Delta t = -2$  band in the data. Small adjustments to the moiré potential, disorder, or indeed the same interactions which lead to FCI and SBCI physics could all in principle change the sizes of smaller gaps enough to generate these discrepancies.

#### *Infinite DMRG Simulations*

Here we present infinite DMRG simulations of the model just derived. Following our discussion, the simulations are not simulations of a tight-binding lattice model, rather,

we project the interactions and lattice potential into the continuum LLs of the ZLL. While a number of numerical works have considered fractional quantum Hall physics in the opposite Harper-Hofstadter tight-binding limit [154, 155, 157, 158, 159, 203, 204, 205, 206, 207, 208], less attention has been paid to the weak-potential limit of the present experiment [209]. We will consider both an FCI and SBCI, in both cases choosing a moiré parameter  $\Theta_M = \pi/8 \sim 0.4$ , which (at the single particle level) is consistent with all the dominant integer CI features.

$$\nu_C = 1/3 \text{ FCI in } -1 \text{ band}$$

The  $\mathcal{C} = -1$  band detailed in Fig. 6.2 of the main text can be accounted for if  $|V_M|/\varepsilon_{10}$  is small, as discussed above. Since the simulations are challenging in the presence of the moiré potential, and  $|V_M|/\varepsilon_{10}$  is small, we make a further approximation by discarding the  $|+\uparrow 1\rangle$  level, projecting entirely into  $|+\uparrow 0\rangle$ . Following our earlier discussion, we consider the Hamiltonian

$$H = \frac{1}{2} \int d^2q \rho(-\mathbf{q}) V_c(q) \rho(-\mathbf{q}) + \int d^2r V_M(\mathbf{r}) \rho(\mathbf{r}), \quad (\text{E.7})$$

$$V_M(\mathbf{r}) = V_M \sum_{m=0,1,2} e^{i\mathbf{G}_M \cdot \mathbf{r}} + h.c., \quad (\text{E.8})$$

where  $\rho(\mathbf{q})$  is the density operator projected into a single  $N = 0$  LL. The Coulomb interaction is  $V_C(q) = E_C \frac{2\pi}{q} \tanh\left(\frac{qd}{2}\right)$  (where  $q$  is in units of  $l_B^{-1}$ ) due to screening from the graphite gates at a distance  $d \sim 10l_B$  from the BLG. Here  $E_C = \frac{e^2}{\varepsilon l_B}$  is the Coulomb scale. However, having projected out the other LLs, to make a more quantitative comparison with experiment we also include RPA screening from the filled LLs below the ZLL [128],

$$V_{RPA}(q) = \frac{V_C(q)}{1 + V_C(q)\Pi(q)}, \quad \Pi(q) = a \frac{4 \log(4) \tanh(bq^2 l_B^2)}{2\pi E_C} \quad (\text{E.9})$$

The screening weakens the short-distance part of the Coulomb interaction. While not essential to the existence of the FCI - we also find the FCI state without it - it does change the range of  $|V_M|/E_C$  where the FCI is stabilized by around  $\sim 20\%$ , since it effectively reduces the Coulomb scale.

Following comparison between DMRG numerics and experimental data in an earlier work[57], we take  $a = 0.2 \frac{E_C}{\hbar\omega_c}$ ,  $b = 0.62$  where  $\hbar\omega_c$  is the cyclotron energy at the desired field. For the moiré, we choose  $V_M = e^{2\pi i/16}|V_M|$  (this choice of  $\Theta_M$  reproduces the experimentally observed CIs in our measurements), while  $|V_M|/E_C$  is a tunable parameter to be explored.

iDMRG proceeds by placing the above continuum quantum Hall problem onto an infinitely long cylinder of circumference  $L$  [136]. iDMRG requires an ordering of the single-particle states into a 1D chain, which arises naturally on the cylinder when the LL orbitals are taken in the Landau gauge. We emphasize again that the “sites” in our chain are not the minima of the moiré potential, but rather the orbitals of the continuum LL. To accommodate the triangular moiré lattice with Bravais vectors  $\mathbf{a}_1, \mathbf{a}_2$ , we form a cylinder by identifying  $\mathbf{r} \sim \mathbf{r} + 9\mathbf{a}_1$ . Working at  $n_\Phi = 2/3$  this corresponds to a cylinder of circumference  $L \approx 19.9l_B$ .  $\nu_C = 1/3$  filling of the  $\mathcal{C} = -1$  band corresponds to  $\nu = 1/3$  of the  $N = 0$  LL. iDMRG[210] using  $m = 3000$  states was used to find the ground state for a range  $|V_M|/E_C$ . The lattice reduces the continuous translation symmetry of the cylinder down to  $\mathbb{Z}_9$ , making the simulations more expensive; nevertheless, the DMRG truncation error was less than  $3 \times 10^{-6}$  throughout the FCI phase.

For an intermediate range of  $0.29 < |V_M|/E_C < 0.74$ , we find a state with a short correlation length ( $\xi \sim 3\lambda$ , where  $\lambda$  is the period of the moiré lattice) and  $t, s = -1/3, 1/3$  (we ignore electrons below the ZLL), which we thus identify as an FCI. The entanglement spectrum of the FCI is shown in Fig. E.11A, and is consistent with a Laughlin type state but with negative Hall conductance [192].



We measure  $(t, s)$  as follows. Since  $\nu = t + sn_\Phi$  (tautologically), it is sufficient to measure either  $s$  or  $t$ , and in our simulations it is most convenient to measure  $s$ . We do so by repeating iDMRG for a series of moiré potentials which are displaced by a distance  $\Delta x$  along the cylinder,  $V(\mathbf{r}) = V(\mathbf{r} - \Delta_x)$ , obtaining a sequence of ground states  $|\Delta x\rangle$ . By definition,  $s$  is the amount of charge per unit cell which should be transported along with the lattice. The charge which passes a cut around the cylinder is  $\Delta Q = sL\Delta x/\mathcal{A}$ , where  $\mathcal{A}$  is the volume of the unit cell.

We can measure the amount of charge transported  $\Delta Q$  by using the entanglement spectrum to compute the charge polarization of  $|\Delta x\rangle$  as discussed for an analogous measurement of the Hall current in Ref. [136]. To ensure adiabaticity,  $\Delta x$  was incremented in units of  $l_B/24$  using the previous ground state to initialize the DMRG. The results give a perfectly quantized value for  $s$  within the  $10^{-6}$  precision of the numerics.

For  $|V_M|/E_C < 0.29$ , the ground state is found to increase the unit cell with a 3x3 reconstruction, forming a triangular Wigner crystal shown in Fig. E.11B. Effectively, all the electrons in the ZLL are inert:  $t = 0, s = 1/9$ . This is to be expected, since the Coulomb interaction alone stabilizes a Wigner crystal at such low fillings ( $\nu = 1/9$ ). The location of the transition can be diagnosed from  $\langle \rho(\mathbf{G}_0/3) \rangle$ , where  $\mathbf{G}_0$  is a reciprocal vector of the moiré. To see the symmetry breaking, the numerics must be done with an enlarged unit cell and lower degree of momentum conservation.

For  $0.74 < |V_M|/E_C$ , there is a change in the correlation length and entanglement properties as the system enters a compressible phase through what appears to be a continuous phase transition. This region is rather complex. When  $|V_M|/E_C \rightarrow \infty$ , the system should be a non-interacting metal due to the small but finite bandwidth of the Chern band. It is very interesting question whether, in 2D, there is a direct transition between the FCI and this metal, or whether an intermediate state (such as a composite Fermi liquid or symmetry broken phase) intervenes. However, this 2D physics is subtle

to address on the cylinder, where we suspect there is in fact a sequence of several KT-transitions. To see this, we used “finite entanglement scaling” [211] to measure the central charge  $c$  of the cylinder state. At  $|V_M|/E_C = 2$ , we find a very precise value of  $c = 3$  (Fig. E.11C), while at  $|V_M|/E_C = 6$  we find  $c = 6$ . Multiples of 3 are expected, because the magnetic algebra at  $n_\Phi = 2/3$  enforces a 3-fold degeneracy in the Fermi surface. The 2D Fermi surface of the metal descends to a several-component Luttinger liquid on the cylinder due to the quantization of the momentum around the cylinder. As  $|V_M|/E_C$  changes the Luttinger exponents, it naturally could drive a sequence of KT-transitions at which some, but not all, of the modes lock.

In precisely the same regime that finite entanglement scaling finds a finite central charge, we also observe a weak “stripe”-like order; translation is preserved along  $\mathbf{a}_1$ , but  $\mathbf{a}_2$  is broken. This can be diagnosed from  $\langle \rho(\mathbf{G}')/2 \rangle$  for an appropriate reciprocal vector. It is difficult to determine whether this is a true property of the ground state, or is instead a finite-entanglement artifact,  $\langle \rho(\mathbf{G}')/2 \rangle \propto \xi_{FES}^{-\Delta}$ , where  $\xi_{FES}$  is a correlation length introduced by the finite bond dimension of our DMRG numerics. Regardless, it gives a very clear indication of the onset of the gapless phase, so is the metric we presented in the phase diagram of the main text.

For comparison with experiment, we note that  $E_C = 48$  meV at  $B = 32$  T ( $n_\Phi = 2/3$ ) assuming a dielectric constant of  $\varepsilon = 0.66$  for the surrounding BN. This gives the estimate  $14 < |V_M| < 38$  meV for an FCI, consistent with the expected moiré amplitude.  $\nu_C = p/3$  SBCI in  $\mathcal{C} = 3$  band.

The  $\mathcal{C} = 3$  band hosting the SBCI state detailed in the main text emanates from  $\nu, n_\Phi = 2, 1/3$ . As discussed, near  $n_\Phi = 1/2$  the stability of this  $\mathcal{C} = 3$  band requires a small  $\varepsilon_{10}$  which mixes the  $N = 0, 1$  levels. However, we have verified that near  $n_\Phi = 1/3$ , the  $\mathcal{C} = 3$  band remains stable even as  $\varepsilon_{10} \rightarrow \infty$ .

In this limit, the  $N = 0$  level is completely filled and inert, and the potential  $V_M$  is effectively projected into an  $N = 1$  level. While a quantitative study of the SBCI may require keeping both  $N = 0, 1$  levels and finite  $\varepsilon_{10}$ , this is numerically challenging, so we take advantage of this finding to take  $\varepsilon_{10} \rightarrow \infty$  and project the problem into the  $N = 1$  level. The Hamiltonian is the same as in Eq. E.9, but now  $\rho(q)$  is the density operator projected into a  $N = 1$  LL (in fact if we incorrectly project into  $N = 0$  level, we do not find an SBCI). We take  $V_M = |V_M|e^{\frac{2\pi i}{16}}$  as before.

We again place the problem on the cylinder, but this time we identify  $\mathbf{r} \sim \mathbf{r} + 12\mathbf{a}_1$ . This was chosen to accommodate a tripled unit cell with enlarged Bravais vector  $\mathbf{a}_1 + \mathbf{a}_2$ . We work at  $n_\Phi = 3/8$ , where  $\nu_C = 1/3, 2/3$  of the  $C = 3$  band correspond to filling  $\nu = 1 + 7/9$  and  $\nu = 1 + 8/9$  (the integer part of the filling is now assumed to occupy an inert  $N = 0$  LL). iDMRG was performed while keeping 3000 states. We have not obtained a full phase diagram for  $|V_M|/E_C$ , but found a range of values (e.g.  $|V_M|/E_C = 0.6$  in the main text) which stabilize an SBCI state and are consistent with the domain of the  $\mathcal{C} = -1$  FCI. The SBCI is diagnosed by a tripled unit cell (seen in the real-space density) and the experimentally predicted  $t, s$  again measured by adiabatically dragging the lattice. We note that working on an infinitely long cylinder greatly simplifies the detection of the symmetry breaking. Because the symmetry is discrete, it can be spontaneously broken in this geometry, unlike in finite-size simulation on a torus.

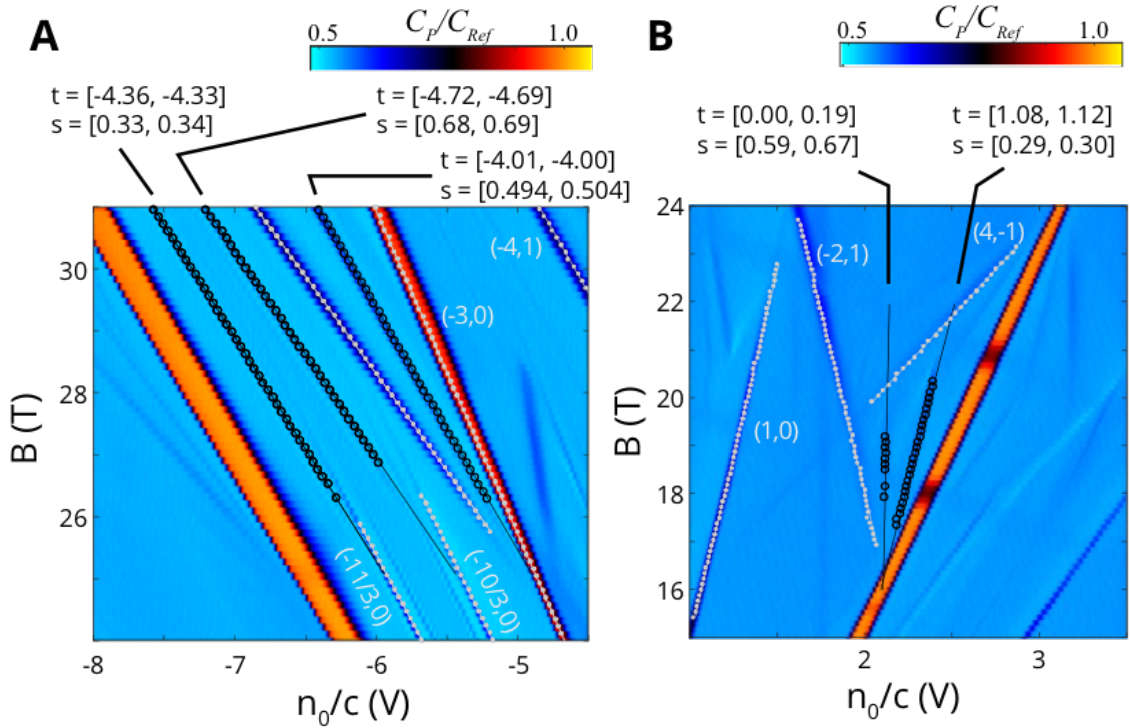


Figure E.1: **Fits to  $t, s$  for FCI and SBCI states.** (A) Peaks corresponding to the FCI states presented in Fig. 6.2A,D (black circles) were fit to obtain their slope and intercept in the  $n_0/c - B$  plane (black lines). The fitted slopes of nearby CI and FQH features (gray lines) were used to convert from the fitted parameters to a fitted  $t, s$ , which match the expected values of  $(-13/3, 1/3)$  and  $(-14/3, 2/3)$  to within 5%. Numbers in brackets are the 95% confidence intervals obtained by linear regression. An SBCI in a  $\Delta t = 2$  band also matches its predicted value of  $(t, s) = (-4, 0.5)$ . (B) Similar analysis performed for SBCI states in Fig. 6.2B, E.  $t, s$  values for these SBCI match within 10% of their expected values of  $(0, 2/3)$  and  $(1, 1/3)$ .

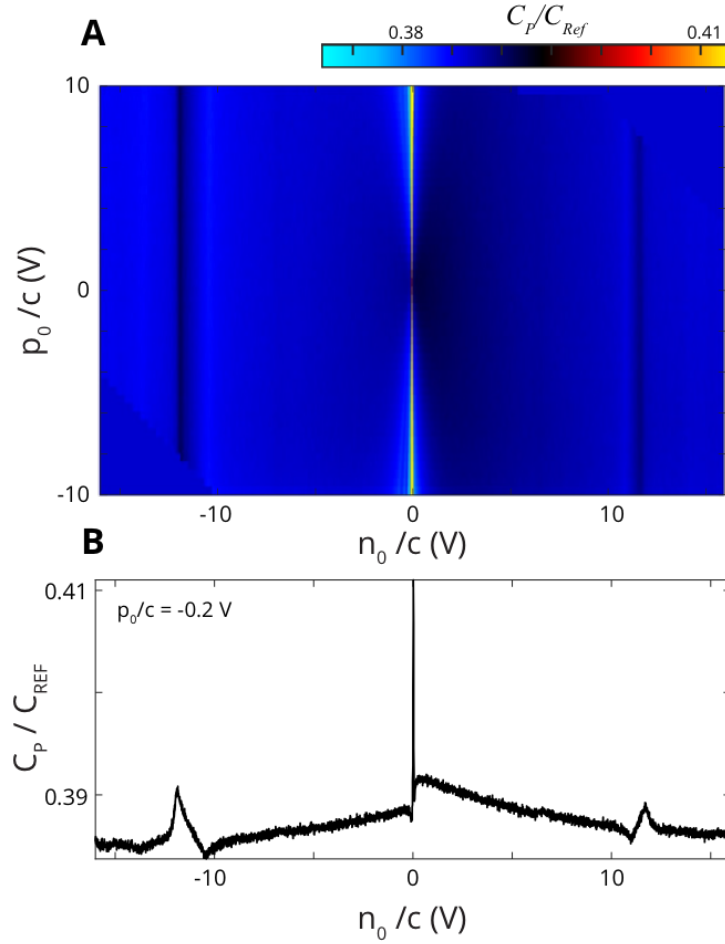


Figure E.2: **Zero magnetic field  $C_P$  showing satellite Dirac points.** (A)  $C_P$  taken as a function of the nominal electron density ( $n_0/c$ ) and polarizing electric field ( $p_0/c$ ). This measurement was taken at the nominal base temperature of our dilution refrigerator ( $T < 50$  mK) at zero applied magnetic field. We find additional peaks in  $C_P$  at  $n_0/c \approx 11.8$  V. The top right and bottom left corners are masked off (data was not taken in those regions) to protect the gates from leakage. (B) Horizontal line cut of (A) taken at fixed  $p_0/c = -0.2$  V.

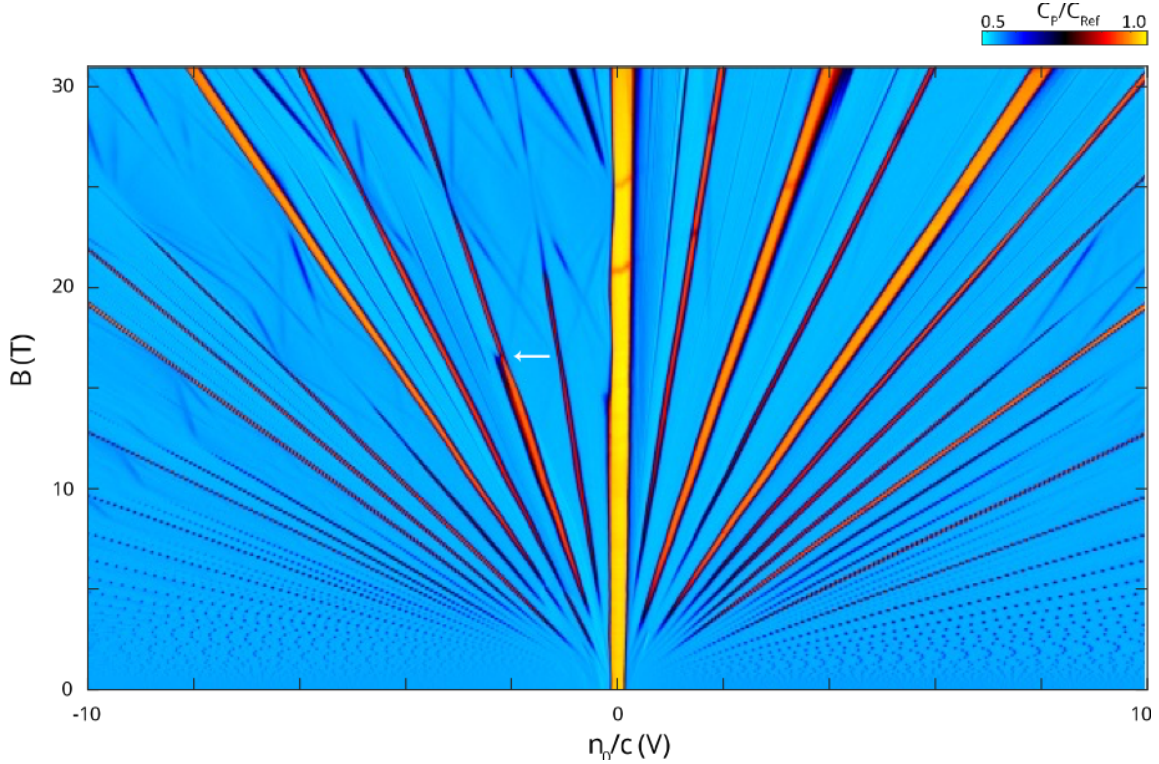


Figure E.3: **Full Landau fan at  $p_0/c = +16$  V.** The effect of the moiré between the top hBN and bilayer graphene is largely suppressed for states localized on the bottom layer (e.g. when  $n_0/c > 0$ ,  $p_0/c = +16$  V). In this regime, Landau levels in the ZLL exhibit the conventional fractional quantum Hall effect up to 31 T and do not show any Hofstadter (non-zero  $s$ ) features. Hofstadter features are, however, observed in higher Landau levels in this regime. Additionally, we observe a feature  $B \sim 16$ T and  $\nu = -2$  (white arrow) which we attribute to a spin transition between a spin-unpolarized  $\nu = -2$  at low fields to a spin-polarized  $\nu = -2$  at high fields, as described in the supplementary text. Above this field, the ZLL fills two  $N = 0$  orbital states first (rather than an  $N = 0$  followed by an  $N = 1$ ). This feature, not previously reported, can be attributed to the very large electric fields used in this experiment as compared with previous work

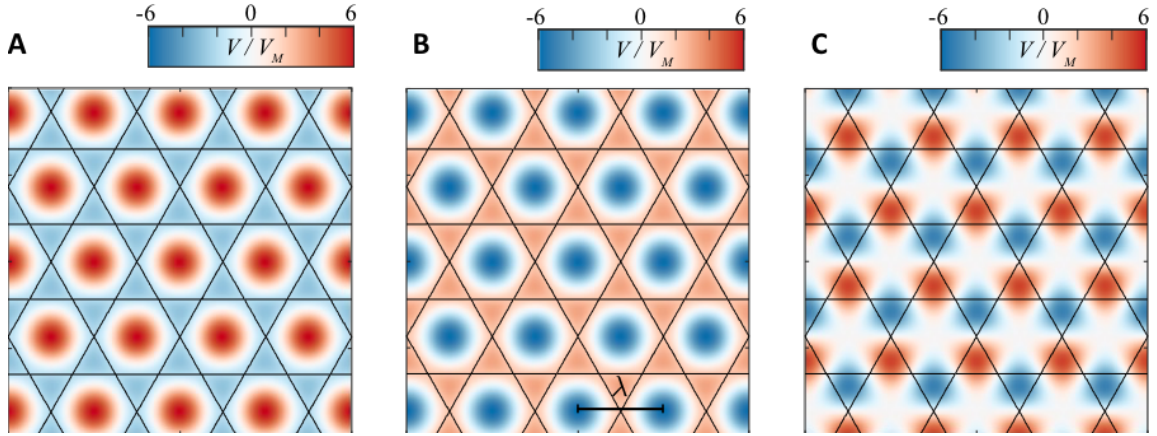


Figure E.4: **Calculated moiré potentials.** Real-space moiré potentials for (A)  $V_M = 1$ , or  $|V_M| = 1, \Theta_M = 0$ , (B)  $V_M = 1$ , or  $|V_M| = 1, \Theta_M = \pi/3$  (C)  $V_M = i$ , or  $|V_M| = 1, \Theta_M = \pi/6$ . The positive (negative)  $V_M$  potential is repulsive (attractive) on the triangular lattice, and attractive (repulsive) on the honeycomb lattice.

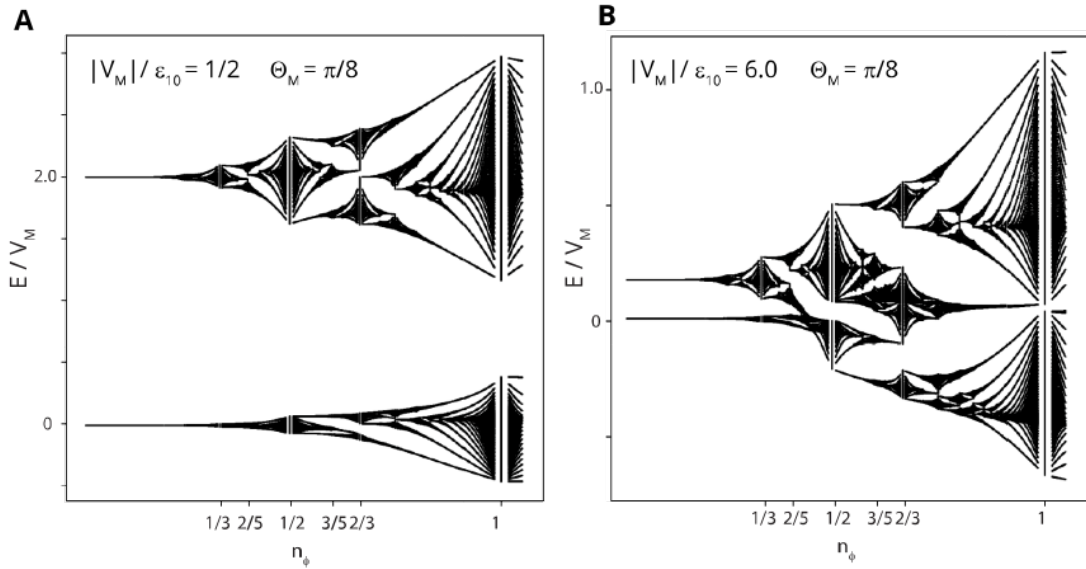


Figure E.5: **Single particle Hofstadter butterfly.** Single-particle Hofstadter spectrum calculated using the moiré parameters (A)  $|V_M|/\epsilon_{10} = 1/2$  and  $\Theta_M = \pi/8$  and (B)  $|V_M|/\epsilon_{10} = 6$  and  $\Theta_M = \pi/8$ .

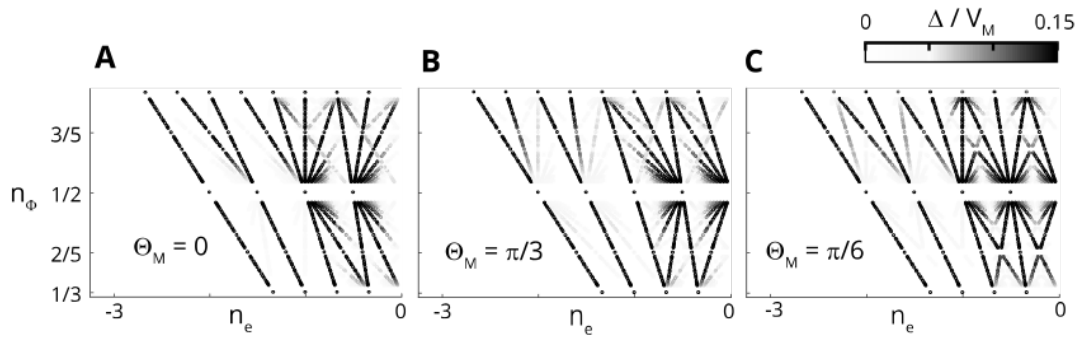


Figure E.6: **Calculated Wannier plots for the  $n_0 < 0, u > 0$  case.** Calculated gap sizes in units of the magnitude of the moiré potential ( $\Delta/V_M$ ) as a function of  $n_e$  and  $n_\phi$  for  $\Theta_M = 0$  (A),  $\Theta_M = \pi/3$  (B), and  $\Theta_M = \pi/6$  (C). The splitting between LLs  $\varepsilon_{10}$  is chosen to be larger than any Hofstadter gaps.



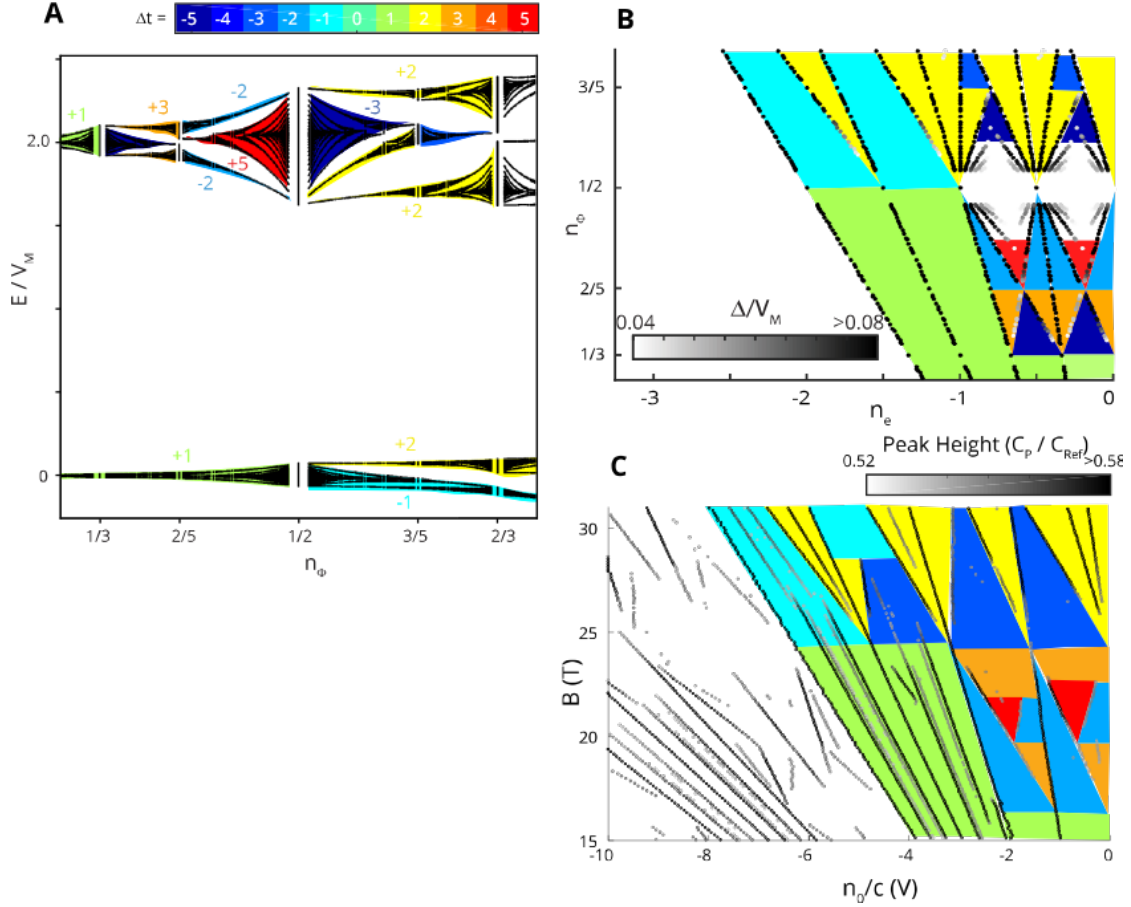


Figure E.7: **Comparison of calculated and observed single particle Chern bands.** (A) Single-particle Hofstadter spectrum calculated using the moiré parameters  $|V_M|/\varepsilon_{10} = 2.0$  and  $\Theta_M = \pi/8$  are chosen to match the  $n_0 < 0, u > 0$  case.  $\Delta_t = C$  bands are labeled from the Wannier plot (B) using the procedure described in the main text (Fig. 6.1G). (B) Calculated Wannier plot constructed from (A). The points are colored according to the size of the gap ( $\Delta/V_M$ ) while the bands are colored according to Chern number. To match the experimental data, the spectrum in (A) was separated by orbital and tiled with filling order  $N = 0, 0, 1, 1$  starting at  $\nu = -4$ . (C) Peak height of gapped states (black to gray points), extracted from data in Fig. 6.1C, as a function of charge carrier density ( $n_0/c$ ) and magnetic field ( $B$ ). The bands are colored according to their single-particle  $\Delta t$ , using the same rules as (B).

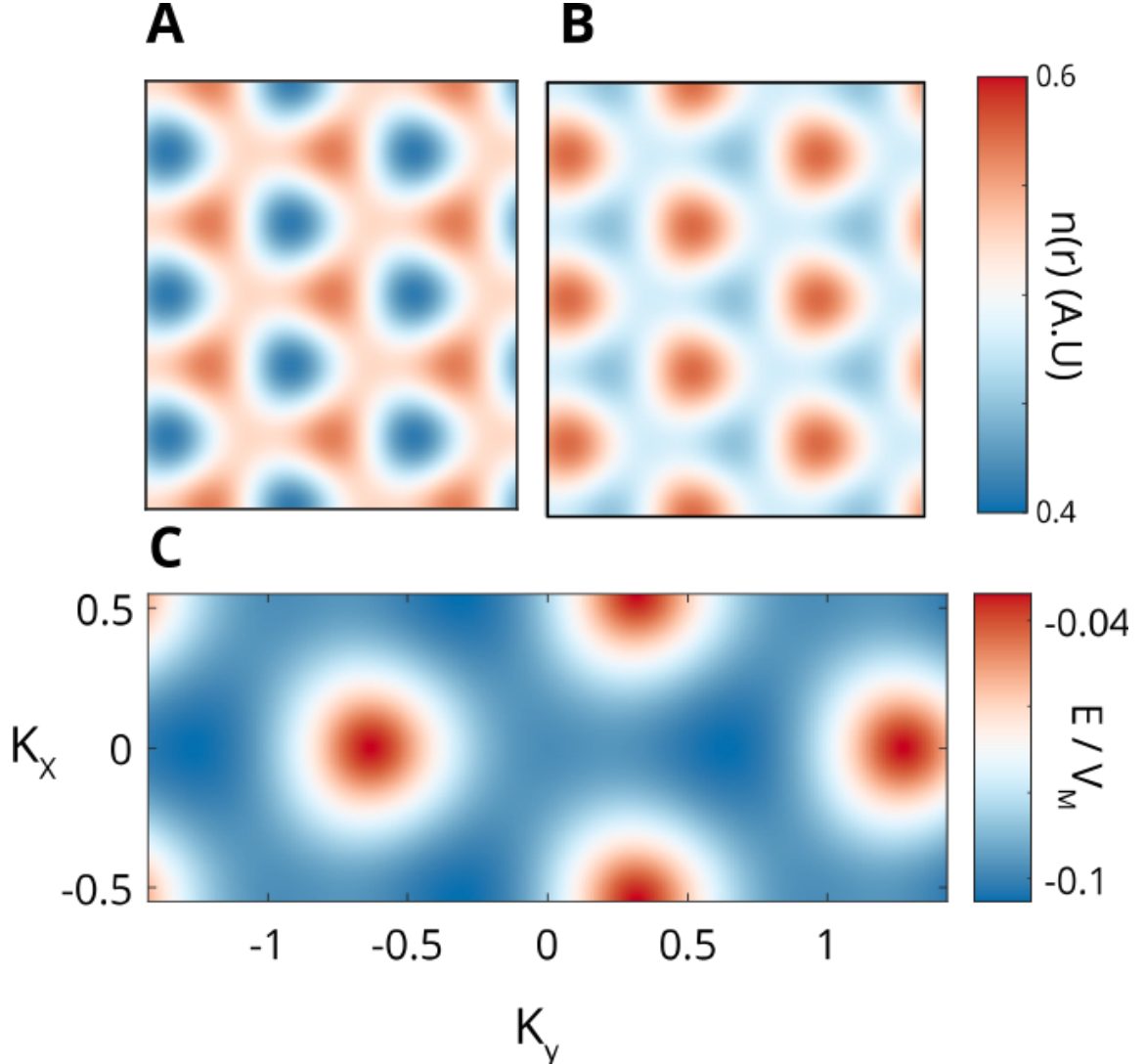


Figure E.8: **Real-space electron density and k-space dispersion of FCI-hosting  $\mathcal{C} = -1$  band.** For large  $\varepsilon_{10}/|V_M|$  at  $n_\Phi = 2/3$ , the  $N = 0$  Landau level splits up into  $\mathcal{C} = -1, 2$  bands. In (A,B), we show the real-space charge density that arises from fully filling each of these bands. We see that the  $\mathcal{C} = -1$  band is localized on the triangular lattice. This is the band which hosts the observed FCI states. (C) The k-space energy dispersion of the  $\mathcal{C} = -1$  band, with axes in units of  $l_B^{-1}$  and energy in units of  $|V_M|$ . At  $n_\Phi = 2/3$ , the bandwidth is about 10% of  $|V_M|$ ; this percentage grows as  $n_\Phi \rightarrow 1/2$ .

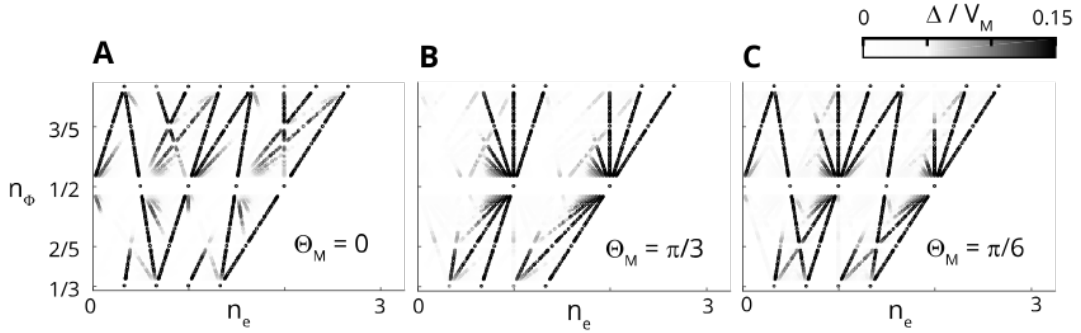


Figure E.9: **Calculated Wannier plots for the  $n_0 > 0, u < 0$  case** Calculated gap sizes in units of the magnitude of the moiré potential ( $\Delta/V_M$ ) as a function of  $n_e$  and  $n_\phi$  for  $\Theta_M = 0$  (**A**),  $\Theta_M = \pi/3$  (**B**), and  $\Theta_M = \pi/6$  (**C**). The splitting between LLs  $\varepsilon_{10}$  is chosen to be larger than any Hofstadter gaps.  $|V_M|/\varepsilon_{10}$  is fixed to 6.0 for all cases. The spin-split  $\nu = 2$  gap is chosen to be larger than any Hofstadter gaps.

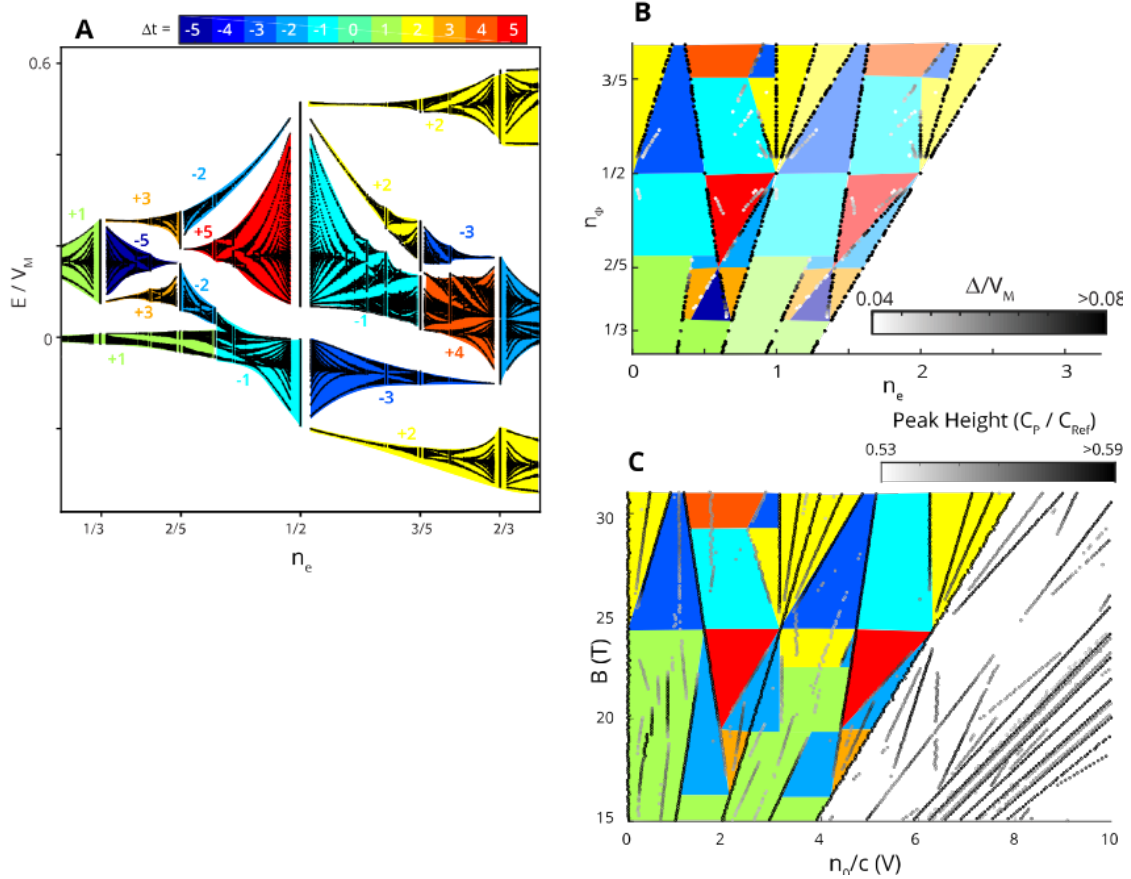


Figure E.10: **Comparison of calculated and observed single particle Chern bands for case II.** (A) Single-particle Hofstadter spectrum calculated using  $|V_M|/\varepsilon_{10} = 1/6$  and  $\Theta_M = \pi/8$ .  $\Delta t = C$  bands are labeled from the Wannier plot (B) using the procedure described in the main text (Fig. 6.1G). (B) Calculated Wannier plot constructed from (A). The whole spectrum was replicated twice to match the experimental data, starting at  $\nu = 0$ . (C) Peak height of gapped states (black to gray points), extracted from data in Fig. 6.1D, as a function of charge carrier density ( $n_0/c$ ) and magnetic field (B). The bands are colored according to their single-particle  $\Delta t$ , using the same rules as (B).

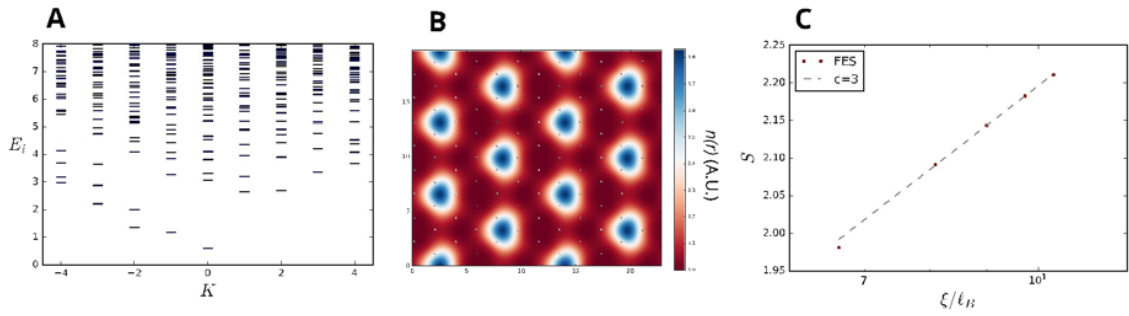


Figure E.11: **Entanglement spectrum of  $\nu_C = 1/3$  FCI and investigation of competing phases.** (A) Entanglement spectrum of  $\mathcal{C} = -1, \nu_C = 1/3$  FCI. The low-lying counting disperses from right to left as 1, 1, 2, 3, (5), where it merges into the higher states. Note that in our convention, the  $\nu = 1/3$  Laughlin state would have counting 1, 1, 2, 3, 5,... with the opposite chirality, left to right. This reversal is a signature of the reversed Hall conductance in a  $\mathcal{C} = -1$  band. (B) Charge carrier density  $\langle n(r) \rangle$  at  $\nu_C = 1/3$  filling of the  $\mathcal{C} = -1$  band in the regime where  $|V_M|/E_C < 0.29$  leads to a Wigner crystal. The dots indicate the moiré unit cell, showing a  $3 \times 3$  reconstruction. (C) Evidence for a gapless phase at  $\nu_C = 1/3$  filling of the  $\mathcal{C} = -1$  band in the regime  $|V_M|/E_C > 0.79$ . We measure the evolution of the bipartite entanglement entropy  $S$  vs. DMRG correlation length  $\xi$  as the DMRG bond dimension increases. In a CFT,  $S = \frac{c}{6} \log \xi + s_0$ . At the point  $|V_M|/E_C = 2$  shown here, we obtain perfect agreement with  $c = 3$ . At higher  $|V_M|/E_C$  (not shown) we find  $c = 6$ .

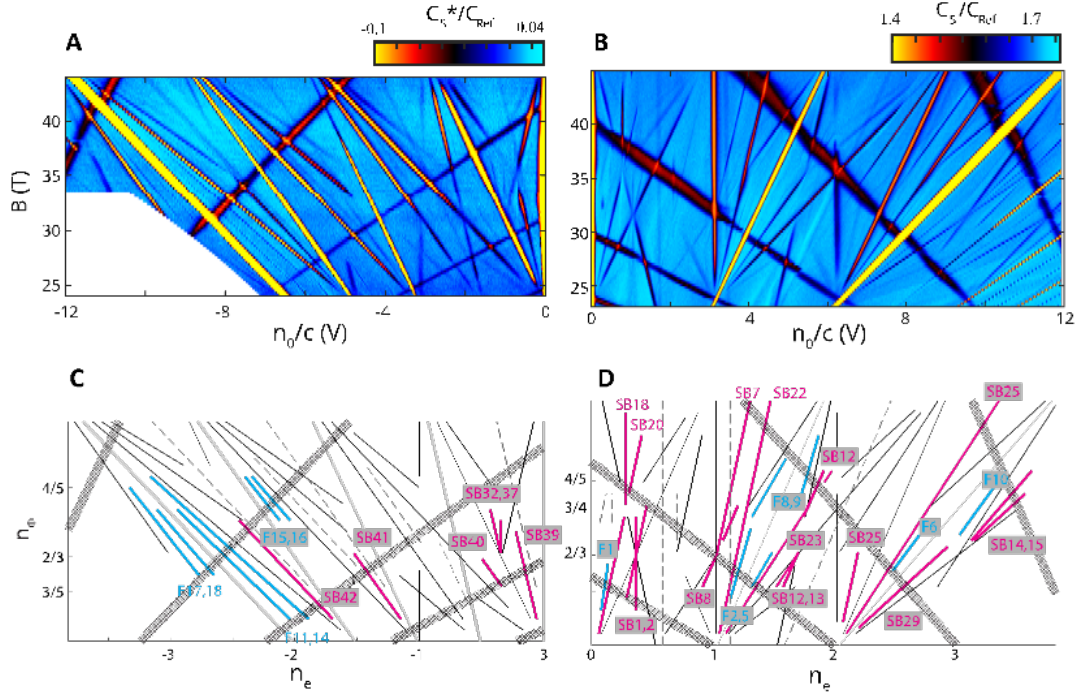


Figure E.12: **Landau fans up to 45T** Landau fans of  $C_S$  for  $p_0/c = 16\text{V}$  (A) and  $-16\text{V}$  (B). We performed a horizontal line-by-line subtraction on (A) to compensate a change in offsets with field. (C,D) Classification of gapped linear trajectories (A) and (B) respectively. Interaction-driven features are labeled and their  $t, s$  are given in Tables E.1 and E.2. We observe two classes of linear trajectories which do not fall into the categories outlined in the main text. The first are associated with Landau Levels in one of the graphite gates, which appear much more prominently in  $C_S$  than in  $C_P$  and only depend on one of the applied gate voltages (wide hatched lines). These states are observed as diagonal features in the  $n_0 - p_0$  plane, and appear as a secondary, broad Landau fan with an x-intercept that depends on  $p_0/c$ . The second are features that either do not have  $t$  and/or  $s$  which clearly match a small-denominator rational fraction, are short-lived in  $B$ , or do not have nearby features which allow us to easily identify their origin (dashed lines). The FCI states described in the main text persist between 27 and nearly 40 T.

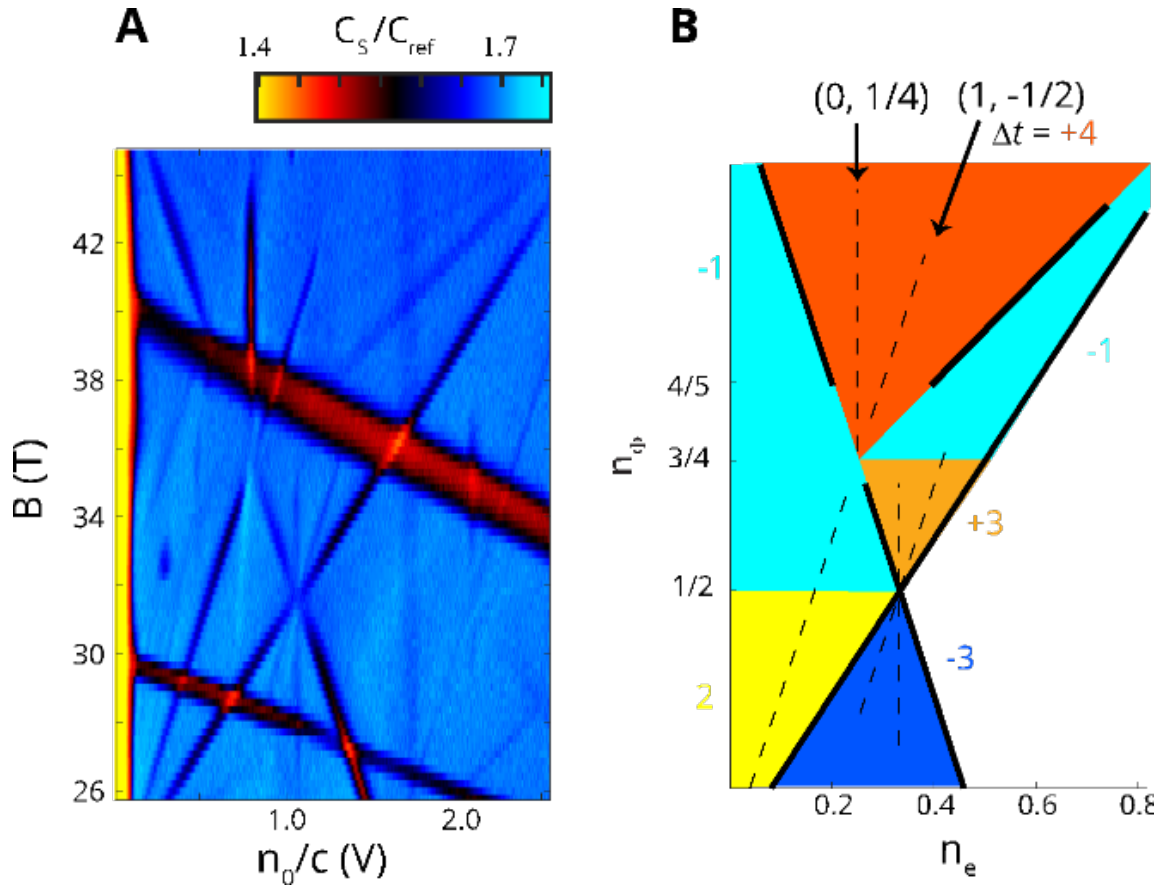


Figure E.13: **Symmetry broken Chern insulators in a  $C = 4$  band.** Detail from Fig. E.12B, highlighting a  $C = 4$  band at high magnetic fields. **(B)** Schematic of **(A)**, SBCI states (dashed lines) with  $t, s = (0, 1/4)$  and  $(1, -1/2)$  occur at  $\nu_C = 1/4$  and  $1/2$  fractional filling of a  $\Delta t = 4$  band (dark orange). SBCI in  $\Delta t = 2$  and  $\Delta t = \pm 3$  are also observed. Broad, negative slope features not represented in the schematic are due to graphite LLs.





Table E.1: List of observed symmetry-broken Chern insulator states (integer  $t$ , fractional  $s$ ). States above 30 T can be observed in data taken up to 45 T (Figs. S1,2).

id	$t$	$s$	B [T] (min,max)	$p_0/c$ [V]
SB1	1	-2/3	(28,36)	-16
SB2	0	2/3	(26,35)	-16
SB3	0	4/3	(17,20)	-16
SB4	1	2/3	(17,21)	-16
SB5	3	-2/3	(17,20)	-16
SB6	0	4/3	(30,31)	-16
SB7	1	2/3	(30,45)	-16
SB8	2	-2/3	(30,36)	-16
SB9	2	4/3	(17,20)	-16
SB10	3	2/3	(17,21)	-16
SB11	5	-2/3	(17,19)	-16
SB12	3	-2/3	(29,32)	-16
SB13	2	2/3	(29,32)	-16
SB14	5	-2/3	(29,31) (33,37)	-16
SB15	4	2/3	(29,39)	-16
SB16	5	2/3	(17,20)	-16
SB17	4	4/3	(17,19)	-16
SB18	0	1/2	(36,44)	-16
SB19	2	1/2	(35,39)	-16
SB20	-1	2/3	(18,20) (32,36)	16
SB21	-2	4/3	(18,20)	16
SB22	-2	2/3	(17,19)	16
SB23	-1	-2/3	(29,32)	16
SB24	-2	2/3	(29,32)	16
SB25	-5	-2/3	(18,20)	16
SB26	-4	-4/3	(18,19)	16
SB27	0	-2/3	(32,35)	16

Table E.2: List of observed fractional Chern insulator states (fractional  $t$ , fractional  $s$ ). States above 30 T can be observed in data taken up to 45 T (Figs. S1,2). \* indicates a lower bound on the field at which states disappear, as these weak states were not clearly observed in the higher field data, possibly due to worse signal to noise.

id	$t$	$s$	B [T] (min,max)	$p_0/c$ [V]
F1	2/3	-2/3	(28,31*)	-16
F2	8/3	-2/3	(28,31*)	-16
F3	5/3	1/3	(29,31*)	-16
F4	4/3	2/3	(28,34)	-16
F5	10/3	2/3	(28,33.5)	-16
F6	11/3	1/3	(28,32*)	-16
F7	8/3	-4/3	(35,40)	-16
F8	4/3	4/3	(33,39)	-16
F9	4/3	4/3	(33,39)	-16
F10	-13/3	2/3	(25,36)	16
F11	-22/5	4/5	(27,32*)	16
F12	-23/5	6/5	(27,32*)	16
F13	-14/3	4/3	(26,38)	16
F14	-11/3	4/3	(28,39)	16
F15	-10/3	2/3	(28,39)	16
F16	-11/3	-2/3	(30,36)	16
F17	-10/3	-4/3	(30,38)	16

# Bibliography

- [1] C. Nayak, S. H. Simon, A. Stern, M. Freedman, and S. Das Sarma, *Non-Abelian anyons and topological quantum computation*, *Reviews of Modern Physics* **80** (Sept., 2008) 1083–1159.
- [2] L. D. Landau and E. M. Lifshitz, *Quantum mechanics : non-relativistic theory*. Pergamon Press, Oxford, New York, 1977.
- [3] K. S. Novoselov, A. K. Geim, S. V. Morozov, D. Jiang, M. I. Katsnelson, I. V. Grigorieva, S. V. Dubonos, and A. A. Firsov, *Two-dimensional gas of massless Dirac fermions in graphene*, *Nature* **438** (Nov., 2005) 197.
- [4] Y. Zhang, Y.-W. Tan, H. L. Stormer, and P. Kim, *Experimental observation of the quantum Hall effect and Berry's phase in graphene*, *Nature* **438** (Nov., 2005) 201.
- [5] A. K. Geim and I. V. Grigorieva, *Van der Waals heterostructures*, *Nature* **499** (July, 2013) 419–425.
- [6] K. I. Bolotin, F. Ghahari, M. D. Shulman, H. L. Stormer, and P. Kim, *Observation of the fractional quantum Hall effect in graphene*, *Nature* **462** (Nov., 2009) 196–199.
- [7] X. Du, I. Skachko, F. Duerr, A. Luican, and E. Y. Andrei, *Fractional quantum Hall effect and insulating phase of Dirac electrons in graphene*, *Nature* **462** (2009).
- [8] C. R. Dean, A. F. Young, P. Cadden-Zimansky, L. Wang, H. Ren, K. Watanabe, T. Taniguchi, P. Kim, J. Hone, and K. L. Shepard, *Multicomponent fractional quantum Hall effect in graphene*, *Nature Physics* **7** (Sept., 2011) 693–696.
- [9] F. Ghahari, Y. Zhao, P. Cadden-Zimansky, K. Bolotin, and P. Kim, *Measurement of the  $\nu = 1/3$  Fractional Quantum Hall Energy Gap in Suspended Graphene*, *Physical Review Letters* **106** (Jan., 2011) 46801.
- [10] B. E. Feldman, B. Krauss, J. H. Smet, and A. Yacoby, *Unconventional sequence of fractional quantum Hall states in suspended graphene*, *Science* **337** (2012).

- [11] Y. Cao, V. Fatemi, A. Demir, S. Fang, S. L. Tomarken, J. Y. Luo, J. D. Sanchez-Yamagishi, K. Watanabe, T. Taniguchi, E. Kaxiras, R. C. Ashoori, and P. Jarillo-Herrero, *Correlated insulator behaviour at half-filling in magic-angle graphene superlattices*, *Nature* **556** (Apr., 2018) 80–84.
- [12] G. Chen, L. Jiang, S. Wu, B. Lyu, H. Li, B. L. Chittari, K. Watanabe, T. Taniguchi, Z. Shi, J. Jung, Y. Zhang, and F. Wang, *Evidence of a gate-tunable Mott insulator in a trilayer graphene moiré superlattice*, *Nature Physics* **15** (Mar., 2019) 237.
- [13] Y. Cao, V. Fatemi, S. Fang, K. Watanabe, T. Taniguchi, E. Kaxiras, and P. Jarillo-Herrero, *Unconventional superconductivity in magic-angle graphene superlattices*, *Nature* **556** (Apr., 2018) 43–50.
- [14] G. Chen, A. L. Sharpe, P. Gallagher, I. T. Rosen, E. J. Fox, L. Jiang, B. Lyu, H. Li, K. Watanabe, T. Taniguchi, J. Jung, Z. Shi, D. Goldhaber-Gordon, Y. Zhang, and F. Wang, *Signatures of tunable superconductivity in a trilayer graphene moiré superlattice*, *Nature* (July, 2019) 1–5.
- [15] L. Pfeiffer and K. W. West, *The role of MBE in recent quantum Hall effect physics discoveries*, *Physica E: Low-dimensional Systems and Nanostructures* **20** (Dec., 2003) 57–64.
- [16] D. J. Thouless, M. Kohmoto, M. P. Nightingale, and M. den Nijs, *Quantized Hall Conductance in a Two-Dimensional Periodic Potential*, *Physical Review Letters* **49** (Aug., 1982) 405–408.
- [17] S. Blundell, *Magnetism in condensed matter*. Oxford University Press, Oxford, New York, 2001.
- [18] R. B. Laughlin, *Anomalous Quantum Hall Effect: An Incompressible Quantum Fluid with Fractionally Charged Excitations*, *Physical Review Letters* **50** (May, 1983) 1395–1398.
- [19] J. Jain, *Composite fermions*. Cambridge University Press, 2011.
- [20] R. L. Willett, R. R. Ruel, K. W. West, and L. N. Pfeiffer, *Experimental demonstration of a Fermi surface at one-half filling of the lowest Landau level*, *Phys. Rev. Lett.* **71** (1993) 3846–3849.
- [21] W. Kang, H. L. Stormer, L. N. Pfeiffer, K. W. Baldwin, and K. W. West, *How real are composite fermions?*, *Phys. Rev. Lett.* **71** (1993) 3850–3853.
- [22] R. Willett, *Observation of an even-denominator quantum number in the fractional quantum Hall effect*, *Phys. Rev. Lett.* **59** (1987).

- [23] B. I. Halperin, *Theory of the quantized Hall conductance*, *Helv. Phys. Acta* **56** (1983).
- [24] L. Tiemann, G. Gamez, N. Kumada, and K. Muraki, *Unraveling the Spin Polarization of the  $\nu = 5/2$  Fractional Quantum Hall State*, *Science* **335** (Feb., 2012) 828–831.
- [25] G. Moore and N. Read, *Nonabelions in the fractional quantum Hall effect*, *Nucl. Phys. B* **360** (1991) 362–396.
- [26] N. R. Cooper and A. Stern, *Observable Bulk Signatures of Non-Abelian Quantum Hall States*, *Physical Review Letters* **102** (Apr., 2009) 176807.
- [27] Z. Papić, *Fractional quantum Hall effect in multicomponent systems*. PhD thesis, Université de Paris XI Orsay, 2010.
- [28] J. I. A. Li, Q. Shi, Y. Zeng, K. Watanabe, T. Taniguchi, J. Hone, and C. R. Dean, *Pairing states of composite fermions in double-layer graphene*, *Nature Physics* (June, 2019) 1–6.
- [29] X. Liu, Z. Hao, K. Watanabe, T. Taniguchi, B. I. Halperin, and P. Kim, *Interlayer fractional quantum Hall effect in a coupled graphene double layer*, *Nature Physics* (June, 2019) 1–5.
- [30] D. R. Hofstadter, *Energy levels and wave functions of Bloch electrons in rational and irrational magnetic fields*, *Physical Review B* **14** (Sept., 1976) 2239–2249.
- [31] J. O. Island, X. Cui, C. Lewandowski, J. Y. Khoo, E. M. Spanton, H. Zhou, D. Rhodes, J. C. Hone, T. Taniguchi, K. Watanabe, L. S. Levitov, M. P. Zaletel, and A. F. Young, *Spin-orbit-driven band inversion in bilayer graphene by the van der Waals proximity effect*, *Nature* **571** (July, 2019) 85–89.
- [32] S. Jiang, J. Shan, and K. F. Mak, *Electric-field switching of two-dimensional van der Waals magnets*, *Nature Materials* **17** (May, 2018) 406–410.
- [33] Z. Fei, B. Huang, P. Malinowski, W. Wang, T. Song, J. Sanchez, W. Yao, D. Xiao, X. Zhu, A. F. May, W. Wu, D. H. Cobden, J.-H. Chu, and X. Xu, *Two-dimensional itinerant ferromagnetism in atomically thin  $Fe_3GeTe_2$* , *Nature Materials* **17** (Sept., 2018) 778–782.
- [34] M. Serlin, C. L. Tschirhart, H. Polshyn, Y. Zhang, J. Zhu, K. Watanabe, T. Taniguchi, L. Balents, and A. F. Young, *Intrinsic quantized anomalous Hall effect in a moiré heterostructure*, *arXiv:1907.00261 [cond-mat]* (June, 2019).
- [35] K. S. Novoselov, A. K. Geim, S. V. Morozov, D. Jiang, Y. Zhang, S. V. Dubonos, I. V. Grigorieva, and A. A. Firsov, *Electric Field Effect in Atomically Thin Carbon Films*, *Science* **306** (Oct., 2004) 666–669.

- [36] Y. Zhang, Z. Jiang, J. P. Small, M. S. Purewal, Y.-W. Tan, M. Fazlollahi, J. D. Chudow, J. A. Jaszczak, H. L. Stormer, and P. Kim, *Landau-Level Splitting in Graphene in High Magnetic Fields*, *Physical Review Letters* **96** (Apr., 2006) 136806.
- [37] Y. Zhang, V. W. Brar, C. Girit, A. Zettl, and M. F. Crommie, *Origin of spatial charge inhomogeneity in graphene*, *Nature Physics* **5** (Oct., 2009) 722–726.
- [38] J. Martin, N. Akerman, G. Ulbricht, T. Lohmann, J. H. Smet, K. von Klitzing, and A. Yacoby, *Observation of Electron-Hole Puddles in Graphene Using a Scanning Single Electron Transistor*, *Nature Physics* **4** (Feb., 2008) 144–148.
- [39] C. R. Dean, A. F. Young, I. Meric, C. Lee, L. Wang, S. Sorgenfrei, K. Watanabe, T. Taniguchi, P. Kim, K. L. Shepard, and J. Hone, *Boron nitride substrates for high-quality graphene electronics*, *Nature Nanotechnology* **5** (Oct., 2010) 722–726.
- [40] S. J. Haigh, A. Gholinia, R. Jalil, S. Romani, L. Britnell, D. C. Elias, K. S. Novoselov, L. A. Ponomarenko, A. K. Geim, and R. Gorbachev, *Cross-sectional imaging of individual layers and buried interfaces of graphene-based heterostructures and superlattices*, *Nature Materials* **11** (Sept., 2012) 764–767.
- [41] A. V. Kretinin, Y. Cao, J. S. Tu, G. L. Yu, R. Jalil, K. S. Novoselov, S. J. Haigh, A. Gholinia, A. Mishchenko, M. Lozada, T. Georgiou, C. R. Woods, F. Withers, P. Blake, G. Eda, A. Wirsig, C. Hucho, K. Watanabe, T. Taniguchi, A. K. Geim, and R. V. Gorbachev, *Electronic Properties of Graphene Encapsulated with Different Two-Dimensional Atomic Crystals*, *Nano Letters* **14** (June, 2014) 3270–3276.
- [42] P. Maher, L. Wang, Y. Gao, C. Forsythe, T. Taniguchi, K. Watanabe, D. Abanin, Z. Papićij, P. Cadden-Zimansky, J. Hone, P. Kim, and C. R. Dean, *Tunable fractional quantum Hall phases in bilayer graphene*, *Science* **345** (July, 2014) 61–64.
- [43] K. I. Bolotin, K. J. Sikes, Z. Jiang, M. Klima, G. Fudenberg, J. Hone, P. Kim, and H. L. Stormer, *Ultrahigh electron mobility in suspended graphene*, *Solid State Communications* **146** (June, 2008) 351–355.
- [44] X. Du, I. Skachko, and E. Y. Andrei, *Towards ballistic transport in graphene*, *International Journal of Modern Physics B* **22** (Oct., 2008) 4579–4588.
- [45] R. T. Weitz, M. T. Allen, B. E. Feldman, J. Martin, and A. Yacoby, *Broken-Symmetry States in Doubly Gated Suspended Bilayer Graphene*, *Science* **330** (Nov., 2010) 812–816.

- [46] D.-K. Ki, V. I. Fal'ko, D. A. Abanin, and A. F. Morpurgo, *Observation of Even Denominator Fractional Quantum Hall Effect in Suspended Bilayer Graphene*, *Nano Letters* **14** (Apr., 2014) 2135–2139.
- [47] A. Kumar, G. A. Csáthy, M. J. Manfra, L. N. Pfeiffer, and K. W. West, *Nonconventional Odd-Denominator Fractional Quantum Hall States in the Second Landau Level*, *Physical Review Letters* **105** (Dec., 2010) 246808.
- [48] L. Wang, I. Meric, P. Y. Huang, Q. Gao, Y. Gao, H. Tran, T. Taniguchi, K. Watanabe, L. M. Campos, D. A. Muller, J. Guo, P. Kim, J. Hone, K. L. Shepard, and C. R. Dean, *One-Dimensional Electrical Contact to a Two-Dimensional Material*, *Science* **342** (Nov., 2013) 614–617.
- [49] A. A. Zibrov, C. Kometter, H. Zhou, E. M. Spanton, T. Taniguchi, K. Watanabe, M. P. Zaletel, and A. F. Young, *Tunable interacting composite fermion phases in a half-filled bilayer-graphene Landau level*, *Nature* **549** (Sept., 2017) 360–364.
- [50] P. Blake, E. W. Hill, A. H. Castro Neto, K. S. Novoselov, D. Jiang, R. Yang, T. J. Booth, and A. K. Geim, *Making graphene visible*, *Applied Physics Letters* **91** (Aug., 2007) 63124.
- [51] S. M. Girvin and K. Yang, *Modern condensed matter physics*. Cambridge University Press, 2019.
- [52] M. O. Goerbig, *Electronic properties of graphene in a strong magnetic field*, *Reviews of Modern Physics* **83** (Nov., 2011) 1193–1243.
- [53] E. McCann, *Electronic properties of monolayer and bilayer graphene*, *arXiv:1205.4849 [cond-mat]* (2011) 237–275.
- [54] E. McCann and M. Koshino, *The electronic properties of bilayer graphene*, *Reports on Progress in Physics* **76** (May, 2013) 56503.
- [55] A. H. Castro Neto, F. Guinea, N. M. R. Peres, K. S. Novoselov, and A. K. Geim, *The electronic properties of graphene*, *Reviews of Modern Physics* **81** (Jan., 2009) 109–162.
- [56] J. Alicea and M. P. A. Fisher, *Graphene integer quantum Hall effect in the ferromagnetic and paramagnetic regimes*, *Physical Review B* **74** (Aug., 2006) 75422.
- [57] B. M. Hunt, J. I. A. Li, A. A. Zibrov, L. Wang, T. Taniguchi, K. Watanabe, J. Hone, C. R. Dean, M. Zaletel, R. C. Ashoori, and A. F. Young, *Direct measurement of discrete valley and orbital quantum numbers in bilayer graphene*, *Nature Communications* **8** (Dec., 2017).

- [58] C. R. Woods, L. Britnell, A. Eckmann, R. S. Ma, J. C. Lu, H. M. Guo, X. Lin, G. L. Yu, Y. Cao, R. V. Gorbachev, A. V. Kretinin, J. Park, L. A. Ponomarenko, M. I. Katsnelson, Y. N. Gornostyrev, K. Watanabe, T. Taniguchi, C. Casiraghi, H.-J. Gao, A. K. Geim, and K. S. Novoselov, *Commensurate- $\sqrt{3}\sqrt{3}$  incommensurate transition in graphene on hexagonal boron nitride*, *Nature Physics* **10** (June, 2014) 451–456.
- [59] E. McCann and V. I. Fal’ko, *Landau-Level Degeneracy and Quantum Hall Effect in a Graphite Bilayer*, *Physical Review Letters* **96** (Mar., 2006).
- [60] Y. Shi, S. Che, K. Zhou, S. Ge, Z. Pi, T. Espiritu, T. Taniguchi, K. Watanabe, Y. Barlas, R. Lake, and C. N. Lau, *Tunable Lifshitz Transitions and Multiband Transport in Tetralayer Graphene*, *Physical Review Letters* **120** (Feb., 2018) 96802.
- [61] M. Koshino and E. McCann, *Gate-induced interlayer asymmetry in ABA-stacked trilayer graphene*, *Physical Review B* **79** (Mar., 2009) 125443.
- [62] B. Partoens and F. M. Peeters, *From graphene to graphite: Electronic structure around the K point*, *Physical Review B* **74** (Aug., 2006) 75404.
- [63] A. A. Avetisyan, B. Partoens, and F. M. Peeters, *Electric-field control of the band gap and Fermi energy in graphene multilayers by top and back gates*, *Physical Review B* **80** (Nov., 2009) 195401.
- [64] M. Serbyn and D. A. Abanin, *New Dirac points and multiple Landau level crossings in biased trilayer graphene*, *Physical Review B* **87** (Mar., 2013) 115422.
- [65] T. Morimoto and M. Koshino, *Gate-induced Dirac cones in multilayer graphenes*, *Physical Review B* **87** (Feb., 2013) 85424.
- [66] I. Sodemann, Z. Zhu, and L. Fu, *Quantum Hall Ferroelectrics and Nematics in Multivalley Systems*, *Physical Review X* **7** (Dec., 2017) 41068.
- [67] B. E. Feldman, M. T. Randeria, A. A. Gyenis, F. Wu, H. Ji, R. J. Cava, A. H. MacDonald, and A. Yazdani, *Observation of a nematic quantum Hall liquid on the surface of bismuth*, *Science* **354** (Oct., 2016) 316–321.
- [68] M. F. Craciun, S. Russo, M. Yamamoto, J. B. Oostinga, A. F. Morpurgo, and S. Tarucha, *Trilayer graphene is a semimetal with a gate-tunable band overlap*, *Nature Nanotechnology* **4** (June, 2009) 383–388.
- [69] A. Kumar, W. Escoffier, J. M. Pomirol, C. Faugeras, D. P. Arovas, M. M. Fogler, F. Guinea, S. Roche, M. Goiran, and B. Raquet, *Integer Quantum Hall Effect in Trilayer Graphene*, *Physical Review Letters* **107** (Sept., 2011) 126806.



- [70] E. A. Henriksen, D. Nandi, and J. P. Eisenstein, *Quantum Hall Effect and Semimetallic Behavior of Dual-Gated ABA-Stacked Trilayer Graphene*, *Physical Review X* **2** (Jan., 2012) 11004.
- [71] T. Taychatanapat, K. Watanabe, T. Taniguchi, and P. Jarillo-Herrero, *Quantum Hall effect and Landau-level crossing of Dirac fermions in trilayer graphene*, *Nature Physics* **7** (Aug., 2011) 621–625.
- [72] W. Bao, L. Jing, J. Velasco Jr, Y. Lee, G. Liu, D. Tran, B. Standley, M. Aykol, S. B. Cronin, D. Smirnov, M. Koshino, E. McCann, M. Bockrath, and C. N. Lau, *Stacking-dependent band gap and quantum transport in trilayer graphene*, *Nature Physics* **7** (Dec., 2011) 948–952.
- [73] Y. Lee, J. Velasco, D. Tran, F. Zhang, W. Bao, L. Jing, K. Myhro, D. Smirnov, and C. N. Lau, *Broken Symmetry Quantum Hall States in Dual-Gated ABA Trilayer Graphene*, *Nano Letters* **13** (Apr., 2013) 1627–1631.
- [74] L. C. Campos, A. F. Young, K. Surakitbovorn, K. Watanabe, T. Taniguchi, and P. Jarillo-Herrero, *Quantum and classical confinement of resonant states in a trilayer graphene Fabry-perot interferometer*, *Nature Communications* **3** (Dec., 2012) 1239.
- [75] Y. Shimazaki, T. Yoshizawa, I. V. Borzenets, K. Wang, X. Liu, K. Watanabe, T. Taniguchi, P. Kim, M. Yamamoto, and S. Tarucha, *Landau level evolution driven by band hybridization in mirror symmetry broken ABA-stacked trilayer graphene*, *arXiv:1611.02395 [cond-mat]* (Nov., 2016).
- [76] P. Stepanov, Y. Barlas, T. Espiritu, S. Che, K. Watanabe, T. Taniguchi, D. Smirnov, and C. N. Lau, *Tunable Symmetries of Integer and Fractional Quantum Hall Phases in Heterostructures with Multiple Dirac Bands*, *Physical Review Letters* **117** (Aug., 2016) 76807.
- [77] B. Datta, S. Dey, A. Samanta, H. Agarwal, A. Borah, K. Watanabe, T. Taniguchi, R. Sensarma, and M. M. Deshmukh, *Strong electronic interaction and multiple quantum Hall ferromagnetic phases in trilayer graphene*, *Nature Communications* **8** (Feb., 2017) 14518.
- [78] M. Koshino and E. McCann, *Landau level spectra and the quantum Hall effect of multilayer graphene*, *Physical Review B* **83** (Apr., 2011) 165443.
- [79] S. Yuan, R. Roldán, and M. I. Katsnelson, *Landau level spectrum of ABA- and ABC-stacked trilayer graphene*, *Physical Review B* **84** (Sept., 2011) 125455.
- [80] J. P. Eisenstein, L. N. Pfeiffer, and K. W. West, *Negative compressibility of interacting two-dimensional electron and quasiparticle gases*, *Physical Review Letters* **68** (Feb., 1992) 674–677.

- [81] L. C. Campos, T. Taychatanapat, M. Serbyn, K. Surakitbovorn, K. Watanabe, T. Taniguchi, D. A. Abanin, and P. Jarillo-Herrero, *Landau Level Splittings, Phase Transitions, and Nonuniform Charge Distribution in Trilayer Graphene*, *Physical Review Letters* **117** (Aug., 2016) 66601.
- [82] A. Varlet, D. Bischoff, P. Simonet, K. Watanabe, T. Taniguchi, T. Ihn, K. Ensslin, M. Mucha-Kruczyński, and V. I. Fal’ko, *Anomalous Sequence of Quantum Hall Liquids Revealing a Tunable Lifshitz Transition in Bilayer Graphene*, *Physical Review Letters* **113** (Sept., 2014) 116602.
- [83] R. Geick, C. H. Perry, and G. Rupprecht, *Normal Modes in Hexagonal Boron Nitride*, *Physical Review* **146** (June, 1966) 543–547.
- [84] X. Li, F. Zhang, and A. H. MacDonald,  *$SU(3)$  Quantum Hall Ferromagnetism in  $SnTe$* , *Physical Review Letters* **116** (Jan., 2016) 26803.
- [85] K. Nomura and A. H. MacDonald, *Quantum Hall Ferromagnetism in Graphene*, *Physical Review Letters* **96** (June, 2006).
- [86] J. G. Checkelsky, L. Li, and N. P. Ong, *Zero-energy state in graphene in a high magnetic field*, *Phys. Rev. Lett.* **100** (2008).
- [87] I. F. Herbut, *Theory of integer quantum Hall effect in graphene*, *Phys. Rev. B* **75** (2007).
- [88] K. Nomura, S. Ryu, and D. H. Lee, *Field-induced Kosterlitz-Thouless transition in the  $n = 0$  Landau level of graphene*, *Phys. Rev. Lett.* **103** (2009).
- [89] M. Kharitonov, *Phase diagram for the  $\nu = 0$  quantum Hall state in monolayer graphene*, *Physical Review B* **85** (Apr., 2012) 155439.
- [90] M. Kharitonov, *Canted antiferromagnetic phase of the  $\nu = 0$  quantum Hall state in bilayer graphene*, *Physical Review Letters* **109** (July, 2012) 46803.
- [91] J. Lee and S. Sachdev, *Deconfined criticality in bilayer graphene*, *Phys. Rev. B* **90** (2014).
- [92] F. Wu, I. Sodemann, Y. Araki, A. H. MacDonald, and T. Jolicoeur,  *$SO(5)$  symmetry in the quantum Hall effect in graphene*, *Phys. Rev. B* **90** (2014).
- [93] J. Lee and S. Sachdev, *Wess-Zumino-Witten Terms in Graphene Landau Levels*, *Physical Review Letters* **114** (June, 2015) 226801.
- [94] T. Senthil, A. Vishwanath, L. Balents, S. Sachdev, and M. P. A. Fisher, *Deconfined quantum critical points*, *Science* **303** (2004).

- [95] J. I. A. Li, *Even denominator fractional quantum Hall states in bilayer graphene*, *Science* **358** (2017).
- [96] A. F. Young, *Tunable symmetry breaking and helical edge transport in a graphene quantum spin Hall state*, *Nature* **505** (2014).
- [97] B. Hunt, *Massive Dirac fermions and Hofstadter butterfly in a van der Waals heterostructure*, *Science* **340** (2013).
- [98] F. Amet, J. R. Williams, K. Watanabe, T. Taniguchi, and D. Goldhaber-Gordon, *Insulating behavior at the neutrality point in single-layer graphene*, *Phys. Rev. Lett.* **110** (2013).
- [99] I. Sodemann and A. H. MacDonald, *Broken  $SU(4)$  symmetry and the fractional quantum Hall effect in graphene*, *Phys. Rev. Lett.* **112** (2014).
- [100] P. Streda, *Quantised Hall effect in a two-dimensional periodic potential*, *J. Phys. C* **15** (1982).
- [101] B. E. Feldman, *Fractional quantum Hall phase transitions and four-flux states in graphene*, *Phys. Rev. Lett.* **111** (2013).
- [102] F. Amet, *Composite fermions and broken symmetries in graphene*, *Nat. Commun.* **6** (2015).
- [103] V. M. Apalkov and T. Chakraborty, *Fractional quantum Hall states of Dirac electrons in graphene*, *Phys. Rev. Lett.* **97** (2006).
- [104] C. ToiŁjke and J. K. Jain, *Theoretical study of even denominator fractions in graphene: Fermi sea versus paired states of composite fermions*, *Phys. Rev. B* **76** (2007).
- [105] C. Toke and J. K. Jain.,  *$SU(4)$  composite fermions in graphene: fractional quantum Hall states without analog in GaAs*, *Phys. Rev. B* **75** (2007).
- [106] N. Shibata and K. Nomura, *Fractional quantum Hall effects in graphene and its bilayer*, *J. Phys. Soc. Jpn* **78** (2009).
- [107] Z. Papić, M. O. Goerbig, and N. Regnault, *Atypical fractional quantum Hall effect in graphene at filling factor  $1/3$* , *Phys. Rev. Lett.* **105** (2010).
- [108] C. Toke and J. K. Jain, *Multi-component fractional quantum Hall states in graphene:  $SU(4)$  versus  $SU(2)$* , *J. Phys. Condens. Matter* **24** (2011).
- [109] Z. Papić, R. Thomale, and D. A. Abanin, *Tunable electron interactions and fractional quantum Hall states in graphene*, *Phys. Rev. Lett.* **107** (2011).

- [110] M. R. Peterson and C. Nayak, *Effects of Landau level mixing on the fractional quantum Hall effect in monolayer graphene*, *Phys. Rev. Lett.* **113** (2014).
- [111] J. Falson, *Even-denominator fractional quantum Hall physics in ZnO*, *Nat. Phys.* **11** (2015).
- [112] D. A. Abanin, I. Skachko, X. Du, E. Y. Andrei, and L. S. Levitov, *Fractional quantum Hall effect in suspended graphene: Transport coefficients and electron interaction strength*, *Physical Review B* **81** (Mar., 2010) 115410.
- [113] Y. W. Suen, L. W. Engel, M. B. Santos, M. Shayegan, and D. C. Tsui, *Observation of a  $\nu = 1/2$  fractional quantum Hall state in a double-layer electron system*, *Phys. Rev. Lett.* **68** (1992).
- [114] J. P. Eisenstein, G. S. Boebinger, L. N. Pfeiffer, K. W. West, and S. He, *New fractional quantum Hall state in double-layer two-dimensional electron systems*, *Physical Review Letters* **68** (Mar., 1992) 1383–1386.
- [115] Y. Liu, S. Hasdemir, D. Kamburov, A. L. Graninger, M. Shayegan, L. N. Pfeiffer, K. W. West, K. W. Baldwin, and R. Winkler, *Even-denominator fractional quantum Hall effect at a Landau level crossing*, *Physical Review B* **89** (Apr., 2014) 165313.
- [116] Y. Liu, *Fractional quantum Hall effect at  $\nu = 1/2$  in hole systems confined to GaAs quantum wells*, *Phys. Rev. Lett.* **112** (2014).
- [117] D. R. Luhman, *Observation of a fractional quantum Hall state at  $\nu = 1/4$  in a wide GaAs quantum well*, *Phys. Rev. Lett.* **101** (2008).
- [118] J. Shabani, T. Gokmen, Y. T. Chiu, and M. Shayegan, *Evidence for Developing Fractional Quantum Hall States at Even Denominator  $1/2$  and  $1/4$  Fillings in Asymmetric Wide Quantum Wells*, *Physical Review Letters* **103** (Dec., 2009) 256802.
- [119] R. R. Du, *Fractional quantum Hall effect around  $\nu = 3/2$ : composite fermions with a spin*, *Phys. Rev. Lett.* **75** (1995).
- [120] A. C. Balram, C. Toke, A. Wójs, and J. K. Jain, *Phase diagram of fractional quantum Hall effect of composite fermions in multicomponent systems*, *Physical Review B* **91** (Jan., 2015) 45109.
- [121] D. A. Abanin, B. E. Feldman, A. Yacoby, and B. I. Halperin, *Fractional and integer quantum Hall effects in the zeroth Landau level in graphene*, *Physical Review B* **88** (Sept., 2013) 115407.

- [122] F. Pientka, J. Waissman, P. Kim, and B. I. Halperin, *Thermal Transport Signatures of Broken-Symmetry Phases in Graphene*, *Physical Review Letters* **119** (July, 2017) 27601.
- [123] D. S. Wei, T. v. d. Sar, S. H. Lee, K. Watanabe, T. Taniguchi, B. I. Halperin, and A. Yacoby, *Electrical generation and detection of spin waves in a quantum Hall ferromagnet*, *Science* **362** (Oct., 2018) 229–233.
- [124] A. Y. Kitaev, *Fault-tolerant quantum computation by anyons*, *Ann. Phys.* **303** (2003) 2–30.
- [125] J. K. Jain, *Composite-fermion approach for the fractional quantum Hall effect*, *Phys. Rev. Lett.* **63** (1989) 199–202.
- [126] B. I. Halperin, P. A. Lee, and N. Read, *Theory of the half-filled Landau level*, *Phys. Rev. B* **47** (1993) 7312–7343.
- [127] N. Read and D. Green, *Paired states of fermions in two dimensions with breaking of parity and time-reversal symmetries and the fractional quantum Hall effect*, *Phys. Rev. B* **61** (2000) 10267–10297.
- [128] Z. Papić and D. A. Abanin, *Topological phases in the zeroth Landau level of bilayer graphene*, *Phys. Rev. Lett.* **112** (2014) 46602.
- [129] K. Lee, B. Fallahazad, J. Xue, D. C. Dillen, K. Kim, T. Taniguchi, K. Watanabe, and E. Tutuc, *Chemical potential and quantum Hall ferromagnetism in bilayer graphene*, *Science* **345** (July, 2014) 58–61.
- [130] J. P. Eisenstein, L. N. Pfeiffer, and K. W. West, *Compressibility of the two-dimensional electron gas: Measurements of the zero-field exchange energy and fractional quantum Hall gap*, *Physical Review B* **50** (July, 1994) 1760–1778.
- [131] M. Levin, B. I. Halperin, and B. Rosenow, *Particle-hole symmetry and the Pfaffian state*, *Phys. Rev. Lett.* **99** (2007) 236806.
- [132] S.-S. Lee, S. Ryu, C. Nayak, and M. P. A. Fisher, *Particle-hole symmetry and the  $\nu = 5/2$  quantum Hall state*, *Phys. Rev. Lett.* **99** (2007) 236807.
- [133] V. M. Apalkov and T. Chakraborty, *Stable Pfaffian state in bilayer graphene*, *Phys. Rev. Lett.* **107** (2011) 186803.
- [134] M. A. Metlitski, D. F. Mross, S. Sachdev, and T. Senthil, *Cooper pairing in non-Fermi liquids*, *Phys. Rev. B* **91** (2015) 115111.
- [135] E. H. Rezayi and S. H. Simon, *Breaking of particle-hole symmetry by Landau level mixing in the  $\nu = 5/2$  quantized Hall State*, *Phys. Rev. Lett.* **106** (2011) 116801.

- [136] M. P. Zaletel, R. S. K. Mong, F. Pollmann, and E. H. Rezayi, *Infinite density matrix renormalization group for multicomponent quantum Hall systems*, *Phys. Rev. B* **91** (2015) 45115.
- [137] E. H. Rezayi, *Landau level mixing and the ground state of the  $\nu = 5/2$  quantum Hall effect*, *Phys. Rev. Lett.* **119** (2017) 26801.
- [138] M. Levin and B. I. Halperin, *Collective states of non-Abelian quasiparticles in a magnetic field*, *Phys. Rev. B* **79** (2009) 205301.
- [139] C. W. von Keyserlingk, S. H. Simon, and B. Rosenow, *Enhanced bulk-edge Coulomb coupling in fractional Fabry-Perot interferometers*, *Phys. Rev. Lett.* **115** (2015) 126807.
- [140] D. S. Wei, *Mach-Zehnder interferometry using spin- and valley-polarized quantum Hall edge states in graphene*, *Sci. Adv.* **3** (2017) e1700600.
- [141] M. Barkeshli, C. Nayak, Z. Papić, A. Young, and M. Zaletel, *Topological Exciton Fermi Surfaces in Two-Component Fractional Quantized Hall Insulators*, *Physical Review Letters* **121** (July, 2018) 26603.
- [142] S. Ryu, A. P. Schnyder, A. Furusaki, and A. W. W. Ludwig, *Topological insulators and superconductors: tenfold way and dimensional hierarchy*, *New Journal of Physics* **12** (June, 2010) 65010.
- [143] K. v. Klitzing, G. Dorda, and M. Pepper, *New Method for High-Accuracy Determination of the Fine-Structure Constant Based on Quantized Hall Resistance*, *Physical Review Letters* **45** (Aug., 1980) 494–497.
- [144] S. M. Girvin, *The Quantum Hall Effect: Novel Excitations and Broken Symmetries*, in *Topological aspects of low dimensional systems. Session LXIX. 7-31 July 1998*, Les Houches - Ecole d'Été de Physique Théorique, pp. 53–175. Springer, July, 1999.
- [145] C.-Z. Chang, J. Zhang, X. Feng, J. Shen, Z. Zhang, M. Guo, K. Li, Y. Ou, P. Wei, L.-L. Wang, Z.-Q. Ji, Y. Feng, S. Ji, X. Chen, J. Jia, X. Dai, Z. Fang, S.-C. Zhang, K. He, Y. Wang, L. Lu, X.-C. Ma, and Q.-K. Xue, *Experimental Observation of the Quantum Anomalous Hall Effect in a Magnetic Topological Insulator*, *Science* **340** (Apr., 2013) 167–170.
- [146] C. R. Dean, L. Wang, P. Maher, C. Forsythe, F. Ghahari, Y. Gao, J. Katoch, M. Ishigami, P. Moon, M. Koshino, T. Taniguchi, K. Watanabe, K. L. Shepard, J. Hone, and P. Kim, *Hofstadter's butterfly and the fractal quantum Hall effect in moiré superlattices*, *Nature* **497** (May, 2013) 598–602.

- [147] L. A. Ponomarenko, R. V. Gorbachev, G. L. Yu, D. C. Elias, R. Jalil, A. A. Patel, A. Mishchenko, A. S. Mayorov, C. R. Woods, J. R. Wallbank, M. Mucha-Kruczynski, B. A. Piot, M. Potemski, I. V. Grigorieva, K. S. Novoselov, F. Guinea, V. I. Fal'ko, and A. K. Geim, *Cloning of Dirac fermions in graphene superlattices*, *Nature* **497** (May, 2013) 594–597.
- [148] F. D. M. Haldane, *Model for a Quantum Hall Effect without Landau Levels: Condensed-Matter Realization of the "Parity Anomaly"*, *Physical Review Letters* **61** (Oct., 1988) 2015–2018.
- [149] G. Jotzu, M. Messer, R. A. Desbuquois, M. Lebrat, T. Uehlinger, D. Greif, and T. Esslinger, *Experimental realization of the topological Haldane model with ultracold fermions*, *Nature* **515** (Nov., 2014) 237–240.
- [150] D. C. Tsui, H. L. Stormer, and A. C. Gossard, *Two-Dimensional Magnetotransport in the Extreme Quantum Limit*, *Physical Review Letters* **48** (May, 1982) 1559–1562.
- [151] A. Tsukazaki, S. Akasaka, K. Nakahara, Y. Ohno, H. Ohno, D. Maryenko, A. Ohtomo, and M. Kawasaki, *Observation of the fractional quantum Hall effect in an oxide*, *Nature Materials* **9** (Nov., 2010) 889–893.
- [152] S. A. Parameswaran, R. Roy, and S. L. Sondhi, *Fractional Quantum Hall Physics in Topological Flat Bands*, *Comptes Rendus Physique* **14** (Nov., 2013) 816–839.
- [153] E. J. Bergholtz and Z. Liu, *Topological flat band models and fractional chern insulators*, *International Journal of Modern Physics B* **27** (Sept., 2013) 1330017.
- [154] A. S. Sørensen, E. Demler, and M. D. Lukin, *Fractional Quantum Hall States of Atoms in Optical Lattices*, *Physical Review Letters* **94** (Mar., 2005) 86803.
- [155] R. N. Palmer and D. Jaksch, *High-Field Fractional Quantum Hall Effect in Optical Lattices*, *Physical Review Letters* **96** (May, 2006) 180407.
- [156] G. Möller and N. R. Cooper, *Fractional Chern Insulators in Harper-Hofstadter Bands with Higher Chern Number*, *Physical Review Letters* **115** (Sept., 2015) 126401.
- [157] D. N. Sheng, Z.-C. Gu, K. Sun, and L. Sheng, *Fractional quantum Hall effect in the absence of Landau levels*, *Nature Communications* **2** (July, 2011) 389.
- [158] T. Neupert, L. Santos, C. Chamon, and C. Mudry, *Fractional Quantum Hall States at Zero Magnetic Field*, *Physical Review Letters* **106** (June, 2011) 236804.
- [159] N. Regnault and B. A. Bernevig, *Fractional Chern Insulator*, *Physical Review X* **1** (Dec., 2011) 21014.

- [160] P. Streda, *Theory of quantised Hall conductivity in two dimensions*, *Journal of Physics C: Solid State Physics* **15** (Aug., 1982) L717–L721.
- [161] A. H. MacDonald, *Landau-level subband structure of electrons on a square lattice*, *Physical Review B* **28** (Dec., 1983) 6713–6717.
- [162] L. Wang, Y. Gao, B. Wen, Z. Han, T. Taniguchi, K. Watanabe, M. Koshino, J. Hone, and C. R. Dean, *Evidence for a fractional fractal quantum Hall effect in graphene superlattices*, *Science* **350** (Dec., 2015) 1231–1234.
- [163] A. Kol and N. Read, *Fractional quantum Hall effect in a periodic potential*, *Physical Review B* **48** (Sept., 1993) 8890–8898.
- [164] A. Kumar, R. Roy, and S. L. Sondhi, *Generalizing quantum Hall ferromagnetism to fractional Chern bands*, *Physical Review B* **90** (Dec., 2014) 245106.
- [165] M. Barkeshli and X.-L. Qi, *Topological Nematic States and Non-Abelian Lattice Dislocations*, *Physical Review X* **2** (Aug., 2012) 31013.
- [166] Y.-L. Wu, N. Regnault, and B. A. Bernevig, *Bloch Model Wave Functions and Pseudopotentials for All Fractional Chern Insulators*, *Physical Review Letters* **110** (Mar., 2013) 106802.
- [167] A. Sterdyniak, C. Repellin, B. A. Bernevig, and N. Regnault, *Series of Abelian and non-Abelian states in  $\mathbb{C}1\mathbb{S}$  fractional Chern insulators*, *Physical Review B* **87** (May, 2013) 205137.
- [168] X. Chen, J. R. Wallbank, M. Mucha-Kruczyński, E. McCann, and V. I. Fal’ko, *Zero-energy modes and valley asymmetry in the Hofstadter spectrum of bilayer graphene van der Waals heterostructures with hBN*, *Physical Review B* **94** (July, 2016) 45442.
- [169] M. Lee, J. R. Wallbank, P. Gallagher, K. Watanabe, T. Taniguchi, V. I. Fal’ko, and D. Goldhaber-Gordon, *Ballistic miniband conduction in a graphene superlattice*, *Science* **353** (Sept., 2016) 1526–1529.
- [170] A. M. DaSilva, J. Jung, and A. H. MacDonald, *Fractional Hofstadter States in Graphene on Hexagonal Boron Nitride*, *Physical Review Letters* **117** (July, 2016) 36802.
- [171] M. Banerjee, M. Heiblum, V. Umansky, D. E. Feldman, Y. Oreg, and A. Stern, *Observation of half-integer thermal Hall conductance*, *Nature* **559** (July, 2018) 205–210.
- [172] Y. Kim, A. C. Balram, T. Taniguchi, K. Watanabe, J. K. Jain, and J. H. Smet, *Even denominator fractional quantum Hall states in higher Landau levels of graphene*, *Nature Physics* **15** (Feb., 2019) 154.



- [173] N. Hartman, C. Olsen, S. LÄEscher, M. Samani, S. Fallahi, G. C. Gardner, M. Manfra, and J. Folk, *Direct entropy measurement in a mesoscopic quantum system*, *Nature Physics* **14** (Nov., 2018) 1083–1086.
- [174] D. Zhang, X. Huang, W. Dietsche, K. von Klitzing, and J. H. Smet, *Signatures for Wigner Crystal Formation in the Chemical Potential of a Two-Dimensional Electron System*, *Physical Review Letters* **113** (Aug., 2014).
- [175] M. S. Dresselhaus and G. Dresselhaus, *Intercalation compounds of graphite*, *Advances in Physics* **51** (Jan., 2002) 1–186.
- [176] C. L. Lu, C. P. Chang, Y. C. Huang, R. B. Chen, and M. L. Lin, *Influence of an electric field on the optical properties of few-layer graphene with AB stacking*, *Physical Review B* **73** (Apr., 2006) 144427.
- [177] F. Guinea, A. H. Castro Neto, and N. M. R. Peres, *Electronic states and Landau levels in graphene stacks*, *Physical Review B* **73** (June, 2006) 245426.
- [178] H. Min, B. Sahu, S. K. Banerjee, and A. H. MacDonald, *Ab initio theory of gate induced gaps in graphene bilayers*, *Physical Review B* **75** (Apr., 2007) 155115.
- [179] A. GrÄEneis, C. Attaccalite, L. Wirtz, H. Shiozawa, R. Saito, T. Pichler, and A. Rubio, *Tight-binding description of the quasiparticle dispersion of graphite and few-layer graphene*, *Physical Review B* **78** (Nov., 2008) 205425.
- [180] B. Datta, H. Agarwal, A. Samanta, A. Ratnakar, K. Watanabe, T. Taniguchi, R. Sensarma, and M. M. Deshmukh, *Landau Level Diagram and the Continuous Rotational Symmetry Breaking in Trilayer Graphene*, *Physical Review Letters* **121** (July, 2018) 56801.
- [181] A. H. MacDonald, *Influence of Landau-level mixing on the charge-density-wave state of a two-dimensional electron gas in a strong magnetic field*, *Physical Review B* **30** (Oct., 1984) 4392–4398.
- [182] F. Zhang, D. Tilahun, and A. H. MacDonald, *Hund’s rules for the  $N=0$  Landau levels of trilayer graphene*, *Physical Review B* **85** (Apr., 2012) 165139.
- [183] R. K. Goodall, R. J. Higgins, and J. P. Harrang, *Capacitance measurements of a quantized two-dimensional electron gas in the regime of the quantum Hall effect*, *Physical Review B* **31** (May, 1985) 6597–6608.
- [184] R. C. Ashoori, H. L. Stormer, J. S. Weiner, L. N. Pfeiffer, S. J. Pearton, K. W. Baldwin, and K. W. West, *Single-electron capacitance spectroscopy of discrete quantum levels*, *Physical Review Letters* **68** (May, 1992) 3088–3091.
- [185] A. F. Young and L. S. Levitov, *Capacitance of graphene bilayer as a probe of layer-specific properties*, *Physical Review B* **84** (Aug., 2011) 85441.

- [186] J. Jang, B. M. Hunt, L. N. Pfeiffer, K. W. West, and R. C. Ashoori, *Sharp tunnelling resonance from the vibrations of an electronic Wigner crystal*, *Nature Physics* **13** (Apr., 2017) 340–344.
- [187] J. Jang, *Private Communication*, 2017.
- [188] S. Luryi, *Quantum capacitance devices*, *Applied Physics Letters* **52** (Feb., 1988) 501–503.
- [189] S. R. White, *Density matrix formulation for quantum renormalization groups*, *Physical Review Letters* **69** (Nov., 1992) 2863–2866.
- [190] S. Girvin and R. Prange, eds., *The Quantum Hall Effect*. Springer-Verlag, 1987.
- [191] J. Jung and A. H. MacDonald, *Accurate tight-binding models for the  $\pi$  bands of bilayer graphene*, *Physical Review B* **89** (Jan., 2014) 35405.
- [192] H. Li and F. D. M. Haldane, *Entanglement Spectrum as a Generalization of Entanglement Entropy: Identification of Topological Order in Non-Abelian Fractional Quantum Hall Effect States*, *Physical Review Letters* **101** (July, 2008) 10504.
- [193] A. Kitaev and J. Preskill, *Topological Entanglement Entropy*, *Physical Review Letters* **96** (Mar., 2006) 110404.
- [194] S. D. Geraedts, M. P. Zaletel, R. S. K. Mong, M. A. Metlitski, A. Vishwanath, and O. I. Motrunich, *The half-filled Landau level: The case for Dirac composite fermions*, *Science* **352** (Apr., 2016) 197–201.
- [195] R. H. Morf, *Transition from Quantum Hall to Compressible States in the Second Landau Level: New Light on the  $\nu = 5/2$  Enigma*, *Physical Review Letters* **80** (Feb., 1998) 1505–1508.
- [196] E. H. Rezayi and F. D. M. Haldane, *Incompressible Paired Hall State, Stripe Order, and the Composite Fermion Liquid Phase in Half-Filled Landau Levels*, *Physical Review Letters* **84** (May, 2000) 4685–4688.
- [197] P. G. Harper, *Single Band Motion of Conduction Electrons in a Uniform Magnetic Field*, *Proceedings of the Physical Society. Section A* **68** (Oct., 1955) 874–878.
- [198] M. Y. Azbel, *Energy spectrum of a conduction electron in a magnetic field.*, .
- [199] D. Langbein, *The Tight-Binding and the Nearly-Free-Electron Approach to Lattice Electrons in External Magnetic Fields*, *Physical Review* **180** (Apr., 1969) 633–648.

- [200] D. Pfannkuche and R. R. Gerhardts, *Theory of magnetotransport in two-dimensional electron systems subjected to weak two-dimensional superlattice potentials*, *Physical Review B* **46** (Nov., 1992) 12606–12626.
- [201] R. R. Gerhardts, D. Weiss, and U. Wulf, *Magnetoresistance oscillations in a grid potential: Indication of a Hofstadter-type energy spectrum*, *Physical Review B* **43** (Feb., 1991) 5192–5195.
- [202] T. Schäfer, K. Ensslin, J. P. Kotthaus, and M. Holland, *Internal structure of a Landau band induced by a lateral superlattice: a glimpse of Hofstadter’s butterfly*, *EPL (Europhysics Letters)* **33** (Mar., 1996) 683.
- [203] G. Möller and N. R. Cooper, *Composite Fermion Theory for Bosonic Quantum Hall States on Lattices*, *Physical Review Letters* **103** (Sept., 2009) 105303.
- [204] A. Sterdyniak, N. Regnault, and G. Möller, *Particle entanglement spectra for quantum Hall states on lattices*, *Physical Review B* **86** (Oct., 2012) 165314.
- [205] T. Scaffidi and S. H. Simon, *Exact solutions of fractional Chern insulators: Interacting particles in the Hofstadter model at finite size*, *Physical Review B* **90** (Sept., 2014) 115132.
- [206] F. Harper, S. H. Simon, and R. Roy, *Perturbative approach to flat Chern bands in the Hofstadter model*, *Physical Review B* **90** (Aug., 2014) 75104.
- [207] C. H. Lee, R. Thomale, and X.-L. Qi, *Pseudopotential formalism for fractional Chern insulators*, *Physical Review B* **88** (July, 2013) 35101.
- [208] D. Bauer, T. S. Jackson, and R. Roy, *Quantum geometry and stability of the fractional quantum Hall effect in the Hofstadter model*, *Physical Review B* **93** (June, 2016) 235133.
- [209] D. Pfannkuche and A. H. MacDonald, *Quantum Hall effect of interacting electrons in a periodic potential*, *Physical Review B* **56** (Sept., 1997) R7100–R7103.
- [210] I. P. McCulloch, *Infinite size density matrix renormalization group, revisited*, *arXiv:0804.2509 [cond-mat]* (Apr., 2008).
- [211] F. Pollmann, S. Mukerjee, A. M. Turner, and J. E. Moore, *Theory of Finite-Entanglement Scaling at One-Dimensional Quantum Critical Points*, *Physical Review Letters* **102** (June, 2009) 255701.